Convected Particle Domain Interpolation Method for Large Deformation Geotechnical Problems

Von der Fakultät für Bau– und Umweltingenieurwissenschaften
der Universität Stuttgart
zur Erlangung der Würde eines Doktors der Ingenieurwissenschaften (Dr.-Ing.)
genehmigte Abhandlung,

vorgelegt von

Shreyas Giridharan
aus Chennai, Indien

Hauptberichter:	Univ.-Prof. Dr.-Ing. habil. Christian Moormann
Mitberichter:	Prof. Dr. Dieter Stolle
	Univ.-Prof. Dr.-Ing. Frank Rackwitz
Tag der mündlichen Prüfung:	11. November 2022

Institut für Geotechnik der Universität Stuttgart

2022

Mitteilung 77
des Instituts für Geotechnik
Universität Stuttgart, Deutschland 2022

Herausgeber:
Univ.-Prof. Dr.-Ing. habil. Christian Moormann

Institut für Geotechnik
Universität Stuttgart
Pfaffenwaldring 35
70569 Stuttgart

Schlagwörter: Material Point Method (MPM), Convected Particle Domain Interpolation Method (CPDI), Theory of Porous Media (TPM), Liquefaction, Monopile Installation Simulation, Offshore Monopile Vibratory Installation.

Druck: FORMAT Druck GmbH, Stuttgart, Deutschland, 2023

ISBN 978-3-921837-77-1
(D93 – Dissertation, Universität Stuttgart)

Preface of the Editor

Over the years, the application of numerical analysis in geotechnical engineering has gained traction, but it is often still limited to small-deformation problems. Simulation of large deformations necessitates a re-evaluation of the methods employed to simulate such cases. Alternatives to the conventional finite element method (FEM), such as the Coupled Eulerian-Lagrangian (CEL), the Arbitrary Lagrangian-Eulerian (ALE), etc., have gained popularity over the years – partly due to their accessibility in commercial simulation software and the abundance of user-defined soil models available for them. The opaque "black box" nature of these codes severely restricts the research potential of these programmes, despite the fact that they provide a straightforward method of calculating soil and soil-structure interaction. For this reason, Dr.-Ing. Shreyas Giridharan chose to focus his research on the Convected Particle Domain Interpolation (CPDI) method, which is an enhanced Material Point Method (MPM) scheme and which was developed and refined at the Institute of Geotechnical Engineering, University of Stuttgart.

The primary objective of Dr. Shreyas Giridharan's research work was to incorporate pore-fluid interaction into the CPDI code in order to simulate two-phase material, especially for fluid-saturated soil systems. In addition, the objective was to implement a constitutive law, known as the UBCSAND model, an elasto-plastic model that captures hardening and softening as well as the liquefaction effects in dynamically loaded soil. To this end, the initial chapters of this work focus on implementing and rigorously validating the accuracy of the implementation by using analytical solutions and experimental results for example by simulation of a granular column test or a shake table test, typical benchmark tests used to model liquefaction of granular soils.

The second objective of this study is the application of the developed and validated CPDI scheme on the numerical simulation of pile installation processes. The investigations focus on the numerical simulation of offshore monopile installation in saturated non-cohesive soils as a fully dynamic process and by considering effects like liquefaction and pore-water pressure changes in a physically adequate manner. Even though offshore installation of wind turbines and their foundations have been extensively studied and documented, the vibrational installation of mono-piles is a fairly new approach with the potential to reduce hydrosonic noise and fatigue of the steel pipe in comparison to an impact-driven installation while increasing penetration rate significantly.

For this study, Dr. Giridharan chose three simulations with distinct time and length

scale, beginning with a model scale monopile installation experiment and progressing to a full-scale offshore monopile. The plan was to validate the numerical package using the small-scale tests against the experimental results made available by the TU Berlin partners. The validated model was utilised for back-calculating results from the VibroPile project, and was subsequently utilised for Class-A simulation of vibratory monopile installations for the VISSKA offshore project in the German Bight. Dr. Giridharan's scientific contributions focus on the application of the two-phase CPDI code to achieve simulation results of Class-A quality which later prove to be in good agreement to the field data gained during execution. These results demonstrated that the CPDI code is capable of simulating highly dynamic processes involving soil-structure interaction and complex boundary conditions. It is worth to highlight that Dr. Giridharan succeeded in simulating the installation process over the whole penetration depth for real scale conditions as a dynamic process in two-phase soil material what can be considered as an outstanding scientific achievement.

Dr. Giridharan's dissertation demonstrates that the CPDI tool developed at the Institute for Geotechnical Engineering at the University of Stuttgart is a potent and versatile tool for not only simulation of large deformations, but also investigating the soil structure interaction during and after dynamic processes.

This research was partially funded by innogy SE as part of the VIBRO CAFÉ (VIBRO III) project, under grant number 92032410, and the project VISSKA, funded by the German Federal Ministry of Economic Affairs and Climate Action and coordinated by the Project Management Jülich (PtJ) under grant number 03EE3034D. Their contributions to the completion of this project are gratefully acknowledged.

Stuttgart, November 2022
Univ.-Prof. Dr.-Ing. habil. Christian Moormann

Acknowledgements

The results presented in this dissertation are the result of work performed between 2017 and 2022 at the Institute of Geotechnical Engineering at the University of Stuttgart. Behind the successful completion of this thesis, a great deal of assistance and contribution must be acknowledged.

I would like to express my deepest appreciation to my advisor, Professor Christian Moormann, for his extensive guidance, patience, and support, as well as for sharing his knowledge and experience. My academic career has advanced to this point because of Professor Moormann's guidance. My heartfelt appreciation extends to Professor Dieter Stolle for sharing his ideas, providing me with encouragement, and serving as a mentor during my PhD journey. I'm grateful for our many video conference calls about everything from research to daily life, and I'm lucky to have worked with him during his many trips to Stuttgart. I would like to thank Professor Frank Rackwitz for the stimulating conversations during my many visits to TU Berlin and for serving on my defence committee. I would also like to thank Prof. Philip Leistner for chairing my defence committee.

My interactions with Lisa Becker, Stefan Crienitz, Seyedfarzad Fatemizadeh, Sujith Gowda, Birgit Hagenau, Bastian Hoffmann, Till Kugler, Matin Liaghi, Jana Liebl, Alessandro Miraldi, Tobias Schlager, Moritz Schleeh, Nadja Springer, Egest Veselaj and Rainer Wellhäußer not only made my time at the institute productive, but also enjoyable. My heartfelt thanks go to them. I'd also like to thank my colleagues Felix Mitlmeier, Mustafa Mustafa and Bernd Zweschper for putting up with my numerous discussions and concerns.

I am grateful to my wife Surya, who provided valuable support as I completed this manuscript.

I am extremely grateful to my parents, Mrs. Hema and Mr. Giridharan, as well as my aunt, Ms. Anuradha, for always believing in me, encouraging me to pursue this academic endeavour, and being happy for me when even the smallest of victories were achieved. This work is dedicated to them.

Stuttgart, November 2022
Shreyas Giridharan

त्वदीयाभिः वाग्भिः

tvadhīyābhih vāghbhih

(written with your words)

Contents

List of Figures

List of Tables

Abstract

Renewable energies are increasingly becoming the energy source of the future, and offshore wind energy is unquestionably one of the most attractive means of producing clean energy, owing in part to its adaptability, scalability, durability of operation, and quick installation time. While the installation method and practise have been well-established over the past few decades, there are still knowledge gaps regarding the vibratory installation of offshore monopiles that need to be filled. The raison d'être of this monograph is to develop and validate a numerical tool that can predict the installation behaviour of these monopiles with reasonable accuracy.

Large displacements of the structures and large deformations of the soil continuum cannot be neglected when numerically modelling pile installation. Convected Particle Domain Interpolation (CPDI), an enhanced version of the Material Point Method (MPM), is used to address this challenge. MPM is ideally suited for granular material simulations and geomechanical simulations. CPDI, as a derivative of the MPM method, avoids spurious stress oscillations, which are inherent to MPM, while simultaneously capturing domain shear, which is not possible with the conventional formulation. In addition, this monograph extends the CPDI method to capture the pore fluid within the soil continuum by applying the Theory of Porous Media (TPM) to the CPDI formulation. Implemented is the UBCSAND constitutive law, an elasto-plastic model that captures hardening/softening behaviour as well as liquefaction of continuum under dynamic load. A combined tool that allows simulation of liquefaction and modelling of the saturated medium offers the best opportunity to replicate and then analyse the state parameter changes around the region of interest, which in this thesis is the region surrounding the jacket of the pile.

At each stage, the implemented method is compared to experimental/analytical results. While the CPDI code is validated using analytical solutions and experimental results, which was the simulation of granular column collapse in this thesis, the UBCSAND constitutive law, implemented in-house, is validated using experimental results from a shake table test, a typical benchmark test used to model liquefaction of sandy soils. The validated code is utilised to reproduce the outcomes of two experiments: i) a lab-scale test of monopile vibration and impact hammering, and ii) a full-scale test of monopile vibration in saturated sand. In the numerical back analysis of the lab-scale test, the objective was to validate the feasibility of using the CPDI numerical package to model pile installation simulation with good quality data about pore pressure changes and soil displacement. In the numerical simulation of the full-scale monopile, however, the focus

was on the ability of the numerical model to accurately capture the pile installation behaviour with changing dynamic forces. Finally, a *Class-A* simulation of the monopile installation behaviour is provided and compared to field measurements to validate the model developed for this thesis.

The thesis consists of seven chapters. Chapter 1 provides an introduction to monopiles, the geomechanical aspects to consider, and the stated research objectives. Chapter 2 examines the techniques for capturing liquefaction in soil continuum, the continuum-based numerical methods for modelling large deformations, and a brief summary of meshless methods. The MPM formulation for a single-phase continuum and its extension to CPDI are described in Chapter 3. The contact algorithm implemented in this work is also briefly discussed. Validity of the current CPDI algorithm is demonstrated by simulating the collapse of a granular column and comparing the results to those of experiments. Chapter 4 describes the extension of CPDI to model pore fluid and the accuracy of its implementation using the well-known Terzaghi's consolidation. The emphasis of Chapter 5 is on the implementation of the UBCSAND model. The constitutive model is evaluated by comparing the element test and shake table test results to experimental data. More emphasis has been placed on the application of the CPDI code to pile installation modelling in Chapter 6. The outcomes of two tests, model scale and real scale, are compared to experimental/field results. In addition, the comparison of Class-A simulation results to field data is discussed. Despite the model's homogenisation, good results are obtained. As a final summary and conclusion, Chapter 7 presents the key findings of this research along with suggestions for future research in this area.

Kurzfassung

Erneuerbare Energien werden immer mehr zur Energiequelle der Zukunft und die Offshore- Windenergie ist zweifellos aufgrund ihrer Anpassungsfähigkeit, Skalierbarkeit, Langlebigkeit und kurzen Installationszeit eine der attraktivsten Möglichkeiten zur Erzeugung sauberer Energie. Während sich die Installationsmethodik in den letzten Jahrzehnten gut etabliert hat, existieren immer noch Wissenslücken in Bezug auf die Vibration von Offshore-Monopiles, die es zu schließen gilt. Die Ziele dieser Monographie sind die Entwicklung und Validierung eines numerisches Werkzeugs, mit dem das Installationsverhalten dieser Monopiles mit angemessener Genauigkeit vorhergesagt werden kann.

Bei der numerischen Simulation der Pfahlinstallation können große Verformungen des Pfahls und des Bodenkontinuums nicht vernachlässigt werden. Die *Convected Particle Domain Interpolation* (CPDI), eine verbesserte Version der Material Point Method (MPM), wird eingesetzt, um diese Herausforderung zu meistern. Die MPM eignet sich gut zur Simulation granularen Materials und geomechanischer Problemstellungen. Die CPDI hat als Nachfolger der Material Point Method gegenüber dieser zwei entscheidende Vorteile: Sie vermeidet störende Spannungsschwankungen und erfasst gleichzeitig die Scherung der sog. Particle Domains. Darüber hinaus wird in dieser Dissertation die CPDI-Methode um die Theorie der porösen Medien (TPM) erweitert, indem Porenwasser innerhalb des Bodenkontinuums erfasst wird. Das mechanische Verhalten des Bodens wird mit dem UBCSAND-Stoffmodell abgebildet. Hierbei handelt es sich um ein elasto-plastisches Modell, das sowohl *Hardening* und *Softening* Effekte als auch die Verflüssigung des Bodens unter dynamischer Belastung erfasst. Es wird also ein numerisches Tool erschaffen, welches erlaubt, das gesättigte Medium sowie Verflüssigungseffekte bestmöglich abzubilden um somit Änderungen der Zustandsparameter des den Pfahl umgebenden Bodens nachzubilden und anschließend zu analysieren.

Der CPDI-Code wird in dieser Arbeit analytisch und experimentell mit Hilfe des *Granular-Column-Collapse* Versuchs validiert. Weiterhin wird das institutsintern implementierte UBCSAND-Stoffmodell anhand experimenteller Ergebnisse eines Shake-Table Tests validiert, einem typischen Referenzversuch zur Verflüssigungsmodellierung von Sandböden. Der validierte Code wird verwendet, um die Ergebnisse von zwei Experimenten zu reproduzieren: i) einen Versuch im Labormaßstab zur Vibration und Rammung von Monopiles und ii) einen Versuch im Realmaßstab mit vibrierten Monopiles. Ziel der ersten numerischen Back-Analysis war es die Anwendbarkeit des entwickelten CPDI-

Codes hinsichtlich der Pfahlinstallation mit qualitativ hochwertigen Daten zu Porenwasserdruckänderungen und Bodenverschiebungen zu überprüfen. In der zweiten Nachrechnung lag der Fokus auf der Eignung des numerischen Modells das Verhalten des Pfahls bei der Installation unter wechselnden dynamischen Kräften genau zu erfassen. Zuletzt wird eine sog. *Class-A*-Prognose zum Verhalten des Monopiles bei der Installation durchgeführt und mit Feldmessungen verglichen, um das für diese Arbeit entwickelte Modell zu validieren.

Diese Monographie besteht aus sieben Kapiteln. In Kapitel 1 werden die Grundlagen zu Monopiles, die dazugehörigen geotechnischen Fragestellungen sowie die in dieser Arbeit festgesetzten Forschun-gsziele erläutert. In Kapitel 2 wird der aktuelle Wissensstand zur Modellierung der Bodenverflüssigung und zu kontinuumsbasierten numerischen Methoden zur Erfassung großer Verformungen erörtert. Die Finite-Elemente-Methoden *Lagrangian* und *Eulerian* sowie netzbasierte Partikelansätze, die ursprünglich zur Entwicklung der in dieser Studie verwendeten CPDI-Methode führten, werden vorgestellt.

Kapitel 3 beschreibt den aktuellen Wissensstand zur Material Point Method (MPM) und zur Convected Particle Domain Interpolation Method (CPDI) sowie deren Implementierung. Außerdem wird der im CPDI-Code verwendete *Penalty*-Algorithmus erläutert. Des Weiteren werden die Simulationen, mit deren Hilfe die Code-Implementierung validiert wurde, und deren Anwendung für kontinuumsbasierte Problemstellungen mit großen Verformungen vorgestellt. Die numerische Abbildung der hydraulischen Strömung in granularem Material wird mit experimentellen Ergebnissen verglichen und die Auswirkungen verschiedener Einflussparameter wie Dämpfung, Partikelanzahl und Glättungsverfahren werden diskutiert.

Die in Kapitel 3 vorgestellte einphasige CPDI wird in Kapitel 4 um die Porenwasser-Phase erweitert. Es werden die maßgebenden Gleichungen der zweiphasigen CPDI, der Lösungsprozess und ein Beispiel zur Validierung der Implementierung diskutiert.

Kapitel 5 enthält die Implementierung des UBCSAND-Modells im CPDI-Code. Die Implementierung des UBCSAND-Modells wird durch Rückrechnung des zyklischen DSS-Versuchs und des Rütteltischversuchs validiert. In diesem Kapitel wird auch der Einfluss des Stoffgesetzes auf die Endergebnisse des Rütteltischversuchs untersucht.

In Kapitel 6 wird die Verwendbarkeit des CPDI-Codes hinsichtlich der Monopile-Installation bewertet. Es werden drei numerische Modelle zur Pfahlinstallation mit zunehmendem Komplexitätsgrad vorgestellt. Zuerst wird die Vibration und die Rammung eines offenen Stahlrohrpfahls simuliert und der Installationsfortschritt mit experimentellen Ergebnissen verglichen. Die Bewertung dieser Modelle erfolgt anhand der Änderung der Bodenzustandsgrößen, der effektiven Spannung und des Porenwasserdrucks. Im zweiten Beispiel werden mit dem CPDI-Code Feldversuche nachgerechnet, die im Rahmen des Projekts *VibroPile* stattfanden. Hier wurde wiederum die Vibration eines

Monopiles numerisch abgebildet und anhand der Ergebnisse der Vibro-Versuche beurteilt. Zuletzt wird in diesem Kapitel die Vibration eines Monopiles simuliert um die Ergebnisse eines später durchgeführten Feldversuchs zu prognostizieren und abzuschätzen.

Kapitel 7 enthält die Schlussfolgerungen dieses Forschungsvorhabens und Empfehlungen für zukünftige Forschung in diesem Fachbereich.

Chapter 1

Introduction

In geomechanical problems, large deformations are prevalent, yet their numerical modelling is challenging and intricate. Modelling landslides, dam failures, and even pile driving requires a technique that numerically captures large material movement while converging to a realistic, stable solution. In addition to capturing massive distortions, it is essential to understand and replicate the physics underlying the events that cause these material movements. Seismic events are known to be very destructive, not only because of the dangers posed by man-made structures, but also because of the massive material shifts induced by auxiliary phenomena like as liquefaction, which can serve as a trigger for destruction.

To capture massive deformations numerically, we must look beyond the traditional finite element method. Limitations of the finite element method that produce mesh distortions make it difficult to achieve a valid solution. Alternative numerical approaches based on an adaptive meshing scheme, such as the well-known and widely available Arbitrary Lagrangian-Eulerian scheme, or other "black-box" methods, are required to represent such issues, notwithstanding the limitations associated with such methods. Instead, the Material Point Method (MPM) and its extension, the Convected Particle Domain Interpolation Method (CPDI) is to be explored. Because the problems of interest are dynamic, it is necessary to employ an explicit time-marching technique. In addition, a multi-phase CPDI can be extended to account for the coupled behaviour of the soil. Regardless of the computational overhead a coupled formulation imposes on a calculation, it is necessary to accurately represent the physics behind complex and dynamic processes.

While it is possible to capture the impacts of highly dynamic processes using a complicated constitutive law, it is not guaranteed to recreate the behaviour of saturated soil without a finite element formulation that accounts for the soil's porous nature. Proper modelling of fully saturated soil is possible with the Theory of Porous Media, which not only accounts for the deformation of the solid soil matrix, but also the changes in the pore fluid matrix [58]. In this case, a homogenisation process must be done to the continuum in order to generate a model with averaged attributes and behaviour. The introduction of volume fractions, which is crucial to the description of fluid-saturated soils, partially mitigates this disregard for microtopology-related infor-

mation and smearing of the continuum. The difficulty remains in precisely defining the motion of both fluid and solid elements. In accordance with the notion of volume fractions, the porous soil always represents a control space. Liquid or gaseous pore fluids can only leave the control space. According to this theory, the pores are considered to be statistically evaluated for the model and uniformly distributed in the reference state. It is presumed that an arbitrary elemental volume consists of the volume components of the actual constituents. The foundation of the formulation of porous media is a model of the macroscopic body for which neither a geometrical representation nor the precise location is addressed. The constituents are smeared across the control space, which consists of the porous solid, after being bonded against one another.

Moreover, it is not only essential that we represent the large mass movements in the numerical model, but also that we capture the underlying physics underpinning these movements. In order to accomplish this, an effort has been undertaken to present a unified numerical package that will represent the massive movements and the fundamental physics underlying such mass movements. Certain obstacles must be overcome in order to construct such an unified solution. First, a simulation tool that can consistently handle large deformations must be developed. Since the soil continuum undergoes significant deformation, conventional finite element approaches reveal severe deficiencies, which are addressed in this work. In addition, a constitutive law that can reproduce the behaviour of the soil under dynamic stress is required. Not only must such a constitutive law be capable of capturing the complicated non-linear behaviour of the soil, but it must also be able to do it in a reasonable amount of time. The precision of the constitutive law in simulating reality has a significant impact on the reliability of the simulations' outcomes. In this study, a suitable constitutive law and the two-phase CPDI were used to model reality and their effectiveness was evaluated.

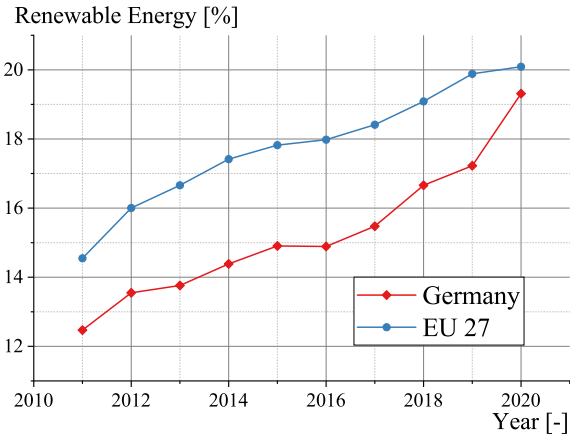

(a) Share of energy from renewables in EU 27 and Germany [32]

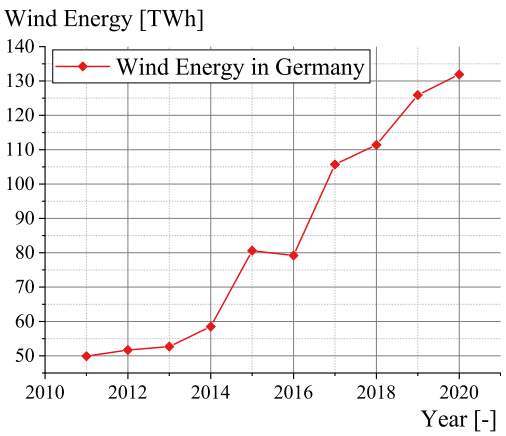

(b) Share of wind energy in Germany

Figure 1.1: Development of renewable energy in EU 27 and Germany

Intended application of the method

Today, nations are urgently tasked with substantially expanding their use of renewable energy sources. This requirement has prompted a discussion in Europe over the most effective and efficient support plan. Figure 1.1a demonstrates that the proportion of renewable energy has continuously increased over the years, necessitating a greater emphasis on phasing out fossil fuels entirely. Wind energy, among others, has been extensively marketed for greater acceptability due to its relative cleanliness, rapid implementation, and long-term dependability. Wind power was utilised by windmills and sailing ships, for water pumping and irrigation, for grinding grain and sawing rice, among other things. The first record of windmills in Europe comes from the ninth century in England, eleventh century in France and on the Polish lands in the thirteenth century [126]. As seen in Figure 1.1b, the production of wind energy in Germany has also increased steadily, aided by the renewed drive towards offshore wind energy projects. While there are various types of foundations for fixed grounded wind turbine systems, such as monopiles, monopod caissons, and gravity base - for sea levels less than 30 metres - and jacketed caissons, tripod pile, tripod caisson, etc. - for sea levels greater than 30 metres, monopiles are becoming the preferred foundations for offshore wind farms in Germany.

Figure 1.2: Offshore installation of wind turbine [43]

Monopiles (as seen in Figure 1.2) are one of the most prevalent offshore wind turbine support structures. This is mostly due to its straightforward manufacturing and installation. The majority of monopiles have been deployed by impact-driving them into the seafloor. Geotechnically speaking, the penetration of impact-driven and vibratory-driven monopiles is one of the most complex processes, involving multiple phenomena.

Considering the interaction between the soil, pore fluid, and the monopile installation process adds to the complexity. Installation of a monopile causes significant soil disturbances in the surrounding area. These variations affect not just the installation's behaviour, but also its axial and lateral bearing capacity. A deeper appreciation of the pile installation procedure will permit the formulation of optimal installation parameters. Developing a model that has been evaluated against model and real scale pile installation is one approach for enhancing installation behaviour predictions. Developing such a model is challenging, as it requires taking into account the highly non-linear response of the soil, capturing and considering the large deformation around the pile, considering the effect of the dynamic installation on the pore fluid, taking into account the contact between the pile and soil, and capturing the effect of wave propagation in both the solid and fluid phases. The installation characteristics, such as pile installation rate, axial and lateral strength, behaviour against dynamic cycle stresses imposed by impinging waves, etc., could be predicted by developing a model that combines all of the aforementioned issues. The offshore monopile planners would benefit from the development of a numerical method that can predict such a pile installation in advance by proving their installation parameters beforehand and providing them with granular information of the pile and soil, which could be used in iterative design.

Any academic work geared toward assisting the industry in comprehending the installation or behaviour of offshore monopile installations would contribute directly to achieving carbon neutrality rapidly. This monograph contains efforts towards that end.

1.1 Contributions

This research aims to address the following questions:

- Can large granular media deformations be captured by the two-phase Material Point Method (MPM), and by extension, the Convected Particle Domain Interpolation (CPDI) method, which is based on the Theory of Porous Media?
- Can the numerical package consistently calculate and reproduce experimental results?
- Can a validated method be developed to forecast the behaviour of saturated media in advance, taking into account their interaction with solid structures?

Validation of the model assesses the performance of the numerical package in modelling real-world behaviour. The primary technique utilised in this study is a comparison of numerical results to actual experiments. This would not only aid in detecting the causes

of inaccuracy in the model or its implementation, but it would also enhance the credibility of the numerical model in reproducing the actual or anticipated results. Chapters 3 and 4 detail the CPDI code's numerical makeup. In both Chapters, analytical and experimental data and results are used to validate the code. In Chapter 5, the implementation of the material model is described in depth, and it is demonstrated that the considered numerical model can replicate the behaviour of fluid-saturated soil under different dynamic forces. In Chapter 6, field data and numerical data are compared in order to validate the existing numerical model against a wide variety of dynamic processes and boundary conditions. If the model passes this test of validation, it is reasonable to believe that it can also predict the behaviour of continuum in advance for future projects.

A significant portion of this monograph focuses on integrating the large deformation CPDI code with two-phase characteristics, which can model both soil and pore fluid, along with an appropriate constitutive law that can not only model the stress-strain relation of the soil continuum, but also capture the dynamic behaviour of the saturated soil, primarily liquefaction. This work demonstrates the tendency of saturated soil to liquefy under dynamic loads within the CPDI framework. In addition to developing a CPDI code that is capable of capturing the massive deformation behaviour of porous fluid saturated soil and structures, this study entails implementing an appropriate and validated constitutive law to reproduce the behaviour of soil. The CPDI code includes the UBCSAND model, a constitutive law capable of capturing liquefaction effects. The numerical package, which comprises of the CPDI code and the constitutive law, is evaluated using a benchmark test. The numerical code is then used to model the installation of open steel pipe piles. Back analysis of model and real scale pile vibration simulation is given careful consideration. The pile installations that were modelled varied in size from small model piles to an large diameter offshore monopile. Finally, a *Class-A* forecast of offshore pile installation is presented and compared to field data.

1.2 Thesis layout

This monograph consists of seven chapters, the introduction being one of them. In Chapter 2, the current status of liquefaction modelling is discussed, followed by a comprehensive literature review of the current state of modelling massive deformations. The *Lagrangian* and *Eulerian* finite element methods and its derivatives, as well as mesh-based particle approaches, which aided in the original creation of the CPDI method utilised in this study, are introduced.

Chapter 3 describes the current state of the Material Point Method (MPM) and the Convected Particle Domain Interpolation (CPDI) methods, as well as their implementation. Also discussed is the penalty contact algorithm employed in the CPDI code. Simulations validating the implementation of the code are provided, along with its application

for modelling continuum subjected to large deformations. The modelling of a granular flow is compared to experimental results, and the effect of various solution parameters, including damping, particles per grid, and smoothing techniques, is discussed.

To account for the effect of pore fluid, the extension of single-phase CPDI introduced in Chapter 3 is extended to the two-phases in Chapter 4. The governing equations of the two-phase CPDI, the solution process, and an example of implementation validation are discussed.

Chapter 5 discusses the implementation of the UBCSAND model within the CPDI framework. The implementation of the UBCSAND model is validated by back-calculating the cyclic direct shear test and shake table test. This chapter also examines the effect of the constitutive law on the final outcomes of the shake table test.

Chapter 6 examines the use of the CPDI code to simulate the installation of open steel pipe piles. There are three models of pile installation, with increasing degrees of complexity. Initially, the back-calculation of vibrated model monopile is presented. In this work, the vertical penetration of the pile is compared to experimental results. Changes in soil state parameters, effective stress, and pore pressure are examined. In addition, simulation of a hammered monopile is also shown, and the findings are compared to those of experiments. The second example of validation offered is the back-calculation of field tests conducted as part of the *VibroPile* project. The CPDI code was used to model the vibratory installation of one monopile. Field data are compared with the outcomes. Finally, *Class-A* forecasts are produced for a vibratory offshore monopile installation, and results compared with field data, which were later obtained and evaluated.

Chapter 7 presents the conclusions and recommendations for future research in this area.

Chapter 2

Review of the numerical treatment of large deformations

For an exact solution, it is necessary to satisfy the requirements of *equillibrium*, *compatiability*, *material behaviour*, and *boundary conditions*, as well as force and displacement. There are three sorts of analysis methods: i) closed form, ii) simple, and iii) numerical analysis. In Table 2.1, the ability of the current methods to meet the main theoretical requirements is presented. This Table is an adaptation of the work of Potts et al. [181]. This reference also contains additional information on the applicability of these methods to the analysis of structures such as wall and support stability, base heave, etc.

The finite element approach has numerous uses in engineering. Although this method has been widely employed in the field of geotechnical, mechanical and fluid engineering and is quite well understood, it is of interest to tabulate the major modelling processes of the finite element method here.

Element discretisation : Here, the geometry of the investigated problem is modelled by a collection of smaller regions referred to as *finite elements*.

Primary variable approximation : Selecting a fundamental variable (such as displacement etc.) and establishing rules for its variation throughout a finite element. This variance is represented by a nodal value, together with interpolation functions. In geotechnical

Method of Analysis		**Solution Requirements**		
		Equillibrium	**Compatiability**	**Constitutive Behaviour**
Closed form		S	S	Linear Elastic
Limit equillibrium		S	NS	Rigid, with a failure criterion
Stress field		S	NS	Rigid, with a failure criterion
Limit analysis	Lower bound	S	NS	Ideal plasticity with associated flow rule
	Upper bound	NS	S	
Beam-Spring approach		S	S	Soil modelled by springs or elastic interaction factors
Full numerical analysis		S	S	Any behaviour can be modelled

Table 2.1: Solution requirements for different numerical methods;
S = Satisfied, NS = Not Satisfied

applications, displacement is frequently used as the primary variable.

Element equations : The element equations are derived using a suitable variational principle (e.g., the principle of minimum potential energy). This usually follows the scheme $[K_E]\,\Delta d_E = \Delta R_E$, where, $[K_E]$, Δd_E and ΔR_E are the element stiffness matrix, the vector of incremental element nodal displacements and the vector of incremental element nodal forces, respectively.

Global equations : Following the scheme, the local elemental equations are merged by considering compatibility of displacements to generate the global equations, $[K_G]\,\Delta d_G = \Delta R_G$, where, $[K_G]$, Δd_G and ΔR_G are the global stiffness matrix, the vector of global nodal displacements and the vector of global nodal forces, respectively.

Boundary conditions : The solution's boundary conditions are applied by modifying the global equations. It is clear that loading (such as line and point loads, pressure and body forces) affects the term ΔR_G, displacement affects Δd_G.

Solution to the global equations : Constructed global equations consist of a large number of simultaneous equations. The displacements Δd_G are then obtained by solving these equations at all the nodes. Secondary quantities such as strains and stresses are then determined based on these nodal displacements.

Equally as important as quantifying experiments and describing events in detail is numerically reproducing these events. Soil mechanicians adore the so-called '*Class-A*' predictions most out of all numerical simulations, in which numerical predictions precede the actual event. Even if we have precise soil characteristics, it is impossible to obtain the loading pattern, magnitude, and characteristics in advance, unless we are working with a controlled model test, which are of course referred to as '*Class-C*' predictions. These are mistrusted by some in the larger engineering community due to the fact that the end result can be achieved by adjusment and manual guidance provided to the model. For the sake of completeness, the intermediate between these two prediction classes would be '*Class-B*', in which computations are performed concurrently with model measurement. The purpose of this chapter is to provide an overview of some of the available numerical methods that have been used to reproduce such events.

2.1 Liquefaction of saturated granular soil

Long ago, liquefaction episodes have been observed during earthquakes. Liquefaction, which occurs in saturated granular soils following dynamic excitation, is frequently found in offshore regions or in the proximity of water bodies such as seas, rivers, and lakes. The term *liquefaction* was previously referenced in the works of Hazen [89] in

relation to the collapse of the Calaveras Dam in the United States. Reference [103] offers a comprehensive study of liquefaction.

The term *liquefaction* is commonly used to refer to *total liquefaction*, or the loss of any and all effective stress. Excess pore pressure generation has also been used to describe partial liquefaction, which occurs more frequently in short, dynamic processes. Non-cohesive soils can be viewed as a collection of grains having water- and/or gas-filled pores. If there are intergranular connections capable of transmitting shear forces, the soil skeleton behaves macroscopically as a solid material. Due to this shear strength, the skeleton is able to withstand additional loads, such as those caused by offshore structures. Intergranular contact in non-cohesive soils can only transmit shear forces via friction if normal forces are also transmitted. Normal forces can also be transmitted through the skeleton and pore water. The two components of total normal stress are, therefore, normal effective stress and pore pressure. Liquefaction occurs when the total stress remains constant and the pore pressure rises to the point where the typical effective stress becomes zero. It also occurs when the pore pressure remains constant and the total stress decreases to the point where the usual effective stress equals zero. When the effective normal stress reaches zero, the intergranular forces vanish and the transferred shear stress reaches zero. At this point, the soil can no longer support any load other than isotropic pressures, which are typical of fluids.

On the basis of the loading type, *partial liquefaction* can be divided into two categories: i) liquefaction owing to monotonic loading, and ii) liquefaction due to dynamic loading. The liquefaction caused by dynamic loading can be further classified as either *instantaneous* or *residual liquefaction*. In addition to these principal types of liquefaction phenomena, there are two more excess pore pressure phenomena: i) *cyclic mobility*, which is a subset of partial liquefaction and is caused by a mix of immediate and residual liquefaction, and ii) negative excess pore pressures (suction).

Liquefaction necessitates significant “excess pore pressure”. Excess pore pressure is defined as the difference between the actual pore pressure and the hydrostatic pressure for a particular water level. In the vicinity of offshore foundations, liquefaction with an excess pore pressure sufficient to eliminate soil strength is rare. However, increased pore pressure frequently causes a major reduction in the shear resistance of a portion of the soil, which can result in significant deformation or even shear collapse. Even though the soil retains shear resistance and does not behave like a Newtonian fluid, the term “liquefaction” is applied to all such situations. De Groot et al. [60] provide in their work the fundamental physics of the rearrangement of grains on the microscale level, a crucial factor in understanding the physics of liquefaction, as well as further information regarding the definition and physics underlying liquefaction.

When a drained granular soil is subjected to monotonic shear, the material exhibits a distinct behaviour. Depending on the initial bulk densities of the sand sample (dense, or loose), two possible distinct volumetric strain values are recorded. The applied

shear stress results in a constant increase in shear strain and two distinct volumetric strain trends. In the case of loose sand, contraction is observed to be the predominant behaviour. Medium to dense sand exhibits contraction at low stress ratios and dilation at higher stress levels. The boundary line between contraction and expansion is known as the phase transformation line. In the case of undrained sand, however, volumetric stresses are nearly non-existent. The measured excess pore pressures assumes the role of parameter of interest. If the soil exhibits contractive behaviour, an increase in pore pressure is detected, whereas a drop in pore pressure indicates dilative soil behaviour.

A loose granular material's initial density is less than a critical value. Under shear stress, the expected drained behaviour is contraction, leading to an increase in pore pressure under undrained conditions. In this case, failure is possible upon hitting the critical state line (CSL). Alternately, an increase in mean effective stress beyond the CSL to a bounding limit causes the state to revert to the CSL and fail. A dense material's initial density exceeds a critical value. In the drained condition under deviatoric stress, the specimen has a tendency to first contract with decreasing void ratio before reaching a compacted state (contraction). As the void ratio increases, the behaviour transforms into dilation. In undrained situations, the contractive tendency causes an increase in pore pressure and a reduction in effective stress. Then, the behaviour changes and the dilative trend increases the mean effective stress until the state surpasses the CSL, at which point a critical failure takes place. The reader is referred to reference [145] for a more comprehensive explanation of this phenomenon.

If the total stress acting in a given direction at any point in the soil is denoted by σ and the pore pressure is denoted by p, then the effective stress (σ'), which controls the changes in volume and strength of the soil, is given after von Terzaghi [212], who experimentally demonstrated the relationship in his work as:

$$\boldsymbol{\sigma}' = \boldsymbol{\sigma} - p\,\boldsymbol{I}\,, \tag{2.1}$$

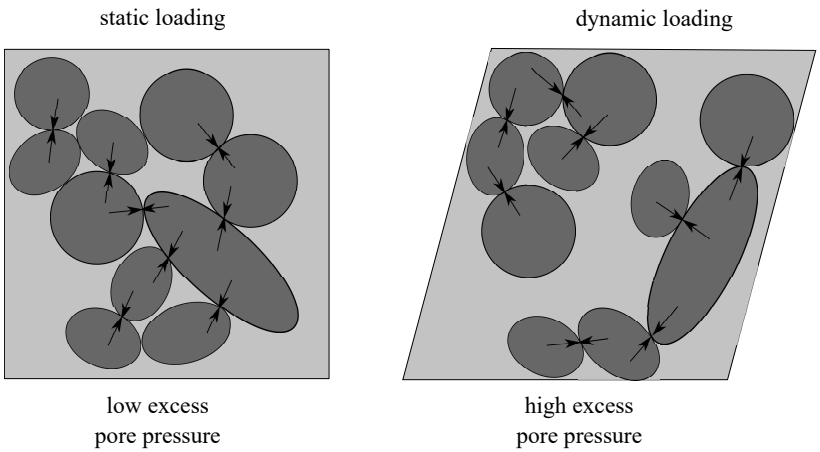

Figure 2.1: Microstructure of granular grains under static (left) and dynamic (right) loading [90]

where, $\boldsymbol{I}$ is an identity tensor. Here, effective stress refers to the intergranular forces acting between the porous material's particles. As shown in Figure 2.1 (left), under static load (or, generally, in the absence of dynamic load), each soil particle is in contact with its neighbouring particles, allowing the solid soil skeleton to carry the majority of the applied load. As depicted in Figure 2.1 (right), under rapid dynamic loading the excess pore pressure begins to increase due to the collapse of contact between the loose soil particles as they move into a denser configuration locally. Once the dynamic loading subsides, the excess pore pressure dissipates according to the seepage velocity, which is influenced by the soil's hydraulic gradient. If the pore fluid is entrapped in the solid matrix due to low permeability of the soil matrix, the pore fluid carries the majority of the applied load, resulting in poor grain-to-grain contact. This in turn decreases the soil's shear strength of loose cohesionless soils. This is known as liquefaction, and the effect of reduced soil strength is most evident in the form of building subsidence and sand boils in areas most susceptible to liquefaction following earthquake loading.

During most significant seismic events, soil liquefaction has been observed. Although the aftereffects of an earthquake are not limited to liquefaction, the events in Japan make the destructive effects of earthquake-induced liquefaction all the more apparent. With a moment magnitude (M_w) of 9.0, the March 11, 2011 Japan earthquake off the coast of Tohoku was the largest earthquake ever recorded in Japan's history. This seismic event proved to be a catalyst not only for liquefaction-induced damage, but also for widespread loss of life and property caused by the subsequent tsunami. In the work of Bhattacharya et al. [25], a comprehensive account of the seismic event is provided. Since the purpose of this portion of the work is to describe liquefaction and its mechanism, the references that will be presented will be limited to this concept. After the 2011 Japan earthquake, geotechnical field investigation reports around Tokyo Bay noted widespread liquefaction and its associated effects. Observations were made regarding the settling of the ground (a classic indicator of ground liquefaction), the elevation of manholes, the buckling of roadway pavement, etc. Much of the damage caused by earthquake-induced liquefaction is due to the settlement or tilting of saturated sandy subsoil caused by liquefaction. Typically, liquefaction manifests itself as i) sand boils or sand volcanoes, ii) water spouting with sand or mud from cracks in the ground or wells, iii) excessive settlement of heavy structures on sand, such as buildings, iv) total destruction of structures, such as earth dam failure, and v) shear failure of underground installations, such as manhole installations and pipe joints.

2.2 Numerical reproduction of the physics of liquefaction

After examining the microscopic explanation of the physics behind liquefaction, the goal of the following discussion is to examine the capabilities and performance of methods and models that can statistically or numerically model and predict liquefaction.

2.2.1 Energy-based method

Energy-based approaches are founded on the premise that pore-pressure buildup is directly proportional to the amount of seismic energy dissipated in a unit volume of soil. This idea is prompted by the microstructural rearrangement of sand particles that occurs during cyclic shearing and results in the densification of dry or saturated (but drained) sand and the liquefaction of saturated undrained sand. This idea is predicated on the observation that the desification of sand includes the rearranging of its grains and, consequently, the expenditure of energy, which increases as the void ratio approaches its minimum. This minimum value depends on significant aspects such as grain structure, size distribution, confining pressure, and others. If the saturated sand is left undrained and subjected to a fixed confining pressure, the trend toward densification generated by cyclic shearing leads to an increase in pore water pressure. Thus, the frictional contact forces at the interface between adjacent sand particles decrease. Consequently, as pore water pressure increases, the energy required to reduce pore volume decreases. Taking into account all of these facts, a relationship was proposed between the energy loss in cyclic shearing and the subsequent change in void ratio for dry sand, as well as the subsequent increase in pore water pressure in the saturated, undrained situation. The hypothesised relation, in the form of a differential equation, was first published in Nemat-Nasser and Shokooh [163]. Existing experimental results for both the densification and liquefaction phenomena were then back-calculated using the theory in its "simplest" form.

This assumption was elaborated upon in subsequent publications [99]. The relationship between the standard penetration value and energy dissipation was found by analysing historical records of liquefaction generated by earthquakes. After calculating the expended energy, the increase in pore pressure follows directly. Increase in pore pressure as a function of earthquake magnitude, distance from epicentre, standard penetration value, and starting effective overburden stress. The resulting relationship lends itself well to analyses of seismic liquefaction risk. This strategy was interesting at the time due to its simplicity and dependence on fundamental earthquake factors, such as magnitude and distance to the centre of energy release, instead of peak ground acceleration. The entire analysis rested on the premise that pore pressure is solely dependent on dissipated energy, an assumption supported by previous research [163]. The model was later modified and expanded. In later publications [23, 56], the fundamental assumptions of the original model are addressed, and a revised model is offered.

In their work, Green and Mitchell [80] proposed energy-based evaluation and remedial strategies. The mechanical energy required to densify loose sand using deep dynamic compaction, vibro-compaction, and explosive compaction was estimated and compared to the energy required to induce liquefaction during an earthquake. Alavi and Gandomi [2] evaluated the liquefaction resistance of sandy soils using machine learning (ML), the multi expression programming (MEP) approach and the linear genetic programming (LGP) method. Kanagalingam [109] presented the theoretical underpinning for

an energy method that additionally accounted for the frictional energy loss along contacts when assessing the liquefaction potential. Research was also presented to analyse the liquefaction potential under random seismic loading [128], as opposed to limiting the energy-based approaches to the reproduction of unit cell testing. In addition, research was done to compare the predictions of energy-based techniques with those of the standard stress-based technique [116].

2.2.2 Probabilistic methods

Probabilistic methods are developed via logistic regression analysis of field, standard penetration test (SPT), and cone penetration test (CPT) data, as well as the mapping function method. On the basis of in-situ tests, simplified methods for evaluating liquefaction potential have been developed and are widely used by geotechnical engineers. For evaluating the liquefaction potential of soils, these methods that rely on in-situ tests. The simplified procedure suggested by Seed and Idriss [192] was based on the number of blow counts from the SPT. This procedure has been revised and updated since that time [29]. In addition, other simplified methods based on other in-situ tests, such as the CPT, have been proposed [221]. In addition to presenting a method that utilises the small-strain shear wave velocity (V_s), a summary of all previous research was also provided [222].

Every conducted test includes inherent uncertainties. Since the majority of simplified methods are based on physical measurements, it is difficult to eliminate these uncertainties. To account for such uncertainties in the data and procedures used to develop these simplified methods, it is desirable and occasionally necessary to conduct a probabilistic assessment of liquefaction potential that incorporates these uncertainties. Numerous scholars have conducted research in this area, focusing on statistical/probabilistic evaluations of liquefaction to demonstrate the application of probability and statistics to deal with uncertainties associated with simplified methods [129, 219, 223]. Employing statistical regression procedures, models for calculating the probability of liquefaction as a function of earthquake load and soil resistance parameters have been developed. However, due to the data limitations, regression models tend to provide conservative estimates of the likelihood of liquefaction.

In subsequent research, a new method for calculating the probability of liquefaction was proposed. The method relies on a mapping function that is dependent on a specific deterministic method. The mapping function is then established in order to "map" the factor-of-safety calculated by a specific deterministic method to the probability of liquefaction inferred from field liquefaction performance data. An artificial neural network (ANN) was used to predict the occurrence of liquefaction based on historical field performance records, to locate data points on the limit state surface, and to approximate the multi-variable limit state function [104]. Juang and Jiang [105] subsequently devel-

oped probabilistic methods through logistic regression analyses of field data, the SPT and CPT data, and those through a newly developed mapping function approach. It was demonstrated that the curves obtained from CPT-based probability analyses were in good agreement with those obtained from the logistic regression analysis independently conducted at the same time by other researchers. However, the SPT-based curves did not perform as well. Thus, the associated mapping function can direct the selection of a suitable factor-of-safety for use with a particular deterministic method. Later, an evaluation of existing and new probabilistic methods for liquefaction potential evaluation was presented [106]. However, comparisons of the probabilities of liquefaction calculated using two distinct methods, logistic regression mapping and Bayesian mapping, were emphasised. It was demonstrated that the Bayesian mapping method is preferable to the logistic regression method for estimating the site-specific probability of liquefaction, despite the fact that both methods produce comparable probabilities. Later works presented a comprehensive methodology for probabilistic and deterministic assessment of seismic soil liquefaction triggering potential based on the cone penetration test [158]. A new correlation for assessing the risk of soil liquefaction due to seismic activity was also presented. A large database of high-quality field performance case histories was utilised in the development of the new correlation. Also presented was a new normalisation procedure for CPT resistance.

In addition to conventional field techniques such as the SPT, CPT, and the Becker Hammer Test (BHT) that are routinely used to assess soil liquefaction potential, the shear-wave velocity (V_s) test is the only one that measures a fundamental property of the soil. However, liquefaction assessment employing in situ penetration tests is more prevalent. CPT has the advantage of directly correlating with the relative density, which has a significant impact on the cyclic behaviour of saturated soil. Compared to CPT and SPT methods, shear-wave velocity is significantly less sensitive to problems in soil compression and reduced penetration resistance when soil fines are present. Using shear-wave velocity measurements, simplified procedures for evaluating the liquefaction resistance of soil were presented [5]. Using a modified relationship between shear-wave velocity and cyclic stress ratio for constant average cyclic shear strain, liquefaction resistance curves were developed. Kayen et al. [110] presents new generalised correlations for shear-wave-based evaluation of seismically-induced soil liquefaction developments that further improve this method.

2.2.3 Modelling methods

Constitutive models, one aspect of modelling are "mathematical relations that can describe the stress-strain relationship at each material point under various loading condition". Modelling provides a useful method for capturing a comprehensive view of the event. Not always, but typically, history and practical experience are given greater weight than prototype testing. By applying case history and experience to modelling,

we can gain a deeper understanding of the problem and calibrate our results to predict future events.

A numerical model is a mathematical approximation of a real-world physical event. A numerical model, which includes a constitutive law or constitutive model, is utilised to characterise the soil's stress-strain behaviour and includes: i) equillibrium equation, ii) constitutive equation, and iii) compatiability and boundary condition considerations. These laws describe the response of matter to external stimuli. With the increasing use of numerical analysis methods in geotechnical engineering, a multitude of constitutive laws have been developed to address the specific problem that is to be solved. However, these fundamental models must be validated to demonstrate that their implementation accurately represents the underlying mathematical model and its solution, after it has been established that the underlying mathematical model is capable of representing the desired physical process. In order to accomplish this, numerous constitutive models have been proposed in the field of geotechnical engineering, ranging from simple models such as linear elastic models to complex models such as the anisotropic visco-hypoplasticity soil model, which accounts for the effects of density change and stress-state changes. Since a multitude of constitutive laws are available for representing the soil, rock, and everything else, several models that can reproduce liquefaction specifically are described in detail.

The theory of elastoplasticity serves as a framework for the nonlinear and hysteresis-based behaviour of soil. For elastoplastic soil models within the field of soil mechanics, there are two possible plasticity theories: associated flow rule and non-associated flow rule. The associated flow rule has been used to model the behaviour of soils, particularly soils with negative dilatancy, such as when simulating the behaviour of normally consolidated clays. On the other hand, the non-associated flow rule has been widely used to model sands with positive-negative dilatancy. A number of constitutive models have been proposed to model sand while accounting for the cyclic effects that affect the strength of sands. These models have been applied to design practise with appropriate numerical methods, such as the finite element method, in order to analyse not only the static strength of soils, but also to predict the dynamic behaviour of saturated soils.

Select examples of models include:

(a) Finn et al. [67] proposed an effective stress model, in which the pore pressure increases are coupled to dynamic response solutions, allowing the full time history of pore pressure increases during an earthquake to be computed. This method also allows the dynamic response solutions to reflect the effects of soil stiffness degradation resulting from an increase in pore pressure. Additionally, the effects of pore pressure redistribution and dissipation can be considered.

(b) Using the theory of generalised plasticity, Pastor and Zienkiewicz [175] developed a constitutive law in which yield and plastic potential surfaces were not explicitly

defined. In the case of sand subjected to monotonic and cyclic loading, positive results were demonstrated.

(c) Constitutive relations for describing the non-linear, inelastic behaviour of sand during an earthquake were developed [166], by employing a yield function in terms of effective stress ratio and a plastic potential function derived from the stress ratio-plastic strain incremental ratio defined as a function of accumulated volumetric strain.

(d) A multiple-mechanism elasto-plastic model for soils applicable to general three-dimensional stress states and cyclic loading was developed by Prevost and Keane [182].

(e) Hashiguchi [88] developed a subloading surface model for cyclic plasticity, which considered the expansion and contraction of the loading surface.

(f) A cyclic elasto-plastic constitutive model based on a non-linear kinematic hardening rule was developed [169]. In addition to a new flow rule and a cumulative strain-dependent property of plastic shear modulus, a fading memory property of the initial anisotropy of the constitutive model was also incorporated.

(g) Reference [127] describes a comprehensive bounding surface sand model described within a critical-state framework. The formulation of this model incorporates the concept of state-dependent dilatancy, which distinguishes it from its predecessors. By adopting this formulation, the model was able to simulate, with a single set of model constants, both the contractive and dilative response of granular soil across a broad range of stress variations.

(h) Elgamal et al. [63] developed a plasticity model for capturing the characteristics of cyclic mobility. With the newly developed flow and hardening rule, the model was created as an extension of an existing multi-surface plasticity formulation. The new flow rule enabled the reproduction of cyclic shear strain accumulation and the subsequent dilative phases observed in the response of a liquefied soil.

(i) Dafalias and Manzari [53] developed a stress-ratio-controlled, critical state-compatible sand plasticity model. The model also incorporated a fabric-dilatancy tensor that accounts for increased contraction upon stress reversal due to fabric changes during the material's dilative behaviour.

(j) PM4Sand model was created as a plasticity model for geotechnical earthquake engineering applications [233]. The model adhered to the fundamental structure of the stress-ratio-controlled, critical-state-compatible, bounding-surface plasticity model for sand.

(k) An earlier model from Dafalias and Manzari [53] was modified and implemented to enhance its ability to approximate engineering design relationships that are used to estimate the stress-strain behaviours that are crucial for predicting liquefaction-induced ground deformations during earthquakes.

The UBCSAND model, proposed in the work of Puebla et al. [183] and later implemented in the work of Beaty and Byrne [15], both of which are currently more widely cited. The UBCSAND model is an elastic-plastic material model developed for sand-like granular materials that have the potential to liquefy under cyclic loading. It derives its name from the university with which its development was associated, the **U**niversity of **B**ritish **C**olumbia. Mohr-Coulomb formulations have the ability to kinematically and isotropically harden through a hyperbolic relationship, which the yield surface followed. After being incorporated into the commercial software FLAC3D™ and PLAXIS™, the model has been widely utilised through these programmes [15, 177]. The UBCSAND model has been implemented in this work is based on the work of Naesgaard [159]. Chapter 5 provides comprehensive explanation of the model is provided.

2.3 Methods to simulate large deformations numerically

It is becoming increasingly apparent that methods capable of numerically modelling large deformations are required for use in geomechanics. During the past few decades, a number of numerical methods have been developed in an effort to capture the material's large deformations. In general, the methods can be divided into two categories: i) mesh-based finite element methods, and ii) mesh-less methods.

2.3.1 Mesh-based methods

The so-called Finite Element Method (FEM) is arguably the most popular and widely used mesh-based method. FEM is a numerical method for approximating the solution to a boundary-value problem. The finite element method has been used successfully to analyse a wide variety of solid and fluid mechanics problems. There are two fundamental FEM formulations: *Lagrangian* and *Eulerian*. *Lagrangian* FEM is commonly used to model problems in solid mechanics, whereas the *Eulerian* formulation is commonly used to solve problems in fluid mechanics.

The work of Rayleigh [185] laid the foundations for determining the approximate solution of boundary-value problems using calculus of variations. Using a test or trial

function that is continuous over the domain and satisfies the imposed boundary conditions, the differential equation was approximated. A finite number of coordinate functions, each with a constant coefficient, are combined to approximate the test function. In addition, methods were developed to approximate the solutions of differential equations using the method of weighted residuals, in which the test function is used in conjunction with an integral form of the differential equation to minimise the error in an average sense over the problem's domain. This method consists of numerous techniques, such as the Collocation method [68], the Subdomain method [26], and the Galerkin method [71]. The Galerkin method is currently the most widely used method for finite element formulation. Earlier methods for approximating the solution to boundary-value problems had a shortcoming. Trial functions that should be valid for the entire domain will contain a large number of terms, making it difficult to solve problems with complex geometries and boundary conditions. In reference [51], the concept of piecewise continuous functions was presented. This can be interpreted as the initial step in developing the finite element method as we know it today. In 1960, when triangular and rectangular finite elements were utilised for plane-stress analysis, Clough [49] coined the term *finite element method*.

Turner et al. [208] contributed towards the numerical simulation of large deformation coupled with thermomechanical effects. In their later works, Zienkiewicz et al. [230] and Zienkiewicz and Cheung [232] made additional advances in the finite element

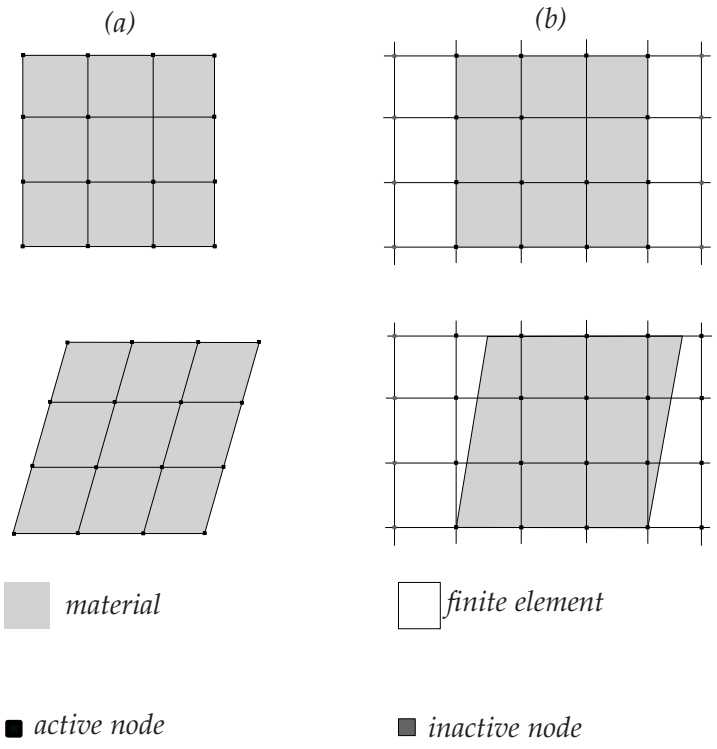

Figure 2.2: Initial and deformed configuration using (a) *Lagrangian* FEM and (b) *Eulerian* FEM

method and its application, with Costantino [50] employing the FEM for dynamic analyses. This method was proposed by Belytschko and Hsieh [17] for small-strain problems with material non-linearities and transient large-displacement problems. The presented formulation consisted of triangular elements with constant strain and Euler-Bernoulli beam elements. Additionally, comparisons were made with the available experiment data at the time.

Eulerian and Lagrangian FEM

Eulerian and *Lagrangian* FEM are two fundamental formulations within the framework of the finite element method, as described previously. As stated previously, the former is commonly used to solve problems in fluid mechanics, while the latter is primarily utilised in solid mechanics applications. Figure 2.2 depicts the initial and deformed configurations of *eulerian* and *lagrangian* FEM.

The deformation of a continuum is described from two distinct perspectives: the *eulerian* description and the *lagrangian* description. In the *eulerian* description, spatial coordinates and time are utilised to track the motion and other physical properties at fixed points in space as the material passes through in time. It employs the spatial arrangement as its frame of reference. In contrast, the time and material coordinates are used as independent variables in the *lagrangian* description to describe the motion and other physical properties of the material with time. It employs the initial configuration as the reference frame and is commonly known as the *material description*. Thus, two formulations can be described in terms of the finite element method.

The formulation can be referred to as a total *lagrangian* FEM if the initial material coordinates are used as the reference configuration. If the updated material coordinates are utilised in the calculation of stresses, the method is referred to as an *updated lagrangian* FEM. In their work, Bathe et al. [13] presented the complete and *updated lagrangian* FE formulation for modelling large deformation. Belytschko et al. [20] demonstrated in detail that both *total* and *updated lagrangian* FEM lead to identical results, and it is merely a matter of convenience to choose one formulation over the other.

In the past, *eulerian* meshes were not widely used in soil mechanics. *Eulerian* meshes are favoured for problems involving extremely large deformation. In these problems, the *eulerian* elements do not deform with the material, which is advantageous. As a result, *eulerian* elements retain their original shape regardless of the magnitudes of deformation during the process. The nodes are fixed in space and the dependent variables are functions of the *eulerian* spatial coordinate and time in the *eulerian* formulation. In comparison to the *lagrangian* formulation, the following four points are significant:

- The equation for mass conservation is expressed as a partial differential equation.

Since the particles are followed in the *lagrangian* method, mass conservation is automatically satisfied.

- In the momentum equation, the *material time derivative* for velocity is expressed in terms of the *spatial time derivative* and a transport (advection) term.
- *Constitutive equation* is expressed in rate form.
- Boundary conditions tends to be imposed on fixed spatial points.

Coupled Eulerian-Lagrangian

The Coupled Eulerian Lagrangian (CEL) is a numerical method that attempts to combine the most advantageous aspects of the *eulerian* and *lagrangian* approaches. Large mesh deformations typically result in mesh distortion. By combining the benefits of *eulerian* and *lagrangian* formulations, the CEL method aims to mitigate and overcome the issue of mesh distortion. In the context of classical finite element analysis, a L*agrangian* formulation is frequently applied to solid mechanics problems. The material is considered to be fixed to a finite element in the *lagrangian* formulation. The material moves alongside the mesh nodes during the computational step. In coupled simulations, where solid and pore water are both simulated, fluid can flow through the mesh, resulting in significant deformations. The surface of the *lagrangian* mesh precisely defines the surface of the continuum. In the *eulerian* formulation, a mesh's nodes are spatially fixed. In order to account for occurring deformations, the material flows through the element mesh. The flow of material through the mesh is monitored by computing the *eulerian* volume fraction (EVF). The *Eulerian Volume Fraction* (EVF) is the fraction of an *eulerian* element that is filled with material. A value of zero indicates that there is no material in the element, while a value of one indicates that the element is completely filled. Contrary to the *lagrangian* formulation, the surface of the continuum does not correspond to the boundaries of the constituent elements. The *eulerian* and *lagrangian* materials are brought into contact by a general contact algorithm based on the *penalty contact method*. A general contact algorithm does not require *lagrangian* and *eulerian* elements to make contact. The *lagrangian* elements can move freely through the *eulerian* mesh until they encounter a material-filled *eulerian* element (EVF $\neq 0$).

Conventionally, the CEL method employs an explicit time marching scheme. For the solution of the nonlinear system of differential equations, the central difference method is employed. The advantage of this method is that the solution for the current time step can be obtained directly from the solution of the previous time step, eliminating the need for iteration. Further advantages include the simplicity of implementing contact conditions and the option to select any solid constitutive model. It should be noted that explicit calculations are not always stable. The numerical stability is only guaranteed

if the time step size used in the calculation is equal to or smaller than the critical time step size (Δt_{crit}), which is dependent on parameters such as the characteristic element length (L_e) and the dilatory wave speed (c_d) and is calculated using the formula $\Delta t_{crit} = L_e/c_d$. It is possible that the stiffness will change during the simulation, resulting in the incorrect critical time step being applied to certain elements with a lower critical time step. To converge to a stable solution, the critical time step size is typically reduced by a factor of 0.1. References [47, 85, 184] provide a detailed explanation of the use of CEL for large deformation problems in geotechnical engineering.

Arbitrary Lagrangian-Eulerian

The arbitrary Lagrangian-Eulerian (ALE) method was developed to handle large deformation problems in solid and fluid mechanics with severe mesh distortion. ALE was first introduced in the work of Noh [167], originally under the name coupled Eulerian-Lagrangian. The method was implemented using the finite difference scheme to solve two-dimensional hydrodynamics problems with moving fluid boundary conditions. In later references [94, 200], the formulation was extended to two and three dimensions, respectively. Reference [18] incorporated the ALE method into a finite element framework to handle non-linear simulations where fluid-structure interaction issues are encountered. The ALE method was used by Nazem et al. [162] to solve large deformation problems - bearing capacity simulation on cohesive soil. Reference [6] described the ALE method for pile penetration into sand, wherein good agreement was found between the experimental investigation and the numerical results. In the multimaterial arbitrary Lagrangian-Eulerian (MMALE) method, [137] formulation, the grid deforms similarly to the traditional *lagrangian* formulation where a new grid with less distortion is generated. The solution variables are then transferred to the new mesh, similar to the *eulerian* formulation. Multiple materials can be considered within a single MMALE element, which greatly improves the formulation for extremely large deformations. Typically, a material-free zone or void is defined without mass or strength within the grid, permitting other materials to flow into these regions of physical space. In addition, reference [9] presented the multimaterial arbitrary Lagrangian-Eulerian (MMALE) method, which is an improved ALE method with geotechnical applications. The reader is referred to reference [7] for a detailed discussion of the method's theoretical basis.

2.3.2 Mesh-less methods

Meshless methods continuously adjust the nodal connectivity as the continuum deforms. This eliminates the mesh distortion issue. Meshless methods may be based on the moving squares approximation, kernels, or the partition of unity [19]. Smoothed particle hydrodynamic is one of the oldest meshless methods, according to the cita-

tion provided by reference [136]. The closed form of the partial differential equations (PDE) is discretised using collocation methods in particle-based SPH. Calculating spatial derivatives with the SPH method does not require a pre-defined mesh. References Lucy [136], Monaghan [155] offer a more comprehensive description of the SPH method.

The element-free Galerkin method, in which the trial functions for the weak form are constructed using the moving least squares interpolation [21], is another relatively recent meshless method. The Particle finite element method (PFEM) is an additional meshless method that employs meshless finite element interpolation [98, 170]. In PFEM, the nodal points represent particles, and the computational mesh is created by connecting these nodal points. The governing equations are subsequently solved *lagrangian*-style. In order to accommodate the resulting large deformations, frequent remeshing is required to adjust the connectivity. Reference [131], a comprehensive literature review of the other meshless methods is presented.

Smoothed Particle Hydrodynamics

Smoothed particle hydrodynamics (SPH) is a meshfree particle method based on the *lagrangian* formulation that has been widely applied to a variety of engineering and scientific disciplines. The SPH method may be regarded as a "truly" meshfree method; it is a particle method originally conceived for continuum scale applications and may be considered the earliest modern meshfree particle method. Bui et al. [37] pioneered the application of SPH to elastoplastic continuum. Since then, the method has found applications in mechanics, granular flow [152], bearing capacity of foundations [36], and soil-structure interaction problems [28], among others.

Without the need to define a mesh, the computational discretised by a finite number of particles (or points). The properties of these particles, which carry all material attributes, are smoothed over their smoothing length by a kernel function. This indicates that a physical quantity is produced at the location of the particle by adding the contributions of all particles within the range of the kernel. The contribution of each particle is weighted according to its distance and density. This is governed mathematically by a kernel function. The Gaussian function and the cubic spline are two frequently used kernel functions. The reader is referred to reference [100] for a condensed study on the geotechnical applications of SPH.

Discrete Element Method

Discrete Element Method (DEM) is a numerical modelling and computer simulation tool that can be used to simulate soils and other granular materials. In contrast to previously observed methods, the DEM approach explicitly considers the individual particles and their interactions in granular materials. When simulating the mechanical behaviour of granular materials, DEM provides an alternative to the conventional approach, which employs a continuum mechanical framework. The benefit of DEM is that, while assuming a continuum model, soil is assumed to behave as a single continuous material and the relative movements and rotations within the particles are not taken into account. Then, complex constitutive models are required to account for the complexity of the material's behaviour. Even if simple numerical models are used in DEM to simulate the inter-particle contacts and idealised approximate particle geometries are employed, a number of the soil's mechanical response characteristics can be captured. By adopting simple geometries and combining them with fundamental contact response models, simulation costs can be drastically reduced, allowing for the simulation of a reasonably large number of particles while simultaneously capturing the most salient soil response characteristics. In contrast to other classical FE models, in which the constitutive model used determines the response that can be obtained from the numerical model, the response characteristics obtained from the numerical model are largely determined by the contact model selected.

The DEM formulation has found varied applications in the field of geomechanics, but there have been two primary motivations for using the method in applied boundary value problems: i) where large-deformations must be simulated when other continuum-mechanics based analysis tools fail to perform satisfactorily, and ii) as a reliable tool in basic research, wherein the method can probe the material response at a much more detailed scale than can be monitored even with experimental techniques. Zhu et al. [228] presented a study that assessed the DEM method's prevalence in engineering and physical sciences between 1985 and 2005. In their work, O'Sullivan [173] evaluated the use of this method in the context of geotechnical engineering by analysing the publications that employ this method over time. It was observed that while the method gained popularity over the years, as evidenced by the number of publications, the number of particles used in the publications also increased steadily, in part due to the development of computer processing power. Also observed was a gradual shift from two-dimensional to three-dimensional simulation.

Particle Finite Element Method

The development of a method for analysing the interaction between water and structures for large movements of fluid-free surfaces and the presence of fully or partially saturated submerged structures attracted increased attention. The objective was to simulate the hydrodynamics of offshore structures, dam spillways, free surface channel flows, mould filling processes, and so on. Although methods such as ALE formulation and standard FE formulation could have been used to simulate fluid-structure interactions, a new class of method called the Particle Finite Element Method was developed. As in the standard FEM, a mesh connects the nodes defining the discretized domain where the integral-form governing equations are solved. This method treats the mesh nodes in the fluid and solid domains as particles that can move freely and even separate from the main fluid domain, simulating the effect of water droplets, for example. Nodes are viewed as free-moving particles that can separate from the primary analysis domain. The Particle Finite Element method (PFEM) has been extensively applied to the analysis of fluid-structure interaction problems. The application of a *lagrangian* description to model the motion of nodes in both the fluid and structural domains is the method's defining characteristic. The reader is referred to reference [170] for a comprehensive overview of PFEM.

Material Point Method

The material point method (MPM) is an advanced numerical technique suitable for simulating large deformation [11, 24, 45, 82, 107]. In MPM, the continuum is represented by material points or particles, which are *lagrangian* points. Particles moving through a fixed *eulerian* mesh are used to model large deformation. The particles carry all of the physical properties of the continuum, including mass, momentum, material parameters, strains, stresses, and external loads, whereas the *eulerian* mesh and its gauss points carry no permanent data. Information is transferred from particles to the computational mesh at the start of a time step. The mesh is then used to determine the *lagrangian* incremental solution of the governing equations. At the conclusion of each time step, the solution is mapped back to particles in order to update their information. MPM combines the most advantageous aspects of *lagrangian* and *eulerian* formulations while avoiding their shortcomings. In fact, numerical diffusion associated with convective terms in the *eulerian* method is absent in the MPM solution. In addition, the MPM framework avoids the mesh distortion problem that an updated *lagrangian* solution exhibits for large deformation. Eventually, the material point method can be considered an extension of the *particle-in-cell* method [86]. In Chapters 3 and 4, respectively, the detailed formulation of MPM and its extension CPDI, the extension to model two-phase medium, is provided.

2.4 Concluding remarks

In conclusion, despite the fact that there are numerous methods for capturing the liquefaction of soil and an equal number of methods for capturing the post-liquefaction large deformations, the Material Point Method was chosen for this study. MPM and its various enhancements circumvent the majority of the shortcomings of classical *eulerian* and *lagrangian* FE methods. In addition, while other methods to capture large deformations have been implemented, they are done so commercially. This adds complexity to the process of implementing new features. The closed-source nature impedes the natural development of the code and forces the user to rely on work-arounds, which either simplify the problem or increase the complexity of solution procedure, both being detrimental. Similarly, while there are a large number of constitutive laws available to model liquefaction, the vast majority of them are available as *dynamic link libraries* (dll) for specific commercial softwares. Although wrappers can be written to exploit these routines, doing so may violate the licence agreements. Here is a logical justification for the motivation to invest in the development of an in-house code that models not only liquefaction but also large deformation. MPM and its improved version, Convected Particle Domain Interpolation (CPDI), are chosen for this purpose. The UBCSAND model, which was developed by Naesgaard [159], is implemented in the code. To simulate the undrained behaviour of saturated soil, two-phase CPDI, based on the Theory of Porous Media, is also implemented. The aim of this work is to further extend the MPM/CPDI method so that it can be applied to geomechanical engineering problems encountered in everyday practise.

Chapter 3

Formulation of the Material Point Method for modelling large deformations

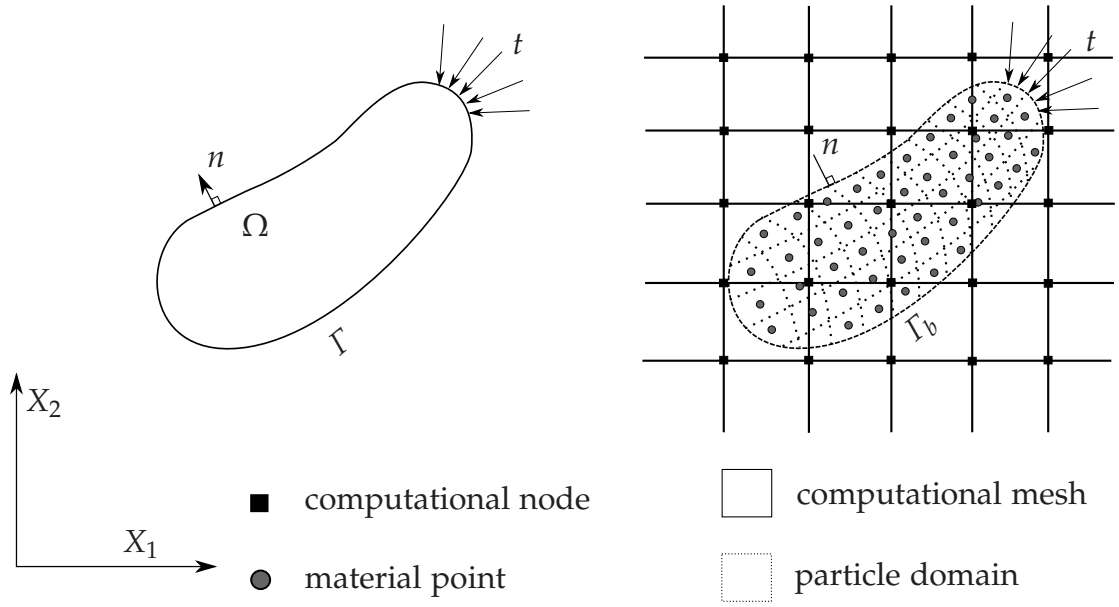

Figure 3.1: Evolution of domains to represent material points in MPM

The material point method (MPM) is an extension of the finite element method (FEM) in which the continuum is represented by so-called '*material points*' that are *lagrangian* in representation [107, 202, 214, 217]. Continuum deformations are tracked by updating the *lagrangian* points that move through a fixed *eulerian* mesh. The MPM discretisation representation is depicted in Figure 3.1. Mapping information from particles to grid points and vice versa requires additional record-keeping. It is assumed that the particles carry all the physical properties and pertinent information about the continuum, including mass, momentum, material parameters, stresses, strains, pore pressures, history variables, and the loads acting on the particles. *Eulerian* mesh, on the other hand, carries no permanent information.

This chapter provides an overview of the material point method. The penalty contact algorithm, used throughout in this work is also briefly introduced in this chapter. In

addition, the implemented code is compared to experimental results using granular flow simulation.

3.1 Development of the material point method

The Material Point Method is an expansion of the *Particle-in-Cell* (PIC) method, which was developed at Los Alamos National Laboratory in 1964 by Harlow [86]. Nonetheless, the original PIC displayed considerable energy loss. This disadvantage was eliminated when reference [34] in their work introduced the *Fluid Implicit Particle* technique (FLIP). PIC and FLIP are both primarily utilised in fluid dynamics. Reference [201] adapted the PIC approach to solid mechanics by computing stress and strain on material points using a constitutive model, as opposed to solving fluid pressure at the cell centroid as in PIC and FLIP. Later, reference [202] presented the axisymmetric version of this method and dubbed it the Material Point Method (MPM) for the first time.

Since then, MPM has been utilised in a variety of applications in the fields of both mechanics and geotechnics. Due to its capabilities of capturing massive deformations in the continuum, MPM has become a popular technique in geotechnical engineering. Reference [24] created a quasi-static MPM formulation and employed it to simulate CPT testing in undrained soils. In their research, reference [11] developed a two-point, two-phase MPM code in which the particles for pore water and soil were evaluated independently, allowing simulation of seepage through porous structures. Later, Kafaji [107] and Ceccato [45] expanded the MPM formulation to account for pore water within one particle and utilised it to simulate hammered pile in sand and CPT tests in clays, respectively. The MPM was utilised to model the dropping of geocontainers, where the dynamics of the soil continuum, the thin-walled geocontainers, and their interaction with free water were modelled [82]. Reference [220] expanded the MPM formulation to account for partial soil saturation and utilised the three-phase MPM to model the influence of precipitation on slopes. In their study, Kularathna [118] presented a solution-splitting method for addressing the incompressibility constraint of the pore water component. In their study, Nøst [168] developed a dynamic implicit MPM formulation coupled with the finite volume method (FVM) to handle both large deformation and coupled flow. Since then, references [70, 73, 79, 83, 156] have used the MPM to successfully model large deformation, i.e., open steel pipe pile installations in saturated sand.

3.1.1 Computation algorithm of MPM

As shown in Figure 3.1, the computational domain is spatially discretised into two parts in MPM. The continuum body is first subdivided into a set of material point. Each material point represents a portion of the domain. These material points are assigned a portion of the mass of the total continuum. One of the most fundamental of MPM is that the mass of each material point remains strictly constant, which means that mass conservation is satisfied. The volume of the material point can, however, change, allowing for compression or extension of the continuum. In standard MPM, mass is regarded as being concentrated at the respective material points. Material points also initialise and carry additional quantities, including velocities, strains, and stresses. The second part is the background computational mesh, which corresponds to a standard finite element mesh. It is designed to encompass the entire problem domain, including the empty spaces into which the material points are anticipated to move during the computation. Typically, the discretised momentum balance equations are solved at the computational mesh nodes, while mass conservation and constitutive equations are solved at the material points. The information necessary to solve the balance equations on the computational mesh at any instance of the analysis is transferred from the material points to the nodes of the mesh by means of mapping (shape) functions. After solving the balance equations with an incremental time integration scheme, the quantities carried by the material points are updated by interpolating the mesh results with the same shape functions. The data associated with the mesh is not of importance for the subsequent step of analysis and is discarded to prevent mesh distortion.

The application of engineering boundary conditions is simple. For instance, stresses and displacements, as well as their rates, can be applied to any boundary mesh node or directly to the material points. The ability to apply well-known constitutive models that describe the stress-strain relationship of materials is an additional advantage of the MPM. As with any FE formulation, MPM's drawbacks include its mesh dependence, its computational costs, and stability issues resulting from material points crossing element boundaries, which will be briefly discussed in this chapter.

Below is the basic algorithm for a single computation step in MPM:

MPM algorithm for a single computation

- Relevant information such as mass and momentum are mapped from the particles to the background *eulerian* grid at the beginning of the computational step using relevant shape functions.
- Solving the field equation on the computational grid in the background yields the solution.
- Using relevant mapping functions, nodal accelerations and velocity are mapped back to particles. Positions of particles are also updated.
- Once the data has been mapped to particles, the background grid is reset in preparation for the subsequent computational step.
- In the case of the USL (Update Stress Last) algorithm, the determined strains on the particles are used to calculate the stresses acting on the particles by employing appropriate constitutive laws. When simulating porous media, fluid component strains are also used to determine pore pressures.
- The history variables that the constitutive law may need for the next computational step are stored in the particles. At this stage, soil properties such as porosity and hydraulic conductivity may also be updated.
- The total total time is updated, and the solution phase returns to Step 1.

3.1.2 Discretisation

The nodes and integration points serve as the material points in *lagrangian* FEM, and this is maintained during the deformation of the continuum. The primary distinction between the *lagrangian* FEM and the MPM is that in the latter, the mesh does not represent the physical property of the continuum, but rather the particles do. In order to evaluate the solution for the particles when they move through the solution space, it is necessary to mesh the entire region where the particles could move. Alternatively, rather than meshing in-situ the fixed background *eulerian* mesh as and when the particles move into the location, it is much more common to anticipate the regions in which the particles may move during the solution phase and define a mesh in those regions prior to the solution phase.

While current MPM codes are based on regular grids and irregular grids, a regular background meshing scheme has been utilised in this work. While the majority of MPM codes permit the definition of a background grid within which a cloud of material points is later defined, this work takes a different approach with the locations of the opposing diagonals being specified. The code then generates a regular background

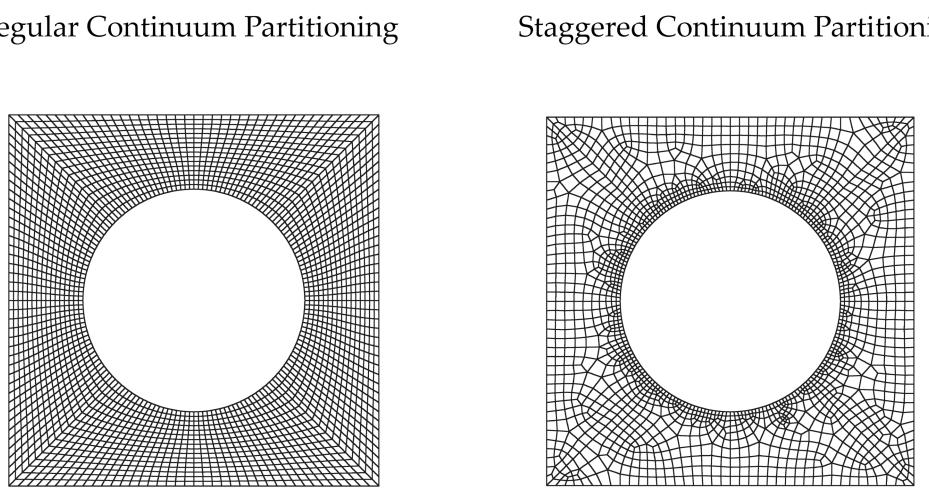

Figure 3.2: Uniform and staggered partitioning of the continuum in MPM

mesh, eliminating the need for them to be entered. The background mesh can now be refined locally by using a tartan background computational grid approach. While the background mesh may consist of relatively regular four-noded elements, particle meshes are anything but. Despite the fact that a 4-noded element has been selected for the work presented in this thesis due to its advantages, such as freedom from volumetric locking, irregular meshing is permitted so long as the element is four-noded. This permits local refinement of the mesh in the region of interest. In Chapter 6, where the case of open steel pipe pile installation is presented, a complex meshing scheme is used in which both the particles and background grids in the vicinity of the pile are locally refined. Prior to beginning the solution, either 1, 4, or 9 particles per discretisation element of the continuum are determined. This allows us to pack more particles into a computation grid and to vary the number of particles in the solution without resorting to a time-consuming remeshing procedure. Regardless of the number of particles chosen for the solution, the mass of a continuum is distributed uniformly throughout. Figure 3.2 presents an example of regular and staggered continuum partitioning used in this work. Below is a summary of the pre-processing steps in the MPM code used in this work.

Procedure for pre-processing in MPM

- Either regular or irregular, four-noded elements are used to discretise the continuum.
- The regions in which multi-body contact is anticipated are defined using two-noded linear line elements for the penalty contact algorithm implemented in this work, which will be explained in greater detail later. Unlike particle discretisation, the discretisation of contact elements is one-dimensional.
- The computational area's extremities and the number of elements in the X and Y directions of the computational mesh are defined.
- If the region of interest is localised in the computational model, a tartan background computational grid is created.
- The problem's boundary conditions are specified. These are created by defining either roller boundaries or full-fixities. Additionally, as will be shown in Chapter 4, it is possible to specify infinite elements, which do not reflect stress waves. To avoid invalidating the addition of the infinite domain, care must be taken to ensure that the Neumann boundary conditions and infinite domains do not interfere.
- The explicit solution parameters, such as the total time, incremental time step, and dynamic time step update rate, as well as global solution variables, such as the local damping coefficient and strain-smoothening algorithm, are selected primarily to improve the solution's quality.

3.1.3 Grid crossing error

The majority of MPM techniques utilise a bilinear shape function of the first order. As a result, the gradients of these shape functions would be constant. While these shape functions may be adequate for the majority of finite element procedures, they occasionally introduce instabilities into the MPM solution. The grid crossing error is one of the instabilities prevalent in the classical MPM formulation. When a particle migrates from one computational grid to another, the grid crossing error introduces spurious stress jumps to the solution. The mathematical justification for this is the application of linear shape functions, whose gradients are constant. When solving for the internal energy,

$$\boldsymbol{F}_{int} = \boldsymbol{B}^T \boldsymbol{\sigma}\,, \tag{3.1}$$

where F_{int} represents the internal energy, B represents the strain displacement matrix, and σ represents the stress tensor. If linear shape functions are selected for the case of one-dimensional background computational grid, it is abundantly clear that the gradients of the shape functions that populate the strain-displacement matrix will be constants. These discontinuities in the gradients result in numerical oscillations in the solution when particles move from one computational grid to another or propagate through the domain. The functions are C^0 continuous; therefore, their derivatives would be constant within the element, but discontinuous at its borders (they change signs). Extending to two-dimensions, when the material point crosses from one grid to another, this change in sign causes non-physical instabilities in the internal energy, degrading the quality of the solution.

Throughout the years, this error inherent and unavoidable to classical MPM has been identified, and efforts have been made to mitigate these non-physical discontinuities. Bardenhagen and Kober [12] proposed a particle characteristic function as an alternative to a dirac delta function; consequently, the mass of the material point can be distributed along delimited domains as opposed to being concentrated on the points. This technique was known as the Generalised Interpolation Material Point (GIMP) technique. This work served as the basis for an entire family of methods in which the mass is distributed across a domain. Rejecting the assumption that a square domain must remain square or deform uniformly on two sides, additional extensions were made. Convected Particle Domain Interpolation (CPDI) methods were able to track domain deformations with greater precision, particularly for problems involving massive deformations [188, 189]. While CPDI1 permitted shear along the elemental domain, which GIMP was incapable of capturing, CPDI2 enabled tracking each node of the element domain independently. Despite the fact that the latter is more accurate in terms of deformation representation, the computation and storage costs of calculating these element nodes must be considered. In their work, Tran et al. [207] identified the shortcomings of the CPDI domain interpolation scheme in the presence of massive deformations and proposed a Convected Particle Least Square (CPLS) scheme. Within the framework of conventional MPM, lower-order shape functions have been replaced by higher-order B-spline shape functions [206]. While this method has proven to be effective, it is important to note that solving the momentum equation requires a higher computational cost than the classical MPM. While all of these methods have performed significantly better than traditional MPM, the solution process requires more computational time as the domains spread to neighbouring cells. In addition, the application of boundary conditions is typically not simple.

3.1.4 Fluid modelling in MPM

In geomechanical applications, the presence of water, and only water in hydromechanical applications, is a common source of difficulty. Due to its near incompressibility or incompressibility, the presence of water makes numerical modelling a challenging task. This medium's density should therefore be assumed to be constant. In turn, the property of incompressibility results in explicit algorithms predicting inaccurate solutions or not converging at all unless prohibitively small time steps are taken.

The Navier-Stokes equations characterise the viscous fluid flow through conservation equations. Mass, momentum, and energy are conserved throughout an infinitesimally small volume of fluid. A fluid is a material that deforms continuously when subjected to shear stress. This is also true for some solids when the applied shear stress exceeds a certain threshold, resulting in plastic deformations. When a fluid undergoes deformation, stresses can be separated into spherical and deviatoric subcomponents. The deviatoric components of a fluid always disappear at rest or during a uniform flow. Fluid stresses are described by the expression:

$$\sigma_{ij} = -p\,\delta_{ij} + s_{ijkl}\,\dot{\varepsilon}_{kl}\,, \tag{3.2}$$

where, σ_{ij} is the stress tensor, p is the pressure, δ_{ij} is the Knonecker delta, s_{ijkl} is a symmetric fourth-order tensor comprising of viscous coefficients. Strain rate tensor, $\dot{\varepsilon}_{ij}$ is the given by the relation:

$$\dot{\varepsilon}_{ij} = \frac{1}{2}\left(\frac{\partial v_i}{\partial x_j} + \frac{\partial v_j}{\partial x_i}\right)\,, \tag{3.3}$$

where, x_i and v_i are the location and the velocity components, respectively. For a linear, isotropic fluid, Equation 3.2 can be reduced to the Navier-Poisson law for a Newtonian fluid [143] as:

$$\sigma_{ij} = -p\,\delta_{ij} + \lambda\,\dot{\varepsilon}_{kk}\,\delta_{ij} + 2\,\mu\,\dot{\varepsilon}_{ij}\,, \tag{3.4}$$

where, parameters λ and μ characterise the viscosity of the fluid. The volumetric strain rate of the fluid is given by $\dot{\varepsilon}_{kk}$. Incorporating a distinction between the spherical and deviatoric strain rate components, where $\dot{\varepsilon}_{ij}$ is given by the relation $\dot{\varepsilon}_{ij} = \dot{\varepsilon}'_{ij} + \dot{\varepsilon}_{kk}\,\delta_{ij}/3$, Equation 3.4 can be represented as:

$$\sigma_{ij} = \left(-p + \kappa\,\dot{\varepsilon}_{kk}\right)\delta_{ij} + 2\,\mu\,\dot{\varepsilon}'_{ij}\,, \tag{3.5}$$

where, $\kappa = \lambda + \frac{2}{3}\,\mu$ is the bulk viscosity term. It is inferred from Equation 3.5 that when the term $\kappa\,\dot{\varepsilon}_{kk}$ vanishes, the thermodynamic pressure p equals the spherical component of the stress tensor, $-\sigma_{kk}/3$.

3.2 Formulation of dynamic MPM for single phase problems

In this section, the formulation for the dynamic single-phase MPM is provided. The strict linearity conformance of linear shape functions is advantageously mitigated by defining a domain for the interpolation of the masses as opposed to a single infinitesimal point. This section's formulation is derived from the work of Sulsky et al. [203], in which only a single phase was considered. While the formulation that will be presented resembles the formulation of a FE code, it must be noted that there is a significant difference between the two methods, despite their common ancestry. In the case of FEM, integration is performed on Gauss points, which can range from 1 to 9 or more for artisan element definitions, whereas numerical integration in the case of MPM is performed on the material point itself, which moves through space, the former remaining spatially immobile throughout the solution procedure.

Beginning with the FEM formulation [112], the numerical formulation for MPM begins with the weak form of momentum balance equation. Momentum balance equation describes the motion equation of a body and is denoted by:

$$\rho\,\dot{\boldsymbol{v}} = div(\boldsymbol{\sigma}) + \rho\,\boldsymbol{g}\,, \tag{3.6}$$

where, ρ is the density, $\boldsymbol{g}$ is the gravitational field, $\boldsymbol{u}$ is the displacement field, $\boldsymbol{v}$ is the velocity field, and $\boldsymbol{\sigma}$ is the Cauchy stress. Rewriting Equation 3.6 in indices notation, we get:

$$\rho\,\frac{dv_i}{dt} = \frac{\partial \sigma_{ij}}{\partial x_j} + \rho\,g_i\,. \tag{3.7}$$

The presented equations are known as the strong form. A weak form is derived for use in the discretised form. This is accomplished by multiplying the strong form by a test

function, $\delta \boldsymbol{u}$, and integrating across the entire domain, Ω. The weak form of Equation 3.7 is denoted as:

$$\int_{\Omega} \delta v_i \, \rho \, \frac{dv_i}{dt} \, d\Omega = \int_{\Omega} \delta v_i \, \frac{\partial \sigma_{ij}}{\partial x_j} \, d\Omega + \int_{\Omega} \delta v_i \, \rho \, g_i \, d\Omega \,, \tag{3.8}$$

with,

$$\delta v_i = 0 \; on \; d\Omega \,. \tag{3.9}$$

By applying integration-by-parts rule on the first part of Equation 3.8, and substituting it back, we get:

$$\int_{\Omega} \delta v_i \, \rho \, \frac{dv_i}{dt} \, d\Omega = \int_{\Omega} \frac{\partial}{\partial x_j} \left(\delta v_i \sigma_{ij} \right) d\Omega - \int_{\Omega} \frac{\partial (\delta v_i)}{\partial x_j} \, \sigma_{ij} \, d\Omega + \int_{\Omega} \delta v_i \, \rho \, g_i \, d\Omega \,. \tag{3.10}$$

By applying Gauss's theorem to the first term of Equation 3.10, we get:

$$\int_{\Omega} \frac{\partial}{\partial x_j} \left(\delta v_i \, \sigma_{ij} \right) , d\Omega = \int_{\Gamma} \delta v_i \, \sigma_{ij} \, n_j \, d\Gamma \,, \tag{3.11}$$

with, Γ the boundary of the domain, Ω. Substituting Equation 3.11 in Equation 3.10 yields the weak form of the momentum balance equation:

$$\int_{\Omega} \delta v_i \, \rho \, \frac{dv_i}{dt} \, d\Omega = \int_{\Omega} \delta v_i \, \rho \, g_i \, d\Omega - \int_{\Omega} \frac{\partial (\delta v_i)}{\partial x_j} \, \sigma_{ij} \, d\Omega + \int_{\Gamma} \delta v_i \, t_i \, d\Gamma \,, \tag{3.12}$$

where, traction $t_i = \sigma_{ij} \; n_j$ is obtained using Cauchy's lemma.

The values of a variable contained within an element are determined by the nodal values and the shape function denoted by N_i. A body is represented by a collection of particles in the MPM. Interpolating the fields to and from the particles necessitates an additional step. Here, integrals are approximated as a sum over particles and denoted as:

$$\int_{\Omega} \rho(*) \, d\Omega \approx \sum_{p} \int_{V_p} \rho(*) \, dV_p \approx \sum_{p} \int_{p} (*) \, m_p \approx \sum_{p} (*) \, m_p \,, \tag{3.13}$$

where, m_p is the mass associated with the material point, p, and V_p is the particle volume. Using these definitions, the discretised momentum equation is expressed as follows:

$$\boldsymbol{M}\,\ddot{\boldsymbol{a}} = \boldsymbol{F}^{ext} - \boldsymbol{F}^{int}\,, \tag{3.14}$$

where, $\boldsymbol{M}$ is the consistent mass matrix, $\ddot{\boldsymbol{a}}$ the acceleration vector, and $\boldsymbol{F}^{ext}$ and $\boldsymbol{F}^{int}$ are external and internal force vectors, respectively. Despite introducing a small amount of numerical dissipation, the use of a lumped-mass matrix is preferred over a consistent mass matrix because its diagonal nature greatly simplifies calculation. On the element level, it is represented as

$$m_i = \sum_{p=1}^{n_p} m_p\, N_i(\boldsymbol{x}_p)\,, \tag{3.15}$$

where, n_p is the number of material point, and $\boldsymbol{x}_p$ indicates the location where shape function, N_i is evaluated and, x_p is the location of particle. Referring to Equation 3.14, the external force vector is given by:

$$\boldsymbol{F}^{ext} = \sum_{p=1}^{n_p} m_p\, \boldsymbol{N}^T(\boldsymbol{x}_p)\, \boldsymbol{g} + \int_{\Gamma} \boldsymbol{N}^T\, \boldsymbol{t}\, d\Gamma\,, \tag{3.16}$$

and, the internal force vector is given by:

$$\boldsymbol{F}^{int} = \sum_{p=1}^{n_p} V_p\, \boldsymbol{B}^T(\boldsymbol{x}_p)\, \boldsymbol{\sigma}_p\,, \tag{3.17}$$

where, $\boldsymbol{B} = \boldsymbol{L}\boldsymbol{N}$ with $\boldsymbol{L}$ being the linear differential operator, and $\boldsymbol{\sigma}_p$ is a vector containing the stress components at material point, p.

The aforementioned equations describe the procedure for solving the unknown quantities at the computational node. When including forces with surface traction, care must be taken. To accommodate tractions, one approach is to assign the corresponding forces to the closest material point [107]. After computing the forces and constructing the mass-matrix, the particle's state and position are updated by resetting the computational mesh at the end of each time step.

Time Integration

Given a diagonal mass matrix, it is trivial to integrate the system of equations over time. Vector of acceleration is given by:

$$\boldsymbol{a}^n = \left[\boldsymbol{M}_l^n\right]^{-1} \left(\boldsymbol{F}^{ext} - \boldsymbol{F}^{int}\right)^n , \tag{3.18}$$

where a forward-Euler time integration scheme is used to update the nodal velocity from the nodal accelerations. In practice, however, a modified algorithm proposed by Sulsky et al. [203] is used. The nodal velocities of the particle is updated according to the relation:

$$\boldsymbol{v}_p^{n+1} = \boldsymbol{v}_p^n + \sum_{i=1}^{n_{dof}} \Delta t \; N_i(\boldsymbol{x}_p) \; \boldsymbol{a}_i^n , \tag{3.19}$$

where, n_{dof} represents the number of grid degrees of freedom, $\boldsymbol{v}_p^n$ and $\boldsymbol{v}_p^{n+1}$ are the velocities of particle p at the beginning and end of time step Δt, respectively. Then, the nodal velocities are mapped from the particles to the nodes, keeping in mind that momentum must be conserved. It is provided by:

$$\boldsymbol{M}_l^n \boldsymbol{v}^{n+1} = \sum_{p=1}^{n_p} m_p \, \boldsymbol{N}^T(\boldsymbol{x}_p) \, \boldsymbol{v}_p^{n+1} , \tag{3.20}$$

where, $\boldsymbol{v}^{n+1}$ is the updated nodal velocity. It is then used to obtain incremental nodal displacement via the relation:

$$\Delta \boldsymbol{u} = \Delta t \, \boldsymbol{v}^{n+1} . \tag{3.21}$$

Position of the particle is updated via the relation:

$$\boldsymbol{v}_p^{n+1} = \boldsymbol{u}_p^n + \boldsymbol{N}(\boldsymbol{x}_p) \, \Delta \boldsymbol{u} , \tag{3.22}$$

where, $\boldsymbol{u}_p^n$ and $\boldsymbol{u}_p^{n+1}$ are positions of particle at time t^n and t^{n+1}, respectively. Since the position of a particle is updated using a continuous velocity field with a single value, particle collisions are avoided. This also enables automatic, non-slip contact

between bodies without the need for a separate algorithm. After obtaining the updated nodal velocities, strain increment, $\Delta\boldsymbol{\varepsilon}_p$ of material point, p is calculated according to the relation:

$$\boldsymbol{\varepsilon}_p = \boldsymbol{B}(\boldsymbol{x}_p)\,\Delta\boldsymbol{u}_e\,, \tag{3.23}$$

where, $\Delta\boldsymbol{u}_e$ is vector of incremental nodal displacements of element, e to which the material point belongs. Given the strain increment, stress increment, $\Delta\boldsymbol{\sigma}_p$ is updated at each material point using the constitutive law unique to that material point. Total stresses are updated via the relation:

$$\boldsymbol{\sigma}_p^{n+1} = \boldsymbol{\sigma}_p^{n} + \Delta\boldsymbol{\sigma}_p\,, \tag{3.24}$$

where, $\boldsymbol{\sigma}_p^n$ and $\boldsymbol{\sigma}_p^{n+1}$ are global stresses at time t^n and t^{n+1}, respectively. The reader is referred to references [11, 45, 107] for a more comprehensive derivation of the single phase dynamic MPM.

3.3 Deformation of particle domains

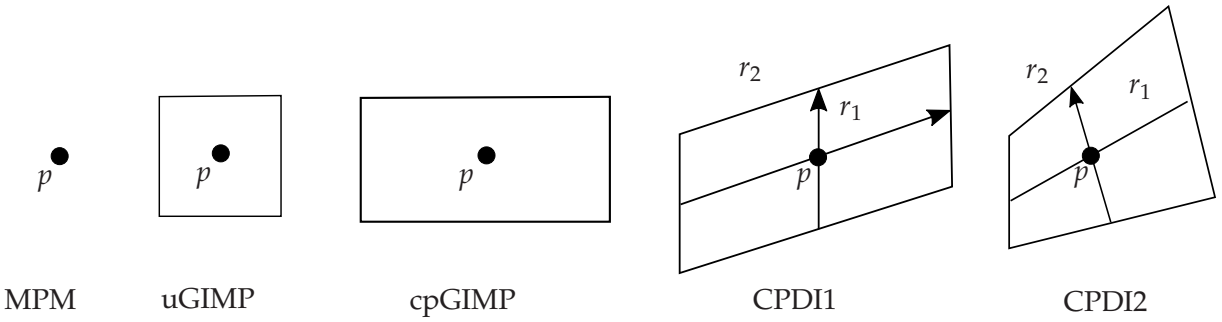

Figure 3.3: Evolution of domains to represent the material points

This section provides an overview of the Convected Particle Domain Interpolation (CPDI) method. Efforts have been made to provide relevant, pertinent information within the context of this work. The material point method is a particle method based on a grid that can be used to solve large deformation problems. As depicted in Figure 3.3, the traditional formulation of MPM treats discretised particles as a single mass. The continuum is discretised by a set of infinitesimally small material points or particles, and a hybrid Lagrangian-Eulerian solution procedure is employed, where the *lagrangian* particles carry history-dependent information such as stress, strain, and displacement, while the *eulerian* background computational grid is used to solve the momentum equations. While the background computational grid is stationary in time and space and undergoes no deformation throughout the simulation, the *lagrangian* particles are tracked

during the deformation. Nonetheless, the classical formulation of MPM is susceptible to the 'cell/grid crossing' error for problems involving massive particle movement.

Earlier versions of the MPM assumed a collocated distribution of material properties throughout the particle domain. Numerical instability was introduced to the model whenever particles crossed element boundaries. Earlier research focused on reducing this artificial oscillation. With the Generalised Interpolation Material Point (GIMP) Method, the concentrated mass of the material point is distributed over a finite subdomain [12]. The classical MPM's dirac delta function was replaced with a smoother function. The smoother function is then used to interpolate the data contained in the material points and evaluate the internal, external, and traction forces. The basis functions in GIMP can be interpreted as the averages of the particle's entire domain's basis functions. GIMP defines a characteristic function for each particle, and when a dirac delta is selected as the characteristic function, the classical MPM formulation is obtained. In GIMP, particle domains are typically represented as rectangles. Two tracking strategies for domains have been proposed. In the first, it is assumed that the particle domains remain unchanged throughout the simulation. This is frequently referred to as uGIMP or undeformed GIMP. In the alternative method, the domain sizes are allowed to change over time so that they continue to be regular rectangles. This technique is known as cpGIMP, which stands for convected particle GIMP. Shear or off-diagonal deformation cannot be captured by cpGIMP, but it performs well for simulations where the deformation is predominantly along the grid direction. Unfortunately, this assumption regarding particle domain deformation is incorrect for problems involving shear or large rotations.

The GIMP method evaluates the effective averages of the grid basis functions ($\boldsymbol{N}_{ip}$) and gradients ($\nabla \boldsymbol{N}_{ip}$) are given using the relationship:

$$\boldsymbol{N}_{ip} = \frac{1}{\Omega_p} \int_{\Omega} \xi \left(\boldsymbol{x} - \boldsymbol{x}_p \right) N_i(\boldsymbol{x}) \, d\Omega \,, \tag{3.25}$$

and,

$$\nabla \boldsymbol{N}_{ip} = \frac{1}{\Omega_p} \int_{\Omega} \xi \left(\boldsymbol{x} - \boldsymbol{x}_p \right) \nabla N_i(\boldsymbol{x}) \, d\Omega \,, \tag{3.26}$$

respectively. Here, $\xi(\boldsymbol{x})$ is the particle characteristic function over domain Ω. A top-hat function is typically used in GIMP and is given by:

$$\xi(\boldsymbol{x}) = \begin{cases} 1, & \boldsymbol{x} \in \Omega_{part} \\ 0, & \text{otherwise} \end{cases} . \tag{3.27}$$

If x^0 and y^0 are the initial dimensions of the regular rectangular particle domain in uGIMP, and the evolution of particle domains in time is ignored, the update relation for the domain at time $t + \Delta t$ can be expressed as follows:

$$\begin{bmatrix} x^{t+\Delta t} \\ y^{t+\Delta t} \end{bmatrix} = \begin{bmatrix} x^0 \\ y^0 \end{bmatrix} . \tag{3.28}$$

Since particle domains are permitted to deform in cpGIMP, under the condition that they always remain rectangular, the update to the domains is given by the relation:

$$\begin{bmatrix} x^{t+\Delta t} \\ y^{t+\Delta t} \end{bmatrix} = \begin{bmatrix} F_{11}^{t+\Delta t} & 0 \\ 0 & F_{22}^{t+\Delta t} \end{bmatrix} \begin{bmatrix} x^0 \\ y^0 \end{bmatrix} , \tag{3.29}$$

where F represents the deformation gradient and the subscripts indicate that only the diagonal terms of F have been utilised. While cpGIMP permits particle deformation in terms of extension or compression, its performance is less than ideal for problems involving bending or shear.

It has been demonstrated that the GIMP method is susceptible to instabilities in extension or large distortions due to its inability to track particle deformation [188, 189]. Alternative methods to reduce particle crossing noise have been proposed. Zhang et al. [226] proposed a method for eliminating the discontinuity of the gradients of linear interpolation functions by employing a Dual Domain Material Point (DDMP). DDMP effectively expands the influence of the material point's domain without following the shape of the material point. This procedure modifies the gradients of the shape function in order to provide a smoother crossing behaviour. By modelling thin structures as

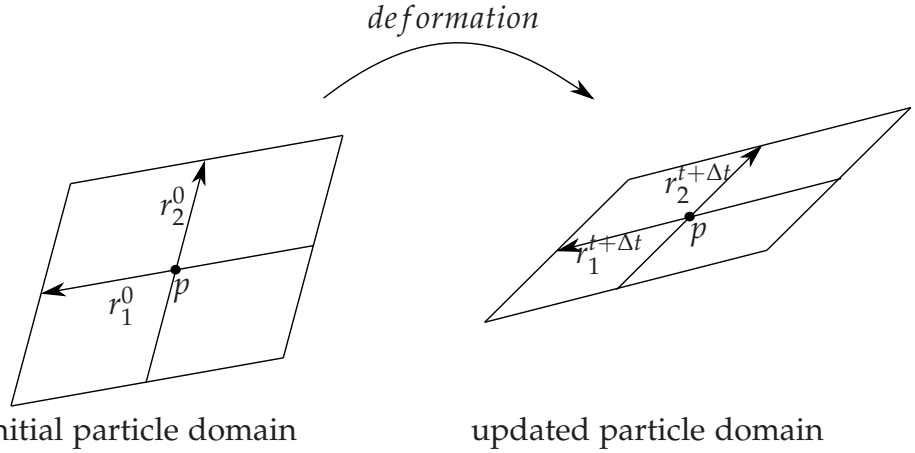

Figure 3.4: Initial and updated particle domain using the CPDI method

finite element membranes that move through a computational mesh, the grid crossing error is eliminated when simulating them.

3.3.1 Convected Particle Domain Interpolation formulation

Using the uGIMP and cpGIMP formulations, rectangles are used to track domains. Over the domain of the particle, only extension/compression deformations parallel to the direction of the grid are permitted, while shear deformations are completely disregarded. The CPDI method is capable of tracking particle domains more precisely, even during shear deformations, as shown in Figure 3.4, by employing an alternative grid function.

Using the fully updated deformation gradient of each particle, the deformations and rigid body rotations computed at each particle are used to calculate the updated particle domain at each step of computation. By defining vertices that define the particle's domains as $\boldsymbol{r}_1^0$ and $\boldsymbol{r}_2^0$, the update of the vertices is computed using the relation:

$$\begin{aligned} \boldsymbol{r}_1^{t+\Delta t} &= \boldsymbol{F}_p^{t+\Delta t}\, \boldsymbol{r}_1^0\,, \\ \boldsymbol{r}_2^{t+\Delta t} &= \boldsymbol{F}_p^{t+\Delta t}\, \boldsymbol{r}_2^0\,, \end{aligned} \tag{3.30}$$

where $t + \Delta t$ represents the current computation step and $\boldsymbol{F}_p$ represents the computed deformation gradient at particle p. This update algorithm is illustrated graphically in Figure 3.4.

The alternative grid basis functions are defined as an interpolation of the standard grid basis functions at the four corners of each particle domain using the relation:

$$\boldsymbol{N}_i^*(\boldsymbol{x}) = \sum_p \boldsymbol{N}_i^p(\boldsymbol{x}), \qquad \text{where} \qquad \boldsymbol{N}_i^p(\boldsymbol{x}) = \begin{cases} \sum_{\alpha=1}^4 \boldsymbol{\phi}_\alpha^p(\boldsymbol{x})\, \boldsymbol{N}_i(\boldsymbol{x}_\alpha^p) : & \boldsymbol{x} \in \Omega_p \\ 0 : & \boldsymbol{x} \notin \Omega_p \end{cases}. \tag{3.31}$$

Here, $\boldsymbol{N}_i(\boldsymbol{x})$ represents the standard grid shape functions associated with grid nodes, i, $\phi_\alpha^p(\boldsymbol{x})$ is the standard FEM-style interpolating function defined as a four-noded element on the particle domain. Here, α represents the corner of the particle domain, and $\boldsymbol{x}_\alpha^p$ specifies this corner's position. $\boldsymbol{N}_i^*(\boldsymbol{x})$ is an interpolation of $\boldsymbol{N}_i(\boldsymbol{x})$ to the particle domain corners. Figure 3.5 is a graphical representation of the grid basis function of standard MPM and the alternate grid basis functions of CPDI. As depicted in the figure, when the continuum stretches sufficiently to cause a significant separation of particles,

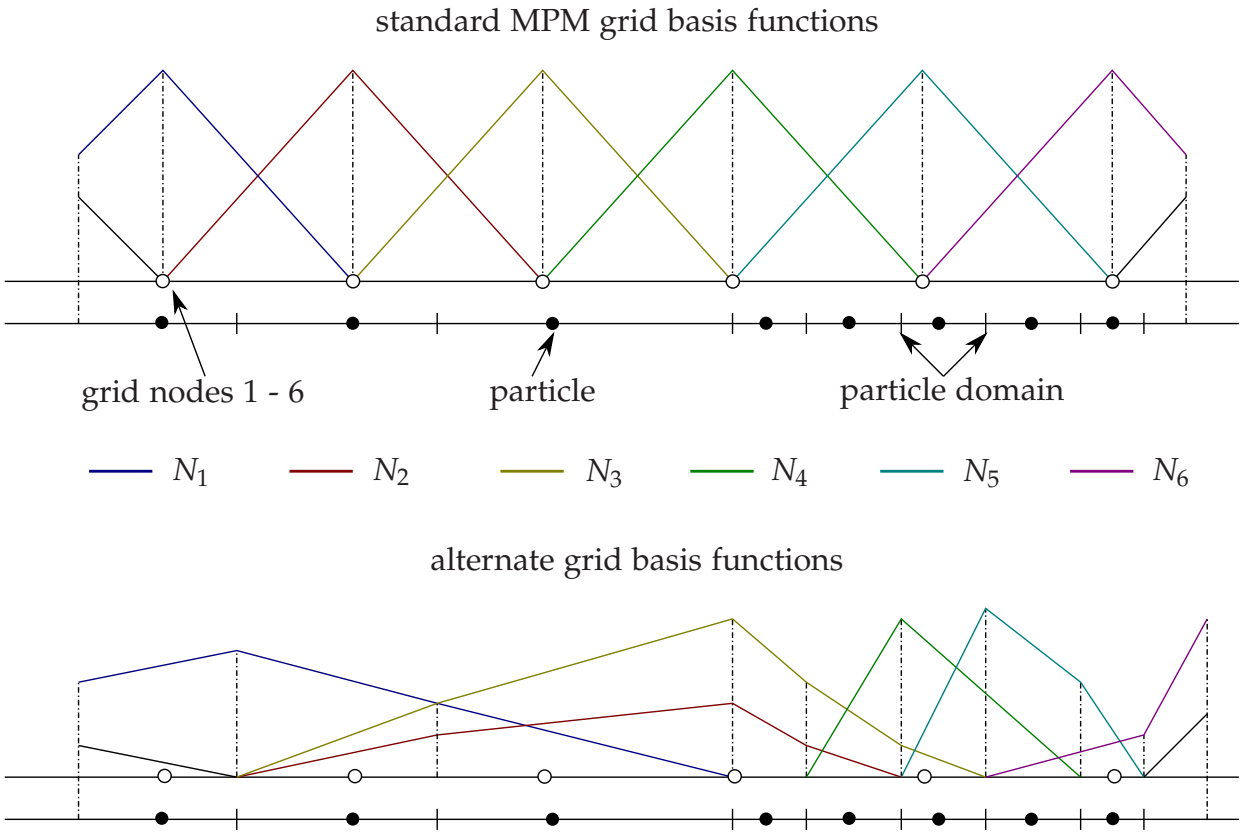

Figure 3.5: Alternate grid basis funtions for a one-dimensional case in CPDI [189]

the CPDI shape functions also stretch, allowing neighbouring particles to interact even when they are separated by more than one computational grid cell of the background. Classical MPM and the GIMP method family lack this feature, making them susceptible to extension instability. The following relations can be used to determine the shape functions and their gradients:

$$N_{ip} = \frac{1}{\Omega_p} \int_\Omega N_i^p(\boldsymbol{x})\, d\Omega = \frac{1}{\Omega_p} \sum_{\alpha=1}^{4} \left(\int_\Omega \boldsymbol{\phi}_\alpha^p(\boldsymbol{x})\, d\Omega \right) N_i(\boldsymbol{x}_\alpha^p)\,, \tag{3.32}$$

and,

$$\nabla N_{ip} = \frac{1}{\Omega_p} \int_\Omega \nabla N_i^p(\boldsymbol{x})\, d\Omega = \frac{1}{\Omega_p} \sum_{\alpha=1}^{4} \left(\int_\Omega \nabla \boldsymbol{\phi}_\alpha^p(\boldsymbol{x})\, d\Omega \right) N_i(\boldsymbol{x}_\alpha^p)\,, \tag{3.33}$$

respectively. The shape functions are calculated analytically according to the relation:

$$\boldsymbol{N}_{ip} = \frac{1}{4}\left[\boldsymbol{N}_i(\boldsymbol{x}_1^p) + \boldsymbol{N}_i(\boldsymbol{x}_2^p) + \boldsymbol{N}_i(\boldsymbol{x}_3^p) + \boldsymbol{N}_i(\boldsymbol{x}_4^p)\right], \tag{3.34}$$

and, their gradients according to the relation:

$$\nabla \boldsymbol{N}_{ip} = \frac{1}{2\Omega_p}\left\{\left(\boldsymbol{N}_i(\boldsymbol{x}_1^p) - \boldsymbol{N}_i(\boldsymbol{x}_3^p)\right)\begin{bmatrix} r_{1y}^n - r_{2y}^n \\ r_{2x}^n - r_{1x}^n \end{bmatrix} + \left(\boldsymbol{N}_i(\boldsymbol{x}_2^p) - \boldsymbol{N}_i(\boldsymbol{x}_4^p)\right)\begin{bmatrix} r_{1y}^n + r_{2y}^n \\ -r_{2x}^n - r_{1x}^n \end{bmatrix}\right\}. \tag{3.35}$$

The components (r_{1x}^n, r_{1y}^n) and (r_{2x}^n, r_{2y}^n) are components of vectors $\boldsymbol{r}_1^n$ and $\boldsymbol{r}_2^n$ at current computational time step n, respectively. The reader is directed to Sadeghirad et al. [189] for a comprehensive formulation of CPDI.

3.3.2 Axi-symmetric CPDI formulation extension

Hamad [83] extended the CPDI formula to solve axisymmetric type problems. Giridharan et al. [73] and Moormann et al. [156] successfully implemented this method to simulate open pipe pile installation problems in saturated sand. While the plane-strain assumption is typically sufficient for geotechnical applications, it can be easily extended to simulate axisymmetric geometry and loading. Sulsky and Schreyer [202] reformulated the early extension of the material point method to exploit the azimuthal symmetry. Nairn and Guilkey [161] extended the corresponding formulation of the GIMP method by truncating the particle supporting domain at its intersection with the centre line. Here, an algorithm based on resizing the CPDI parallelogram domains so that their vertices remain within the valid territory along the axis of symmetry is utilised.

As in the case of the plane-strain problem, shape functions and their gradients are given via the equations 3.34 and 3.35. The vectors defining the parallelogram of the particle domain, as depicted in Figure 3.4, are updated utilising the relations depicted in Equation 3.30. Here, $\boldsymbol{F}_p$ represents the computed deformation gradient at particle, p. The deformation gradient is continuously updated using the relation:

$$\boldsymbol{F}_p^{t+\Delta t} = \left(\boldsymbol{I} + \nabla \boldsymbol{v}_p^{t+\Delta t}\,\Delta t\right)\boldsymbol{F}_p^{t+\Delta t}, \tag{3.36}$$

where, Δt is the time step increment and $\boldsymbol{I}$ is a second-order identity tensor. For axisymmetric problems, the velocity gradient, $\nabla \boldsymbol{v}_p$ at location of particle, p is updated via relation:

$$\nabla \boldsymbol{v}_p^{t+\Delta t} = \begin{bmatrix} \frac{\partial v_x}{\partial x} & 0 & \frac{\partial v_x}{\partial z} \\ 0 & \frac{v_x}{x_p} & 0 \\ \frac{\partial v_z}{\partial x} & 0 & \frac{\partial v_z}{\partial z} \end{bmatrix}, \tag{3.37}$$

where, v_x is the nodal velocity along the x-direction, and x_p provides the coordinates of the location of particle, p. The gradient in the hoop direction is interpolated from the information of grid according to the relation:

$$\frac{v_x}{x_p} = \frac{1}{x_p} \sum_{i=1}^{n_{nodes}} \boldsymbol{N}_i \, v_i^{t+\Delta t}. \tag{3.38}$$

The components corresponding to the x and z directions are given via the relation:

$$\nabla \boldsymbol{v}_p^{t+\Delta t} = \sum_{i=1}^{n_{nodes}} \nabla \boldsymbol{N}_i \, \boldsymbol{v}_i^{t+\Delta t}. \tag{3.39}$$

The gradients are evaluated according to Equation 3.33 and the nodal velocities, $\boldsymbol{v}_i^{t+\Delta t}$ is calculated according to the relation:

$$\boldsymbol{v}_i^{t+\Delta t} = \frac{\sum_p N_{ip} \, m_p \, \boldsymbol{v}_p}{m_i} + \boldsymbol{a}_i \, \Delta t, \tag{3.40}$$

where $\boldsymbol{a}_i$ is the nodal acceleration in accordance with a typical explicit Euler forward integration scheme to obtain the velocity.

3.4 Comparison of performance between MPM and CPDI

The Material Point Method allows the particles to move throughout the computational space when dealing with large deformation problems, which results in the migration of particles from one computational background grid to another. In the context of classical MPM, this migration of particles from one computational grid to another presents significant numerical challenges. In dynamic problems, the equilibrium could fail, with the computation in extreme cases failing entirely. This issue arises because when particles cross from one element boundary to another, the crossing causes a significant imbalance in the computed forces at the nodes.

The Method of Manufactured Solutions (MMS) is utilised to evaluate the accuracy and performance of MPM versus CPDI. The MMS provides a general method for generating an analytical solution for verifying code accuracy. The objective of the procedure is to produce an exact solution without regard for its physical realism. The work of Roache [187] offers a more comprehensive overview of the MMS. The performance of the methods presented here is compared using the MMS for the two-dimensional problem solved in references [188, 189]. Since the model's solution is used as an input, the external force necessary to achieve this solution can be determined analytically. The resultant numerical solution can then be compared to the calculated analytical solution by executing the problem with the computed external forces and calculating the difference between the assumed and actual solutions. This method is typically employed for the verification of nonlinear codes and algorithms, but in this instance it is used to compare the MPM and CPDI methods. The method quantifies comparisons by calculating the error norm given by the relationship:

$$\text{error} = \frac{\sqrt{\sum_{n=1}^{N_t} \sum_{n=1}^{N_p} \left\| \boldsymbol{u}^{calc}(\boldsymbol{x}_p,\, t_i) - \boldsymbol{u}^{exact}(\boldsymbol{x}_p,\, t_i) \right\|^2}}{N_t \times N_p}\,, \tag{3.41}$$

where, N_t and N_p are total number of time steps and particles, respectively. $\boldsymbol{u}^{calc}(\boldsymbol{x}_p,\, t_i)$ and $\boldsymbol{u}^{exact}(\boldsymbol{x}_p,\, t_i)$ are the numerically calculated and analytical displacement vectors of the solution, respectively. In this problem, the time step used is also specified by the following relation:

$$\Delta t = 0.4\,\frac{\Delta x}{C}\,, \tag{3.42}$$

where, Δx is the cell spacing, C is the wave speed, given by the relation:

$$C = \sqrt{\frac{E}{\rho_0}}\,, \tag{3.43}$$

in which, E and ρ_0 are the modulus of elasticity and the initial density, respectively. As assumed in references [188, 189], the Neo-Hooken material model was assumed for the solid constituent and is represented as follows:

$$\boldsymbol{\sigma} = \frac{\lambda \ln J}{J}\boldsymbol{I} + \frac{\mu}{J}(\boldsymbol{F}\,\boldsymbol{F}^T - \boldsymbol{I})\,, \tag{3.44}$$

where, $\boldsymbol{I}$ is the identity tensor, $\boldsymbol{F}$ the deformation gradient and J is its determinant. λ and μ are the first and second Lamé parameters, respectively. This frame-independent model is adequate for comparing models, even though more complex models have been implemented within the MPM framework.

A axis-aligned unit square's displacement is computed. In a unit square, it is assumed that the displacement field is given by the equations:

$$\begin{aligned} u_x &= A \sin\left(\frac{2\,\pi\,X}{L}\right) \sin\left(\frac{C\,\pi\,t}{L}\right), \\ u_y &= A \sin\left(\frac{2\,\pi\,X}{L}\right) \sin\left(\frac{C\,\pi\,t}{L} + \pi\right), \end{aligned} \tag{3.45}$$

where X and Y are the global coordinate system components of the reference configuration. In this calculation, A represents the maximum amplitude of displacement and is assumed to be 5 cm. t represents time, L is the unit of square length (L = 1 m), and the wavespeed constant C is defined in Equation 3.43. The body forces necessary to attain the assumed displacement field are given by the following relations:

$$\begin{aligned} b_x &= \frac{\pi^2\,u_x}{L^2}\left(\frac{4\,\mu}{\rho_0} - C^2 - 4\frac{\lambda\,[\ln F_x\,F_y - 1] - \mu}{\rho_0\,F_x^2}\right), \\ b_y &= \frac{\pi^2\,u_y}{L^2}\left(\frac{4\,\mu}{\rho_0} - C^2 - 4\frac{\lambda\,[\ln F_x\,F_y - 1] - \mu}{\rho_0\,F_y^2}\right). \end{aligned} \tag{3.46}$$

Reference [189] contains a detailed derivation of the body forces. Referring to equation 3.46, F_x and F_y are the non-zero components of the deformation gradient tensor $\boldsymbol{F}$. In addition, it can be observed that, for the axis-aligned problem, only the diagonal terms of $\boldsymbol{F}$ are non-zero and can be expressed by the following relations:

$$\begin{aligned} F_x &= 1 + \frac{2\,A\,\pi}{L}\cos\left(\frac{2\,\pi\,X}{L}\right)\sin\left(\frac{C\,\pi\,t}{L}\right), \\ F_y &= 1 + \frac{2\,A\,\pi}{L}\cos\left(\frac{2\,\pi\,Y}{L}\right)\sin\left(\frac{C\,\pi\,t}{L} + \pi\right). \end{aligned} \tag{3.47}$$

The problem domain is discretised using five different grid resolutions: 8×8, 16×16, 32×32, 64×64 and 128×128. Each grid contains a single particle, although studies with four and nine particles are also conducted. It is assumed that the modulus of elasticity

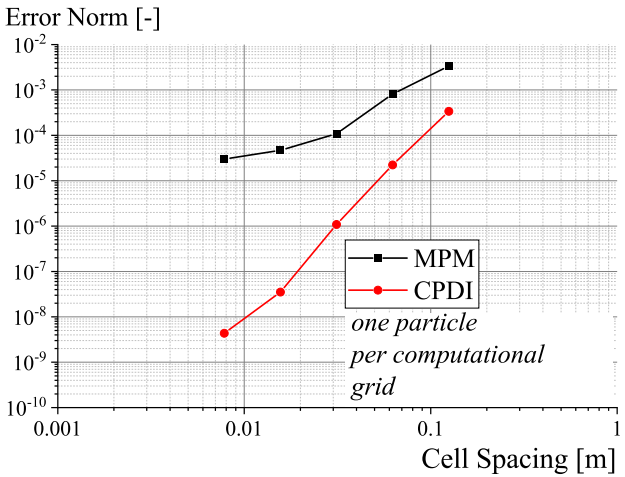

(a) Convergence curves for the standard MPM and CPDI method
for axis-aligned displacement in a unit square problem,
1 particle per computational grid

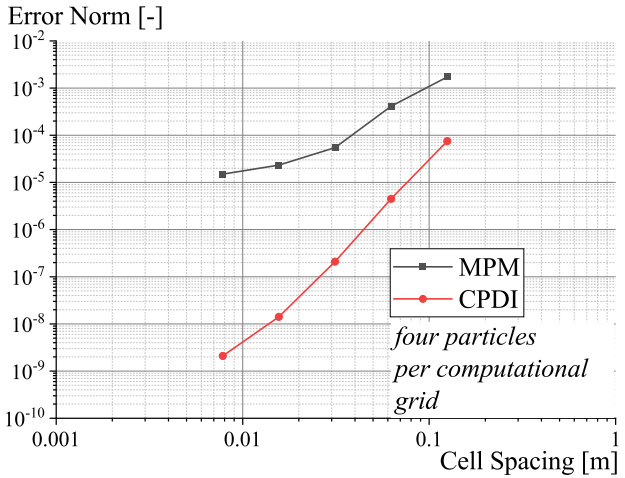

(b) Convergence curves for the standard MPM and CPDI method
for axis-aligned displacement in a unit square problem,
4 particles per computational grid

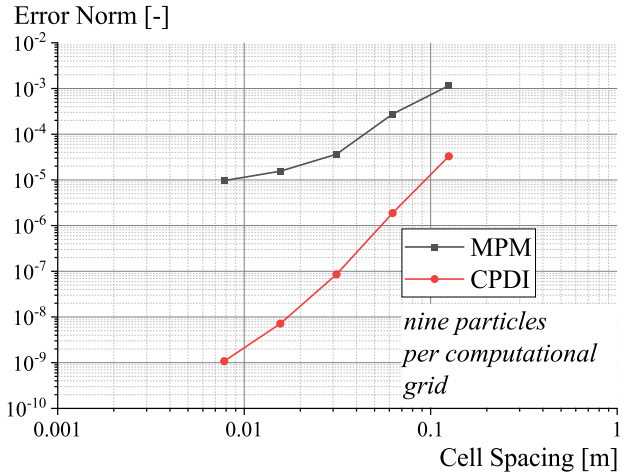

(c) Convergence curves for the standard MPM and CPDI method
for axis-aligned displacement in a unit square problem,
9 particles per computational grid

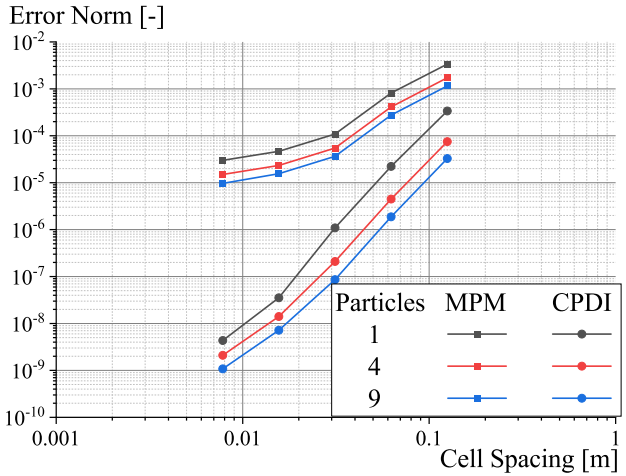

(d) Convergence curves for the standard MPM and CPDI method
for axis-aligned displacement in a unit square problem,
all particles comparison grid

Figure 3.6: Convergence curves for the standard MPM and CPDI method for axis-aligned displacement in a unit square problem

(E) is 1×10^4 kPa, Poisson's ratio is 0.3, and that the initial density (ρ_0) is one (g/cm^3). One full period of oscillation is represented by 0.02 seconds in the real-time simulation. Calculations were conducted for both MPM and CPDI discretisations, and errors were computed. Figure 3.6a shows the results of the calculation using one particle per grid. Figure 3.6a demonstrates that the MPM model had a slower convergence rate than the CPDI model. This enables us to conclude that the alternative grid basis functions proposed by the CPDI method can help us more accurately evaluate the mapping matrix that couples grid values to particle values ϕ_{ip} and its gradients, $\nabla\phi_{ip}$.

Figures 3.6b and 3.6c depict the results of repeated calculations in which the cell was populated with four and nine particles, respectively. A similar trend emerges compared to when only one particle was used. As a result of using nine particles per grid as opposed to one, the error standard is reduced by a factor at the expense of increased computational expense. Increasing the number of particles per grid while keeping the grid size constant reduces the error approximately linearly. Figure 3.6d compares the MPM and CPDI error norms for the cases of one, four, and nine particles per grid. For problems in which the region of interest is already determined, either by design or by experience, a non-uniform particle distribution meshing scheme can be used that is computationally less expensive than a global particle density refinement. In the work of Hamad [83], this localisation was utilised within the context of CPDI. This information is utilised in Chapter 6 when simulating open steel pipe piles. The performance of MPM, GIMP and CPDI is analysed in greater detail in Appendix A.

3.5 Formulation of the penalty contact algorithm

As the displacement constraints are unknown in advance, the treatment of the contact problem using the constrained optimisation method is a difficult task. Consequently, it is frequently transformed into a series of unconstrained optimisation problems by employing the Lagrange multiplier method or the penalty method. Although the penalty method yields approximations, it is widely used due to its ease of use in weakly satisfying kinematic constraints. Using a penalty function P, the potential energy is penalised proportionally to the amount of constraint violation in a region Γ_c where contact violation exists. The penalty function is expressed as:

$$P = \frac{1}{2}\omega_n \int_{\Gamma_c} g_n^2 \, d\Gamma_c + \frac{1}{2}\omega_t \int_{\Gamma_c} g_t^2 \, d\Gamma_c \,, \tag{3.48}$$

where, ω is the penalty parameter, g is the gap function, and the subscripts n and t refer to the normal and tangential direction, respectively. This equation is added to the total potential energy to transform the constrained minimization problem into

an unconstrained minimization problem. From the variation of Equation 3.48, which yields the contact variational form, the contact variational form is derived, and is given by:

$$\delta P\left(\boldsymbol{u}, \delta \boldsymbol{u}\right) = \omega_n \int_{\Gamma_c} g_n \; \delta g_n \, d\Gamma_c + \omega_t \int_{\Gamma_c} g_t \; \delta g_t \, d\Gamma_c \,, \tag{3.49}$$

in which, δ denotes the variation of a quantity, and $\boldsymbol{u}$ in the displacement vector. The gap functions are defined using the relations:

$$g_n = \left(\boldsymbol{x}_s - \boldsymbol{x}_{\bar{s}}\right) \, \boldsymbol{e}_n^T \qquad \text{and} \qquad g_t = \|\boldsymbol{t}^0\| \, \left(\xi_{\bar{s}} - \xi_{\bar{s}}^0\right) \,, \tag{3.50}$$

with, $\boldsymbol{x}_s$ is the position vector of the slave node $\boldsymbol{s}$, $\bar{s}$ being the projection of s on the master segment, and $\boldsymbol{e}_n$ is the unit vector in the normal direction. The superscript 0 in Equation 3.50 denotes the values at previous time step, $\boldsymbol{t}$ is the tangential vector, and ξ is the natural coordinate defined as:

$$\xi = \frac{1}{\|\boldsymbol{t}\|} \, \left(\boldsymbol{x}_s - \boldsymbol{x}_1\right)^T \, \boldsymbol{e}_t \qquad \text{and} \qquad 0 \leq \xi \leq 1 \,, \tag{3.51}$$

where, $\boldsymbol{x}_1$ is the position vector of one of the master segment ends, and $\boldsymbol{e}_t$ is the unit vector in the tangential direction. Taking the variation of Equation 3.50 and substituting it back into Equation 3.49 yields the following result:

$$\begin{aligned} \delta P\left(\boldsymbol{u}, \delta \boldsymbol{u}\right) = \omega_n \int_{\Gamma_c} g_n \, \boldsymbol{e}_n^T \left(\delta \boldsymbol{u}_s - \delta \boldsymbol{u}_{\bar{s}}\right) \, d\Gamma_c \\ + \omega_t \int_{\Gamma_c} g_t \, \|\boldsymbol{t}^0\| \left(\frac{\|\boldsymbol{t}\| \, \boldsymbol{e}_t^T \left(\delta \boldsymbol{u}_s - \delta \boldsymbol{u}_{\bar{s}}\right) + g_n \, \boldsymbol{e}_n^T \, \delta \boldsymbol{u}_{\bar{s},\xi}}{\|\boldsymbol{t}\|^2 - g_n \, \boldsymbol{e}_n^T \, \boldsymbol{x}_{\bar{s},\xi\xi}} \right) \, d\Gamma_c \,, \end{aligned} \tag{3.52}$$

which is discretised to the form:

$$\delta P(\boldsymbol{u}, \delta \boldsymbol{u}) \approx \sum_{i=1}^{n_s} \delta \hat{\boldsymbol{u}}^T \left(\omega_n \, g_n \, \boldsymbol{C}_n + \omega_t \, g_t \, \boldsymbol{C}_t\right)_i \,, \tag{3.53}$$

where $\hat{\boldsymbol{u}}$ is the nodal displacement, n_s is the number of the slave nodes that penetrate into the master segments. $\boldsymbol{C}_n$ and $\boldsymbol{C}_t$ in Equation 3.53 read [113, 178]

$$\boldsymbol{C}_n = \boldsymbol{N} - \frac{g_n}{l}\,\boldsymbol{Q}\,, \qquad \text{and} \qquad \boldsymbol{C}_t = \boldsymbol{T} + \frac{g_n}{l}\,\boldsymbol{P}\,, \tag{3.54}$$

where,

$$\boldsymbol{u} = \begin{bmatrix} \boldsymbol{u}_s \\ \boldsymbol{u}_1 \\ \boldsymbol{u}_2 \end{bmatrix} \qquad \boldsymbol{N} = \begin{bmatrix} \boldsymbol{e}_n \\ -(1-\xi)\,\boldsymbol{e}_n \\ -\xi\,\boldsymbol{e}_n \end{bmatrix} \qquad \boldsymbol{T} = \begin{bmatrix} \boldsymbol{e}_t \\ -(1-\xi)\,\boldsymbol{e}_t \\ -\xi\,\boldsymbol{e}_t \end{bmatrix} \qquad \boldsymbol{P} = \begin{bmatrix} \boldsymbol{0} \\ -\boldsymbol{e}_n \\ \boldsymbol{e}_n \end{bmatrix} \qquad \boldsymbol{Q} = \begin{bmatrix} \boldsymbol{0} \\ -\boldsymbol{e}_t \\ \boldsymbol{e}_t \end{bmatrix}\,, \tag{3.55}$$

where $\boldsymbol{u}_1$ and $\boldsymbol{u}_2$ represent the displacement of the two ends of the master element, with lenght l. The formula for the final frictional force expressed on the slave and master nodes is:

$$\boldsymbol{f}^{intr} = \sum_{i=1}^{n_s} \left(\omega_n\, g_n\, \boldsymbol{C}_n + \omega_t\, g_t\, \boldsymbol{C}_t\right)\,, \tag{3.56}$$

in which $\boldsymbol{f}^{intr}$ is the assembly of the interaction forces. The reader is directed to reference [84] for additional information about the contact algorithm and its implementation.

3.5.1 Detection of a contact pair

For the majority of dynamic impact algorithms implemented in explicit schemes, the majority of computational time is consumed by the search for the contact pair. To reduce the number of required iterations, commercial FE software frequently employs a bucket-sorting algorithm, which is also implemented for a coupling between FEM and MPM [48]. The detection of contact pairs in the present work is accomplished in three steps, which has proven to be quite efficient and accurate. The initial step is to determine if the momenta of various interface discretisations contribute to the same computational node. Elements attached to this node are then marked as belonging to a zone containing a surface node that may be in contact. Therefore, the next iteration will be performed on the surface nodes that are contained within the tagged elements, which is typically a significantly smaller number than the total number of surface nodes. In the second step of the search algorithm, it is determined whether the distance between a node of an entity and a node of a different entity is less than a minimum search size. For the adopted explicit procedure, in which the propagating wave is constrained by the grid size during a time step, the minimum search size is the computational grid spacing.

To complete the definition of a node-segment pair, the following conditions must be met:

$$g_n < 0 \quad \text{and} \quad 0 \leq \xi \leq 1\,, \tag{3.57}$$

where, the first condition ensures that the slave node penetrates the master segment, while the second condition verifies that the slave node is within the master element's space.

3.5.2 Calculation of the contact forces

When a pair of a slave node and a master segment is established, the resisting forces to oppose the penetration is calculated using Equation 3.56. After assembling the global vectors, a predictor-corrector procedure can be carried out to enhance the resolution of the nodal forces. Nevertheless, it is assumed that the force estimation error is small when explicit time step is considered, so no iteration procedure is performed in this paper. To couple the surface mesh with the MPM solution, the contact forces are mapped from the one-dimensional boundary mesh to the four-node computational mesh using the following relation:

$$\boldsymbol{f}_i^{cont} = \sum_{j=1}^{n_c} N_i^j \, \boldsymbol{f}_j^{intr}\,, \tag{3.58}$$

in which n_c is the total number of the contact nodes, N_i^j is the shape function of the computational node i being evaluated at the location of the boundary node j, $\boldsymbol{f}^{cont}$ is the contact forces expressed at the computational grid. The interaction of the bodies will contribute to the momentum equation of an entity through the relation:

$$m_i \, \boldsymbol{a}_i = \boldsymbol{f}_i^{int} + \boldsymbol{f}_i^{ext} + \boldsymbol{f}_i^{cont}\,, \tag{3.59}$$

with m_i is the lumped mass at grid node i, $\boldsymbol{a}$ is the nodal acceleration, and $\boldsymbol{f}^{int}$ and $\boldsymbol{f}^{ext}$ are the internal and external force vectors, respectively. Validation examples of the contact algorithm are provided in Appendix B.

3.6 Validation of CPDI : Granular column collapse simulation

This chapter aimed to present the fundamental formulations of CPDI for numerically addressing large deformations. Therefore, it is essential to validate the method's implementation. The collapse of a granular column is reproduced numerically for this purpose. Simulating granular material is essential not only in geotechnical engineering, but also in production engineering, particularly in the powder metallurgical industry, where the compaction of metal powders in dies must be simulated. Geotechnical engineering is particularly interested in simulating granular material. Applications such as debris flow, avalanches, failure of slopes, and landslides, among others, would benefit from the simulation of granular material. Large scale models of avalanches [72, 149] and landslides [4, 132, 195] have been created; however, extensive limitations in simulating large-scale models have led to the simulation of experiments involving smaller prototypes.

3.6.1 Review of previous numerical simulations

The granular column experiment involves the sudden release of a granular column that was initially contained due to gravity. Lifting the restraining container swiftly or swinging open the gate have previously been employed [10, 134]. Cylindrically confined [123, 135] or two-dimensional sample columns[10, 61, 133] have also been employed. Previous research examined the relationship between the final run-out and the initial geometry, or aspect ratio, of the column. The relation between the run-out distance and the normalised initial height [123] varied for axisymmetric and two-dimensional columns followed a power law. For columns with high aspect ratios, an initial acceleration stage is identified, followed by a stage of constant velocity. Here, aspect ratio is defined as the proportion of the column's height to its width. A high aspect ratio would indicate that the column is much taller than it is wide. Only during the final stages of deceleration and stopping does the coefficient of friction become a factor in determining run-out, as demonstrated by Lube et al. [133].

Numerous numerical simulations of granular column collapse have been exhaustively performed. Naturally, the discrete element method (DEM) has been utilised to simulate such problems [111, 209, 225]. In the work of Kumar et al. [119], the mechanics of granular column collapse under the influence of a fluid medium surrounding it have been analysed. Continuum models have also been used successfully to simulate granular flow in references [3, 135, 148]. According to numerical studies, continuum models overestimate the run-out distance relative to granular models (such as DEM) for columns with aspect ratios greater than 0.70 [144]. Continuum models overestimate the driving force behind the collapse compared to granular models. Similar conclu-

sions were reached in the case of the material point method, in which a greater-than-anticipated run-off was observed for aspect ratios greater than 2.0 [120]. For columns with high aspect ratios, artificial damping should be added to mitigate this error [196]. However, the amount of damping to be added to the system is unclear. In this section, efforts have been made to measure the effect of damping on the final runoff, as well as the effect of volumetric/deviatoric smoothing on the system, in addition to studying the effect of particle number on the system.

3.6.2 Problem Description

As stated previously, the purpose of this simulation is to validate the code by comparing the results to those of experiments described in Lube et al. [134], for different i) number of particles, ii) damping coefficients, and iii) smoothening schemes are used in a parameter study to determine whether the numerical simulation can reproduce the experiment with a high degree of accuracy. The purpose of the experiment is to examine inertial granular flows caused by the instantaneous release of a granular column. While various aspect ratios for the column were investigated, only one is selected for this simulation, allowing for a more concentrated parameter study. Experiments are conducted to examine a two-dimensional granular flow formed by the collapse of a rectangular sand column into a wide horizontal channel. The column width is 9.05 centimetres, and the aspect ratios ranged from 3 to 9.5. In this study, an aspect ratio of 7 was chosen, resulting in a column height of 63.35 cm. For this purpose, a wide variety of granular materials were evaluated. Cohesion effects were found to be negligible. The granular material utilised in the experiment was 1.4 ± 0.4 mm quartz sand of industrial quality. Regarding the characteristics of the sand, the original authors provided scant details. The following properties were recorded for the quartz sand: solid density of 2,650 kg/m^3 and an angle of repose of 31° [133]. Glass walls were used to observe the resulting deformation and the free surface after the removal of the frontal gates.

The entire collapse of the sand column is modelled using CPDI. Similar simulations were conducted using GIMP [196], with MPM and GIMP being subsequently compared [82]. This simulation employs two-dimensional regular elements with a dimension of 0.67 mm. In different simulations, the elements were populated with 1, 4, and 9 particles, respectively. To model sand, an elastic-plastic Mohr-Columb failure criterion is selected. The modulus of elasticity is 840 kPa, and the ratio of possession is 0.3. Assigning the angle of repose as the friction angle and selecting a small dilatancy angle of 1° is performed here in this study. A non-slip condition between the granular material and the ground is assigned, as used in reference [133]. Various numerical damping coefficients were selected to examine the effects on the final runoff. One drawback with the numerical concept presented in reference [196] does not adequately describe the effects of damping.

To avoid introducing too many variables into the calculation, it is determined that the size of the background grid will remain constant at 0.67 mm. For this simulation, a frictionless side wall is used. Calculating the column's initial stresses involves assigning roller boundaries to both sides of the column. In lieu of simulating the lifting of the gate to remove the confining side boundaries, the CPDI code eliminates the roller support to the right of the model instantaneously. This methodology has been utilised in prior research and can be deemed accurate [82, 196]. In the numerical model, removing the supporting gate requires 0.0417 seconds less time. This is subtracted from the duration of the experiment. It is assumed that the acceleration due to gravity in the vertical direction is 10 m/s^2. Simulations were conducted with a total of 9,108, 34,433, and 81,972 particles for 1, 4, and 9 particles per grid mesh, respectively.

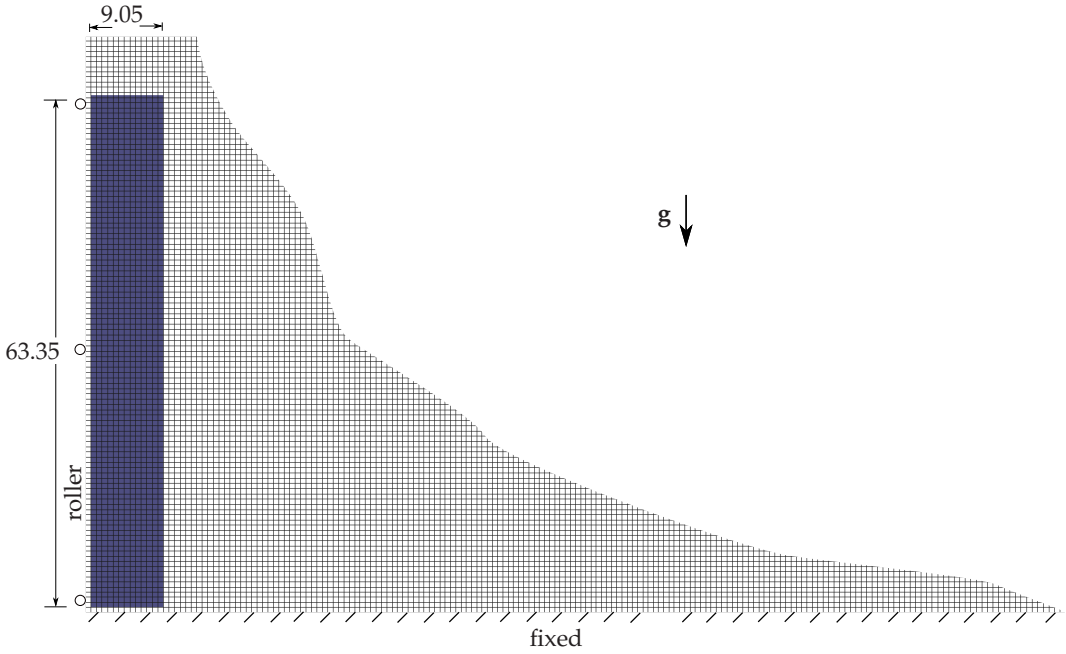

Figure 3.7: CPDI model for granular column, dimensions in cm

The initial mesh setup for the numerical model is depicted in Figure 3.7, with the background computational grid and particles (in blue). Results from the work of reference Hamad [82] is used to digitise experimental data. The numerical simulation results are compared to the contour plot from the CPDI simulations. Three different aspects of numerical modelling were investigated: i) the effect of number of particles per grid, ii) the effect of numerical damping, and iii) the effect of strain smoothening on the final runout. Incorporating the lessons learned from the parameter study, one simulation with the optimal number of particles, damping, and smoothing parameters is performed and compared to the experiment. This enabled us to answer the question regarding the optimal damping parameter range that must be considered when simulating dynamic simulation of granular material using CPDI to achieve a better fit with experiments.

3.6.3 Results and discussions

Herein are presented the findings of the parameters study.

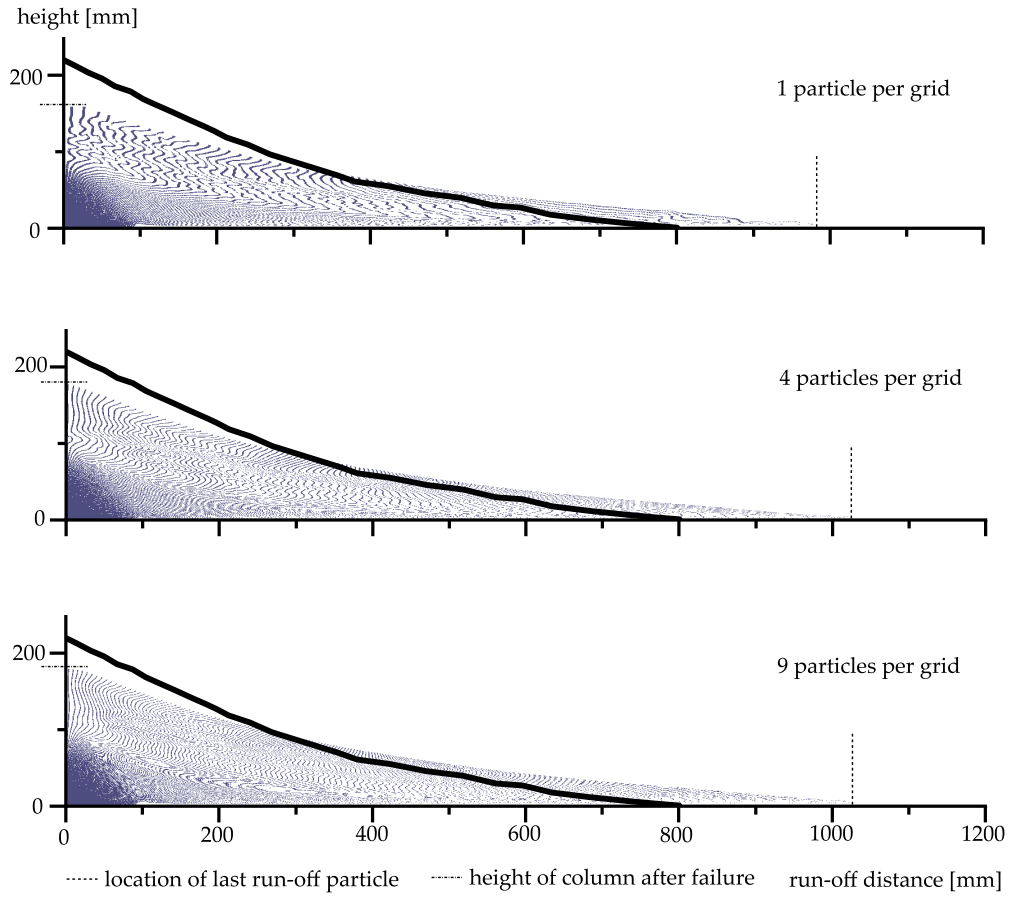

Figure 3.8: Effects of number of particles per grid on the final run-off

Effect of number of particles

Regardless of the number of simulated particles, the final run-off was overestimated by the numerical model, as Figure 3.8. This phenomenon is by no means unexpected, as it was previously been observed in numerical studies employing a continuum model as opposed to a granular setup [144]. Not only was the run-off overpredicted in the case of 1 particle per grid, but the final height of the column was also underestimated. For the 4 and 9 particle systems, an overprediction of run-off to the same magnitude was observed, whereas the final height of the column for the 1 particle system is closer to the experiment, despite its magnitude being smaller. In all cases, the run-off is in the

range of 1000 mm, whereas the experimental run-off was limited to approximately 800 mm.

Fern et al. [66] conducted a similar study in which the effect of particle number on the dynamic system was investigated. Reportedly, the mesh dependence disappears as the mesh is refined from a coarse mesh to a medium-fine or fine mesh. There should be a distinction between that work and the current study. In the work of reference [66], the number of particles was altered alongside the number of computational grids in the background. In this study, however, the size of the computational grid in the background remains constant, while the number of particles in the system changes. In spite of this modification to the study's methodology, a similar result was observed: the difference in final results between the 4- and 9-particle systems is found to be negligible.

Although computationally efficient, the 1-particle system tends to be numerically inefficient, regardless of the size of the background computational grid. In line with what has been proposed in reference [66], the results of this study support a recommendation to use either the 4- or 9-particle system. The 9 particle system will be used moving forward in this section. The computation time for the parallelised code on a 4-Core Intel i5-4590 CPU was 6 hours for a 9-particle system, 2.5 hours for a 4-particle system, and approximately 35 minutes for a 1-particle system.

Effect of local damping

Subsequently, the effect of numerical damping was studied for the 9 particle system. The outcomes of any numerical simulation can be influenced by energy dissipation mechanisms such as surface contact and/or numerical damping, among others. Numerical damping is utilised to rapidly dissipate the system's kinetic energy and achieve a steady-state for the entire system. In the context of MPM/CPDI, a small damping coefficient also contributes to the overall numerical stability of the system. The physical justification, however, for employing this force is to simulate the energy loss caused by plastic particle contacts.

The numerical damping was utilised by reference [197] to not only improve the convergence of the overall MPM solution, but also to approximate the loss of energy of grain upon movement without strain change. This occurs primarily in the form of particle friction. Reference [227] chose not to implement numerical damping in their work due to the difficulty of accurately estimating the magnitude of energy dissipated. In the code, numerical damping was implemented by the following equation:

$$a_n^{t+1} = a_n^{t+1} - c_d \, v_n^{t+1} \,, \tag{3.60}$$

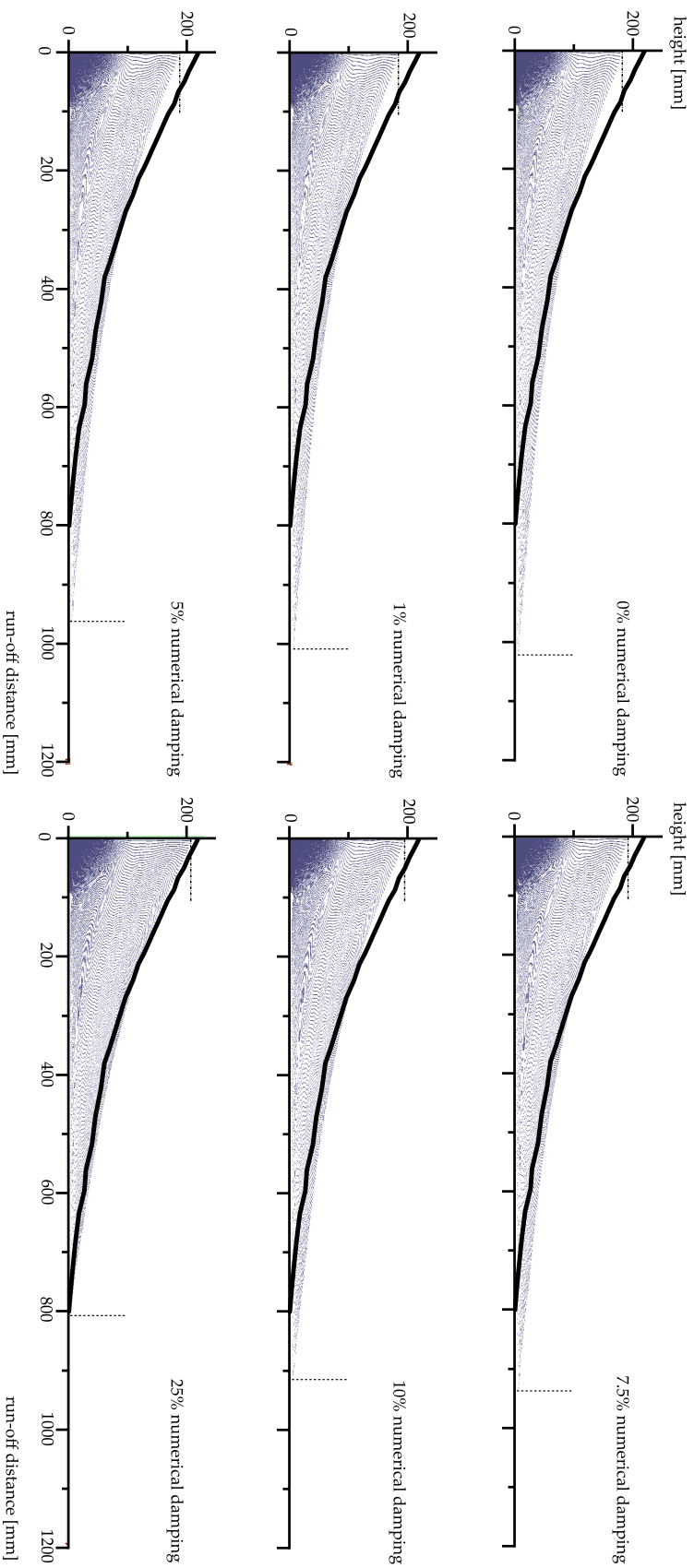

Figure 3.9: Effects of damping on the final run-off

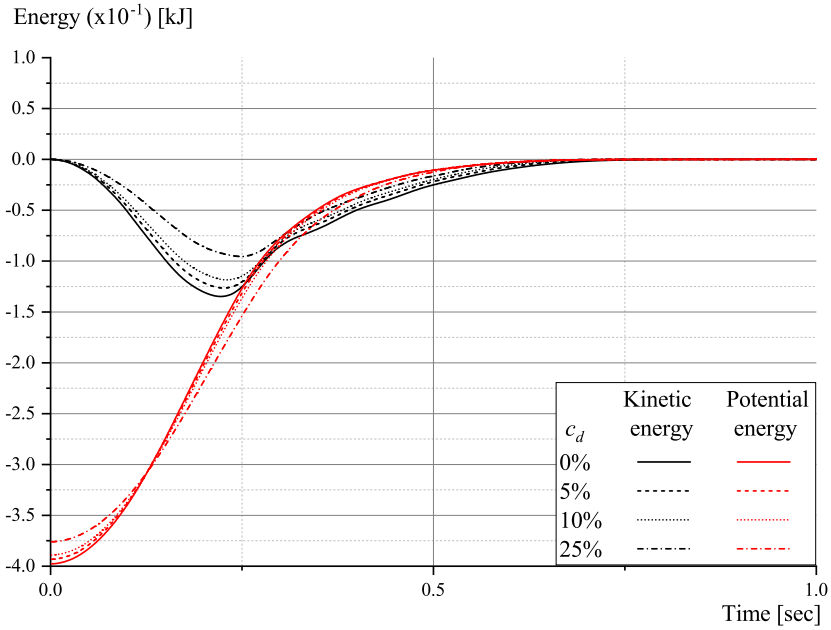

Figure 3.10: Kinetic and Potential energies of the system for different damping coefficients (c_d)

where, n refers to the nodal value, $t+1$ to the updated values of a and v, the acceleration and velocities, respectively. Damping coefficient c_d in Equation 3.60 varies between 0 and 1 (0 - 100%). The study is carried out for 6 different damping parameters: 0, 1, 5, 7.5, 10 and 25%. All simulations employ 9 particles per grid, as stated earlier.

Figure 3.9 illustrates the effect of damping parameter on the column's final run-off. The location of the final run-off and its height are displayed. The results of the simulation with no damping and the simulation with 1% damping are qualitatively identical. Each of these simulations results in a final run-off of approximately 1000 mm. The final height of the sand mound is, as expected, less than what was observed during the experiment. Compared to the case with 1% damping, the simulation results with 5% damping begin to approach the experimental result. Not only is the final run-off shorter, but the final sand mound height is also greater. As the damping coefficient is increased to 25%, the results match the experiment precisely, despite the fact that this level of damping may be considered excessive. While the results of 7.5% and 10% damping do not match the experimental data, these values may be regarded as typical in terms of contact-induced energy loss.

Figure 3.10 shows the kinetic and potential energies of the system. As the damping coefficient is increased from 0 to 25%, the system's kinetic energies decrease while the potential energies remain relatively constant, with the minor deviations being attributed to the explicit numerical integration solver. Reference [209] conducted 3D-DEM simulations of the collapse of granular columns, including analyses of energy dissipation. According to the results, the majority of the column's energy was dissipated by in-

terparticle frictions. From DEM simulations in the reference [199], similar conclusions were drawn. Experiments from reference [75] also suggest comparable outcomes for the specified aspect ratio.

Effect of smoothing

The effect of strain smoothing is investigated next. Three simulations are conducted: i) no smoothening; ii) deviatoric strain smoothening; and iii) pressure smoothening is applied. To aid in the numerical stability, the strains are smoothened during each computational step via the relation:

$$\bar{\varepsilon} = \frac{\sum_e \varepsilon \, M_p \, S_i}{\sum_e M_p \, S_i} \tag{3.61}$$

where, $\bar{\varepsilon}$, ε, M_p and S_i are the smoothened strains, computed strains, particle mass and

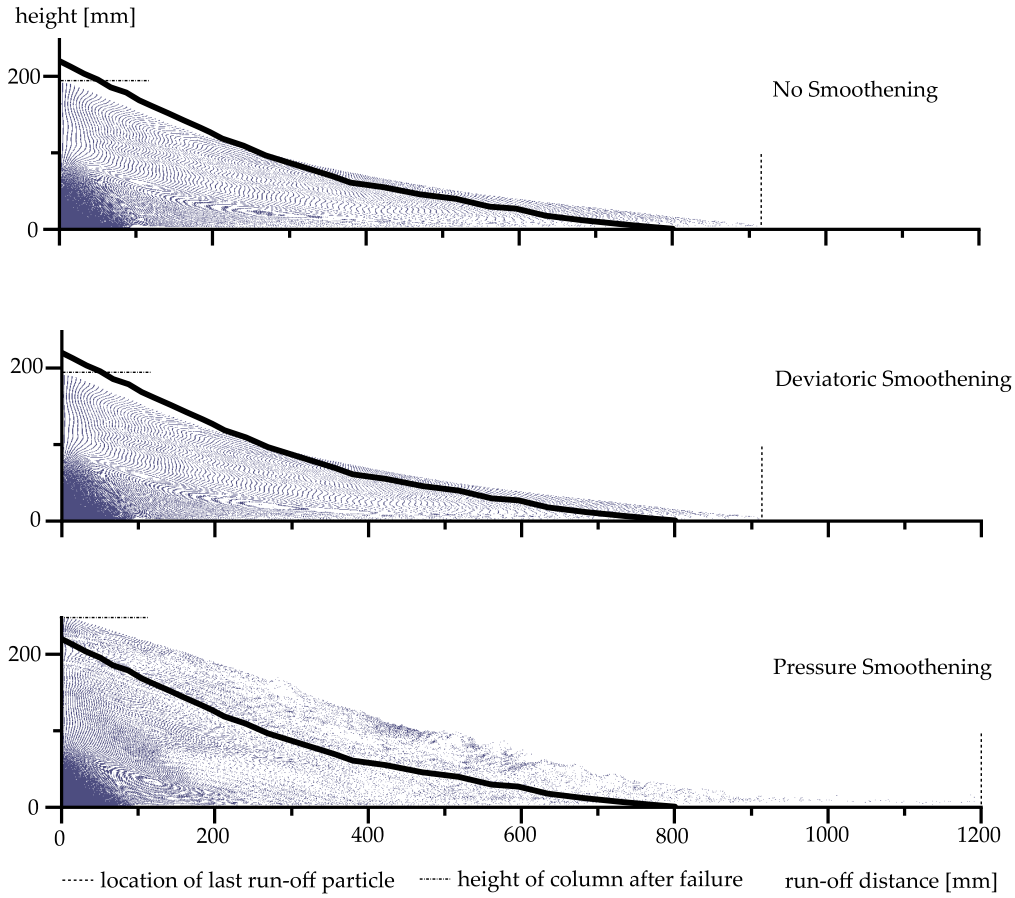

Figure 3.11: Effects of smoothing the final run-off

grid basis functions, respectively. During each computation step, either the deviatoric, the volumetric, or both components can be smoothed. Prior to using this algorithm, it was necessary to analyse their impact on the continuum during massive material movements.

Figure 3.11 shows the results of this research. Results from simulations in which smoothing is not applied are identical to those presented thus far. In this instance, the simulation was conducted assuming a numerical damping of 7.5%, which can be considered realistic. In this instance, the damping is applied to account for the intergranular friction. While the results of deviatoric smoothening do not differ significantly, the results of pressure strain smoothening demonstrate fluid-like behaviour. This method was previously used to model dam failure in reference [78]. Because the purpose of this simulation is not to simulate a fluid-like behaviour and the bulk modulus is not as high as water, which would necessitate pressure smoothing, only the deviatoric portion of the strains need to be smoothed, saving valuable computational time.

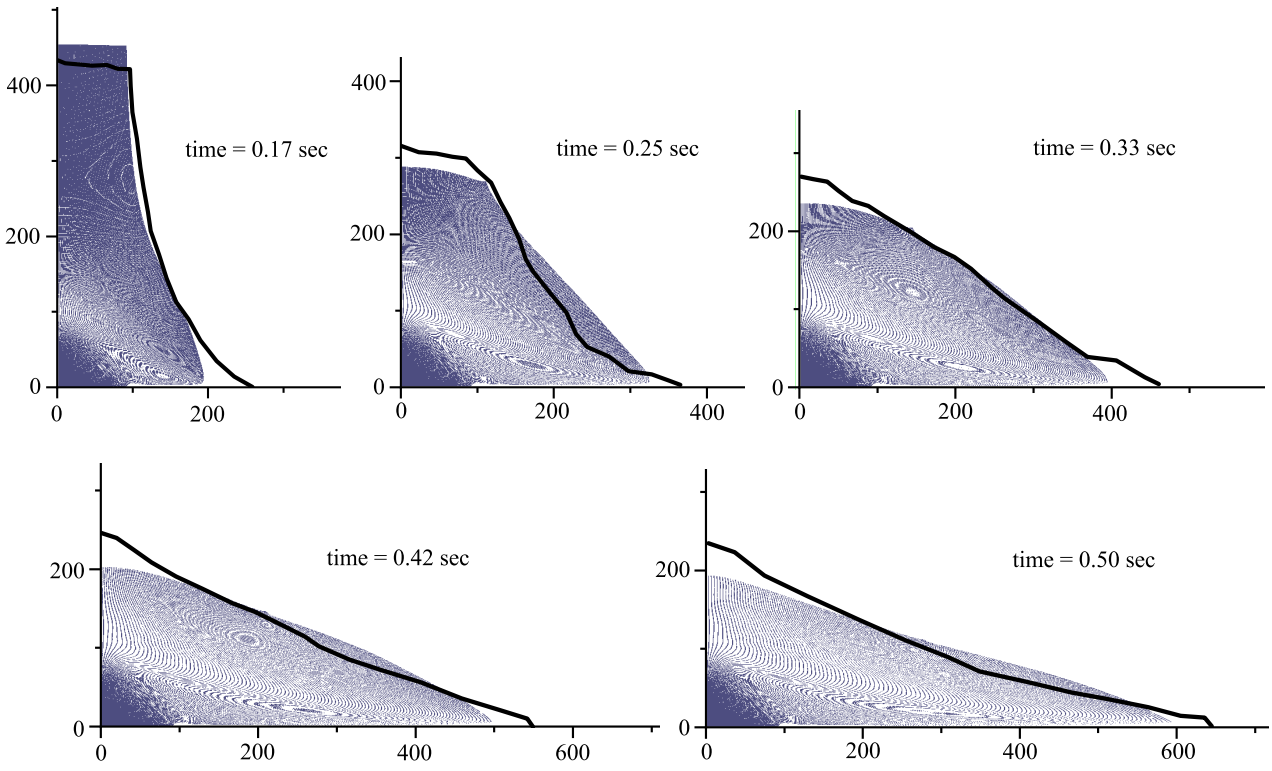

Figure 3.12: Granular Column Collapse: Evolution of shape of column at different snapshots in time (dimensions in mm)

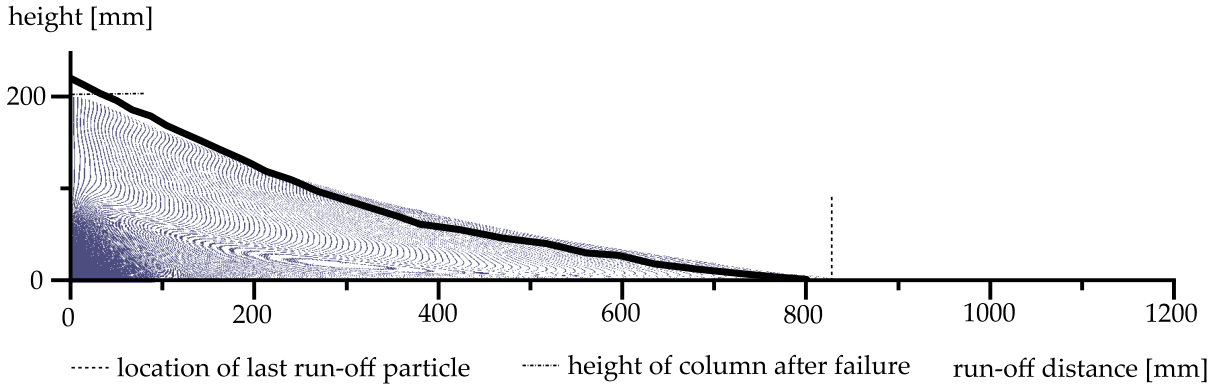

Figure 3.13: Granular Column Collapse using recommended parameters

Recommendation for parameters

A parameter recommendation for the granular collapse using CPDI is provided based on the findings of the parameter study conducted thus far. While the same nine-particle-per-grid system is considered, numerical damping is set to 10%, which was determined to be the most practical value for this type of simulation. At every step of the calculation, deviatoric strain smoothing was performed. In this case, the gradual collapse of the column is compared to the experimental results at various points in time.

Figure 3.12 depicts the simulation results at various time intervals in comparison to the experiment. Here, there are two distinct regimes: i) the spreading phase, and ii) the final avalanche phase. The advancing soil layer moves as a deforming and dense bulk flow during the spreading phase. As the simulation advances to the avalanche phase, the particles acquire greater momentum, which slows as they reach a state of lower energy, and eventually stops. When the flow overtakes the flow front, particles at the free surface layer remain or are incorporated into a thin layer. Due to the high aspect ratio, the bulk of the soil column is moving downwards with negligible lateral movement. This can be observed at 0.17 seconds. Currently, material movement is marginally slower than in the experiment. At this stage, a distinct triangle of stationary material is already visible.

Presented in Figure 3.13 are the outcomes of the deviatoric smoothing model. In this simulation, 10% local damping was incorporated into the calculation procedure. Since the damping algorithm involves artificially reducing the system's kinetic energy, the less damping is applied, the more plausible can the results be.

In their simulation, Hamad [82] reported good convergence at 0.17 seconds. At 0.25 seconds, the column's flow catches up to the experiment. While reference [82] already reported a discrepancy with the experiment due to a lack of energy dissipation corresponding to the grains' rolling, this discrepancy is due to the lack of dissipation in

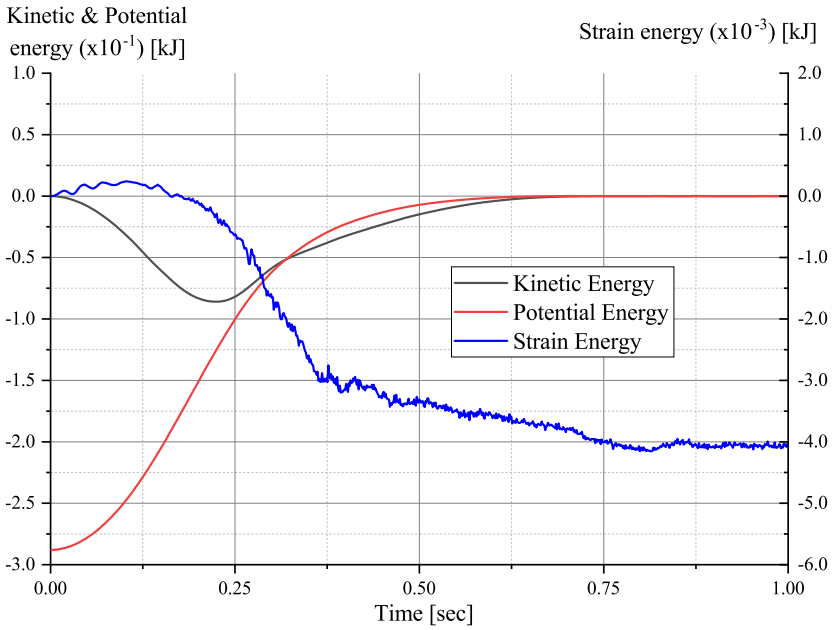

Figure 3.14: Kinetic, Potential and Strain energies of the system

the experiment. The triangular region in the lower left corner hardly moves, indicating a region with no flow, whereas the upper right portion deforms. From 0.33 to 0.50 seconds, the deformation closely resembles the experiment, as seen in Figure 3.12. The subsequent phase of the collapse is the final avalanche phase, during which the particles flow along the free surface as a thin moving layer and a central deposit. Slow particles form thin avalanches that alter the free surface until they cease. After 0.50 seconds, the soil column begins to decelerate and eventually comes to rest at the conclusion of the simulation. Based on Figure 3.13, the experimental and numerical model outcomes are comparable.

Through this analysis, it can be concluded that a simple constitutive law such as Mohr-Coulomb, coupled with the CPDI method, incorporating numerical enhancements such as smoothening, and accounting for physical phenomena such as energy loss by means of numerical damping, can simulate complex dynamic processes such as the collapse of granular column collapse with good agreement to experiment. Complex constitutive models can undoubtedly enhance the outcomes. Consideration of pressure dependency in alternative failure criterions such as Matsuoka-Nakai or Drucker-Prager does not significantly improve the final height of column or maximum run-off, but rather alters the final shape of the soil mound [147]. The system's energies are depicted in Figure 3.14. As depicted in Figure 3.10, the outcomes match expectations.

Alternately, the Mohr-Coulomb model's parameters could have been calibrated to better match the final results. The so-called 'Inverse Analysis' entails calibrating the input parameters until the computed results of the model match the observed behaviour of the system [42]. Nonetheless, the purpose of this study was to determine the impact

of smoothing and damping on the final results. The plan was to also account for the energy loss caused by granular friction, which was accounted for by artificial damping, and to eliminate spurious numerical locking, which was mitigated by strain smoothing. Although this was a *scientia ac labore*, the results of the simulation using recommended parameters, which are quite similar to the experimental results, provide a foundation for future research into the dynamics of granular columns.

3.6.4 Concluding remarks

Owing to the CPDI's ability to capture large deformations, these issues can be modelled more accurately. The findings of this study, namely the effects of the number of particles per grid, the effect of the smoothing algorithm, and the effect of damping are crucial for this method to be applied to dynamic real-world problems. As a result of this study, the selection of parameters can direct the simulation to the desired solution. Although these parameters are essential for ensuring the stability of the solution process, their role must be limited to assisting in the convergence to a stable solution and not in the solution's production. In subsequent chapters, a highly dynamic soil-structure interaction problem will be presented, noting the findings of this study.

Chapter 4

Modelling Saturated Media using Material Point Method

In geotechnical engineering, it is not uncommon to encounter problems involving the coupling of the solid and fluid phases, despite the fact that solving problems involving only solid- or fluid-phase constituents may be straightforward and simple at times. This chapter focuses on the extension of the dynamic material point method, and by extension CPDI, introduced in Chapter 3 to fully saturated two-phase problems. The gaseous phase is not considered in this work.

4.1 Saturated porous media mechanics

In this study, a biphasic porous medium with a solid skeleton and an interstitial fluid is considered. Individual components of a heterogeneously composed porous medium exist in an ideal state of disarrangement. The theoretical framework of the macroscopic structure is provided by the theory of porous media (TPM), in which biphasic porous media is considered *de-facto* immiscible and composed of two constituents, solid and fluid aggregates. Each constituent is statistically homogeneously distributed over a Representative Volume Element (RVE) of the overall aggregate. By homogenising the RVE, we obtain a continuum, φ with overlapping, interacting, and statistically distributed solid and fluid aggregates, φ^{α} where, α=F for fluid phase, and α=S for solid. The following definition should hold true for every macroscopic subspace:

$$\varphi = \bigcup_{\alpha} \varphi^{\alpha} = \varphi^{S} \cup \varphi^{F} \,. \tag{4.1}$$

Separate mathematical field functions, defined over the entire aggregate, φ characterise the geometrical and physical properties of each constituent. Through a volumetric homogenisation procedure, the effective values of the constituents are dispersed throughout the RVE. The homogenisation method is depicted schematically in Figure 4.1. The

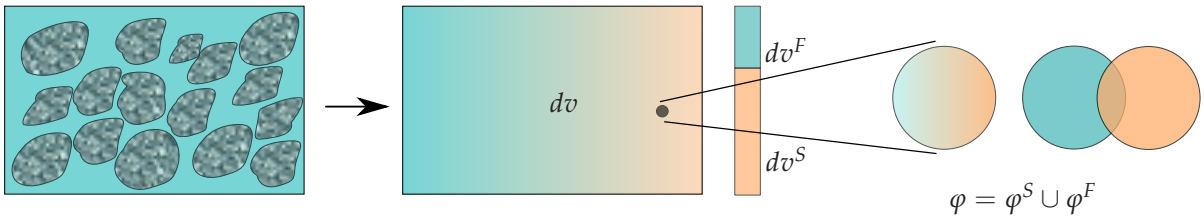

Figure 4.1: RVE of fluid-saturated sand and the macroscopic approximation of the model obtained through volumetric homogenisation

local volumetric ratios of the partial volume element, dv^α with respect to the bulk volume element, dv capture the microstructural composition of the mixture, as seen from Equation 4.1. Here, the concept of volume fractions is explained. Over the REV, the volume fraction, n^α of a constituent, ϕ^α is defined as:

$$n^\alpha = \frac{dv^\alpha}{dv}\,, \tag{4.2}$$

where, dv^α and dv are the partial and total volume elements, respectively. The following constraint holds if the element is completely saturated:

$$\sum_\alpha = n^F + n^S = 1\,, \tag{4.3}$$

where, n is the porosity. In addition, a further implicit constraint is imposed, with n^α ranging between 0 and 1, with 0 denoting the complete absence of the constituent and 1 denoting the complete absence of its complementary constituents. Realistically, in the current treatment of multiphasic materials, it is always assumed that $0 < n^\alpha < 1$, i.e., the case under study is not restricted to a pure solid or liquid, but rather a saturated mixture.

Implementing the hydro-mechanical forces that capture the interaction between pore water (i.e., the liquid phase) and the solid skeleton is necessary for numerically simulating saturated soils. Various coupled theories have been proposed to solve the problem of saturated media. The Biot theory was one of the earliest theories. According to Biot's theory, the soil is assumed to be a porous, water-filled skeleton. The skeleton's material is incompressible, but it is assumed to be elastic [27]. Terzaghi et al. [205] also proposed theories to address such issues. The hypothesis that the soil's grains or particles are more or less held together by certain molecular forces and constitute a porous, elastic material. Comparable to a sponge soaked in water, the voids of the elastic skeleton are filled with water. Depending on the rate at which water is being squeezed out, the load

applied to this system will produce a gradual settlement. In a one-dimensional sense, this concept was applied to the analysis of soil settlement for a variety of soil types. The following basic properties of the soil are assumed regardless of the theory: i) isotropy of the material, ii) reversibility of stress-strain relations, iii) linearity of stress-strain relations, iv) small strains, v) water contained within the pores is incompressible, and vi) water flows through the porous skeleton according to Darcy's law.

4.2 Formulation of two-phase MPM

The purpose of this section is to define the essential quantities for the mathematical model of porous media. We begin by examining the phase relationship of porous media. The subsequent subsections then examine the concept of effective stress.

4.2.1 Phase relation on porous media

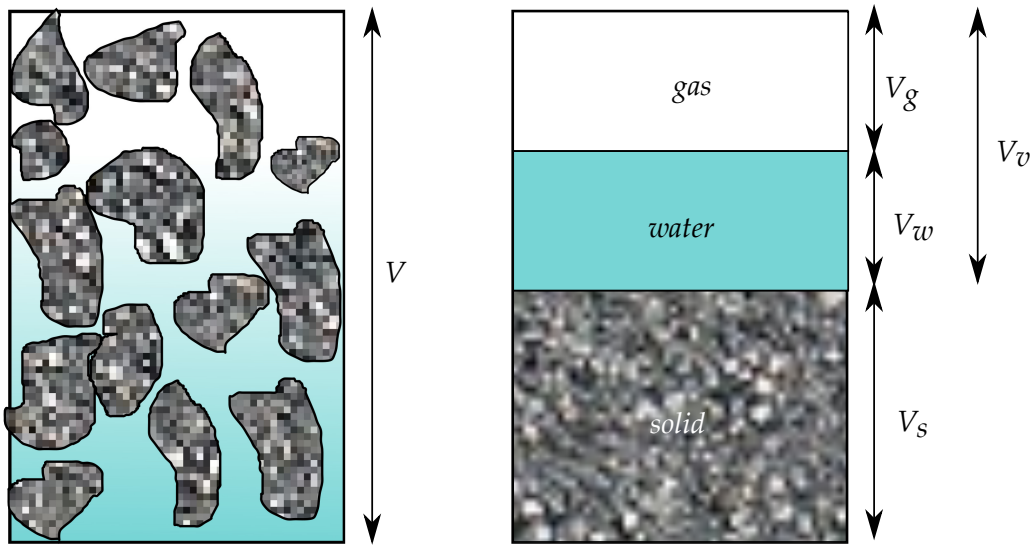

Figure 4.2: a) Soil element with gaseous, fluid and solid phases and its b) representative volume diagram

As is common knowledge, soil consists of three phases: solid, liquid, and gas. Consider the element of soil depicted in Figure 4.2. The entire soil element has a volume V. This volume consists of three phases: solid, fluid, and gas, with respective volumes V_s, V_f and V_g. Additionally, the volumes of fluid and gaseous phases can be combined to create void volume, V_v. Thus, the relationship:

$$V = V_s + V_v = V_s + V_f + V_g \,. \tag{4.4}$$

From the phase relationship presented above, the soil properties void ratio (e) and porosity (n) can be defined as follows:

$$e = \frac{V_v}{V_s} \qquad \text{and} \qquad n = \frac{V_v}{V} \,, \tag{4.5}$$

these two quantities are related in that:

$$e = \frac{n}{1-n} \,. \tag{4.6}$$

In this work, one of two values for saturation ratio (S_r) is chosen, with $S_r = \frac{V_f}{V_V} \times 100\%$, with $S_r = 0$ for soil that is assumed to be completely dry and $S_r = 100\%$ for soil that is completely saturated. In other words, this research will be limited to situations in which the soil is completely dry or completely saturated. Soil that is partially saturated is outside the scope of this study. When analysing saturated soils, various densities can be defined. The formula for dry density (ρ_d) is as follows:

$$\rho_d = (1-n)\,\rho_s \,, \tag{4.7}$$

where ρ_s represents the *grain density* of the solid phase, which can be expressed as the ratio of solid grain mass to solid grain volume. On the other hand, saturated density (ρ_{sat}) can be expressed by the relation:

$$\rho_{sat} = (1-n)\,\rho_s + n\,\rho_w = \rho_d + n\,\rho_w \,, \tag{4.8}$$

where, ρ_w is the *water density*. *Submerged density* (ρ'), is defined via the relation:

$$\rho' = \rho_{sat} - \rho_w \,. \tag{4.9}$$

4.2.2 Concept of effective stress

The term *effective stress* was coined by von Terzaghi [212] in 1923. This idea was proposed as a solution to the one-dimensional problem of consolidation in a column of completely saturated soil. The reader is referred to the works of De Boer [57] and De Boer and Ehlers [59] for a more comprehensive overview of the continued development of the effective stress concept in relation to the theory of porous media. In accordance with the concept of effective stress for saturated soils, the *total stress* (σ_{ij}) component can be decomposed as follows:

$$\sigma_{ij} = \sigma'_{ij} + p\,\delta_{ij}\,, \tag{4.10}$$

where σ'_{ij} represents the effective strain and p represents the pore pressure. δ_{ij} is a tensor of unity in the relation. σ and p assume positive values in this study under tension and suction, respectively.

4.2.3 Incremental time step estimation in saturated media

There are two types of waves in saturated media: i) undrained, and ii) rigid solid matrix waves after reference [211]. In the case of undrained waves, one can imagine fluids and solids moving together. This can be considered in situations where the permeability (n) is extremely low. The speed of undrained waves is given by the relationship:

$$c_u = \sqrt{\frac{E^c_u}{\rho_{sat}}}\,, \tag{4.11}$$

where, E^c_u is the undrained constrained modulus of the soil. It follows from the relationship:

$$E^c_u = E^c + \frac{K_w}{n}\,, \tag{4.12}$$

where, K_w is the bulk modulus of water and E^c is the confined modulus of solid grains. In the second type of wave, the rigid solid matrix wave, it is assumed that solid and liquid particles move in opposite directions. Owing to the interaction of solid and fluid particles, these waves exhibit significant damping. This phenomenon is observed when the solid matrix is extremely rigid, as in the case of a very rigid porous rock or in

the vicinity of the loading source. These waves travel with the velocity given by the equation:

$$c_{rm} = \sqrt{\frac{n\,\frac{E^c}{K_w}}{1-n+n\,\frac{E^c}{K_w}}}\,c_w\,, \tag{4.13}$$

where, speed of compression wave propagating through pure water, $c_w = \sqrt{\frac{K_w}{\rho_w}}$. The wave speed of the rigid solid matrix is less that c_w, as the term preceeding c_w is less than 1.

4.3 Governing equation of the coupled MPM

The section presents the governing equations required to describe the coupled, dynamic, two-phase model. References [211, 231] explain the physics of two-phase materials. Using *u,w, and p* and simplified *u, p* relations, Zienkiewicz et al. [231] provide a formulation for a fully saturated behaviour with a single pore fluid. In their work, Zienkiewicz and Shiomi [229] discuss the fundamental equations of motion for porous media and the available alternate forms, as well as the relative efficiency of solution in a numerical context. Reference [107] elaborates on the formulation to which the readership is directed. In the interest of completeness, only the most relevant equations describing two-phase media have been presented.

4.3.1 Conservation of mass

Solid phase mass conservation is described by the equation:

$$\frac{d}{dt}\left[(1-n)\,\rho_s\right] + \frac{\partial}{\partial x_j}\left[(1-n)\,\rho_s\,\hat{v}_j\right] = 0\,, \tag{4.14}$$

where, $\hat{v}_j$ is the velocity vector of the solid phase. The mass conservation relationship for the water phase is as follows:

$$\frac{d}{dt}\left[(n\,\rho_w)\right] + \frac{\partial}{\partial x_j}\left[n\,\rho_w\,\hat{w}_j\right] = 0\,, \tag{4.15}$$

where, $\hat{w}_j$ is the vector of true velocity of the water phase. Two reasonable assumptions will be made moving forward: i) the grains will be considered incompressible, and ii) the spatial variation in porosity and density of the control mass will be disregarded. As a result of the first assumption, we can reach the conclusion in Equation 4.14, $\frac{d\rho_s}{dt} = 0$. Moreover, as a result of the second assumption, in Equations 4.14 and 4.15, the terms $\frac{\partial n}{\partial x_j}$, $\frac{\partial \rho_s}{\partial x_j}$ and $\frac{\partial \rho_w}{\partial x_j}$ all equate to 0 and drop out. Hence, Equation 4.14 and Equation 4.15 simplifies to the form:

$$-\frac{dn}{dt} + (1-n)\,\frac{\partial \hat{v}_j}{\partial x_j} = 0\,, \tag{4.16}$$

and,

$$n\,\frac{d\rho_w}{dt} + \rho_w \frac{dn}{dt} + n\,\rho_w\,\frac{\partial \hat{w}_j}{\partial x_j} = 0\,, \tag{4.17}$$

respectively. Substituting Equation 4.16 into 4.17 eliminates the rate of change in porosity with time and produces the relationship:

$$\frac{n}{\rho_w}\frac{d\rho_w}{dt} + (1-n)\,\frac{\partial \hat{v}_j}{\partial x_j} + n\frac{\partial \hat{w}_j}{\partial x_j} = 0\,. \tag{4.18}$$

Assuming water is linearly compressible based on the relationship:

$$\frac{\partial \rho_w}{\partial p} = -\frac{\partial \rho_w}{K_w}\,, \tag{4.19}$$

rearranging the equation yields the relationship between the change in pore pressure and time as:

$$\frac{d\rho_w}{dt} = -\frac{\rho_w}{K_w}\,\frac{dp}{dt}\,. \tag{4.20}$$

Substituting Equation 4.20 time into Equation 4.18 yields the *storage equation*, or the constitutive relation for pore fluid as follows:

$$\frac{dp}{dt} = \frac{K_w}{n}\left[(1-n)\frac{\partial \hat{v}_j}{\partial x_j} + n\frac{\partial \hat{w}_j}{\partial x_j}\right]. \tag{4.21}$$

4.3.2 Conservation of momentum

Momentum conservation in solid and liquid phases can be expressed by the following equations:

$$(1-n)\rho_s\frac{d\hat{v}_j}{dt} - \frac{\partial \sigma'_{ij}}{\partial x_i} - (1-n)\frac{\partial p}{\partial x_j} - (1-n)\rho_s g_j - \frac{n^2\rho_w g}{k}(\hat{w}_j - \hat{v}_j) = 0\,, \tag{4.22}$$

and,

$$n\rho_w\frac{d\hat{w}_j}{dt} - n\frac{\partial p}{\partial x_i} - n\rho_w g_j - \frac{n^2\rho_w g}{k}(\hat{w}_j - \hat{v}_j) = 0\,. \tag{4.23}$$

Here, k is the hydraulic conductivity of the soil. The term $n(\hat{w}_j - \hat{v}_j)$, represents the specific discharge, often denoted by the term q. By adding the momentum of solid phase (Equation 4.22) and fluid phase (Equation 4.23), the momentum of the mixture, which represents the saturated soil, can be expressed as:

$$(1-n)\rho_s\frac{d\hat{v}_j}{dt} + n\rho_w\frac{d\hat{w}_j}{dt} = \frac{\partial \sigma_{ij}}{\partial x_j} + ((1-n)\rho_s + n\rho_w)g_j\,. \tag{4.24}$$

4.3.3 Initial and boundary conditions

The following condition must be met for the formulation of two-phase problems:

$$\partial\Omega = \partial\Omega_u \cup \partial\Omega_\tau = \partial\Omega_w + \partial\Omega_p\,, \tag{4.25}$$

where, $\partial\Omega$ is the boundary of domain Ω. Here, Ω_u and Ω_τ are the prescribed displacement (velocity) and prescribed total stress boundaries, respectively. Ω_w and Ω_p are the prescribed velocity and pressure boundaries of the fluid phase. The condition indicated by the following relation must subsequently be met at the boundary:

$$\partial\Omega_u \cap \partial\Omega_\tau = \varnothing, \qquad \text{and} \qquad \partial\Omega_w \cap \partial\Omega_p = \varnothing. \tag{4.26}$$

The displacement boundary conditions for the solid and liquid phases can be determined using the following relations:

$$\hat{v}_i(\boldsymbol{x}, t) = \hat{V}_i(t) \qquad \text{on} \qquad \partial\Omega_u(t) \tag{4.27}$$

and,

$$\hat{w}_i(\boldsymbol{x}, t) = \hat{W}_i(t) \qquad \text{on} \qquad \partial\Omega_w(t)\,, \tag{4.28}$$

respectively.

We define the prescribed total traction as $\tau_i(\boldsymbol{x}, t) = \widetilde{\tau}_i(\boldsymbol{x})\,\mathcal{T}(t)$ and the prescribed pressures as $\bar{p}_i(\boldsymbol{x}, t) = \widetilde{p}(\boldsymbol{x})\,n_i\,\mathcal{T}(t)$. The total traction and pressure limits are therefore expressed as:

$$\sigma_{ij}(\boldsymbol{x}, t)\,n_j = \tau_i(\boldsymbol{x}, t) \qquad \text{on} \qquad \partial\Omega_\tau(t)\,, \tag{4.29}$$

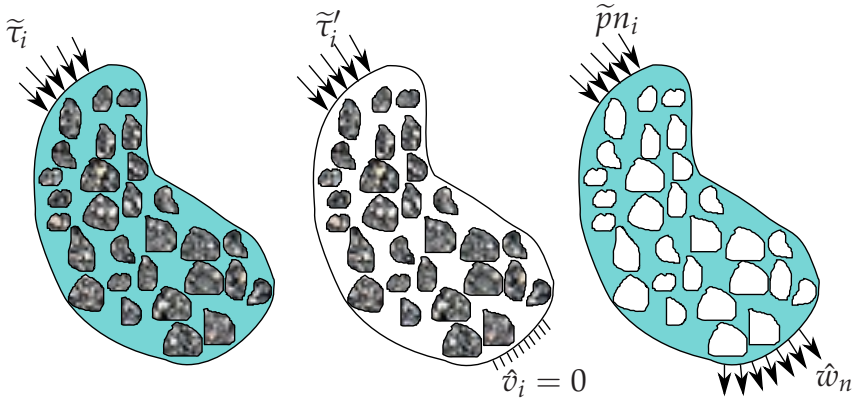

Figure 4.3: Boundary conditions for saturated soil and solid and liquid constituents [107]

and,

$$p(\boldsymbol{x},\, t)\, n_i = \bar{p}_i(\boldsymbol{x},\, t) \qquad \text{on} \qquad \partial\Omega_p(t)\,, \tag{4.30}$$

respectively. Here, n_i denotes the unit outward normal vector to the $\partial\Omega$ boundary. Figure 4.3 depicts the boundary condition for the saturated soil, the solid and the fluid phases. The distinction between $\widetilde{\tau}_i$ and $\widetilde{\tau}_i{}'$ is made for the sake of completeness, where the latter is the effective traction. The term $\hat{w}_n$ represents the normal component of the fluid velocity. Considered are the initial conditions for the solid and fluid velocities:

$$\hat{v}_i(\boldsymbol{x},\, t_0) = \hat{V}_{0i} \qquad \text{and} \qquad \hat{w}_i(\boldsymbol{x},\, t_0) = \hat{W}_{0i}\,, \tag{4.31}$$

respectively. Initial total stress and pore pressure are derived from the following relationships:

$$\sigma_{ij}(\boldsymbol{x},\, t_0) = \sigma_{0,ij} \qquad \text{and} \qquad p(\boldsymbol{x},\, t_0) = p_0\,, \tag{4.32}$$

respectively.

4.3.4 Weak formulation of momentum and traction

Momentum conservation is a fundamental principle of continuum mechanics. The so-called *strong form* must be transformed into its *weak form* or the virtual work equation in order to discretise the equation. The momentum equations introduced in Equations 4.23 and 4.24 are multiplied by a *test function*, $\delta\hat{t}_j$, also known as a *virtual velocity*, and integrated over the continuum's current domain Ω, the relationship between fluid and mixture reads:

$$\int_\Omega \delta\hat{t}_j\, \rho_w\, \frac{d\hat{w}_j}{dt}\, d\Omega = \int_\Omega \delta\hat{t}_j\, \frac{\partial p}{\partial x_i}\, d\Omega + \int_\Omega \delta\hat{t}_j\, \rho_w\, g_j\, d\Omega - \int_\Omega \delta\hat{t}_j\, \frac{n\, \rho_w\, g}{k} (\hat{w}_j - \hat{v}_j)\, d\Omega\,, \tag{4.33}$$

and,

$$\int_\Omega \delta\hat{t}_j\,(1-n)\,\rho_s\,\frac{d\hat{v}_j}{dt}\,d\Omega = -\int_\Omega \delta\hat{t}_j\,n\,\rho_w\,\frac{d\hat{w}_j}{dt}\,d\Omega + \int_\Omega \delta\hat{t}_j\,\frac{\partial\sigma_{ij}}{\partial\sigma_i}\,d\Omega + \int_\Omega \delta\hat{t}_j\,\rho_{sat}\,g_j\,d\Omega\,, \tag{4.34}$$

respectively. Applying *Gauss' theorem*, also known as the *divergence theorem*, to Equations 4.33 and 4.34, the relations follow:

$$\begin{aligned}\int_\Omega \delta\hat{t}_j\,\rho_w\,\frac{d\hat{w}_j}{dt}\,d\Omega = \int_{\partial\Omega_p} \delta\hat{t}_j\,\bar{p}_j\,dS - \int_\Omega \frac{\partial\delta\hat{t}_j}{\partial x_j}\,p d\Omega + \int_\Omega \delta\hat{t}_j\,\rho_w\,g_j\,d\Omega \\ - \int_\Omega \delta\hat{t}_j\,\frac{n\,\rho_w\,g}{k}(\hat{w}_j - \hat{v}_j)\,d\Omega\,,\end{aligned} \tag{4.35}$$

and,

$$\begin{aligned}\int_\Omega \delta\hat{t}_j\,(1-n)\,\rho_s\frac{d\hat{v}_j}{dt}\,d\Omega = -\int_\Omega \delta\hat{t}_j\,n\,\rho_w\,\frac{d\hat{w}_j}{dt}\,d\Omega + \int_{\partial\Omega_\tau} \delta\hat{t}_j\,\tau_j\,dS \\ - \int_\Omega \frac{\partial\delta\hat{t}_j}{\partial x_i}\,\sigma_{ij}\,d\Omega + \int_\Omega \delta\hat{t}_j\,\rho_{sat}\,g_j\,d\Omega\,,\end{aligned} \tag{4.36}$$

respectively, are obtained for the fluid and mixture relations.

4.3.5 Spatial and temporal discretisation

Next, the spatial discretisation of momentum equations will be discussed. In the finite element method, the discrete form is obtained by approximating the accelerations ($\boldsymbol{a}$), velocities ($\boldsymbol{v}$), and displacements ($\boldsymbol{u}$) in accordance with the corresponding relations.

$$\hat{\boldsymbol{a}}(\boldsymbol{x},\,t) = \bar{\boldsymbol{N}}(\boldsymbol{x})\,\boldsymbol{a}(t)\,, \qquad \hat{\boldsymbol{v}}(\boldsymbol{x},\,t) = \bar{\boldsymbol{N}}(\boldsymbol{x})\,\boldsymbol{v}(t)\,, \qquad \hat{\boldsymbol{u}}(\boldsymbol{x},\,t) = \bar{\boldsymbol{N}}(\boldsymbol{x})\,\boldsymbol{u}(t)\,. \tag{4.37}$$

Similarly, corresponding virtual quantities are approximated; for example, $\delta\hat{\boldsymbol{v}} \approx \bar{\boldsymbol{N}}\,\delta\hat{\boldsymbol{v}}$. The *shape functions* or the *interpolation function* matrix has the form:

$$\bar{\boldsymbol{N}}(\boldsymbol{x}) = \begin{bmatrix}\bar{\boldsymbol{N}}_1(\boldsymbol{x}) & \bar{\boldsymbol{N}}_2(\boldsymbol{x}) & \bar{\boldsymbol{N}}_3(\boldsymbol{x}) & \bar{\boldsymbol{N}}_4(\boldsymbol{x}) & \ldots & \bar{\boldsymbol{N}}_{n_\mathcal{T}}(\boldsymbol{x})\end{bmatrix}\,, \tag{4.38}$$

where, the bar atop the shape function ($\bar{\boldsymbol{N}}$) indicates that it was written using a global coordinate system, $n_{\mathcal{T}}$ denotes the total number of nodes in the mesh and $\bar{\boldsymbol{N}}_i(\boldsymbol{x})$ is denoted by the relation:

$$\bar{\boldsymbol{N}}_i(\boldsymbol{x}) = \begin{bmatrix} \bar{N}_i(\boldsymbol{x}) & 0 & 0 & 0 \\ 0 & \bar{N}_i(\boldsymbol{x}) & 0 & 0 \\ 0 & 0 & \bar{N}_i(\boldsymbol{x}) & 0 \\ 0 & 0 & 0 & \bar{N}_i(\boldsymbol{x}) \end{bmatrix} \tag{4.39}$$

The acceleration, velocity, and displacement vectors can then be expressed as:

$$\begin{aligned} \boldsymbol{a}_\theta(t) &= \begin{bmatrix} a_{1x} & a_{1y} & a_{2x} & a_{2y} & \cdots & a_{n_{\mathcal{T}-1}x} & a_{n_{\mathcal{T}-1}y} & a_{n_{\mathcal{T}}x} & a_{n_{\mathcal{T}}y} \end{bmatrix}^T, \\ \boldsymbol{v}_\theta(t) &= \begin{bmatrix} v_{1x} & v_{1y} & v_{2x} & v_{2y} & \cdots & v_{n_{\mathcal{T}-1}x} & v_{n_{\mathcal{T}-1}y} & v_{n_{\mathcal{T}}x} & v_{n_{\mathcal{T}}y} \end{bmatrix}^T, \textit{and} \\ \boldsymbol{u}_\theta(t) &= \begin{bmatrix} u_{1x} & u_{1y} & u_{2x} & u_{2y} & \cdots & u_{n_{\mathcal{T}-1}x} & u_{n_{\mathcal{T}-1}y} & u_{n_{\mathcal{T}}x} & u_{n_{\mathcal{T}}y} \end{bmatrix}^T. \end{aligned} \tag{4.40}$$

Here, a_{2x} represents the acceleration at node 2 in the x-direction, and θ can refer to either the solid component (s) or the fluid component (w). The relation provides the kinematic relation:

$$\dot{\boldsymbol{\varepsilon}}(\boldsymbol{x},\, t) = \boldsymbol{B}(\boldsymbol{x})\, \boldsymbol{v}(t)\,, \tag{4.41}$$

where, $\boldsymbol{B}$ is the *strain-displacement* matrix and is expressed by the relation:

$$\boldsymbol{B}_i(\boldsymbol{x}) = \begin{bmatrix} N_{1,x} & N_{2,x} & N_{3,x} & N_{4,x} & 0 & 0 & 0 & 0 \\ 0 & 0 & 0 & 0 & N_{1,y} & N_{2,y} & N_{3,y} & N_{4,y} \\ N_{1,y} & N_{2,y} & N_{3,y} & N_{4,y} & N_{1,x} & N_{2,x} & N_{3,x} & N_{4,x} \end{bmatrix}, \tag{4.42}$$

where, the term $N_{1,\alpha}$ is the shorthand of $\frac{\partial N_1(\boldsymbol{x})}{\partial \alpha}$, and α is either x or y. Thus, the Equation 4.41 for one four-noded element would be written as:

$$\dot{\boldsymbol{\varepsilon}}(\boldsymbol{x},\, t) = \begin{bmatrix} N_{1,x} & N_{2,x} & N_{3,x} & N_{4,x} & 0 & 0 & 0 & 0 \\ 0 & 0 & 0 & 0 & N_{1,y} & N_{2,y} & N_{3,y} & N_{4,y} \\ N_{1,y} & N_{2,y} & N_{3,y} & N_{4,y} & N_{1,x} & N_{2,x} & N_{3,x} & N_{4,x} \end{bmatrix} \begin{bmatrix} v_{1x} \\ v_{2x} \\ v_{3x} \\ v_{4x} \\ v_{1y} \\ v_{2y} \\ v_{3y} \\ v_{4y} \end{bmatrix} . \tag{4.43}$$

In the case of two-phase problems, the result of substituting the previously discussed approximation into Equations 4.35 and 4.34 is:

$$\begin{aligned} \int_\Omega \bar{\boldsymbol{N}}^T \rho_w \, \bar{\boldsymbol{N}} \, \boldsymbol{a}_w \, d\Omega = \int_{\partial\Omega_p} \bar{\boldsymbol{N}}^T \, \bar{\boldsymbol{p}} \, dS - \int_\Omega \boldsymbol{B}^T \, p \, \boldsymbol{I} \, d\Omega \\ + \int_\Omega \bar{\boldsymbol{N}}^T \rho_w \, \boldsymbol{g} \, d\Omega - \int_\Omega \bar{\boldsymbol{N}}^T \, \frac{n \, \rho_w \, g}{k} \bar{\boldsymbol{N}} \, (\boldsymbol{w} - \boldsymbol{v}) \, d\Omega \,, \end{aligned} \tag{4.44}$$

and,

$$\begin{aligned} \int_\Omega \bar{\boldsymbol{N}}^T \, (1-n) \, \rho_s \, \bar{\boldsymbol{N}} \, \boldsymbol{a}_s \, d\Omega = - \int_\Omega \bar{\boldsymbol{N}}^T \, n \, \rho_w \, \bar{\boldsymbol{N}} \, \boldsymbol{a}_w \, d\Omega + \int_{\partial\Omega_\tau} \bar{\boldsymbol{N}}^T \, \boldsymbol{\tau} \, dS \\ - \int_\Omega \boldsymbol{B}^T \, \boldsymbol{\sigma} \, d\Omega + \int_\Omega \bar{\boldsymbol{N}}^T \, \rho_{sat} \, \boldsymbol{g} \, d\Omega \,, \end{aligned} \tag{4.45}$$

respectively. The vector $\boldsymbol{a}_w$ contains the nodal acceleration of the fluid phase, $\bar{\boldsymbol{p}}$ refers to a vector of prescribed water pressure and the symbol $\boldsymbol{I}$ refers to a unity tensor represented by $\boldsymbol{I} = \begin{bmatrix} 1 & 1 & 1 & 0 & 0 & 0 \end{bmatrix}^T$.

In the finite element method, the integrals in Equations 4.44 and 4.44 are computed on each element when the mesh is looped over. After sweeping through all the elements, the resulting elemental matrices are assembled into a global matrix using the *assembly* procedure. The Equations 4.44 and 4.45 are described by the relation:

$$\left(\bigtriangleup_{e=1}^{n_{elm}} \int_{\Omega_e} \boldsymbol{N}^T \rho_w \boldsymbol{N}\, d\Omega\right) \boldsymbol{a}_w = \bigtriangleup_{e=1}^{n_{pelm}} \int_{\partial\Omega_{pe}} \boldsymbol{N}^T \bar{\boldsymbol{p}}_e\, dS + \bigtriangleup_{e=1}^{n_{elm}} \int_{\Omega_e} \boldsymbol{N}^T \rho_w \boldsymbol{g}\, d\Omega - \bigtriangleup_{e=1}^{n_{elm}} \int_{\Omega_e} \boldsymbol{B}^T p\, \boldsymbol{I}\, d\Omega - \left(\bigtriangleup_{e=1}^{n_{elm}} \int_{\Omega_e} \boldsymbol{N}^T \frac{n \rho_w g}{k} \boldsymbol{N}\, d\Omega\right) (\boldsymbol{w} - \boldsymbol{v}), \tag{4.46}$$

and,

$$\left(\bigtriangleup_{e=1}^{n_{elm}} \int_{\Omega_e} \boldsymbol{N}^T (1-n) \rho_s \boldsymbol{N}\, d\Omega\right) \boldsymbol{a}_s = -\left(\bigtriangleup_{e=1}^{n_{elm}} \int_{\partial\Omega_e} \boldsymbol{N}^T n \rho_w \boldsymbol{N}\, d\Omega\right) \boldsymbol{a}_w + \bigtriangleup_{e=1}^{n_{\tau elm}} \int_{\partial\Omega_{\tau e}} \boldsymbol{N}^T \boldsymbol{\tau}_e\, dS + \bigtriangleup_{e=1}^{n_{elm}} \int_{\Omega_e} \boldsymbol{N}^T \rho_{sat} \boldsymbol{g}\, d\Omega - \bigtriangleup_{e=1}^{n_{elm}} \int_{\Omega_e} \boldsymbol{B}^T \boldsymbol{\sigma}\, d\Omega, \tag{4.47}$$

respectively. Here $\bigtriangleup$ is the assembly operator, e ranges between 1 and total number of elements. n_{pelm} and $n_{\tau elm}$ refer to the number of surface elements for which water pressure and traction are specified, respectively.

4.3.6 Numerical space integration

Obtaining a solution to a closed-form integration for Equations such as 4.46 and 4.47 can be challenging or impossible at times. For such problems, an alternative would be to employ *numerical integration*. *Numerical integration* or *quadrature* involves approximating the value of a definite integral through the use of numerical methods. By defining the number of *gaussian quadrature* in an element e as n_{gp}, the *gaussian quadrature* can be represented for the Equations 4.46 and 4.47 as:

$$\underbrace{\left(\sum_{e=1}^{n_{elm}}\sum_{q=1}^{n_{gp}} w_q\, \boldsymbol{N}^T(\boldsymbol{\xi}_q)\, \rho_w(\boldsymbol{x}(\boldsymbol{\xi}_q))\, \boldsymbol{N}(\boldsymbol{\xi}_q)\, \left|\boldsymbol{J}(\boldsymbol{\xi}_q)\right|\right)}_{\mathbf{M}_w} \boldsymbol{a}_w = \overbrace{\sum_{e=1}^{n_{pelm}} \int_{\partial\Omega_{pe}} \boldsymbol{N}^T(\boldsymbol{\xi})\, \bar{\boldsymbol{p}}_e\,(\boldsymbol{x}(\boldsymbol{\xi}),\, t)\, dS}^{\mathbf{F}_w^{trac}}$$
$$+ \underbrace{\sum_{e=1}^{n_{elm}} \int_{\Omega_e} w_q\, \boldsymbol{N}^T(\boldsymbol{\xi}_q)\, \rho_w(\boldsymbol{x}(\boldsymbol{\xi}_q))\, \boldsymbol{g}\, \left|\boldsymbol{J}(\boldsymbol{\xi}_q)\right|}_{\mathbf{F}_w^{grav}} - \underbrace{\sum_{e=1}^{n_{elm}} \int_{\Omega_e} w_q \boldsymbol{B}^T(\boldsymbol{\xi}_q)\, p\, \boldsymbol{I}\,(\boldsymbol{\xi}_q,\, t)\, \left|\boldsymbol{J}(\boldsymbol{\xi}_q)\right|}_{\mathbf{F}_w^{int}}$$
$$- \underbrace{\left(\sum_{e=1}^{n_{elm}} \int_{\Omega_e} w_q\, \boldsymbol{N}^T\,(\boldsymbol{\xi}_q)\, \frac{n\, \rho_w\,(\boldsymbol{x}(\boldsymbol{\xi}_q))\, \boldsymbol{g}}{k} \boldsymbol{N}(\boldsymbol{\xi}_q)\, \left|\boldsymbol{J}(\boldsymbol{\xi}_q)\right|\right) \cdot \Big(\boldsymbol{w}(\boldsymbol{x}(\boldsymbol{\xi}_q)) - \boldsymbol{v}(\boldsymbol{x}(\boldsymbol{\xi}_q))\Big)}_{\mathbf{F}_w^{drag}}, \quad (4.48)$$

and,

$$\underbrace{\left(\sum_{e=1}^{n_{elm}}\sum_{q=1}^{n_{gp}} w_q\, \boldsymbol{N}^T(\boldsymbol{\xi}_q)\, (1-n)\, \rho_s\,(\boldsymbol{x}(\boldsymbol{\xi}_q))\, b\, \boldsymbol{N}(\boldsymbol{\xi}_q)\, \left|\boldsymbol{J}(\boldsymbol{\xi}_q)\right|\right)}_{\mathbf{M}_s} \boldsymbol{a}_s =$$
$$- \underbrace{\left(\sum_{e=1}^{n_{elm}}\sum_{q=1}^{n_{gp}} w_q\, \boldsymbol{N}^T(\boldsymbol{\xi}_q)\, n\, \rho_w\,(\boldsymbol{x}(\boldsymbol{\xi}_q))\, \boldsymbol{N}(\boldsymbol{\xi}_q)\, \left|\boldsymbol{J}(\boldsymbol{\xi}_q)\right|\right)}_{\bar{\mathbf{M}}_w} \boldsymbol{a}_w + \underbrace{\sum_{e=1}^{n_{\tau elem}} \int_{\partial\Omega_{\tau e}} \boldsymbol{N}^T(\boldsymbol{\xi})\, \boldsymbol{\tau}_e(\boldsymbol{x}(\boldsymbol{\xi}),\, t)\, dS}_{\mathbf{F}_m^{trac}}$$
$$+ \underbrace{\sum_{e=1}^{n_{elm}} \int_{\Omega_e} w_q\, \boldsymbol{N}^T(\boldsymbol{\xi}_q)\, \rho_{sat}(\boldsymbol{x}(\boldsymbol{\xi}_q))\, \boldsymbol{g}\, \left|\boldsymbol{J}(\boldsymbol{\xi}_q)\right|}_{\mathbf{F}_m^{grav}} - \underbrace{\sum_{e=1}^{n_{elm}} \int_{\Omega_e} w_q\, \boldsymbol{B}^T(\boldsymbol{\xi}_q)\, \boldsymbol{\sigma}(\boldsymbol{\xi}_q,\, t)\, \left|\boldsymbol{J}(\boldsymbol{\xi}_q)\right|}_{\mathbf{F}_m^{int}}, \quad (4.49)$$

respectively. Here, $\left|\boldsymbol{J}\right|$ represents the determinant of the Jacobian matrix, $\boldsymbol{\xi}$ represents the coordinate of quadrature point, and w the integration weight of the quadrature point. The discrete system of equations can be represented as:

$$\boldsymbol{M}_w\, \boldsymbol{a}_w = \boldsymbol{F}_w^{trac} + \boldsymbol{F}_w^{grav} - \boldsymbol{F}_w^{int} - \boldsymbol{F}_w^{drag}, \quad (4.50)$$

and,

$$\boldsymbol{M}_s\,\boldsymbol{a}_s = -\bar{\boldsymbol{M}}_w\,\boldsymbol{a}_w + \boldsymbol{F}_m^{trac} + \boldsymbol{F}_m^{grav} - \boldsymbol{F}_m^{int}\,, \tag{4.51}$$

for Equations 4.48 and 4.49, respectively.The subscripts f, s and m represent fluid, solid, and mixture quantities, respectively. The bar on top of the mass matrix $\bar{\boldsymbol{M}}_w$ represents the porosity scaling of water particle mass. The superscripts $trac, grav, int$ and $drag$ represent the traction, gravitational, internal, and drag forces, respectively. All matrices are lumped in the preceding equations.

4.3.7 Time marching and solution procedure

To advance in time, the *Explicit Euler* or *Forward Euler* scheme is adopted. The velocity is explicitly updated, and the displacement increment is calculated based on the updated velocity. As described by Equation 4.50:

$$\boldsymbol{M}_w\,\frac{d\boldsymbol{w}}{dt} = \boldsymbol{F}_w^{trac} + \boldsymbol{F}_w^{grav} - \boldsymbol{F}_w^{int} - \boldsymbol{Q}\,(\boldsymbol{w}-\boldsymbol{v})\,, \tag{4.52}$$

where, $\boldsymbol{Q}$ is the lumped matrix for the initial component of the drag force term. The result of integrating the preceding equation with limits $[t, t+\Delta t]$ yields:

$$\int_t^{t+\Delta t} \boldsymbol{M}_w\,d\boldsymbol{w} = \int_t^{t+\Delta t} \left[\boldsymbol{F}_w^{trac} + \boldsymbol{F}_w^{grav} - \boldsymbol{F}_w^{int} - \boldsymbol{Q}\,(\boldsymbol{w}-\boldsymbol{v})\right]\,dt\,. \tag{4.53}$$

Explicit integration of the preceding relation yields:

$$\boldsymbol{M}_w\,\left(\boldsymbol{w}^{t+\Delta t} - \boldsymbol{w}^t\right) \approx \left[\boldsymbol{F}_w^{trac,t} + \boldsymbol{F}_w^{grav,t} - \boldsymbol{F}_w^{int,t} - \boldsymbol{Q}\,(\boldsymbol{w}^t - \boldsymbol{v}^t)\right]\,\Delta t\,, \tag{4.54}$$

and by rearranging the terms, the velocity of fluid at time $t+\Delta t$ can be expressed as:

$$\boldsymbol{w}^{t+\Delta t} \approx \boldsymbol{w}^t + \boldsymbol{M}_w^{-1}\,\left[\boldsymbol{F}_w^{trac,t} + \boldsymbol{F}_w^{grav,t} - \boldsymbol{F}_w^{int,t} - \boldsymbol{Q}\,(\boldsymbol{w}^t - \boldsymbol{v}^t)\right]\,\Delta t\,. \tag{4.55}$$

The same method may be applied to the mixture. From Equation 4.51,

$$\boldsymbol{v}^{t+\Delta t} \approx \boldsymbol{v}^{t} + \boldsymbol{M}_{s}^{-1} \left[\bar{\boldsymbol{M}}_{w}^{-1} \, \boldsymbol{a}_{w}^{t} + \boldsymbol{F}_{m}^{trac,t} + \boldsymbol{F}_{m}^{grav,t} - \boldsymbol{F}_{m}^{int,t} \right] \Delta t \,, \tag{4.56}$$

where, $\boldsymbol{a}_{w}^{t} = \frac{\boldsymbol{w}^{t+\Delta t} - \boldsymbol{w}^{t}}{\Delta t}$.

Once the velocity of the solid at the current time step ($\boldsymbol{v}^{t+\Delta t}$) is calculated, the strain increment of the solid at *gauss point*, q and element, e is computed using the relation:

$$\Delta \boldsymbol{\varepsilon}_{q}^{t+\Delta t} = \boldsymbol{B}_{q} \, \boldsymbol{v}_{e}^{t+\Delta t} \, \Delta t \,, \tag{4.57}$$

where, $\boldsymbol{v}_e$ is the velocity vector of element e. The global velocity vector, v is assembled using these elemental vectors. By integrating the storage equation (Equation 4.21), pore pressure is obtained, and is given by the relation:

$$p_{q}^{t+\Delta t} \approx p_{q}^{t} + \Delta t \, \frac{K_{w}}{n} \, \boldsymbol{I}^{T} \left[(1-n) \; \boldsymbol{B}_{q} \, \boldsymbol{v}_{e}^{t+\Delta t} + n \, \boldsymbol{B}_{q} \, \boldsymbol{w}_{e}^{t+\Delta t} \right] . \tag{4.58}$$

Calculating the effective stress at the current time step requires a constitutive law that accepts the effective stress at the previous time step and the updated strain tensor.

$$\left\{ \boldsymbol{\sigma}', \text{ state variables} \right\}^{t} \xrightarrow[\Delta \boldsymbol{\varepsilon}^{t+\Delta t}]{\text{constitutive law}} \left\{ \boldsymbol{\sigma}', \text{ state variables} \right\}^{t+\Delta t} .$$

The total stress is updated based on the relationship:

$$\boldsymbol{\sigma}_{q}^{t+\Delta t} = \boldsymbol{\sigma}_{q}^{'t+\Delta t} + p_{q}^{t+\Delta t} \, \boldsymbol{I} \,. \tag{4.59}$$

4.3.8 Extension of Kelvin-Voigt elements for saturated media

When dealing with an unbounded saturated domain, there is always the possibility of stress and pressure waves bouncing off the boundaries, which could lead to incorrect results if not dampened adequately. Moreover, these wave reflections are not indicative of a natural unbounded domain. In the past, various methods for dealing with wave reflections have been proposed [76, 121, 130]. The method proposed by Lysmer and Kuhlemeyer [138] to reduce these spurious wave reflections has been utilised in this work. It is not the intention of this work to cover this topic exhaustively, but rather to introduce the equations used in its implementation. This work implements viscous

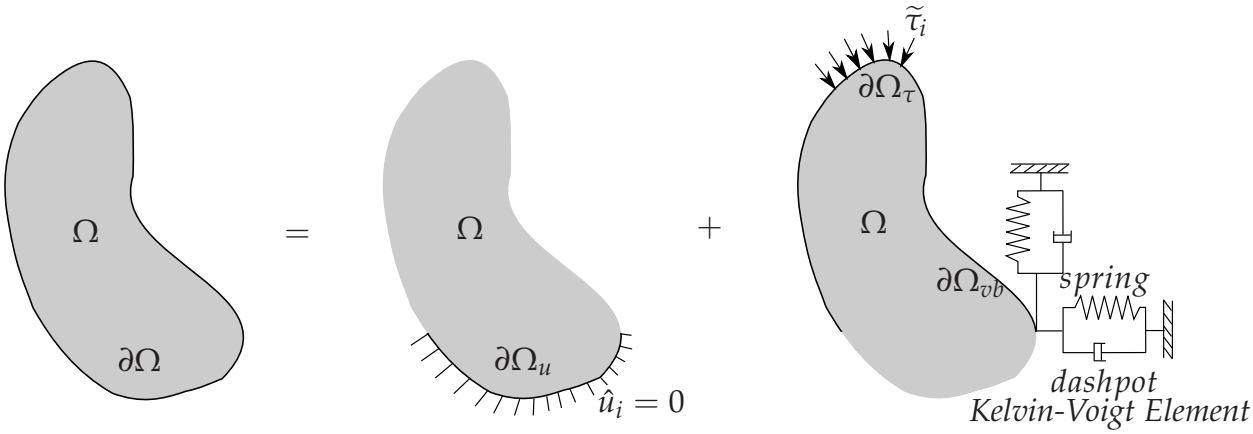

boundary of domain displacement boundary traction boundary

Figure 4.4: Kelvin-Voigt elements at the boundary of continuum

damping forces with the aid of dashpots. Kafaji [107] observed that a boundary supported only by dashpots has a propensity to creep continuously when loaded. As shown in Figure 4.4, dashpot elements were substituted with Kelvin-Voigt elements to mitigate this issue.

To account for the presence of saturated soil, it is necessary to define two sets of Kelvin-Voigt elements, one for the solid phase and the other for the fluid phase. The relation provides the element's reaction.

$$\boldsymbol{p}^{vb} = -\underbrace{\boldsymbol{k}_w\,\hat{\boldsymbol{u}}_w}_{spring} - \overbrace{\boldsymbol{\eta}_w\,\hat{\boldsymbol{w}}}^{dashpot}\,, \tag{4.60}$$

and for the solid phase given by the relation:

$$\boldsymbol{\tau}^{vb} = -\underbrace{\boldsymbol{k}_s\,\hat{\boldsymbol{u}}_s}_{spring} - \overbrace{\boldsymbol{\eta}_s\,\hat{\boldsymbol{v}}}^{dashpot}\,. \tag{4.61}$$

In Equations 4.60 and 4.61, $\boldsymbol{k}$ and $\boldsymbol{\eta}$ are the spring and dashpot constants, respectively. The matrices for $\boldsymbol{\eta}_w$ and $\boldsymbol{k}_w$ can be provided by the relations:

$$\boldsymbol{\eta}_w = \begin{bmatrix} a\,\rho_w\,c_w & 0 & 0 \\ 0 & 0 & 0 \\ 0 & 0 & 0 \end{bmatrix} \qquad \text{and} \qquad \boldsymbol{k}_w = \begin{bmatrix} \frac{\rho_w\,c_w^2}{\delta} & 0 & 0 \\ 0 & 0 & 0 \\ 0 & 0 & 0 \end{bmatrix}, \tag{4.62}$$

and, for $\boldsymbol{\eta}_s$ and $\boldsymbol{k}_s$ by the relations:

$$\boldsymbol{\eta}_s = \begin{bmatrix} a\,\rho_s\,c_p & 0 & 0 \\ 0 & b\,\rho_s\,c_s & 0 \\ 0 & 0 & b\,\rho_s\,c_s \end{bmatrix} \qquad \text{and} \qquad \boldsymbol{k}_s = \begin{bmatrix} k_p & 0 & 0 \\ 0 & k_s & 0 \\ 0 & 0 & k_s \end{bmatrix}. \tag{4.63}$$

In the preceding equations, c_w, c_p and c_s represent the velocity of pure waves in fluid, primary waves in solid, and secondary waves in solid, respectively. The parameters, a and b are dimensionless parameters chosen based on the incidence angle of the wave in order to maximise absorption. In their paper, Lysmer and Kuhlemeyer [138] demonstrate that the absorption cannot be perfect over the entire range of incidence angles, regardless of the values of a and b. As a result of a series of numerical tests, the recommended values for a and b were determined to be 1 for both primary and secondary waves. The coefficients k_p and k_s are chosen so as to produce a viscous layer that extends beyond the mesh's boundaries. The relation provides the stiffness:

$$k_p = \frac{E^c}{\delta} \qquad \text{and} \qquad k_s = \frac{G}{\delta}, \tag{4.64}$$

where, $E^c = \rho_s\,c_p^2$ and $G = \rho_s\,c_s^2$. The term δ is the thickness of the virtual viscous layer, and the has range $0 \leq \delta \leq \infty$. As $\delta \to 0$, the element reduces to a rigid boundary, whereas as $\delta \to \infty$, it reduces to a pure dashpot boundary. δ must be excluded from the critical time step size restriction for any given problem. In this regard, δ should be chosen based on the relationship:

$$\delta \geq max\left[\frac{h_{min}}{2a}, \frac{h_{min}}{2b}\right],$$

where, h_{min} is the characteristic length of the finite element mesh. The velocity vectors $\hat{\boldsymbol{w}}$ and $\hat{\boldsymbol{v}}$, and displacement vectors $\hat{\boldsymbol{u}}_w$ and $\hat{\boldsymbol{u}}_s$ are defined as

$$\begin{aligned} \hat{\boldsymbol{w}} &= \begin{bmatrix} \hat{w}_n & \hat{w}_{t1} & \hat{w}_{t2} \end{bmatrix} \qquad \text{and} \qquad \hat{\boldsymbol{u}}_w = \begin{bmatrix} \hat{u}_{wn} & \hat{u}_{wt1} & \hat{u}_{wt2} \end{bmatrix}, \\ \hat{\boldsymbol{v}} &= \begin{bmatrix} \hat{v}_n & \hat{v}_{t1} & \hat{v}_{t2} \end{bmatrix} \qquad \text{and} \qquad \hat{\boldsymbol{u}}_s = \begin{bmatrix} \hat{u}_{sn} & \hat{u}_{st1} & \hat{u}_{st2} \end{bmatrix}, \end{aligned} \tag{4.65}$$

where, the first component of the vectors represents the normal component (n) and the second and third components ($t1$, $t2$) represent the tangential components. Accounting for the boundary term as an additional traction term, Equation 4.44 can be recast as:

$$\begin{aligned} \int_\Omega \bar{\boldsymbol{N}}^T \rho_w \, \bar{\boldsymbol{N}} \, \boldsymbol{a}_w \, d\Omega = \int_{\partial\Omega_p} \bar{\boldsymbol{N}}^T \, \bar{\boldsymbol{p}} \, dS - \int_{\partial\Omega_{p^{vb}}} \bar{\boldsymbol{N}}^T \, \boldsymbol{\eta}_w \, \bar{\boldsymbol{N}} \, \boldsymbol{w} \, dS - \int_{\partial\Omega_{p^{vb}}} \bar{\boldsymbol{N}}^T \, \boldsymbol{k}_w \, \bar{\boldsymbol{N}} \, \boldsymbol{u}_w \, dS \\ - \int_\Omega \boldsymbol{B}^T \, p \, \boldsymbol{I} \, d\Omega + \int_\Omega \bar{\boldsymbol{N}}^T \rho_w \, \boldsymbol{g} \, d\Omega - \int_\Omega \bar{\boldsymbol{N}}^T \, \frac{n \, \rho_w \, g}{k} \, \bar{\boldsymbol{N}} \, (\boldsymbol{w} - \boldsymbol{v}) \, d\Omega, \end{aligned} \tag{4.66}$$

and, Equation 4.45 can be recast as:

$$\begin{aligned} \int_\Omega \bar{\boldsymbol{N}}^T \, (1-n) \, \rho_s \, \bar{\boldsymbol{N}} \, \boldsymbol{a}_s \, d\Omega = &- \int_\Omega \bar{\boldsymbol{N}}^T \, n \, \rho_w \, \bar{\boldsymbol{N}} \, \boldsymbol{a}_w \, d\Omega + \int_{\partial\Omega_\tau} \bar{\boldsymbol{N}}^T \, \boldsymbol{\tau} \, dS \\ &- \int_{\partial\Omega_{\tau^{vb}}} \bar{\boldsymbol{N}}^T \, \boldsymbol{\eta}_s \, \bar{\boldsymbol{N}} \, \boldsymbol{v} \, dS - \int_{\partial\Omega_{\tau^{vb}}} \bar{\boldsymbol{N}}^T \, \boldsymbol{k}_s \, \bar{\boldsymbol{N}} \, \boldsymbol{u}_s \, dS \\ &- \int_{\partial\Omega_{p^{vb}}} \bar{\boldsymbol{N}}^T \, \boldsymbol{\eta}_w \, \bar{\boldsymbol{N}} \, \boldsymbol{w} \, dS - \int_{\partial\Omega_{p^{vb}}} \bar{\boldsymbol{N}}^T \, \boldsymbol{k}_w \, \bar{\boldsymbol{N}} \, \boldsymbol{u}_w \, dS \\ &- \int_\Omega \boldsymbol{B}^T \, \boldsymbol{\sigma} \, d\Omega + \int_\Omega \bar{\boldsymbol{N}}^T \, \rho_{sat} \, \boldsymbol{g} \, d\Omega \, . \end{aligned} \tag{4.67}$$

The momentum equations now takes the form:

$$\boldsymbol{M}_w \, \boldsymbol{a}_w = \boldsymbol{F}_w^{trac} - \boldsymbol{F}_w^{vb} + \boldsymbol{F}_w^{grav} - \boldsymbol{F}_w^{int} - \boldsymbol{F}_w^{drag}, \tag{4.68}$$

and,

$$\boldsymbol{M}_s \, \boldsymbol{a}_s = -\bar{\boldsymbol{M}}_w \boldsymbol{a}_w + \boldsymbol{F}_m^{trac} - \boldsymbol{F}_w^{vb} - \boldsymbol{F}_s^{vb} + \boldsymbol{F}_m^{grav} - \boldsymbol{F}_m^{int} \, . \tag{4.69}$$

The newly introduced viscous boundary terms in the above equations are defined as:

$$\boldsymbol{F}_w^{vb} = \boldsymbol{C}_w\,\boldsymbol{w} + \boldsymbol{K}_w\,\boldsymbol{u}_w, \qquad \text{and} \qquad \boldsymbol{F}_s^{vb} = \boldsymbol{C}_s\,\boldsymbol{v} + \boldsymbol{K}_s\,\boldsymbol{u}_s\,. \tag{4.70}$$

Individually, the relations that define the spring and dashpot matrices are as follows:

$$\begin{aligned}
\boldsymbol{C}_w &= \int_{\partial\Omega_{p^{vb}}} \bar{\boldsymbol{N}}^T\,\boldsymbol{\eta}_w\,\bar{\boldsymbol{N}}\,dS\,,\\
\boldsymbol{K}_w &= \int_{\partial\Omega_{p^{vb}}} \bar{\boldsymbol{N}}^T\,\boldsymbol{k}_w\,\bar{\boldsymbol{N}}\,dS\,,\\
\boldsymbol{C}_s &= \int_{\partial\Omega_{p^{vb}}} \bar{\boldsymbol{N}}^T\,\boldsymbol{\eta}_s\,\bar{\boldsymbol{N}}\,dS\,,\\
\boldsymbol{K}_s &= \int_{\partial\Omega_{p^{vb}}} \bar{\boldsymbol{N}}^T\,\boldsymbol{k}_s\,\bar{\boldsymbol{N}}\,dS\,.
\end{aligned} \tag{4.71}$$

After integrating and summing the preceding matrices, the forces for fluid and solid in their incremental form are accumulated over time and are given by the following relations:

$$\begin{aligned}
\boldsymbol{F}_w^{vb,t} &= \boldsymbol{F}_w^{vb,t-\Delta t} + \Delta\boldsymbol{F}_w^{vb,t}\,, \qquad \text{and}\\
\boldsymbol{F}_s^{vb,t} &= \boldsymbol{F}_s^{vb,t-\Delta t} + \Delta\boldsymbol{F}_s^{vb,t}\,,
\end{aligned} \tag{4.72}$$

where,

$$\begin{aligned}
\Delta\boldsymbol{F}_w^{vb,t} &= \boldsymbol{C}_w^t\,\Delta\boldsymbol{w}^t + \boldsymbol{K}_w^t\,\Delta\boldsymbol{u}_{\boldsymbol{w}}^{\boldsymbol{t}}\,, \qquad \text{and}\\
\Delta\boldsymbol{F}_s^{vb,t} &= \boldsymbol{C}_s^t\,\Delta\boldsymbol{v}^t + \boldsymbol{K}_s^t\,\Delta\boldsymbol{u}_{\boldsymbol{s}}^{\boldsymbol{t}}\,.
\end{aligned} \tag{4.73}$$

4.4 Extension of discretisation from FE to MPM

In the previous section, coupled hydromechanical formulation differential equations and finite element discretisation were presented. In this section, the formulation is extended to MPM and the solution for a single time step is provided. While every effort has been made to present only the most important aspects of the formulation, readers are encouraged to refer to Ceccato [45] and Kafaji [107] for a comprehensive treatment of the formulation of the hydromechanical dynamic coupled model in the context of the Material Point Method.

4.4.1 Particle discretisation and initialisation

The underlying assumption of this formulation is that the solid and fluid phases share the same particle. As a result, no distinction is made between solid and liquid particles. The continuum is discretised into discrete particles that possess the characteristics of both the solid and liquid phases. In this instance, the position of the particle is updated based solely on the solid constituent's displacement. Next, the initialisation of the particles with the computational mesh background is considered. This includes the assignment of mass, body forces, tractions, and other continuum properties to particles. Since each particle is initially positioned at a predetermined location within the discretised element of the continuum, the local position vector, $\boldsymbol{\xi}_p$ is initialised for any particle, p. Initializing the global position vector is the relation:

$$\boldsymbol{x}(\boldsymbol{\xi}_p) \approx \sum_{i=1}^{n_{en}} N_i(\boldsymbol{\xi}_p)\, \boldsymbol{x}_i\,, \tag{4.74}$$

where, n_{en} represents the number of nodes per element, which in this case is 4, and $N_i(\boldsymbol{\xi}_p)$ represents the shape function of node i evaluated at the local position of particle p. Using the particle's local and global positions, the volume associated with the particle, Ω_p is calculated using the relationship:

$$\Omega_p = \frac{1}{n_{ep}} \int_{\partial\Omega_e} d\Omega \approx \frac{1}{n_{ep}} \sum_{q=1}^{n_{eq}} w_q \left| \boldsymbol{J}(\boldsymbol{\xi}_q) \right| . \tag{4.75}$$

It is evident from the above relationship that the volumes are calculated such that all particles within the element have the same volume. n_{eq} represents the number of *gauss points*, n_{ep} represents the number of particles per element, w_q represents the local integration weight associated with *gauss point*, q and $\boldsymbol{J}$ is the Jacobian matrix. In this context, the volume under consideration is the total volume, which consists of the volumes of the solid and fluid phases. The particles are then assigned quantities such as bulk modulus, density, porosity, and hydraulic conductivity. Using the relationship, the mass quantities of the particle are calculated:

$$m_{s,p} = \rho_{s,p}\, \Omega_p\,, \qquad m_{w,p} = \rho_{w,p}\, \Omega_p\,, \qquad \text{and} \qquad m_p = \rho_{sat,p}\, \Omega_p\,. \tag{4.76}$$

These masses are then utilised to integrate the necessary mass matrices for solving the momentum equations. The body forces associated with each particle are computed based on their masses using the relationship:

$$\boldsymbol{f}_{s,p}^{grav} = m_{s,p}\,\boldsymbol{g}\,, \qquad \boldsymbol{f}_{w,p}^{grav} = m_{w,p}\,\boldsymbol{g}\,, \qquad \text{and} \qquad \boldsymbol{f}_{p}^{grav} = m_{p}\,\boldsymbol{g}\,. \tag{4.77}$$

The prescribed traction in an element is integrated using conventional FEM techniques. The relation for traction force in an element is:

$$\begin{aligned} \widetilde{\boldsymbol{F}}_e^{trac} &= \int_{S_e} \boldsymbol{N}^T(\boldsymbol{\xi})\,\widetilde{\boldsymbol{\tau}}_e(\boldsymbol{x})\,dS \\ &\approx \sum_{q=1}^{n_{gpe}} w_q\,\boldsymbol{N}^T\left(\boldsymbol{\xi}_q\right)\left(\sum_{i=1}^{n_{nodes}} N_i(\boldsymbol{\xi})\,\widetilde{\boldsymbol{\tau}}_e(\boldsymbol{x})\right)\,S_e\,. \end{aligned} \tag{4.78}$$

$\widetilde{\boldsymbol{\tau}}_e(\boldsymbol{x})$ represents the traction vector at node, i of surface element, e. S_e represents the surface area of an element, while n_{gpe} and n_{nodes} represent the number of *gauss points* per element and the number of nodes, respectively. The terms w_q and $\boldsymbol{\xi}_q$, which were introduced in previous sections, represent the local integration weight and local coordinate vector of *gauss point*, q respectively. After integrating Equation 4.78 for a 4-noded quadrilateral element, the traction forces vector has 8 components, with each pair corresponding to a node of the 4-noded element. Each node's traction vector can be represented as:

$$\widetilde{\boldsymbol{F}}_e^{trac} = \begin{bmatrix} \widetilde{\boldsymbol{f}}_1^{trac} & \widetilde{\boldsymbol{f}}_2^{trac} & \widetilde{\boldsymbol{f}}_3^{trac} & \widetilde{\boldsymbol{f}}_4^{trac} \end{bmatrix}\,. \tag{4.79}$$

Each $\widetilde{\boldsymbol{f}}$ consists of two components, one each for the $x-$ and $y-$ directions. The traction vector, $\widetilde{\boldsymbol{\tau}}_e$ is interpolated from the element's nodes to the boundary particles in the element's vicinity. Traction at any boundary particle can be calculated using the formula:

$$\widetilde{\boldsymbol{\tau}}_e(\boldsymbol{x}_p) \approx \sum_{i=1}^{n_{nodes}} N_i(\boldsymbol{\xi}_p)\,\widetilde{\boldsymbol{\tau}}_e(\boldsymbol{x}_i)\,, \tag{4.80}$$

where N_i is the shape function of the node, i of the quadrilateral element and $\boldsymbol{\xi}_p$ are the boundary particle's coordinates. The coordinates represent the location of the particle within the element where traction forces are being applied. The relation for the traction force vector, $\widetilde{\boldsymbol{f}}_p^{trac}$ of a boundary particle is:

$$\begin{aligned} \widetilde{\boldsymbol{f}}_p^{trac} &= \widetilde{\boldsymbol{\tau}}_e\left(\boldsymbol{\xi}_p\right)\frac{S_e}{n_{ebtp}}, \\ &= \frac{S_e}{n_{ebtp}}\sum_{i=1}^{n_{nodes}} N_i(\boldsymbol{\xi}_p)\,\widetilde{\boldsymbol{\tau}}_e(\boldsymbol{x}_i)\,, \end{aligned} \tag{4.81}$$

where, n_{ebtp} represents the number of border traction particles located on the element's loaded face. Considering only uniform tractions and the fact that the particles are initially uniformly distributed with respect to the loaded face by design, the equation simplifies to the form:

$$\widetilde{\boldsymbol{f}}_p^{trac} = \widetilde{\boldsymbol{\tau}}_e\,\frac{S_e}{n_{ebtp}} = \frac{1}{n_{ebtp}}\sum_{i=1}^{n_{nodes}} \widetilde{\boldsymbol{f}}_i^{trac}\,. \tag{4.82}$$

The total traction force vector corresponding to prescribed pressure for particle, p is calculated as:

$$\widetilde{\boldsymbol{f}}_{w,p}^{trac} = \widetilde{\boldsymbol{p}}_e\,\frac{S_e}{n_{ebtp}}\,, \tag{4.83}$$

where, $\widetilde{\boldsymbol{p}}_e$ represents the prescribed boundary pressure vector. Pressure is a scalar quantity and follows the notation $\widetilde{\boldsymbol{p}} = \widetilde{p}\boldsymbol{n} = \widetilde{p}n_i$, where $\widetilde{p}$ is the prescribed pressure on the boundary and $\boldsymbol{n}$ is the unit normal vector on the boundary.

During the initialisation phase, particles are assigned all relevant continuum properties, including initial conditions, material parameters, state parameters, and constitutive variable. Other pertinent bookkeeping parameters are also assigned.

4.4.2 Solution procedure involving a single time increment

By mapping the state of the continuum onto the nodes of the particles and obtaining a solution on the nodes, we will now concentrate on the solution of the momentum equation. On the particles, properties of the continuum such as strain, pressure, and stresses are calculated, and variables such as velocity and displacement are mapped from the nodes to the particles using the collocation function. Here, a description of this procedure is discussed.

As it is widely known, the application of the *consistent mass* matrix adds a level of numerical complexity to the solution procedure. A large system of algebraic equations

must be solved, which can consume considerable of computational time. The use of a *lumped mass* matrix would be a practical alternative. As demonstrated by Burgess et al. [38], although this method is computationally more efficient and requires less storage space, it suffers from numerical dissipation of energy. There are numerous ways to create a *lumped mass* matrix. The work of Hughes [96] provides a comprehensive analysis of the various methods. In this monograph, the mass matrix is derived from the *consistent mass* matrix. Entries of the *lumped mass* matrix correspond to the sum of the rows of its *consistent* matrix counterpart. The global mass matrix is given the relations:

$$\boldsymbol{M}^G = \bigwedge_{e=1}^{n_{elm}} \boldsymbol{M}_e^G \,, \tag{4.84}$$

where, $\boldsymbol{M}^G$ and $\boldsymbol{M}_e^G$ are the global and element *lumped mass* matrix, respectively. The element mass matrix is given by the form:

$$\boldsymbol{M}_e^G = \begin{bmatrix} \boldsymbol{m}_1 & \boldsymbol{0} & \cdots & \boldsymbol{0} \\ \boldsymbol{0} & \boldsymbol{m}_2 & \cdots & \boldsymbol{0} \\ \vdots & \vdots & \ddots & \cdots \\ \boldsymbol{0} & \boldsymbol{0} & \cdots & \boldsymbol{m}_{en} \end{bmatrix} . \tag{4.85}$$

Each sub-matrix $\boldsymbol{m}_i$ can be given by the relation

$$\boldsymbol{m}_i = \begin{bmatrix} m_1 & 0 \\ 0 & m_2 \end{bmatrix} , \tag{4.86}$$

where,

$$m_i \approx \sum_{q}^{n_{gp}} w_q N_i(\boldsymbol{\xi}_q)\, \rho_s\left(\boldsymbol{x}(\boldsymbol{\xi}_q)\right) \left|\boldsymbol{J}(\boldsymbol{\xi}_q)\right| \approx \sum_{p=1}^{n_{ep}} m_p\, N_i\left(\boldsymbol{\xi}_p^t\right). \tag{4.87}$$

The submatrix, $\boldsymbol{0}$ is simply a matrix containing only zeros. It should be noted that the mass matrix is not simply the row sum of its corresponding *consistent mass* matrix; rather, it is constructed using *direct lumping*. Due to the effectiveness of this method, it is possible to rapidly construct the mass matrix at each time step as particles move through the computational mesh in the background. Reference [107] provides the proof that this method is equivalent to the row sum method of construction. At the start

of each time step, the mass matrices in Equations 4.50 and 4.51 must be integrated. Equation 4.87 can therefore be formulated for mass matrices, and given as:

$$\begin{aligned} m_{w,i}^{t} &\approx \sum_{p=1}^{n_{ep}} m_{w,p}\, N_i\left(\boldsymbol{\xi}_p^t\right), \\ \bar{m}_{w,i}^{t} &\approx \sum_{p=1}^{n_{ep}} n_p^t\, m_{w,p}\, N_i(\boldsymbol{\xi}_p^t), \\ m_{s,i}^{t} &\approx \sum_{p=1}^{n_{ep}} (1-n_p^t)\, m_{s,p}\, N_i(\boldsymbol{\xi}_p^t), \end{aligned} \tag{4.88}$$

corresponding to the matrices $\boldsymbol{M}_w$, $\bar{\boldsymbol{M}}_w$, and $\boldsymbol{M}_s$, respectively. Next, the velocities of particles in both solid and fluid phases are mapped to the nodes. This is achieved through the relation:

$$\begin{aligned} \bar{\boldsymbol{M}}_w^t\, \boldsymbol{w}^t &= \boldsymbol{P}_w^t, \\ \boldsymbol{M}_s^t\, \boldsymbol{v}^t &= \boldsymbol{P}_s^t, \end{aligned} \tag{4.89}$$

where, the vectors containing mapped momentum from particle,s $\boldsymbol{P}_w^t$ and $\boldsymbol{P}_m^t$ are assembled and given by the relations:

$$\begin{aligned} \boldsymbol{P}_w^t &\approx \bigwedge_{e=1}^{n_{elm}} \sum_{p=1}^{n_{ep}} n_p^t\, m_{w,p}\, \boldsymbol{N}^T \boldsymbol{\xi}_p^t)\, \hat{\boldsymbol{w}}_p^t, \\ \boldsymbol{P}_s^t &\approx \bigwedge_{e=1}^{n_{elm}} \sum_{p=1}^{n_{ep}} (1-n_p^t)\, m_{s,p}\, \boldsymbol{N}^T(\boldsymbol{\xi}_p^t)\, \hat{\boldsymbol{v}}_p^t, \end{aligned} \tag{4.90}$$

respectively. Using the relations, the nodal force vector that corresponds to the prescribed tractions is constructed as:

$$\begin{aligned} \tilde{\boldsymbol{F}}_w^{trac,t} &\approx \bigwedge_{e=1}^{n_{pelm}} \sum_{p=1}^{n_{ebp}} \boldsymbol{N}^T(\boldsymbol{\xi}_p^t)\, \tilde{\boldsymbol{f}}_{w,p}^{trac}, \\ \tilde{\boldsymbol{F}}_m^{trac,t} &\approx \bigwedge_{e=1}^{n_{\tau elm}} \sum_{p=1}^{n_{ebp}} \boldsymbol{N}^T(\boldsymbol{\xi}_p^t)\, \tilde{\boldsymbol{f}}_p^{trac}, \end{aligned} \tag{4.91}$$

for the prescribed pressure and tractions, respectively. Here, n_{ebp} refers to the boundary

particles where traction is prescribed. Applying the time function $\mathcal{T}(t)$ as a multiplier, the prescribed traction vectors can be written as:

$$\begin{aligned} \boldsymbol{F}_w^{trac,t} &= \tilde{\boldsymbol{F}}_w^{trac,t}\,\mathcal{T}(t)\,, \\ \boldsymbol{F}_m^{trac,t} &= \tilde{\boldsymbol{F}}_m^{trac,t}\,\mathcal{T}(t)\,, \end{aligned} \tag{4.92}$$

respectively. Gravitational body forces for the fluid and solid phases can be integrated by the relations:

$$\begin{aligned} \boldsymbol{F}_w^{grav,t} &\approx \bigtriangleup_{e=1}^{n_{elm}} \sum_{n=1}^{n_{ep}} \boldsymbol{N}^T(\boldsymbol{\xi}_p^t)\,\boldsymbol{f}_{w,p}^{grav}\,, \\ \boldsymbol{F}_m^{grav,t} &\approx \bigtriangleup_{e=1}^{n_{elm}} \sum_{n=1}^{n_{ep}} \boldsymbol{N}^T(\boldsymbol{\xi}_p^t)\,\boldsymbol{f}_p^{grav}\,, \end{aligned} \tag{4.93}$$

respectively. Internal forces due to pore pressure and total stress are given by the relations:

$$\begin{aligned} \boldsymbol{F}_w^{int,t} &\approx \bigtriangleup_{e=1}^{n_{elm}} \sum_{n=1}^{n_{ep}} \boldsymbol{B}^T(\boldsymbol{\xi}_p^t)\,p_p^t\,\boldsymbol{I}\,\Omega_p^t\,, \\ \boldsymbol{F}_m^{grav,t} &\approx \bigtriangleup_{e=1}^{n_{elm}} \sum_{n=1}^{n_{ep}} \boldsymbol{B}^T(\boldsymbol{\xi}_p^t)\,\boldsymbol{\sigma}_p^t\,\Omega_p^t\,, \end{aligned} \tag{4.94}$$

respectively. The nodal vector of interaction forces or the drag force is calculated using the relation:

$$\boldsymbol{F}_w^{drag,t} = \boldsymbol{Q}^t\,(\boldsymbol{w}^t - \boldsymbol{v}^t)\,, \tag{4.95}$$

where, $\boldsymbol{Q}$ is a lumped matrix, whose individual constituents, q_i are integrated using the relation:

$$q_i \approx \sum_{p=1}^{n_{ep}} \frac{n_p^t\,m_{w,p}\,g}{k_p^t}\,\boldsymbol{N}(\boldsymbol{\xi}_p^t)\,. \tag{4.96}$$

The discrete momentum equations can hence be written as:

$$\boldsymbol{M}_w^t\, \boldsymbol{a}_w^t = \boldsymbol{F}_w^{trac,t} + \boldsymbol{F}_w^{grav,t} - \boldsymbol{F}_w^{int,t} - \boldsymbol{F}_w^{drag,t}\,, \tag{4.97}$$

and,

$$\boldsymbol{M}_s^t\, \boldsymbol{a}_s^t = -\bar{\boldsymbol{M}}_w^t\, \boldsymbol{a}_w^t + \boldsymbol{F}_m^{trac,t} + \boldsymbol{F}_m^{grav,t} - \boldsymbol{F}_m^{int,t}\,, \tag{4.98}$$

for the fluid and solid phases, respectively. The Equation 4.97 above is solved for nodal accelerations of the fluid phase, $\boldsymbol{a}_w^t$ by the relation:

$$\boldsymbol{a}_w^t = \boldsymbol{M}_w^{t,-1} \left[\boldsymbol{F}_w^{trac,t} + \boldsymbol{F}_w^{grav,t} - \boldsymbol{F}_w^{int,t} - \boldsymbol{F}_w^{drag,t}\right]. \tag{4.99}$$

Once $\boldsymbol{a}_w^t$ is calculated, it is subsequently used to calculate the nodal acceleration vector of solid phase, $\boldsymbol{a}_s^t$ by the relation:

$$\boldsymbol{a}_s^t = \boldsymbol{M}_s^{t,-1} \left[-\bar{\boldsymbol{M}}_w^t\, \boldsymbol{a}_w^t + \boldsymbol{F}_m^{trac,t} + \boldsymbol{F}_m^{grav,t} - \boldsymbol{F}_m^{int,t}\right]. \tag{4.100}$$

Nodal velocities for the fluid and solid phases are calculated as:

$$\bar{\boldsymbol{M}}_w^t\, \boldsymbol{w}^{t+\Delta t} = \bigwedge_{e=1}^{n_{elm}} \sum_{p=1}^{n_{ep}} n_p^t\, m_{w,p}\, \boldsymbol{N}^T(\boldsymbol{\xi}_p^t)\, \hat{\boldsymbol{w}}_p^{t+\Delta t}\,, \tag{4.101}$$

and,

$$\bar{\boldsymbol{M}}_s^t\, \boldsymbol{v}^{t+\Delta t} = \bigwedge_{e=1}^{n_{elm}} \sum_{p=1}^{n_{ep}} (1 - n_p^t)\, m_{s,p}\, \boldsymbol{N}^T(\boldsymbol{\xi}_p^t)\, \hat{\boldsymbol{v}}_p^{t+\Delta t}\,, \tag{4.102}$$

where, the updated particle velocities based on the nodal accelerations are given by the following equations:

$$\begin{aligned} \hat{\boldsymbol{w}}_p^{t+\Delta t} &= \hat{\boldsymbol{w}}_p^t + \sum_{i=1}^{n_{nodes}} \Delta t\, N_i(\boldsymbol{\xi}_p^t)\, \boldsymbol{a}_{w,i}^t\,, \\ \hat{\boldsymbol{v}}_p^{t+\Delta t} &= \hat{\boldsymbol{v}}_p^t + \sum_{i=1}^{n_{nodes}} \Delta t\, N_i(\boldsymbol{\xi}_p^t)\, \boldsymbol{a}_{s,i}^t\,, \end{aligned} \tag{4.103}$$

respectively, for the fluid and solid accelerations. Using the relationship, incremental nodal displacements are calculated only for the solid phase by:

$$\Delta \boldsymbol{u}^{t+\Delta t} = \Delta \boldsymbol{v}^{t+\Delta t}\, \Delta t\,. \tag{4.104}$$

Strains in the solid phase are computed using the relation:

$$\boldsymbol{\varepsilon}_p^{t+\Delta t} = \boldsymbol{B}(\boldsymbol{\xi}_p^t)\, \Delta \boldsymbol{u}_e^{t+\Delta t}\,, \tag{4.105}$$

where, $\Delta \boldsymbol{u}_e^{t+\Delta t}$ has the following components:

$$\Delta \boldsymbol{u}_e^{t+\Delta t} = \begin{bmatrix} \Delta u_{11} & \Delta u_{12} & \cdots & \Delta u_{n_{en1}} & \Delta u_{n_{en2}} \end{bmatrix}^T\,. \tag{4.106}$$

While effective stress, $\boldsymbol{\sigma}_p^{'t+\Delta t}$ is calculated on the particles using a constitutive model of choice, and the pore pressure is updated on the particle via relation:

$$p_p^{t+\Delta t} \approx p_p^t + \Delta t\, \frac{K_{w,p}}{n_p^t} \left[(1 - n_p^t)\, \boldsymbol{B}(\boldsymbol{\xi}_p^t)\, \boldsymbol{v}_e^{t+\Delta t} + n_p^t\, \boldsymbol{B}(\boldsymbol{\xi}_p^t)\, \boldsymbol{w}_e^{t+\Delta t} \right] \boldsymbol{I}\,. \tag{4.107}$$

Total particle stress can now be updated using the relation:

$$\boldsymbol{\sigma}_p^{t+\Delta t} = \boldsymbol{\sigma}_p^{'t+\Delta t} + p_p^{t+\Delta t}\, \boldsymbol{I}\,. \tag{4.108}$$

The particle volumes are updated using the relation:

$$\Omega_p^{t+\Delta t} = \left(1 + tr(\varepsilon_p^{t+\Delta t})\right)\, \Omega_p^t, \qquad \text{where,} \qquad tr(\varepsilon_p^{t+\Delta t}) = \Delta\varepsilon_{11} + \Delta\varepsilon_{22} + \Delta\varepsilon_{33}\,. \tag{4.109}$$

Using the updated incremental particle displacement, the new position of the particle is calculated using the relation:

$$\boldsymbol{x}_p^{t+\Delta t} = \boldsymbol{x}_p^t + \sum_{i=1}^{n_{nodes}} N_i(\boldsymbol{\xi}_p^t)\, \Delta \boldsymbol{u}_i^{t+\Delta t}\,. \tag{4.110}$$

With this, it is implied that the current time step has concluded. The bookkeeping for the particles is updated, the grid is reset, and the computation is advanced to the next step.

4.5 One-dimensional consolidation example in CPDI

Parameter	Value
Young's Modulus [kPa]	10,000
Poisson's ratio [-]	0
Bulk Modulus of Water [GPa]	2.1
Porosity [-]	0.3
Permeability [m/s]	1×10^{-3}
Number of Particles	400, 1,600, 3,600

Table 4.1: Simulation parameters for one-dimensional consolidation problem

The well-known one-dimensional consolidation simulation, based on the one-dimensional consolidation theory after Terzaghi [204], is simulated to verify the implementation of the two-phase CPDI code. Owing to the availability of a closed-form solution, the numerical model's performance can be compared to the expected outcomes. A 1 m tall column of saturated soil is meshed with 400, 1,600, and 3,600 particles, which corresponds to 1, 4, and 9 particles per computational grid background, respectively. For this numerical calculation, a linear elastic model was used. The soil continuum parameters are tabulated in Table 4.1. In the simulation, the full value of the Bulk Modulus of water is assumed. The model's base is completely fixed, while the lateral surfaces are assigned roller boundaries.

A constant stress of 10 kPa is applied to both the soil and pore water portions until the soil reaches its steady state. Since the load is also applied to the pore water continuum, the entire load is carried by the water as the system reaches equilibrium. The pressure applied to the pore water portion of the model is eliminated while the soil stress remains unchanged. This allows water to flow out of the column's head, thereby decreasing pore pressure.

The consolidation coefficient describes the procedure:

$$c_v = \frac{k}{\rho_w g \, (1/E)}, \tag{4.111}$$

where, k is the permeability of the soil, ρ_w is the density of water, g is the acceleration

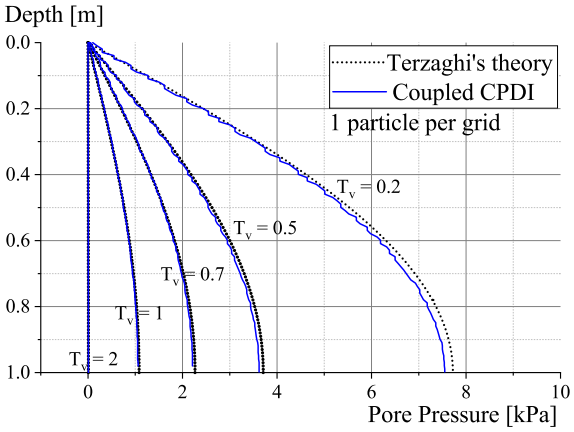

(a) Pore Pressure profile : 1 particle per grid

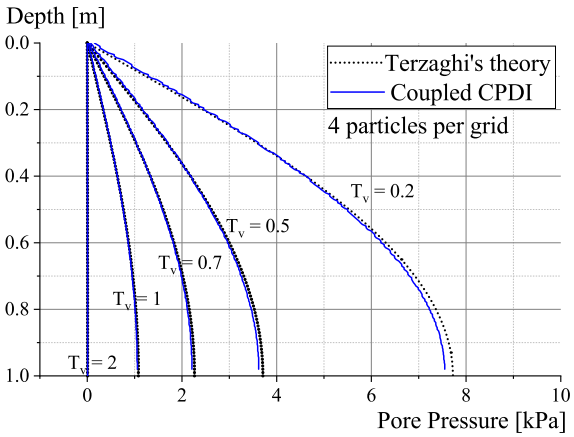

(b) Pore Pressure profile : 4 particle per grid

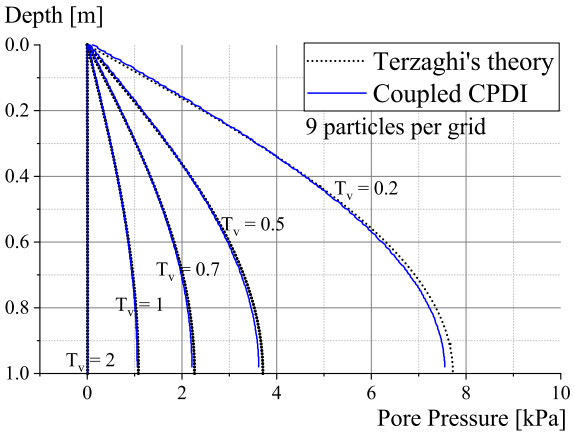

(c) Pore Pressure profile : 9 particle per grid

Figure 4.5: Comparison of pore pressure profiles for the Terzaghi's one-dimensional consolidation test, 1 particle per grid (top), 4 particles per grid (middle), and 9 particles per grid (bottom)

due to gravity, and E is the Young's modulus of soil. The non-dimensional time factor T_v is given by the relation:

$$T_v = \frac{c_v\, t}{h^2}\,, \tag{4.112}$$

where, h is the drainage length.

Figure 4.5 depicts the evolution of pore pressure over time. The outcomes are compared to the analytical solution. It can be seen that, for all models, the coupled CPDI tool provides results that are nearly identical to those of the analytical result. To determine whether the number of particles per grid has a significant effect on the results, a parameter study was conducted by varying the number of particles per grid. Figure 4.5a demonstrates that while the pore pressure versus column depth exhibits some oscillation in the case of one particle per grid (top), this decreases when the number of particles per grid is increased to four, as seen in Figure 4.5b. Figure 4.5c displays a very smooth pore pressure versus depth response when nine particles per grid are considered.

4.6 Concluding remarks

This chapter presented a two-phase one-point MPM formulation capable of modelling fully coupled hydromechanical problems, as well as the numerical treatment of the coupled formulation. This formulation was implemented as an extension to the MPM/CPDI code introduced in Chapter 3. This formulation is required for simulating saturated media in a code that has already demonstrated its ability to capture large deformation. No special treatment is required for the contact elements, as the previously introduced and implemented penalty contact algorithm was found to be capable of handling contact between two saturated continuums or a saturated and dry continuum. Additionally, the absorbent boundaries have been implemented to reduce the number of spurious waves that rebound from the boundaries. Through the simulation of the one-dimensional consolidation problem, a validation of the coupled formulation is presented. This will later be utilised in simulations conducted in Chapter 6. This provides one of the components for the simulation of a saturated continuum applicable to real-world issues.

Chapter 5

Constitutive Modelling

5.1 The UBCSAND Model

The UBCSAND model was developed at the University of British Columbia in order to simulate soil liquefaction during dynamic processes such as earthquake shaking. In this work, the UBCSAND model and the two-phase CPDI code are used to represent the saturated soil continuum. UBCSAND is an effective stress model that simulates the elasto-plastic mechanical behaviour of the sand skeleton. In references [14, 15, 40], the model has previously been used to simulate the behaviour of saturated soil; i.e., sand skeleton and pore water fluid. The plastic shear modifies the soil skeleton volume and, as a result, alters the pore fluid pressure. The changes in pore pressure changes the soil's effective stress.

The model employs a yield surface related to the continuum's stress ratio and a non-associative flow rule. The flow rule models contractive soil behaviour when the stress ratio is less than the angle of phase transformation friction, and dilatant soil behaviour when the stress ratio is greater than the angle of phase transformation friction. The stress ratio η, is proportional to the shear stress on the plane of maximum shear, τ divided by the mean effective stress, (σ'_m) as τ/σ'_m, where the σ'_m is given by the relation $\sigma'_m = \frac{\sigma'_x+\sigma'_y}{2}$. When the stress ratio increases, the soil is loaded, and it decreases when it is unloaded. A change from loading to unloading or vice versa occurs when the sign of the shear stress on the horizontal plane, τ_{xy} reverses. The model's behaviour under unloading and reloading represents pure elastic behaviour. The bulk modulus and shear modulus are functions of the mean effective stress. Yield surface, $d\eta$ depends on the plastic shear modulus (G^p/σ') and the hardening parameter, $d\gamma^p$.

The UBCSAND model can be calibrated using triaxial and simple shear laboratory tests. It can simulate both the drained and undrained behaviours of loose sandy soils. In the case of drained soil, contractive behaviour is modelled when the continuum is sheared below the phase transformation angle, ϕ_{cv} and dilatant behaviour is modelled when the continuum is sheared above ϕ_{cv}, and Modelling the excess pore pressure build-up and soil liquefaction can be modelled in the case of undrained soils. The elastic and plastic

response of the model is briefly described below, but readers are referred to the work of Naesgaard [159], from which the UBCSAND model implemented in this work was adapted.

Elastic Response

It is assumed that the model's elastic response is linear, incremental, and isotropic. The behaviour is specified by Hooke's law of elasticity. In this model, the unloading-reloading process follows an elastic path, with the elastic isotropic shear and bulk modulus being functions of the mean effective stress, σ' and atmospheric pressure, P_a, usually taken as 100 kPa. The relationships between elastic moduli are as follows:

$$\begin{aligned} G^e &= K_G^e \cdot P_a \cdot \left(\frac{\sigma'}{P_a}\right)^n , \\ K^e &= K_K^e \cdot P_a \cdot \left(\frac{\sigma'}{P_a}\right)^m , \end{aligned} \tag{5.1}$$

where, G^e and K^e are the elastic shear and bulk modulii. Exponents m and n are the elastic bulk and shear modulus exponents, respectively and are taken to be around 0.5. Mean effective normal stress, σ' is given by the relation $\sigma' = \frac{\sigma'_x + \sigma'_y}{2}$. The shear modulus number, K_G^e is a function of relative density. It can be estimated using the relation $K_G^e = 21.7 \cdot A \cdot \left(N_{1_{60}}\right)^{0.33}$, with $N_{1_{60}}$ being the Standard Penetration Test (SPT) blowcount standardised to 60% energy and corrected for overburden. Here, A is a factor ranging between 15 to 20. Where the shear wave velocity (V_s) data is available, the correlation $K_G^e = \rho\, V_s^2 / P_a \cdot (\sigma' / P_a)^n$ can be used, in which, ρ is the soil density.

Plastic Response

Plastic volumetric (ϵ_v^p) and shear (γ_s^p) strains are generated when the stress state is on the yield surface. Below the phase transformation angle, the plastic volumetric strains are contractive and above, they are dilatant. The flow rule is specified by the following relation:

$$\frac{d\epsilon_v^p}{d\gamma_s^p} = -tan(\psi) , \tag{5.2}$$

where, $-sin(\psi) = (sin(\phi_{cv}) - \eta)$, the dilation angle is given by ψ, η corresponds to the developed stress ratio with $\eta \leq sin(\phi_f)$, where ϕ_f is the peak friction angle. Raising the yield surface ($d\eta$) is carried out through the plastic shear modulus (G^p) and the plastic shear strain increment ($d\gamma_s^p$) via the relation:

$$d\eta = \frac{d\gamma_s^p \cdot G^p}{\sigma'} . \tag{5.3}$$

The plastic shear modulus is defined by a hyperbolic relationship and is a function of the developed stress ratio (η) and failure stress ratio (η_f). In references [62, 117, 150], hyperbolic relations have been used successfully to capture the shear stress - shear strain response of granular soils. The sign of the stress ratio is determined by the sign of the horizontal shear stress. Positive and negative values are recorded independently. As a result, the plastic hardening is characterised by kinematic rather than isotropic behaviour. For initial loading (or virgin loading), the following relation is adopted:

$$G^p = G_i^p \cdot \left(1 - \frac{\eta}{\eta_f} \cdot R_f\right)^2 , \tag{5.4}$$

where, G_i^p is the plastic shear modulus at $\eta = 0$ and R_f is a constant that is used to truncate the hyperbolic curve to prevent the overprediction of strength at failure. It varies between 0.7 and 1.0.

Plastic strain rates are governed by yield loci, which are assumed to be radial lines emanating from the origin of stress space. For initial loading, the yield locus is determined by the soil's current stress state. As the shear stress increases, so does the stress ratio, activating the primary yield surface in accordance with an isotropic hardening rule given by the relationship:

$$\eta_d = \frac{\gamma_s^p}{\left[\left(\frac{\sigma'}{G^e}\right) + \left(\frac{\gamma_s^p R_f}{\eta}\right)\right]} . \tag{5.5}$$

Consequently, the yield surface is dragged to the new location, expanding the model's elastic zone. In this model, the ultimate strength and stress state are assumed to be determined by a Mohr-Coulomb type failure criterion, i.e.,

$$f_f = \sigma_1' - \sigma_3' N_{\phi_f} + 2\,c\,\sqrt{N_{\phi_f}} , \tag{5.6}$$

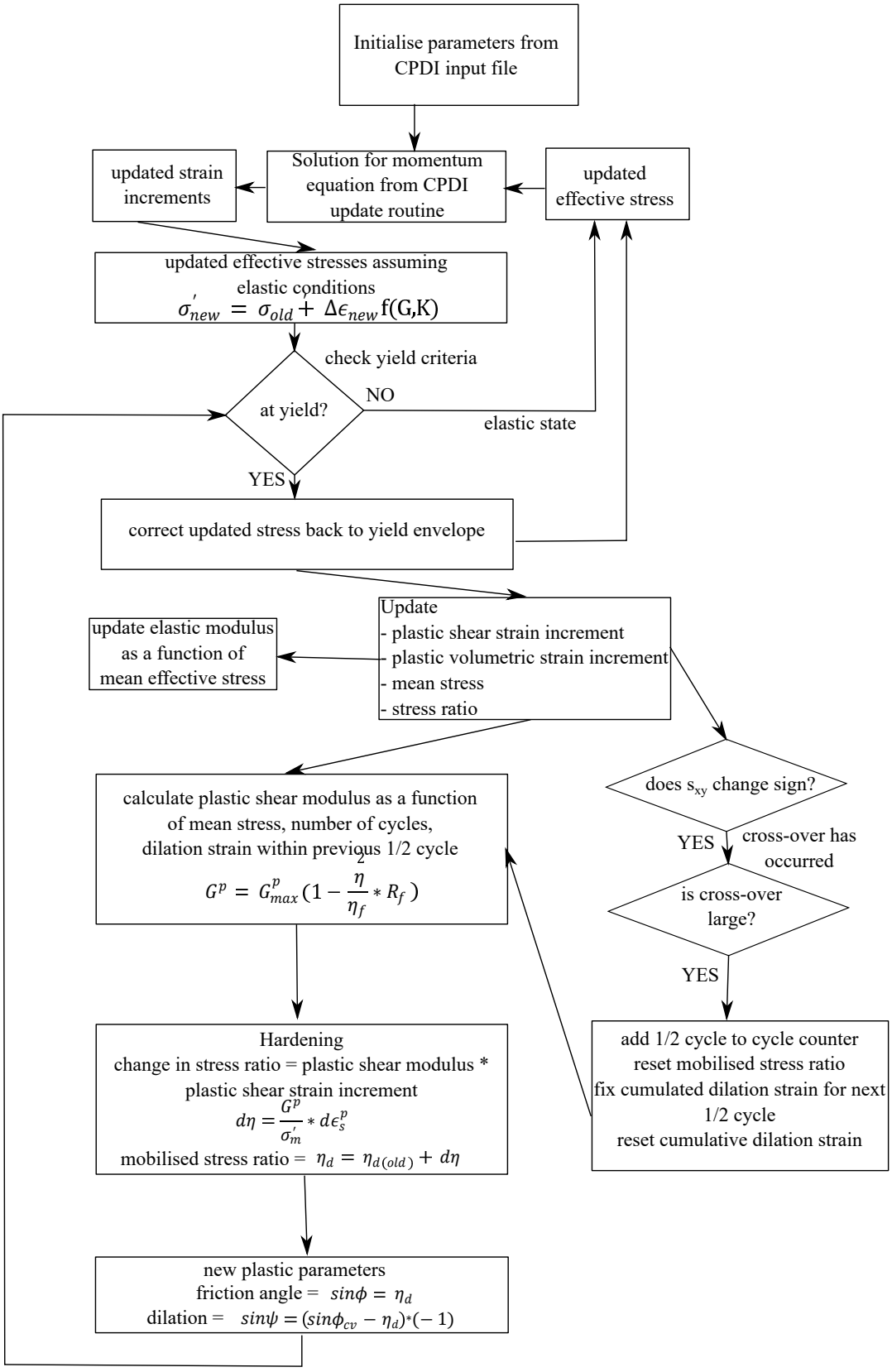

Figure 5.1: Flowchart for one computational step using the UBCSAND Model in CPDI, adapted from [159]

with σ_1' and σ_3' being the effective major and minor principal stresses, respectively. The parameter c is the cohesion, and N_{ϕ_f} is given by the relation:

$$N_{\phi_f} = \frac{1 + sin(\phi_f)}{1 - sin(\phi_f)}, \tag{5.7}$$

in which, ϕ_f is the peak friction angle. In addition to the physical parameters, parameters $hfac_1$ through $hfac_6$ are introduced to control plasticity hardening and hysteresis loop details. These hardening factors affect the following: number of cycles required to initiate liquefaction; shape of pore pressure rise with the number of cycles; dilatation characteristics to control the post-trigger response; secondary dilatation characteristics after triggering failure; and failure envelope pull-down below ϕ_{cv} upon unloading.

Figure 5.1 depicts the flowchart for a single computational step utilising the UBCSAND model. For a detailed description of the model, please see references [14, 15, 40, 159, 183].

5.2 Verification of constitutive law

Reference [159] provides the FLAC's FISH implementation of the UBCSAND model (UBCSAND1v02). While the code can be utilised within the commercial geotechnical software FLAC (Fast Lagrangian Analysis of Continua), a direct and clean implementation within the CPDI code is not possible. To achieve this, the FISH code was translated into FORTRAN. This allowed for a CPDI-compliant implementation that was optimised. This in-house implementation route allowed for the utilisation of the existing Mohr-Coulomb failure criterion with the implementation of the UBCSAND as an add-on.

Implementing the constitutive law in the CPDI numerical package necessitates rigorous testing of the code. This serves two purposes: i) to confirm the veracity of the implementation of the constitutive law, and ii) to ascertain whether the constitutive law functions as expected within the framework of the two-phase CPDI code.

Element test

In order to test the implementation of the constitutive law, a 1 gauss point finite element code was developed and the UBCSAND constitutive law was implemented. In their work, Makra [142] validated the UBC3D-PLM Constitutive law, an advanced version of the UBCSAND model implemented in PLAXIS™, a commercial finite element

$N1_{60}[-]$	$m_e[-]$	$n_e[-]$	$n_p[-]$	$K_G^e[-]$	$K_B^e[-]$
7.4	0.5	0.5	0.4	845.2	591.6
$K_G^p[-]$	$\phi_{pt}[^\circ]$	$\phi_f[^\circ]$	$c[kPa]$	$Pa[kPa]$	$\sigma_t[kPa]$
238.8	33	33.7	0	100	0
$hfac_1[-]$	$hfac_2[-]$	$hfac_3[-]$	$hfac_4[-]$	$hfac_5[-]$	$hfac_6[-]$
0.45	0.1	1.0	0.6	1.0	0.95

Table 5.1: UBCSAND model parameters for Nevada Sand

widely used in geotechnical engineering. Fraser River sand, and its corresponding parameters, was used to test the implementation of the constitutive law. Reference [142] provided the calibrated parameters for the loose sand. Both the PLAXIS™ implementation and the CPDI implementation utilise nearly identical parameter sets. Therefore, the provided parameters were utilised. The relative density, D_r of the loose sand was 40%. The K_0 value was set to 0.46, and the test's cyclic stress ratio (CSR) was set to 0.08. The element test parameters are tabulated in Table 5.1.

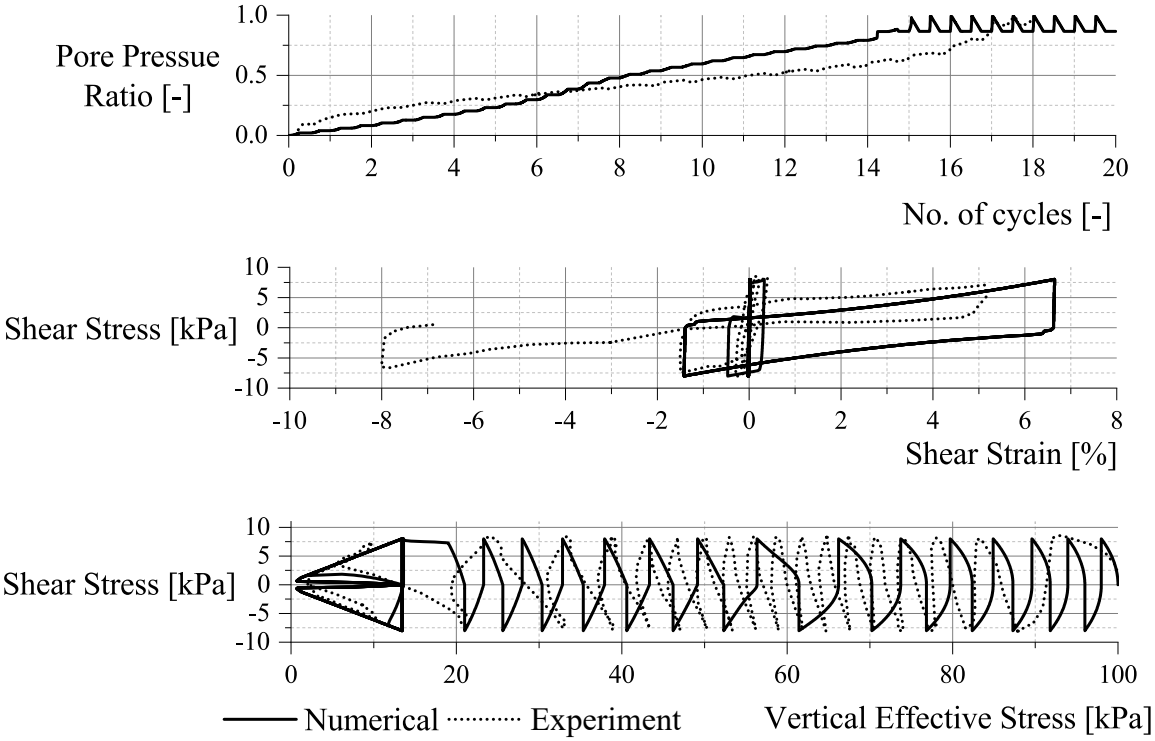

Figure 5.2: Cyclic undrained Direct Simple Shear (DSS) test for UBCSAND Numerical model and Laboratory test; I_d = 40%, CSR = 0.08, K_0 = 0.46

Figure 5.2 shows the results of the element test that was conducted. When compared to the experiment, it is evident that the questioned model is capable of capturing the completed liquefaction of the soil and the excess pore pressure ratio within a reasonable range. The results shown in Figure 5.2 from reference [142] are comparable to those depicted in this figure. Due to the two models' implementations of hardening factors being different, it is not reasonable to expect that the results of the element test conducted here will be exactly comparable to the results reported in the reference [142]. After confirming that the implementation for an element test was accurate, additional dynamic problems are selected and evaluated to validate the implementation of the constitutive models. The objective was to ensure that the element test implementation was correct, and could be considered fulfilled.

5.3 Shake Table Test

The classic shake table benchmark test was simulated using the UBCSAND model after performing the element test. To alleviate concerns regarding the liquefaction susceptibility of large embankment dams, centrifuge tests were commissioned to investigate the behaviour of saturated soils under the high confining stresses encountered in deep deposits [77]. One of the most important factors contributing to the earthquake resistance of embankment dams is liquefaction. Despite the fact that there have been no historical observations of liquefaction at greater depths (i.e., greater than 30 m [222], which suggests that there would be no significant excess pore pressure response under dynamic loads), corrective measures would be required if this were not the case.

There have been numerous centrifuge tests conducted to examine the development of soil liquefaction, including both homogeneous and multi-layered samples. However, the majority of these tests simulated shallow deposits (between 6 and 15 m). Prior

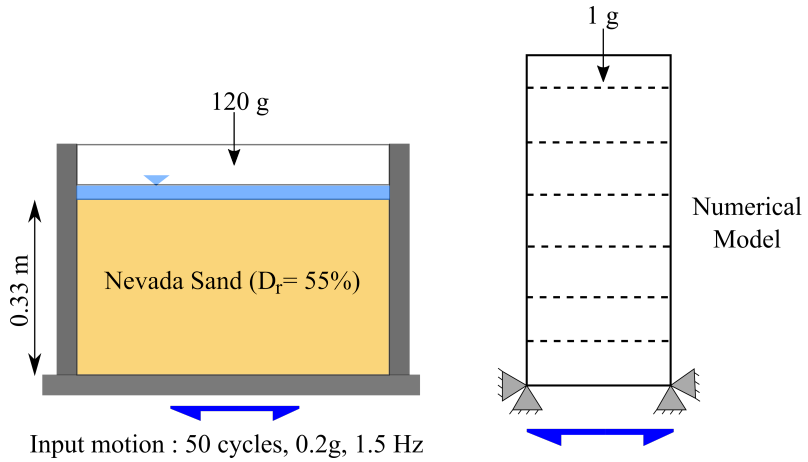

Figure 5.3: Diagram depicting the Shake Table Test

$N1_{60}[-]$	$m_e[-]$	$n_e[-]$	$n_p[-]$	$K_G^e[-]$	$K_B^e[-]$
10.7	0.5	0.5	0.5	800	1100
$K_G^p[-]$	$\phi_{pt}[^\circ]$	$\phi_f[^\circ]$	$c[kPa]$	$Pa[kPa]$	$\sigma_t[kPa]$
500	31	32	0	100	0
$hfac_1[-]$	$hfac_2[-]$	$hfac_3[-]$	$hfac_4[-]$	$hfac_5[-]$	$hfac_6[-]$
0.3	0.85	1.0	0.6	1.0	0.95

Table 5.2: UBCSAND model parameters for Nevada Sand

to the work described in reference [77], either field or laboratory tests provided scant information on the development of liquefaction under greater confining stresses. As they are 1 g tests, laboratory model tests conducted under controlled conditions are not representative of field conditions. Due to the high dependence of soil behaviour on stress, these miniature models cannot adequately represent reality. In contrast, centrifuges utilise a high acceleration field that preserves the stress-strain response of the prototype soils and can provide a more accurate representation of the field behaviour. When such models are subjected to a controlled base motion, validation of numerical approaches can be accomplished. In order to accomplish this, the shake table tests described in reference [77] were simulated.

Byrne and colleagues [40] performed the numerical modelling of the shake table depicted in Figure 5.3 by combining FLAC and UBCSAND. The column was subjected to a vertical centrifugal acceleration of 120 g as well as a horizontal cyclical load of 0.2 g at a frequency of 1.5 Hz. Figure 5.3 also depicts the numerical model corresponding to the 1 g prototype that was used for this study. It was comprised of 0.33 metres of uniform, saturated Nevada sand with an assumed initial relative density of D_r = 55%, which corresponded to an effective height of 38 metres under the centrifuge's acceleration. The centrifuge study's horizontal loading scheme was adopted for the numerical model as well. Table 5.2 summarises the simulation parameters. While the first two rows of parameters were previously defined in terms of well-established properties, the third row contains calibration parameters that fine-tune the stress-strain details. The viscosity of the experiment's fluid was sixty times that of water. The water table is at the surface of the model, and no surface surcharge was applied. At the base, the maximum initial effective stress corresponded to 380 kPa.

The prototype CPDI models contained 468 background grid elements and 3,429 particles. The purpose of this simulation was to determine whether or not a one-dimensional representation could accurately represent the experiment. To enforce simple shear and, by extension, uniform pressure and effective stresses along each horizontal layer of particles, the particles on the left and right boundaries were "tied together". Vertical strains were the only cause of volumetric strains. Secondary response modes such as rocking were omitted. The centrifuge's spin-up was modelled by progressively increasing gravitational forces. This gradually established the initial stresses and pore

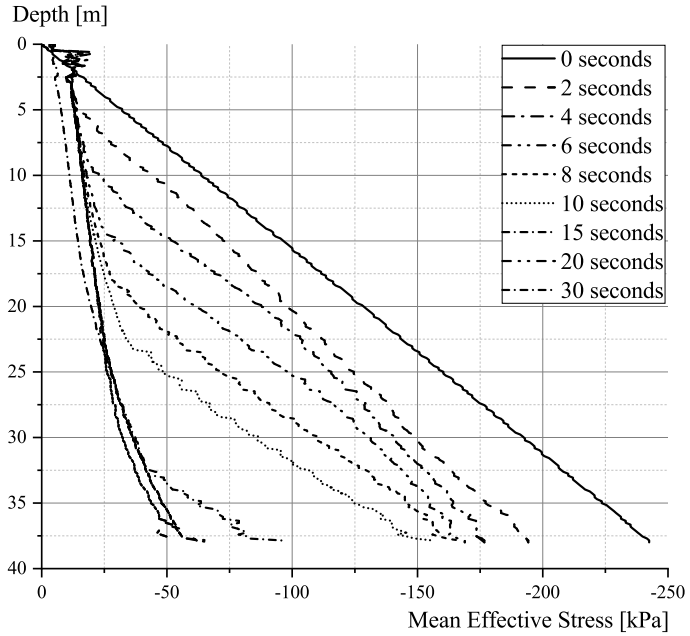

Figure 5.4: Mean Effective Stress throughout the column at various simulation stages

pressures over the course of 20 seconds and ensured that the continuum did not fail due to gravitational loading and that any stress waves that may have been generated were given sufficient time to dissipate. Similar to the experimental model, the water table in the computational model was located at the model's surface. Initial saturation, S_r was not measured for the experimental models, and in this work, one hundred percent ($S_r = 100\%$) has been assumed. Reference [40] however suggests that assumed saturation values of 98.5% before spin-up were found to provide the best agreement with Rensselaer Polytechnic Institute (RPI) model measurements.

The particles were subjected to the acceleration effects via d'Alembert's principle. The momentum equations were integrated using a forward-Euler time-stepping algorithm with a nominal 1 percent Particle-in-Cell damping [160] applied when calculating the particle velocities of both phases. In contrast to reference [40], interface elements were not implemented to account for potential silo effects caused by soil interaction with the walls of the container.

Figure 5.4 depicts the predicted effective stress variation with depth, which demonstrates the decrease in mean effective stress at different times. Since effective stresses were not recorded during the experiment, the simulation results provide insight into the development of effective stresses in the column during simulation. It should be noted that the numerical model captured the experimentally observed decrease in recorded stress rate at different heights of the column [40, 77]. The trend of top-down liquefaction reported by Gonzalez et al. [77] was also predicted by the CPDI model. Near the conclusion of the simulation, when the effective stresses were close to zero, numerical instabilities arose at the column's top. Because the increase in pore pressures was di-

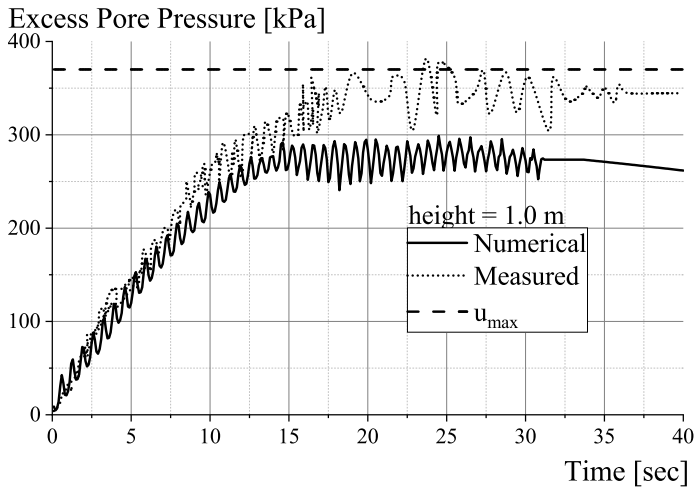

(a) Evolution of Excess Pore Pressure at height 1.0 m

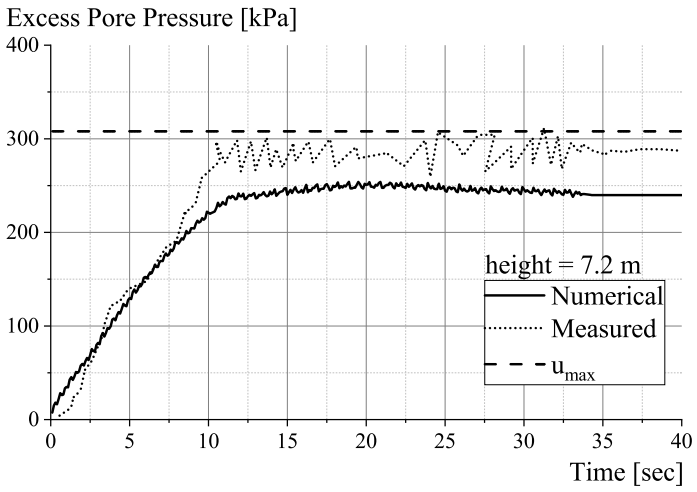

(b) Evolution of Excess Pore Pressure at height 7.2 m

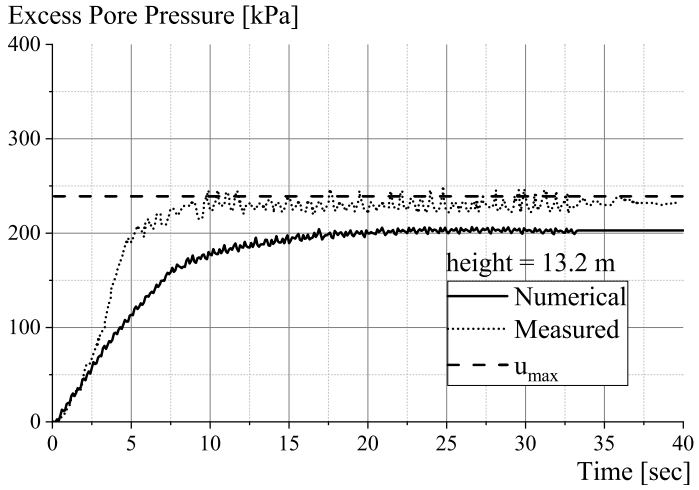

(c) Evolution of Excess Pore Pressure at height 13.2 m

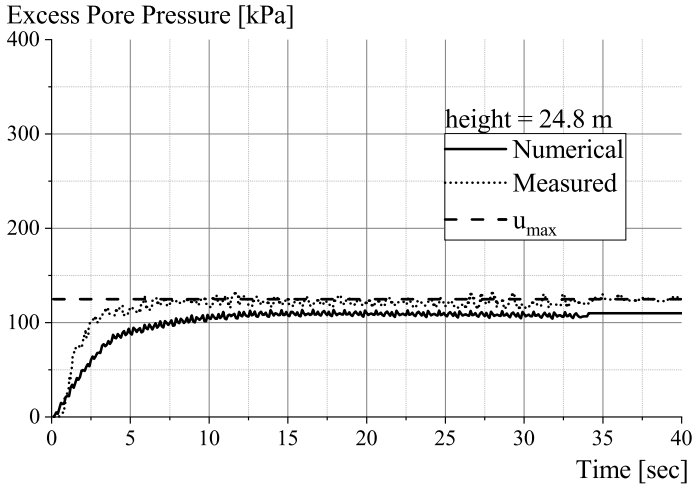

(d) Evolution of Excess Pore Pressure at height 24.8 m

Figure 5.5: Evolution of Excess Pore Pressure at heights: a) 1 m and b) 7.2 m, (upper row), c) 13.2 m and d) 24.8 m (lower row)

rectly proportional to the decrease in effective stresses, it is reasonable to conclude that the predictions were consistent with the experimental findings.

Comparing the experimental results presented in reference [40] to the predicted excess pore pressure evolution plotted in Figure 5.5 at different heights reveals the CPDI's ability to reproduce the rate of liquefaction. In general, Figure 5.5 demonstrates that the maximum excess pore pressure predicted by the numerical solution is lower than what was observed in the experiment. This is consistent with the fact that the effective stresses in these regions did not reach zero. This discrepancy can probably be eliminated by calibrating the parameters to better match the experimental values.

Figure 5.5c demonstrates, for instance, that the simulated rate of generation of excess pore pressure corresponding to a height of 13.2 m is initially close to what had been measured experimentally until 2.5 seconds. The rate of generation of excess pore pressures deviates from the experiment thereafter, resulting in a lower final excess pore pressure than measured. In addition to the different predicted excess pore pressures, the predicted times at which the excess pore pressures remained constant tended to vary. At a height of 1 m, as depicted in Figure 5.5a, the predictions indicated a more rapid increase to a constant pore pressure than was actually observed. The minute fluctuations in pore pressure suggest that the effective stresses were not zero. The rationale for this is that pore pressures were calculated as a contribution of fluid strains and mixture strains, i.e., changes in mixture strains resulted from the variation in pore pressures and effective stress. Despite differences, the comparisons in this section demonstrate that the two-phase CPDI method incorporating the UBCSAND model were able to capture the liquefaction phenomenon with a reasonable degree of accuracy.

Figure 5.5d demonstrates that the excess pore pressure generation rate corresponds to the experiment for the first few seconds, but then begins to deviate. As shown in Figure 5.5c, the predicted final pore pressures are also lower. Notably, the CPDI model is able to capture the different rate of excess pore pressure generation, depending on the depth of measurement, with a higher rate observed at the top of the model, where the stress state is considerably lower, than in the lower portions, where the stress state is significantly higher. Figure 5.5b demonstrates that for the first 10 seconds of simulation, the rate of excess pore pressure generation from the CPDI model and the experiment are comparable. As observed at other depths, the predicted final excess pore pressure is less than the measured value.

Effect of hydraulic conductivity on liquefaction

Figure 5.5 demonstrates that the CPDI model predicts slightly lower excess pore pressure. Consequently, using a 1-D, 38-element finite element model of the shake table test, the dependence of excess pore pressure on hydraulic conductivity was studied. Again, the UBCSAND model with parameters for Nevada sand was adopted.

Equation describing the 1-D model that avoids wave reflections from vertical boundaries:

$$\frac{\partial \sigma_{xy}}{\partial y} + \rho \frac{\partial u_{base}}{\partial t} = \rho \frac{\partial u}{\partial t}, \tag{5.8}$$

and,

$$\frac{\partial \sigma'_{yy}}{\partial y} + \rho' g = \bar{\rho} \frac{\partial v}{\partial t} + \frac{\rho_w g}{k} v, \tag{5.9}$$

where, σ_{xy} is the shear stress, $\frac{\partial u_{base}}{\partial t}$ is the base acceleration, and u and v are the x- and y-direction velocities, respectively. The hydraulic conductivity is k. ρ and ρ_w represent

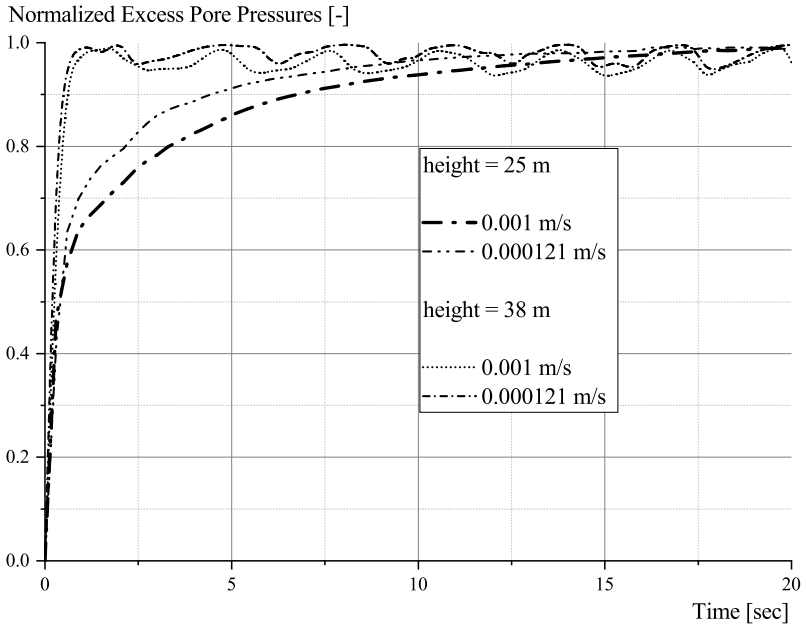

Figure 5.6: Normalised Excess Pore Pressures - Varying hydraulic conductivities for Nevada Sand

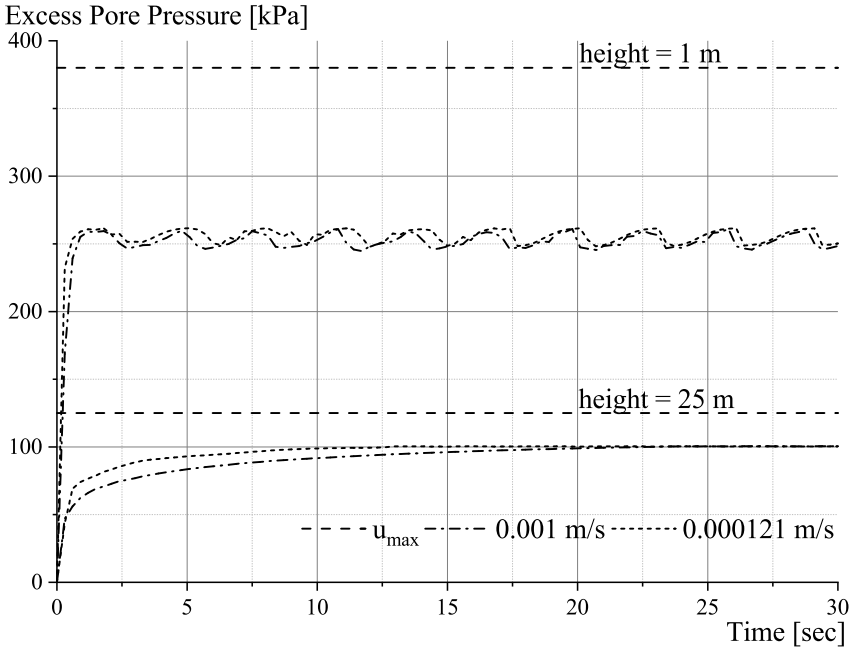

Figure 5.7: One-dimensional test - Effect of hydraulic conductivity on liquefaction

the unit weights of the mixture and water, respectively. $\bar{\rho}$ is given by $\bar{\rho} = \rho' + \frac{\rho}{n}$, buoyant unit weight ρ' is given by $\rho' = \rho - \rho_w$, and n represents the porosity. These differential equations are derived under the assumption of complete incompressibility $(1-n)\frac{\partial v}{\partial y} + n\frac{\partial w}{\partial y} = 0$, where w is the water's velocity. It should be noted that there are no vertical boundaries in this model. Therefore, considering wave reflections from the vertical boundary is unnecessary.

Figure 5.6, which depicts the excess pore pressure development normalised with respect to the initial effective stress, demonstrates that k = 0.001 m/s and 0.000121 m/s capture the salient features of excess pore pressure generation. At a height of 25 m, we observe that the excess pore pressure at a lower k-value causes liquefaction to occur sooner, whereas at a higher k-value, the generated excess pore pressure levels off prior to complete liquefaction occurring. Near the bottom, both permeabilities values causes the soil to undergo liquefaction, which is to be expected given the length of the drainage path. The loading-unloading sequences are reflected in the cyclical variation of pore pressure at the bottom. The faster development of pore pressure in the 1-D model relative to the CPDI model can be attributed to the stricter enforcement of incompressibility. The predicted lower excess pore pressures are consistent with those observed in Figure 5.5 based on these results. Figure 5.7 depicts the excess pore pressure calculated from the 1-D model at heights of 1 m and 25 m.

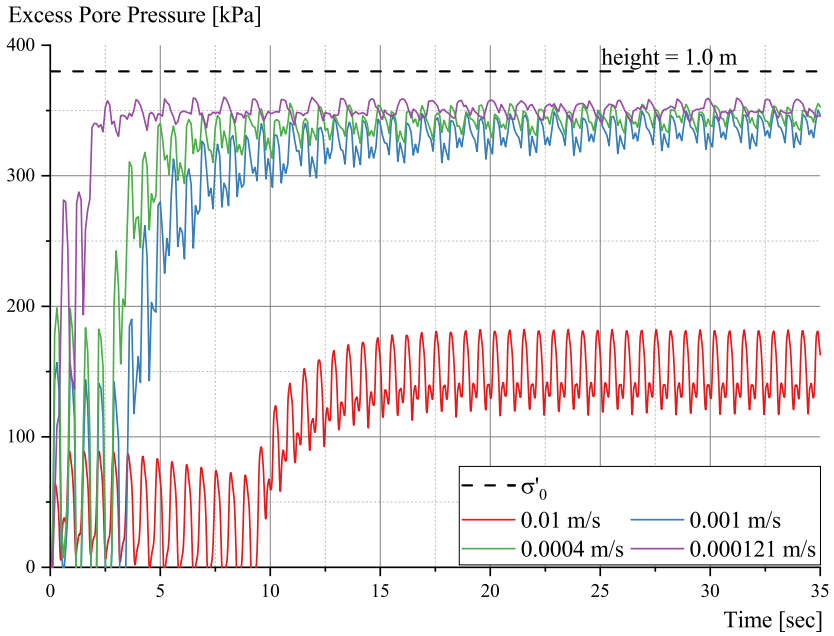

Figure 5.8: Effect of hydraulic conductivity on liquefaction - 2D Model

Figure 5.8 depicts that the exact same test was conducted for the 2-D FE model. When the hydraulic conductivity was low, i.e. 0.01 m/s, the maximum excess pore pressure was approximately half of what was calculated for lower hydraulic conductivities. Similar findings were reported in reference [16]. In this study, the relationship between excess pore pressure and hydraulic conductivity at various fines contents was examined. It was observed that, for a given density, the excess pore pressure increases linearly with decreasing hydraulic conductivity. Using a two-dimensional, 38-element model, analyses were conducted assuming UBCSAND and Nevada sand parameters in order to estimate the computational time with varying hydraulic conductivities. For k = 0.001 m/s, the calculation took approximately 12 minutes, while k = 0.000121 m/s required 55 minutes. To reduce computational time, higher values of k were selected. Reference [151] provides the relationship between hydraulic conductivity and time-step.

It should be noted that the CPDI predictions of the shake table prototype, like those reported in reference [40], correspond to a one-dimensional situation. The experimental setup was in fact a two-dimensional problem. The conditions at the walls of the sand container were not considered as indicated previously, and the assumption of uniform properties may be overly optimistic, despite the fact that the physical test specimen was likely fabricated with great care. Therefore, it is reasonable to anticipate some differences between measurements and predictions. It is essential that the overall characteristics have been captured.

Figure 5.9 illustrates a comparison between the results from the CPDI model and those from the commercial finite element code FLAC, as performed in reference [40]. Compared to the experiments, both FLAC and CPDI were able to capture the rate of increase

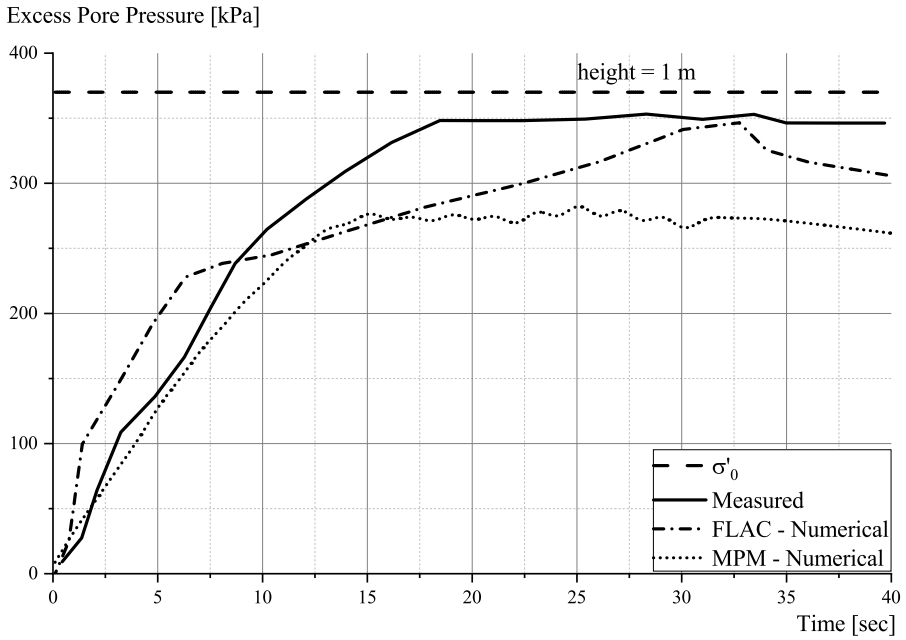

Figure 5.9: Excess Pore Pressure comparison - Numerical: FLAC and CPDI vs. Measured, for Nevada Sand

of pore pressure quite accurately. As predicted by the CPDI simulations, the maximum value of excess pore pressure is lower than both the experimental and FLAC numerical results. FLAC employs the finite difference method (FDM), which permits a more stringent application of the compressibility criterion [101].

5.4 Conclusion

In this chapter, the UBCSAND model, which was initially described in Reference [159], has been presented. The justification for implementing an in-house constitutive law as opposed to using one of the commercially available ones is the flexibility it provides in adapting it to the application at hand and, if necessary, improving it. The implemented model is examined for accuracy using an element test, in which cyclic direct shear tests are conducted. When the results of the numerical model were compared to those of the experiments, it was determined that they were in good agreement. In addition, a dynamic simulation, the shake table test, was conducted and compared to the experimental findings. Additional results of the model are compared favourably to the experimental data in Appendix D. Having gathered all the necessary components for application to a real-world problem, this topic will be covered in the following chapter.

Chapter 6

Contributions towards numerical simulation of pile installation

Vibratory driving of monopiles is not a well-understood offshore pile foundation installation technique, causing engineers to be rather cautious in their applications. In the case of vibratory driving, there is a significant potential for cost and time savings over impact driving. Through the application of two-phase CPDI model together with the UBCSAND constitutive law described in the preceding sections, this chapter attempts to shed more light on the vibratory installation of offshore monopiles.

According to a 2012 report cited in reference [140], approximately three-quarters of offshore wind parks were constructed on monopile foundations. In sandy soils, the use of monopiles for offshore wind farms is likely the most logical option; however, little is known about the installation behaviour due to a lack of visual access and the inability to reliably measure and document changes in the soil state during installation. Changes in the state of the soil surrounding a pile affect its resistance, either positively or negatively. Reference [1] investigated the distinction between the lateral bearing behaviour of vibrated and impact-driven large monopiles in dense sand. Typically, a hammer powered by hydraulics is utilised to install monopiles by impact driving. To drive the pile into the subsoil, several thousand blows must be delivered to it.

While the impact driving method of installation is prevalent due to its cost-effectiveness and overall versatility, i.e. the capability to install the pile to its final installation depth, it is not the only method. An issue with this method of installation is that it induces a high level of noise (pressure waves) in the water, which is harmful to marine life [64]. Although there are methods employed to keep the noise level low, such as using a bubble curtain, isolation casings, and coffer-dams, this only serves to increase operational costs and at times fails to maintain noise emission levels below the prescribed values.

6.1 Vibratory pile installation

Alternatively, the monopile foundations can be installed using vibratory driving. The system consists of a suspended vibrator that clamps onto the driving material and a power unit that supplies the required hydraulic pressure, to provide the adequate clamping force. Frequently, a crane is employed to manipulate and position the suspended vibrator. The crane regulates the system's static weight during the vibratory driving process. When resistance is encountered, the crane can raise the vibrator-pile system or release tension for maximum static force. The majority of experimental and field investigations of vibratory driven piles have concentrated on their axial behaviour [33, 35, 122]. The observations indicate that, compared to impact-driven piles, vibratory-driven piles generally exhibited a lower axial pile capacity and axial stiffness. According to references [87, 122], vibrated piles have higher skin friction and lower pile tip resistance than hammered piles. According to Labenski [122], vibrated piles have a greater capacity in loose and medium-dense soils. This is the result of densification around the pile shaft zone. On the other hand, loosening appears in dense and extremely dense soils, resulting in diminished capacity.

During the vibratory installation of piles, conventional soil dynamics issues such as shear resistance of soils, local densification of soil body, and fluidisation of soil, to name a few, become relevant. When sand is sheared, the grains rearrange and reorient themselves in an effort to occupy a stable position with maximum inter-particle contact. Whether this rearrangement results in densification or loosening dependens on soil-specific parameters and the vibration process. In highly dynamic processes occurring in saturated granular soils, liquefaction or fluidisation is an additional factor that must be considered. When fully saturated soils that have been subjected to cyclic or monotonic loading undergo liquefaction, the shear strength is significantly reduced. Contractive loose sand attains its critical state, resulting in a condition of continuous flow with significant shear distortion and strength decrease. This state is maintained by the soil as long as the acting shear stresses are less than its reduced shear strength [44]. When the soil reaches the critical state, it flows with a constant void ratio, effective mean stress, and deviatoric stress.

Reference [193] investigated the influence of void ratio, confining pressure, and the magnitude of the stress/strain cycle on liquefaction. It was inferred that the liquefaction ceased only after the excitation ceased. Regarding liquefaction, a comparison can be made between the pile and the soil surrounding the pile. Sand deposits with a void ratio above the critical state line exhibited a tendency to contract during shearing, and positive pore pressure development was observed under undrained conditions, resulting in liquefaction. On the other hand, deposits with an initial void ratio below the critical state line exhibited a tendency to dilate upon shear, resulting in a decrease in pore pressure that causes an increase in the effective stress, which in turn increases the strength and stability.

During the vibratory installation of a pile, it is known that pore water pressure increases in a zone surrounding the pile. This is supported by numerous studies, including references [139, 141, 176]. Therefore, the possibility of liquefaction cannot be disregarded. Although the development of excess pore pressure can be modelled using a coupled formulation, the accuracy of the magnitude of generated excess pore pressure and the resulting reduction in effective stresses is dependent highly on the constitutive model used for the soil. Using ABAQUS™ to model the phenomenon, reference [191] implemented a multi-phase formulation that incorporated the hypoplastic soil model [213]. The analysis captured the excess pore pressures as well as the corresponding reduction in effective stress around the pile. A finite element analysis simulating a vibratory-driven pile was presented in [172]. Using the hypoplastic soil model once more, their analyses were able to simulate a liquefaction zone around the pile.

The mechanism of liquefaction has been used to describe the reduced shear strength in saturated soils that makes pile installations possible. According to reference [193], the grains temporarily lose a portion of their interparticle forces and are supported solely by the pore water pressure. High acceleration and amplitude were also reported to significantly increase the development of pore water pressure. For soil grains near the pile shaft experiencing high acceleration amplitudes, the occurrence of soil fluidisation is constant, regardless of the degree of saturation. It was also evident that the formation of excess pore pressure greatly facilitated the process of penetration. However, its magnitude was contingent on the cyclic strain amplitude. It was observed that the amplitude of pile displacement is proportional to the amplitude and mean value of excess pore water pressure [31].

In this study, an effort was made to employ a model capable of capturing the liquefaction effects, so that the phenomena described in the aforementioned literatures are accounted for by the model. In addition, the capability of the code to model the extremely dynamic and complex pile installation is evaluated.

6.2 Numerical simulation of model pile installation

The purpose of the model test, which was originally conducted at Techincal University of Berlin, is to realistically simulate the vibratory driven (and impact driven) pile installation of an open steel pipe pile. According to Remspecher et al. [186], the individual dimensions of geotechnical model tests conducted under 1 g conditions were scaled.

The test apparatus consisted of a steel container with an inner base measuring 1.70 metres by 0.70 metres and a height of 1.15 metres, with an additional drainage layer measuring 0.25 metres at the bottom. The pile has a 20 cm outer diameter, a 4 mm wall thickness, and a final installation depth of 0.87 m. A system of guide rollers positioned atop the container ensured that the pile could only penetrate the glass panel

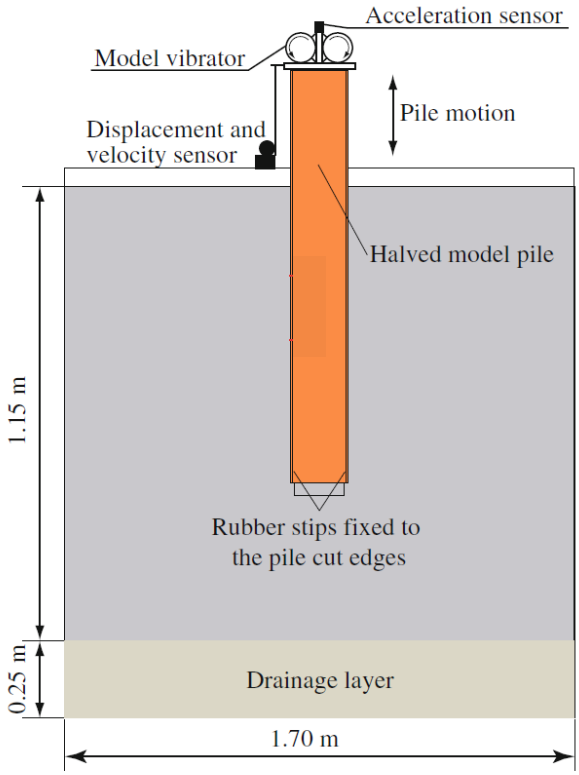

Figure 6.1: Schematic model test set up of the model vibratory pile [186]

in a vertical direction. This also served to prevent the pile from tilting. The design of the model vibrator was based on the mode of operation of large-scale vibrators, in which two sets of centrifugal masses rotate in opposite directions, allowing for a truly vertical acceleration of the pile with no horizontal movement. The model vibrator's centrifugal force was set to 1,670 N at a constant frequency of 23 Hz. Table 6.1 provides the vibration motor's technical specifications. The model vibrator has a total static load of 225 N. Figure 6.1 depicts a diagrammatic summary of the experiment. Reference [186] provides a comprehensive explanation of the utilised testing setup and testing procedure.

Parameter	Value
Working Moment	16.0 kg cm
Centrifugal force, at 23 Hz	1,670 N
Mass of the vibration motor and mounting	22.91 kg
Mass of the pile	19.021 kg
Combined mass of motor, mounting and pile	41.93 kg

Table 6.1: Overview of the vibration motor parameters [186]

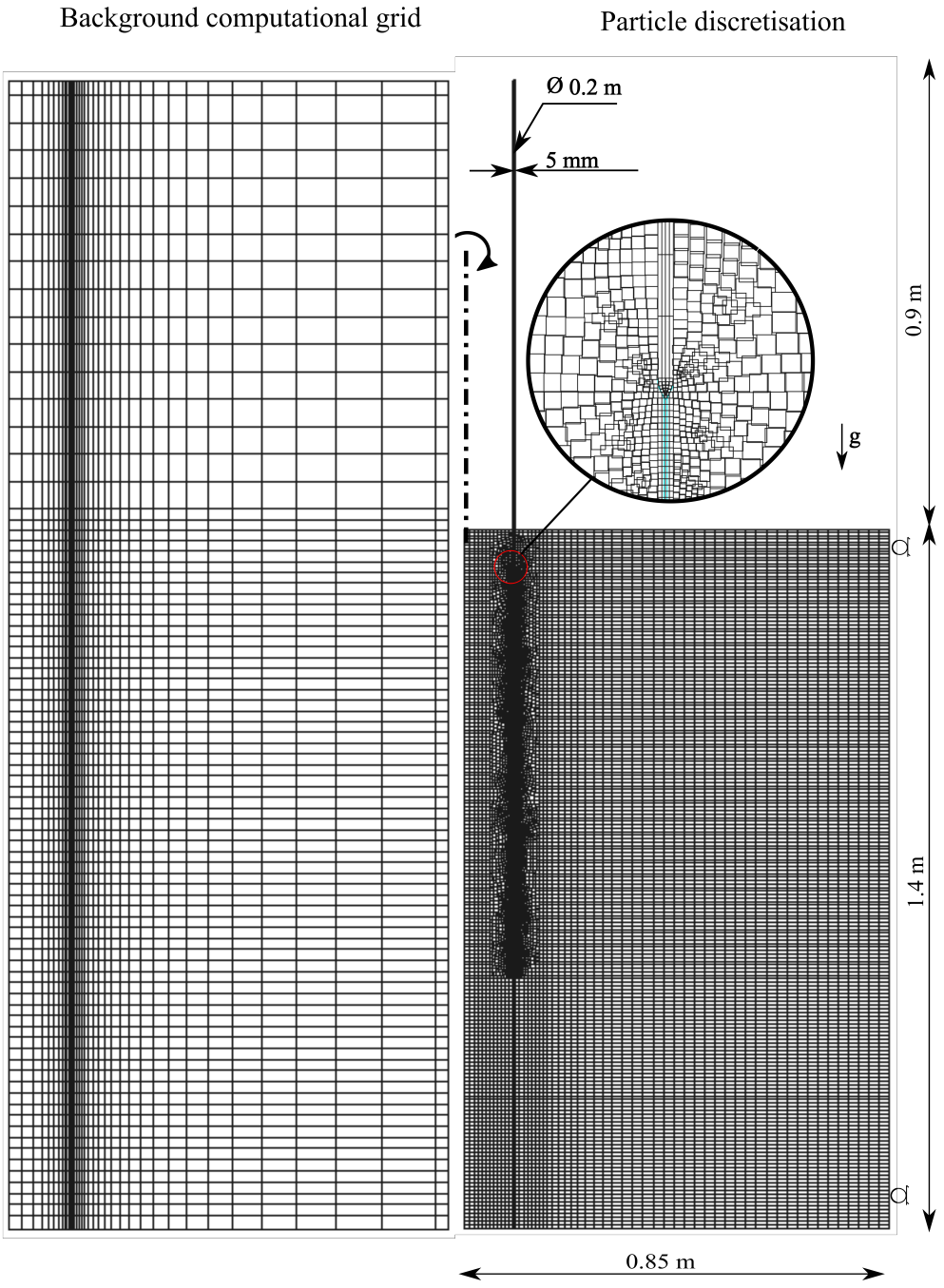

Figure 6.2: Background computational grid discretisation (Left) and Particle discretisation of pile and soil (Right)

Model and boundary conditions

A pile installation was modelled using an axially-symmetric CPDI formulation and the penalty contact procedure described in Chapter 3. For a scaled model test, the predictions were compared to previously published experimental data. In the present study, a multi-phase CPDI model was employed alongside the hypoplastic sand (elaborated in Appendix C) and UBCSAND sand models. The goal was to model the evolution of pore pressure and compare predictions to measured values at a single control point, along with other state parameters including effective stresses.

A hollow model pile with a diameter of 0.2 m was vibrated into an assumed homogeneous and completely saturated soil. It was assumed that initial stresses corresponded to K_0 conditions (K_0 = 0.5) The CPDI model was allowed to reach steady state before a harmonic load was applied. A loading frequency of 23 Hz was directly applied to the pile head. The particles on top of the pile were subjected to a dynamic centrifugal force amplitude of 1,670 N, similar to the experimental setup, as tabulated in Table 6.1 together with a static force of 419.3 N was applied. $F = F_s + F_d = 419.3 + 1670\,sin\,(2\,\pi \cdot 23 \cdot t)$, where t is the time in seconds, provides the relationship for the total force.

The bulk modulus of water was assumed to be 2.2 GPa (K_f). The adopted explicit time-stepping scheme imposed a significant computational burden on such a high value. In the work of Osinov et al. [172], it is demonstrated that a higher effective stress state for the zone of liquefaction is observed when the bulk modulus of water is decreased by a factor of 10. To provide more realistic conditions, a more precise, and therefore higher and complete value was adopted. It was assumed that the pile vibrated only in the vertical direction, with its horizontal movement constrained. The friction coefficient, μ for interface elements used to model contact between the pile and the soil was assumed to be 0.38.

The axially symmetric boundary depicted in Figure 6.2 was discretised using approximately 25,000 particles representing the soil and pile domain, in addition to 1,500 interface elements. More particles were packed near the pile's foot and jacket, requiring an irregular meshing strategy. This allowed the process dynamics and solution

$N1_{60}[-]$	$m_e[-]$	$n_e[-]$	$n_p[-]$	$K^e_G[-]$	$K^e_B[-]$
11.5	0.5	0.5	0.4	1224	1120
$K^p_G[-]$	$\phi_{pt}[^\circ]$	$\phi_f[^\circ]$	$c[kPa]$	$Pa[kPa]$	$\sigma_t[kPa]$
423	31.5	37.5	0	100	0
$hfac_1[-]$	$hfac_2[-]$	$hfac_3[-]$	$hfac_4[-]$	$hfac_5[-]$	$hfac_6[-]$
0.65	0.85	1.0	0.6	1.0	0.95

Table 6.2: UBCSAND model parameters for Berlin Sand

$\phi_c[^\circ]$	$p_t[-]$	$h_s[MPa]$	$n[-]$	$e_{d0}[-]$
31.5	-	230e6	0.3	0.391
$e_{c0}[-]$	$e_{i0}[-]$	$\alpha[-]$	$\beta[-]$	$m_R[-]$
0.688	0.791	0.13	1	4.4
$m_T[-]$	$R[-]$	$\beta_r[-]$	$\chi[-]$	$e_0[-]$
2.2	$1e-4$	0.2	6	-

Table 6.3: Hypoplastic model parameters for Berlin Sand

convergence to be realised more rapidly. The pile was initially embedded 0.1 m, which approximated the experiment-observed pile penetration due to gravity. A continuously updated time-stepping scheme was implemented, wherein the time step was updated every 100 time steps based on the continuously evolving stress-dependent stiffness parameter. As described in the previous section, particle-in-cell damping was assigned a value of 1% for both the solid and fluid phases. Both the hypoplastic soil and UBC-SAND models were adopted using the parameters shown in Tables 6.2 and 6.3, with a relative density of 75% assumed for both constitutive models.

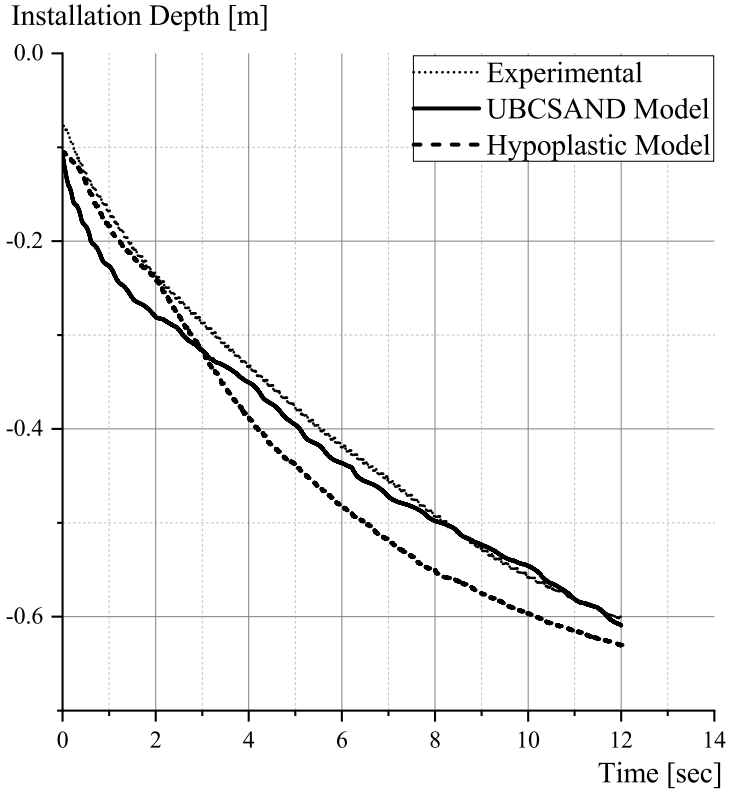

Figure 6.3: Vertical penetration of the vibrated pile - Experimental vs. Numerical (Hypoplastic and UBCSAND Model)

6.2.1 Vibratory installation simulation results for a model pile

Referring to Figure 6.3, there is a reasonable match between the experiment and numerical predictions with both constitutive laws. Together with the CPDI multi-phase formulation, the constitutive models were able to reproduce the measured installation depth over time quite accurately. Both the hypoplastic and UBCSAND models captured the initial relatively high rate of installation and the gradual decrease in rate of penetration, which can be attributed to factors such as the increase in skin friction along the length of the shaft.

Evaluation of effective radial stresses

Figures 6.4a and 6.4b depict the predicted effective radial stresses in the soil with depth at a radius of 1 cm from the axis of rotation (inside the pile) and 12 cm from the axis (outside the pile) corresponding to a vertical pile penetration of 47 cm, respectively. The simulations began with the geostatic stress condition. As the vibration began, a rise in effective radial stress was observed, which can be attributed to the pile's dynamic action on the soil skeleton. Outside the pile, the UBCSAND sand model predicts a maximum increase of 40 kPa, while the increase inside the pile is slightly greater. In contrast, the hypoplastic model predicts an increase of 15 kPa inside the pile and a similar increase in radial stress outside the pile. The location of the pile foot corresponds to the region of maximum stress. As anticipated, the radial stresses surpass the K_0 values.

During the vibration process, high stresses were observed under the pile's tip, with a zone of elevated stresses surrounding the pile's location $3D$ to $4D$ distance from the center line. This result agrees well with the work of reference [141], who calculated a comparable response. Referring to Figure 6.4, the same elevated stress response is observed on the exterior of the pile. For the UBCSAND predictions, a similar trend is observed both inside and outside the pile, but the magnitude of the effective radial stress is significantly greater than that corresponding to K_0 conditions. This is due to the fact that the hypoplastic sand model accounts for changes in the void ratio. Eventually, the stress distribution beneath the pile followed the geostatic distribution.

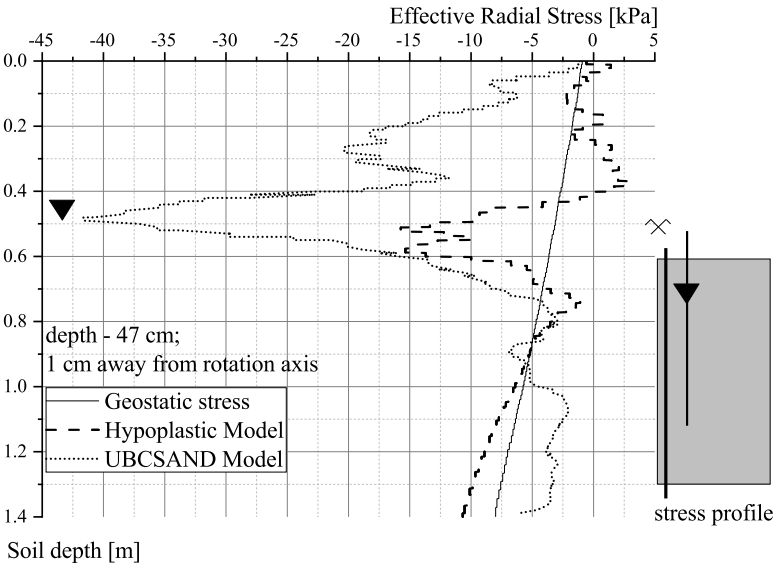

(a) Effective Radial Stress distribution inside vibrated pile

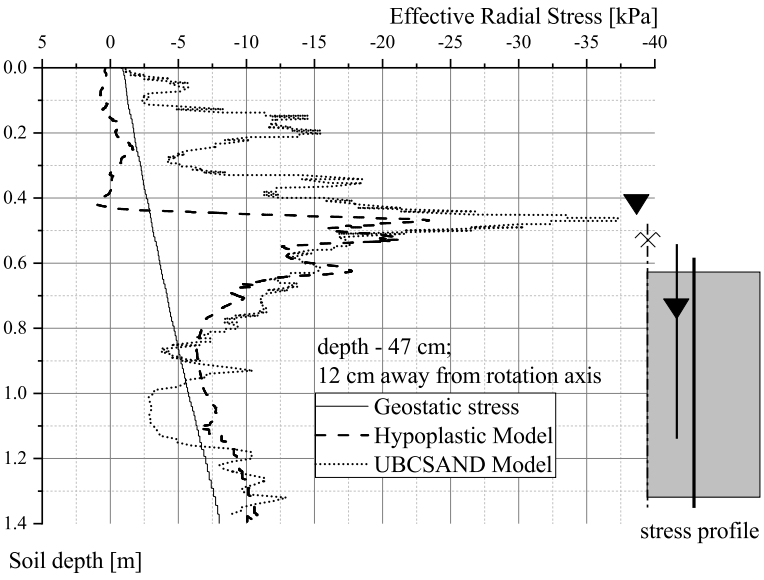

(b) Effective Radial Stress distribution outside vibrated pile

Figure 6.4: Effective Radial Stress disctribution inside (Left), and outside (Right) of the vibrated pile - Hypoplastic and UBCSAND Models

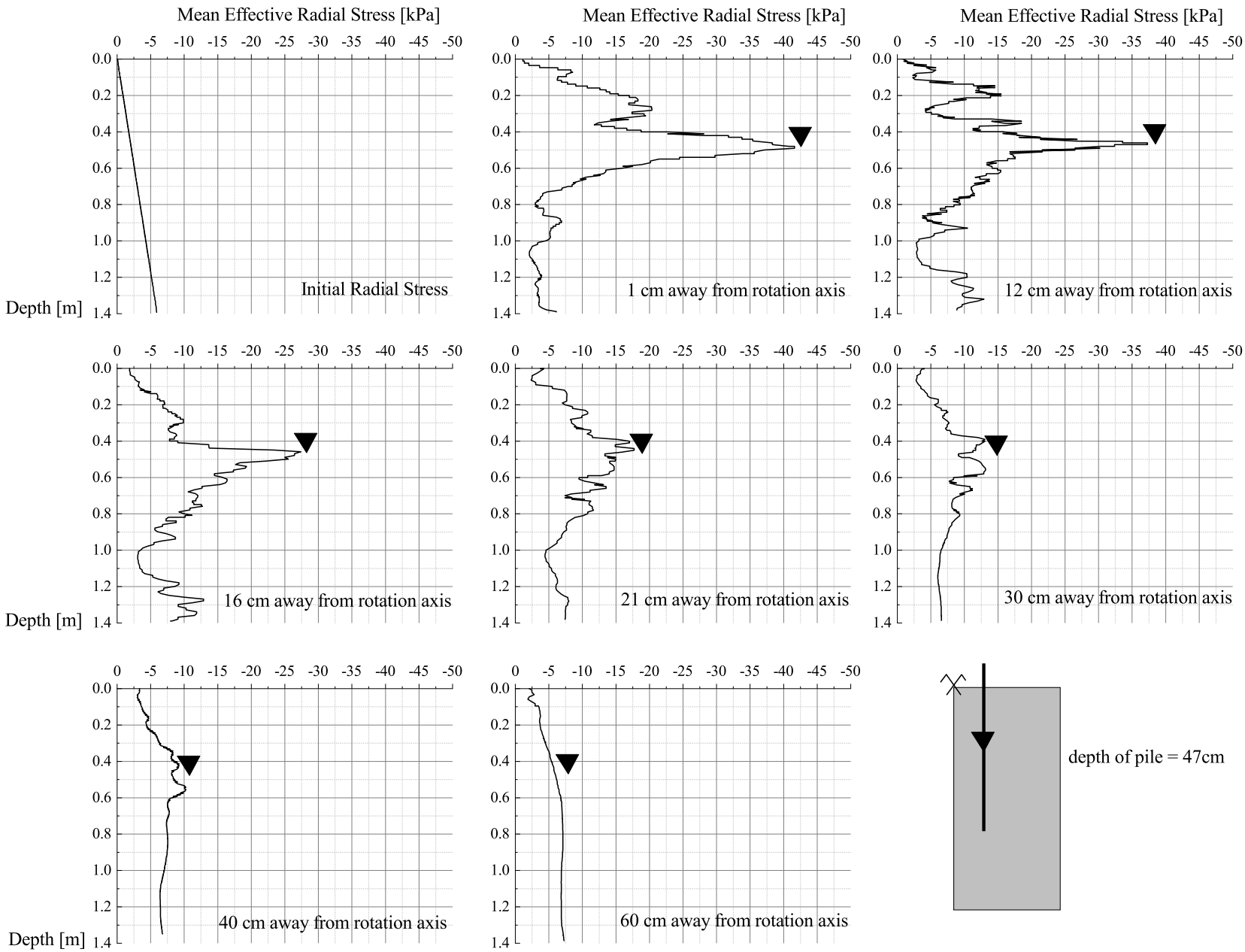

Figure 6.5: Effective Radial Stresses for vibrated pile at a depth of 47 cm at varying distances from rotation axis

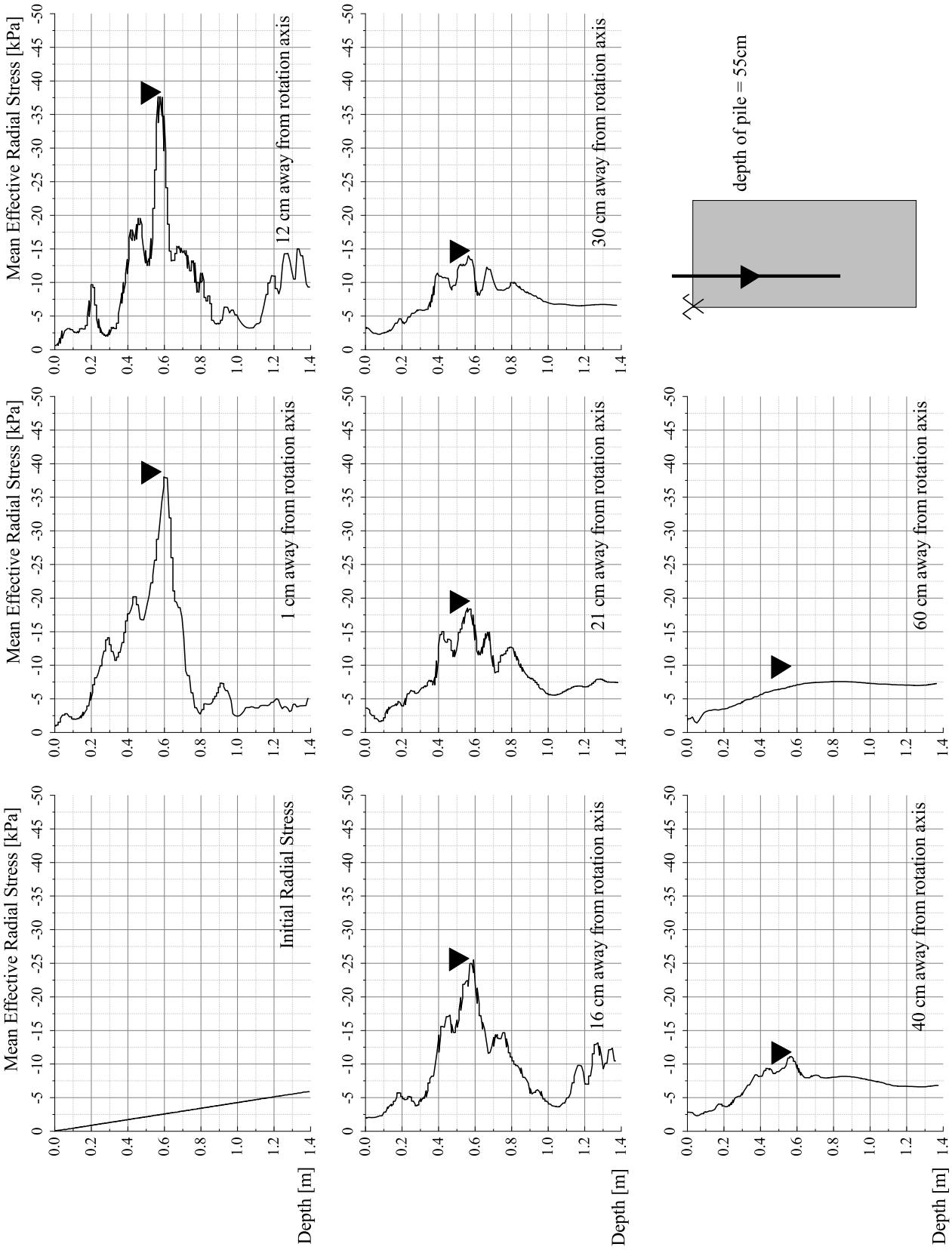

Figure 6.6: Effective Radial Stresses for vibrated pile at a depth of 55 cm at varying distances from rotation axis

Figures 6.5 and 6.6 depict the effective radial stresses calculated using the UBCSAND model of the pile at a depth of 47 cm and 55 cm from the surface, respectively. As anticipated, an elevated stress response is observed close to the pile shaft, and it returns to its geostatic value further away. The maximum value of effective radial stress is approximately eight times the geostatic value. Reference [55] observed a similar increase in radial stresses for a similar back-calculation. The simulations in reference [55] were performed using the MMALE method, assuming dry soil continuum and instead assuming the buoyant density for the soil to obtain the correct stress conditions. It should be noted that the continuum was represented using the hypoplastic soil model. In the reference, an effective stress increase of 3 to 7 times its initial value was noted, as opposed to the roughly 8-fold increase in this work. On a qualitative level, the results are consistent with the hypotheses.

Remarks on excess pore pressure close to the pile shaft

Figure 6.7 compares the excess pore pressure evolution for numerical and experimental results at a depth of 35 cm from the top of the soil and a distance of 2 cm from the pile. Beginning with a distribution of hydrostatic pressure, one observes an increase in pore

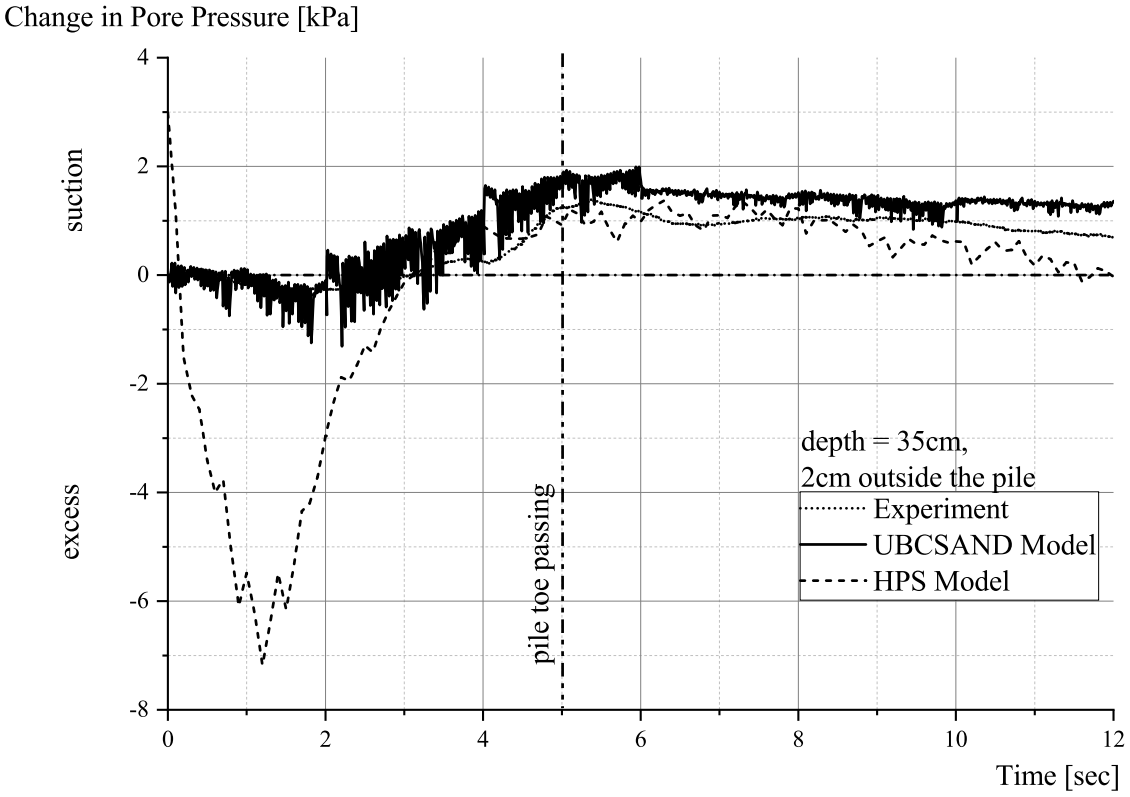

Figure 6.7: Excess Pore Pressure development of vibrated pile - HPS and UBCSAND Model, compared against experiments

pressure. Negative values indicate an increase in excess pore pressure, while positive values indicate suction. In addition, it can be observed that both the hypoplastic model and UBCSAND models can replicate the trend of excess pore pressure generation for approximately 5 seconds of vibration, which corresponds to a 35 cm installation depth (see Figure 6.3); however, the results during the first 5 seconds are significantly different. The models also account for the observed development of suction in the region after the pile toe has passed the control level. Simulations and measurements confirm that an excess of pore pressure develops until the pile tip reaches the control point, after which the regime changes to suction. While the UBCSAND model is capable of accurately capturing the development of excess pore pressure, oscillations in the pore pressure values are observed. Why the Hypoplastic model predicts a -7 kPa spike in excess pore pressure at approximately 3 seconds when the measured value is -0.5 kPa requires further investigation. At this time, it is believed to be a numerical artefact of the MPM code. Noting that a state of total liquefaction is not observed indicates that the effective stresses do not completely disappear.

Comparison of soil displacement with Particle Image Velocimetry results

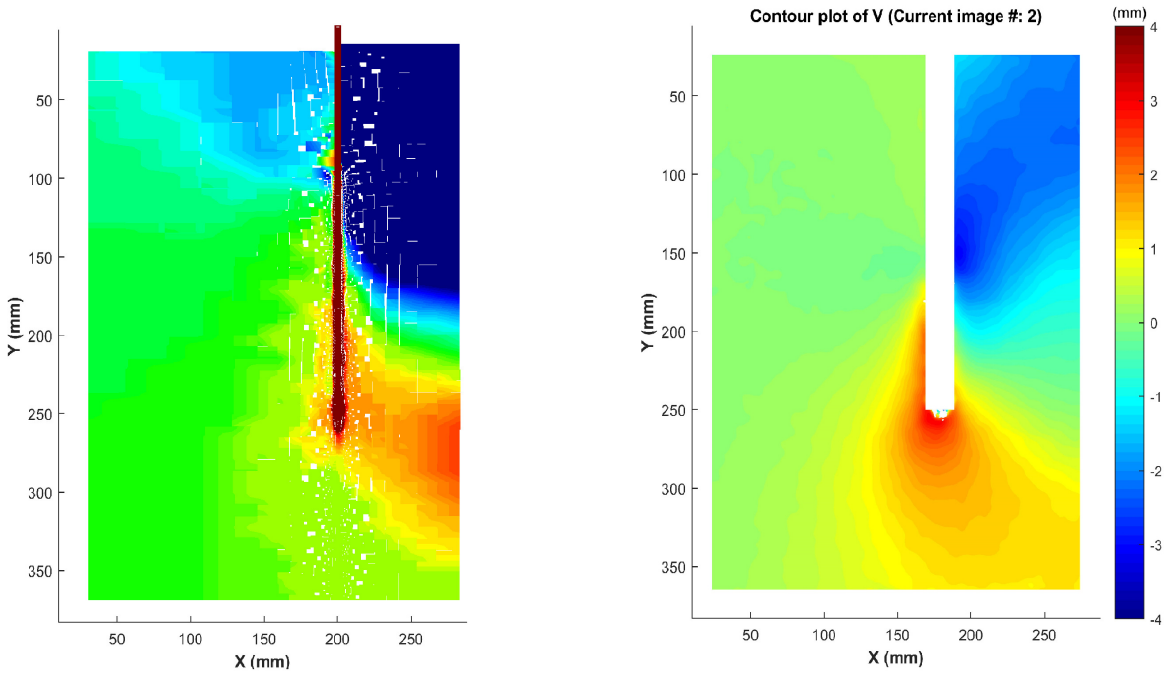

Figure 6.8: Vertical Soil displacement during the pile installation by vibration; CPDI (Left) and Experiment (Right)

From the CPDI calculation, vertical soil displacement was plotted and compared to the Particle Image Velocimetry results from the experiments. Particle Image Velocimetry

(PIV) is a method used to obtain instantaneous velocity and displacement measurements in fluids. This method has found success in the field of geotechnical engineering as well. Figure 6.8 depicts the computed value of vertical soil displacement at the conclusion of 25 cm of pile installation and compares it to the experimentally determined values. The CPDI model captures quite accurately the movement of the soil near the top surface within the pile and the movement of the soil around the pile shaft downwards. Presumably as a result of friction between the pile and sand, the soil in a small region surrounding the pile shaft moves downwards. In addition, sand is pushed downwards by the tip of the pile, and the outcomes are comparable.

Remarks on the computational time

This study demonstrated that UBCSAND and hypoplastic model responses are comparable. However, one must answer the question,"What advantage does one model have over another?" Having observed that the responses of both models are qualitatively comparable, we can now begin using the model with the lower computational cost instead of the model with the higher computational cost if the objective is not a comprehensive simulation of the stress and soil state, but rather to estimate the penetration depth and pore pressure. For a similar response, the computational time for the UBCSAND model is significantly less than for the hypoplastic sand model. To simulate 12 seconds of pile vibration, the UBCSAND model required 62 hours while the hypoplastic model required 96 hours. Both models ran on Workstation processors from the Intel Xeon family with comparable clockspeeds. The UBCSAND model utilised 16 threads while the hypoplastic model utilised 20 threads. Here, the UBCSAND model can be substituted for the hypoplastic sand model in the context of CPDI pile installation simulation with confidence.

6.2.2 Impact driven model pile installation simulation

The mesh shown in Figure 6.2 was used to simulate the impact-driven installation of a model pile in saturated soil, together with parameters of impact device, listed in Table

Parameter	Value
Mass of drop weight	22.1 kg
Fall height	0.28 m
Potential energy at impact	60 Nm
Mounting and hammer mass	48.12 kg
Total static load	67.38 kg

Table 6.4: Overview of the parameters for the impact hammer [55]

6.4. The simulation uses the Berlin sand properties listed in Table D.2. It is assumed that the soil continuum is fully saturated. In actuality, the dynamic force for impact is reported as energy per blow; however, this cannot be directly realised in the numerical model. Instead, the relationship presented in reference [107] approximates the dynamic force over time, F_d using a half-sine wave, given by relation:

$$F_d = \frac{\pi \eta m \sqrt{2gh}}{2t}, \tag{6.1}$$

where, m is the mass of drop weight, h is the fall height, g is the acceleration due to gravity and t is the impact duration, which is 0.01 seconds in this experiment. The efficiency factor, η was introduced into the force equation to account for the energy lost during impact that does not contribute to pile installation. Reference [55] estimates a load transfer efficiency factor of approximately 0.765 based on measurements conducted at TU Berlin. Simultaneously, it was reported that an efficiency factor of approximately 0.7 provided the best fit between the results and experiments. According to the findings of a parameter study, the efficiency factor plays the most significant role in determining the final penetration depth of a numerical model. In this work, the value 0.7 is assumed to be the case. Maximum dynamic force is calculated to be 5.695

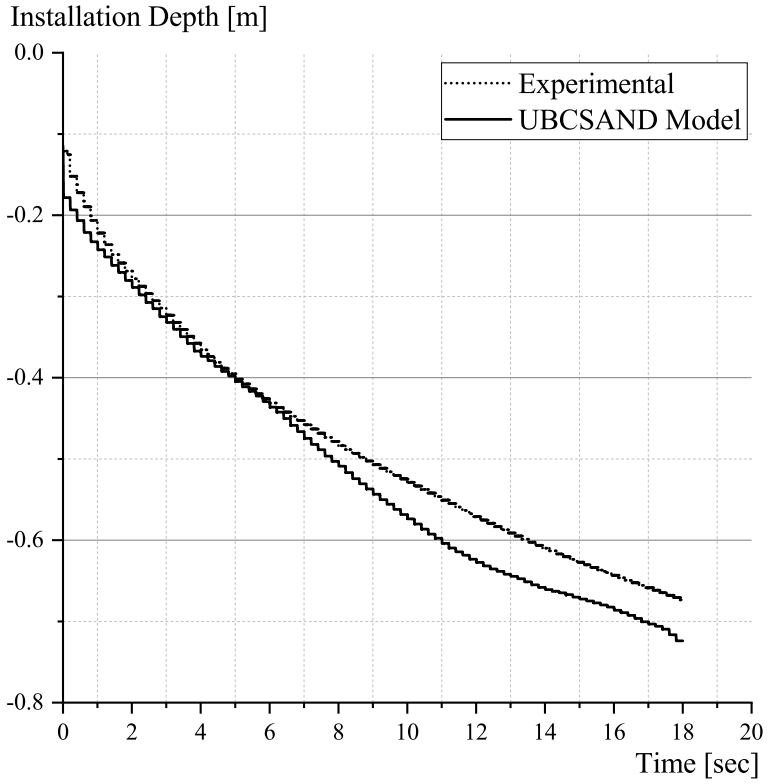

Figure 6.9: Vertical penetration of hammered pile - Experimental vs. Numerical

kN by substituting appropriate model values into Equation 6.1. The calculated static load on the pile is approximately 0.674 kN.

At a frequency of 0.5 Hz, the experiment was conducted for a total of 354 seconds. The length of time between blows is merely operational; the mass must be lifted and prepared for the subsequent blow. In order to reduce computational costs, reference [55] conducted a numerical analysis to determine the time at which the pile returns to equilibrium, i.e., when both the pile acceleration and the excess pore pressure beneath the pile's tip subside. Accordingly, the ideal time between blows was estimated to be 0.15 seconds, which is also assumed for the purposes of this study. The calculation was performed for a total of 18 seconds, resulting in a total of 120 blows.

Figure 6.9 depicts the penetration curve for the impact driven pile. The pile penetrates nearly 0.08 metres after the initial blow. While this is not observed in the experimental results, such a soft behaviour can be attributed to insufficient stiffness on the surface of the soil continuum, since the stiffness of the soil is directly proportional to the current mean effective stress (Equation 5.1). As the simulation continues, the disparity between the simulation and the experiment diminishes. The numerical model and the experiment diverge by approximately 5 percent as the simulation continues. Nevertheless, the numerical model reproduces the experimental results arguably quite well.

Evaluation of effective radial stresses for impact driven pile

Figures 6.10 and 6.11 depict the radial effective stress during hammering at pile depths of 47 cm and 55 cm, respectively. The radial stresses are calculated to be approximately 14 times their geostatic value, a value also observed in reference [55]. Bakroon [9] performed two sets of simulations using similar boundary conditions and Multi-Material Arbitrary Lagrangian Eulerian (MMALE) method to that of the study being described here: one simulation assuming a locally drained formulation and the other assuming a locally undrained formulation. In the case of drained simulation, the pile was observed to punch through the soil, whereas in the case of undrained simulation, the soil within the pile exhibited plugging behaviour. While such plugging behaviour was not observed in the CPDI simulation, a qualitatively similar increase in stress was observed near the pile tip. The peak radial stresses for the drained simulation occur near the pile's tip, whereas for the undrained simulation, they are observed to occur above the pile's tip. The CPDI simulation reveals the maximum horizontal stresses beneath the pile's tip. This variation in results can be attributed to the fact that the CPDI calculates pore pressure using a fully coupled formulation. In the case of CPDI, the drag force, which is a function of the hydraulic conductivity, also plays a role, whereas it is completely ignored in the case of MMALE, where a locally undrained formulation is utilised. Despite the differences in modelling method, there is a strong convergence between the CPDI results, the MMALE method and the experimental results.

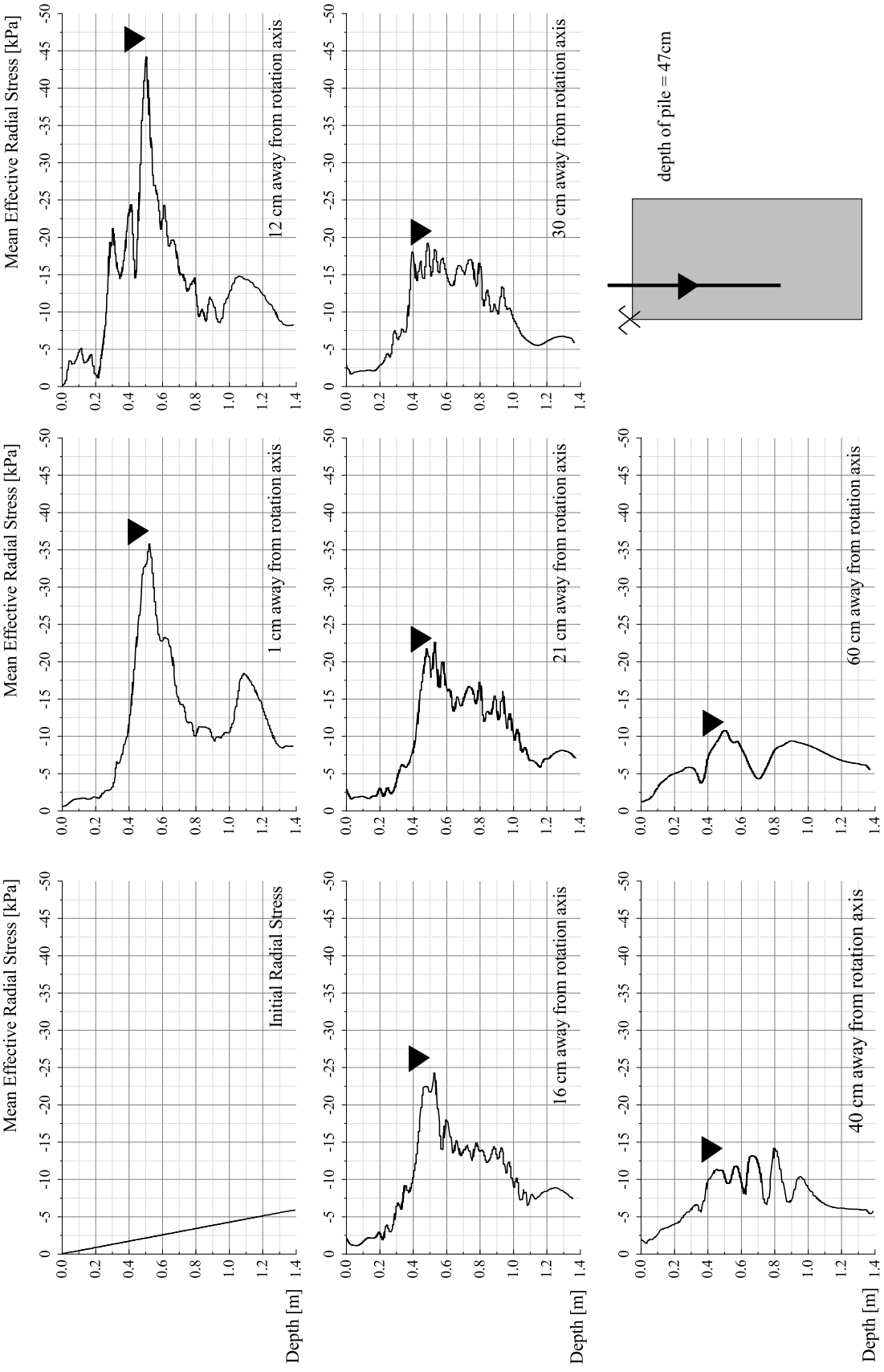

Figure 6.10: Effective Radial Stresses for hammered pile at a depth of 47 cm at varying distances from rotation axis

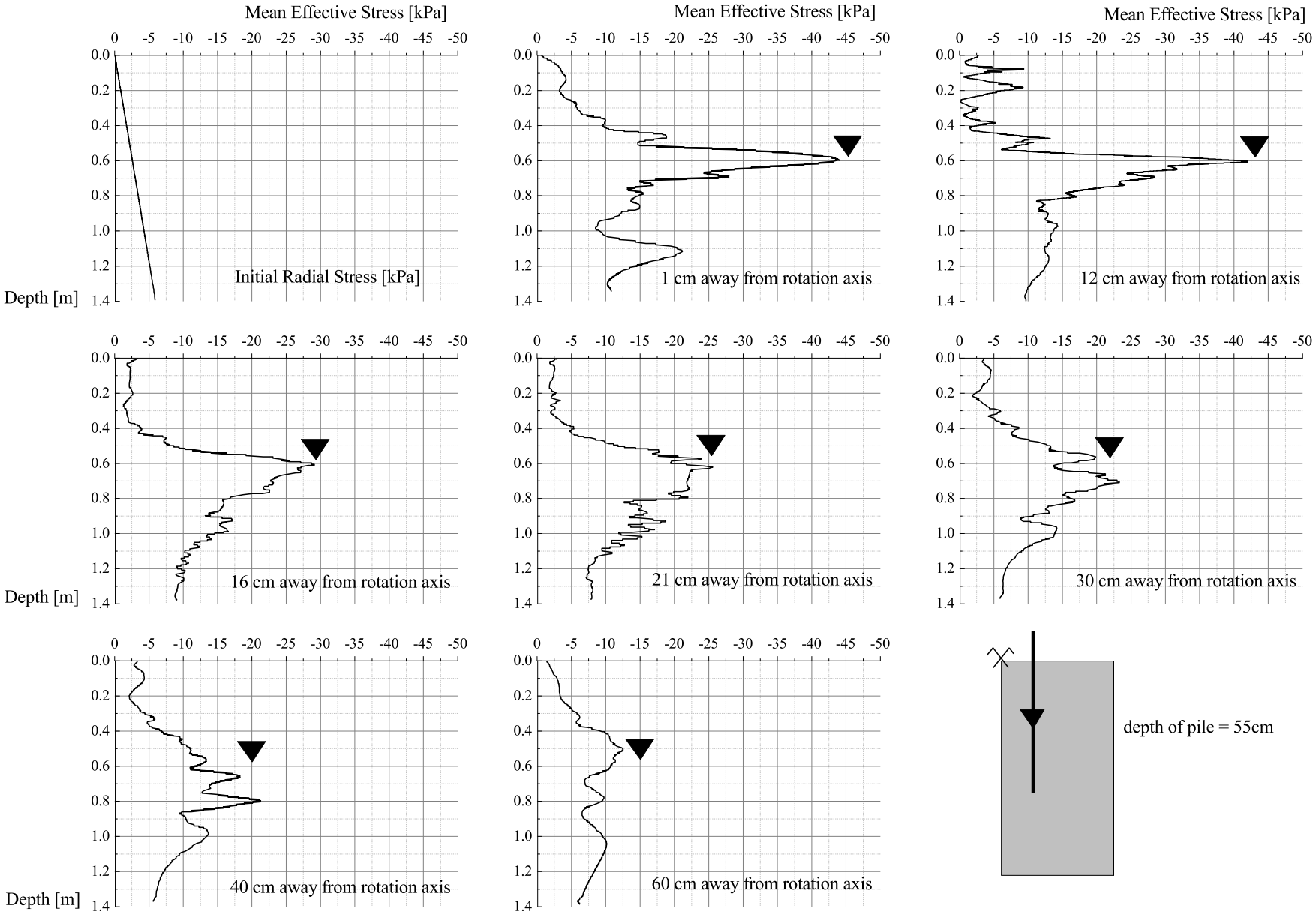

Figure 6.11: Effective Radial Stresses for hammered pile at a depth of 55 cm at varying distances from rotation axis

Remarks on excess pore pressure close to the pile shaft for impact driven pile

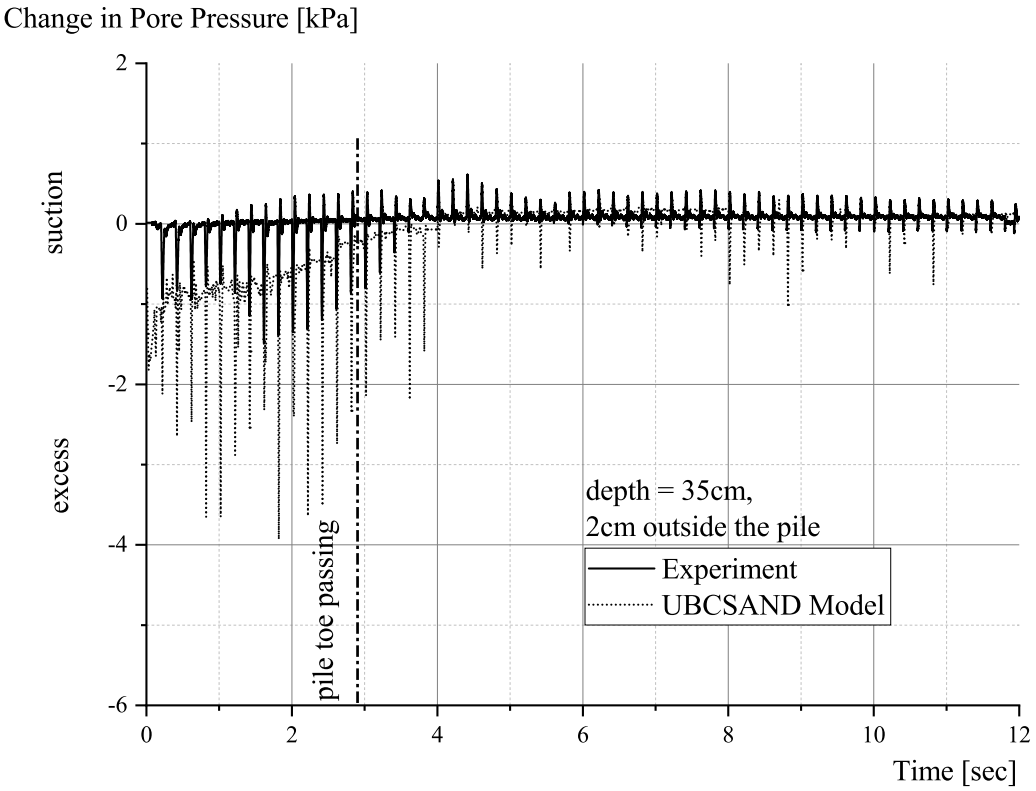

Figure 6.12: Excess Pore Pressure development of hammered pile - HPS and UBCSAND Model, compared against experiments

Figure 6.12 depicts the excess pore pressures measured at a depth of 35 cm from the surface and 2 cm outside the pile in comparison to the numerical results. The numerical model captures an area of excess pore pressure as the pile approaches the measurement point. This trend is supported well by the experimental findings. Positive values indicate suction zone pressure, while negative values indicate excess pore pressure. The excess pore pressure is roughly double the amount measured during the experiment. As illustrated in Figure 6.7, this pattern of variation has also been observed in the vibratory driven process. Until approximately 3 seconds, when the pile toe passes the control point, the numerical model overestimates the excess pore pressure. However, after 3 seconds, the results are significantly different. In addition to accurately capturing the excess pore pressure, the numerical model also captures the suction regime that develops in the control zone. There is still some discrepancy between the experimental and numerical results, which is attributed to numerical artefacts in the CPDI code and requires further investigation. Overall, there is a close correlation between the experimental and numerical results.

Concluding remarks

This section presented the initial step taken in the modelling of vibratory and impact driven pile installation. In both instances, an acceptable correlation, both qualitative and quantitative, with experimental data was observed. In addition, the numerical model was able to capture the generated excess pore pressure for both vibrated and impact driven piles with reasonable accuracy. Using both the UBCSAND and hypoplastic soil models, the CPDI model was able to predict the installation behaviour and stress state changes in the soil. This section demonstrates that the numerical method developed for this study is capable of simulating the highly dynamic vibratory and impact-driven model piles in saturated soil. Verifying that the numerical method can model the installation of a real-scale monopile is the next step in this regard.

6.3 Numerical simulation of a full-scale pile installation

To investigate the impact of vibratory installation in comparison to the conventional installation method of impact hammering, a joint industry project with a total budget of approximately 6 million euros was commissioned. The objective of the project was to examine the viability of employing the vibratory installation method for monopiles to achieve a quicker and more environmentally friendly offshore foundation installation. The pile installations for the *VibroPile* project were carried out in Cuxhaven, a coastal city on Germany's North Sea coast. A quarry was selected as the installation location for the monopiles. As shown in Figure 6.13, the site consisted of glacial, overconsolidated, dense sand deposits with a 1 m thick clay layer approximately 5 m below the surface. According to Moormann et al. [157], the geological history of the site is comparable to the planned development site for offshore wind projects in the North Sea.

Project background

Six installation tests of monopiles were conducted. Three monopiles were vibrated into the ground, while the remainder were installed using the conventional impact hammer technique. The installation of Pile P4 was back-calculated in this study. In the preceding section, the CPDI tool developed for this project was used to calculate the results of a model pile. Due to a lower geostatic stress state, although good correlations were found between the experimental and numerical results, it should be appreciated that the transfer of the numerical model to a full-scale model is not always guaranteed. In addition, approximately 20 seconds of vibration and hammering were simulated for the model pile. While it is impossible to say with certainty how long it would take for a pile to be vibrated to the planned installation depth, as it depends on many

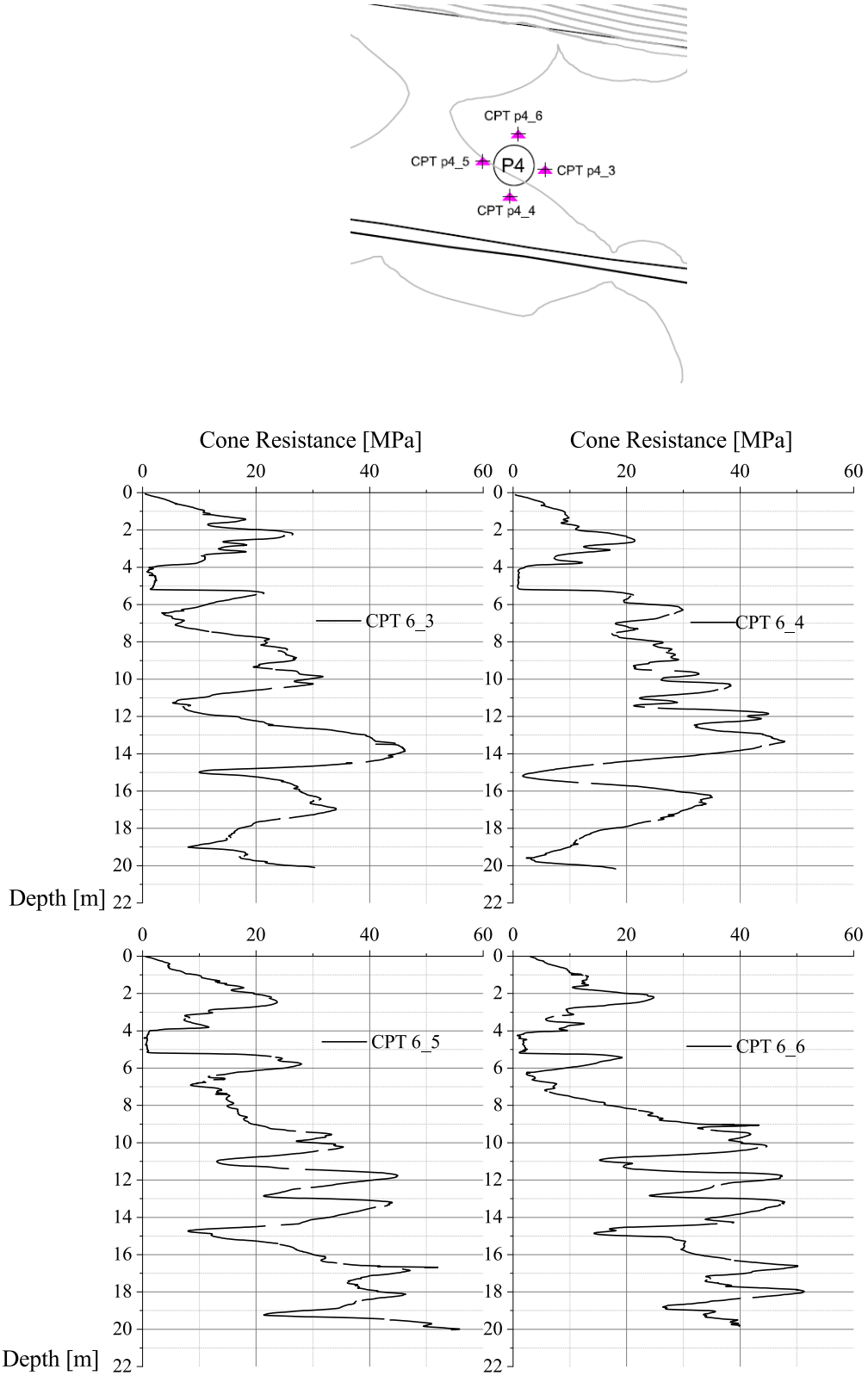

Figure 6.13: Overview of CPT data from pile locations CPT6-3 through CPT6-6; measured near location of pile P4

Parameter	Value
Working moment	500 kgm
Total weight	1,536 kN
Maximum centrifugal force	10,748 kN at 1,400 rpm

Table 6.5: Data of vibration motor [157]

variables such as vibration parameters and ground conditions, it is certain that real-world monopile installation would take significantly longer to reach final installation depth. The vibration motor's parameters are tabulated in Table 6.5. The Pile P4 was vibrated for a total of four minutes on January 7, 2014.

Model and boundary conditions

In the wake of the simulation of model scale pile installation, a similar approach to the numerical simulation was adopted for the simulations presented in this section. As described in Chapter 3, an axially-symmetric model and the penalty contact algorithm were used to describe the soil continuum and the soil-pile interaction, respectively. The soil and pore fluid were modelled using the two-phase CPDI formulation described in Chapter 4. The stress-strain relationship was calculated using the UBCSAND model, which was described in detail previously in Chapter 5. The results of the numerical simulation were compared to the field measurements.

The open steel pipe pile with a diameter of 4.30 metres was vibrated into the soil, which is assumed to be homogeneous and completely saturated. Initial stresses were set according to K_0 conditions, with K_0 assumed to be 0.5. Before applying the dynamic load, F_D, the CPDI model was allowed to reach steady-state conditions. While the CPDI model achieved steady-state conditions, the static load was activated. The pile's parameters are tabulated in Table 6.6,.

The installation of piles occurred in two stages. Initially up to approximately 9 m from

Parameter	Value
Outer diameter	4.3 m
Wall thickness	45 mm
Total length	21 m
Total mass of pile	99.57 ton
Motor mass	65.10 ton
Total static load	164.67 ton

Table 6.6: Pile parameters from *VibroPile* project for Pile P4 [157]

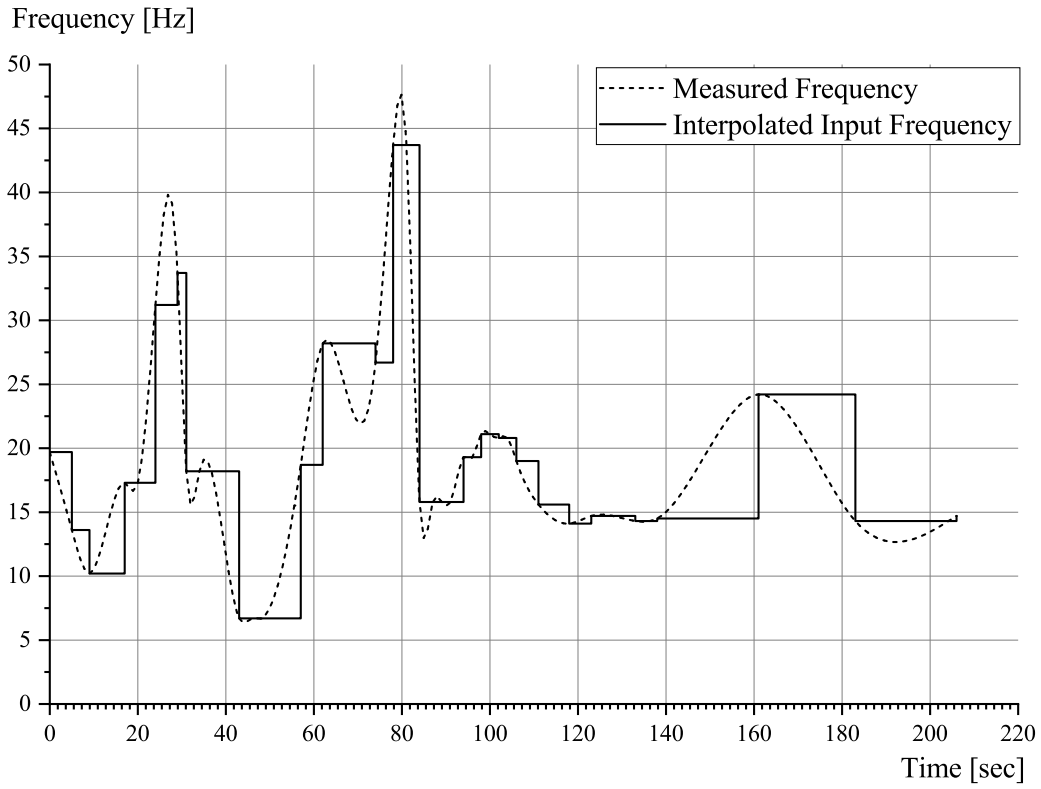

Figure 6.14: Measured vs. Input frequency for the numerical model for Pile P4

Time [sec]	0-5	5-9	9-17	17-24	24-29	29-31	31-43
Frequency [Hz]	19.7	13.6	10.2	17.3	31.2	33.7	18.2

Time [sec]	43-57	57-62	62-74	74-78	78-84	84-94	94-98
Frequency [Hz]	6.7	18.7	28.2	26.7	43.7	15.8	19.3

Time [sec]	98-102	102-106	106-111	111-118	118-123	123-133	133-138
Frequency [Hz]	21.2	20.8	19	15.6	14.1	14.7	14.3

Time [sec]	138-161	161-183	183-206
Frequency [Hz]	14.5	24.2	14.3

Table 6.7: Frequency of the vibrator, approximated to a step function, from Figure 6.14

the surface, the pile was intermittently vibrated with a lower frequency and lower load. Beyond 9 m and up to approximately 18.5 m from the surface, the pile was vibrated with a frequency that was nearly constant. Consequently, the vibrator's frequency does not remain constant throughout the duration of pile installation. Resultantly, the dynamic force also changes, as indicated by the relationship:

$$F_d = M \cdot (2\,\pi\,f)^2 \cdot sin(2\,\pi\,f\,t)\,, \tag{6.2}$$

where, M is the eccentric moment, taken as 500 kgm, and f is the frequency of the vibrator, which changes according to the step function shown in Figure 6.14. The values of the approximated step function of frequency is tablulated in Table 6.7. As the simulation progresses, the frequency is fed into the CPDI code and varies dynamically. The bulk modulus of water is assumed to be 2.2 GPa (K_f). The pile's horizontal acceleration and displacement are constrained by imposing a strict boundary condition. The interface elements meshed to represent the pile's contact with the soil are assigned a coefficient of friction, μ of 0.3.

Figure 6.15 depicts an axially-symmetric continuum consisting of pile and soil particles. This continuum was discretised with approximately 36,000 particles and 11,000 interface elements. From the lessons learned in the previous section, where instabilities with the contact elements occured at deeper pile installation depths, a deliberate decision to adopt a finer discretisation for the interface elements was made. Utilising an irregular meshing pattern enabled the packing of more particles near the pile's toe and jacket, which is the region of interest.

An effort was made to install the pile from the surface. However, due to numerical instability that occurs when the pile vibrates in a region of very low stress state, it was decided to embed the pile 5 m, which not only approximated the pile penetration due to gravity, but also approximately 30 seconds of pile vibration. Utilising a dynamic time-stepping scheme, the incremental timestep for the marching scheme is updated every 1,000 time steps. After reference [160], particle-in-cell damping was activated, with 1 percent value assignment for both solid and fluid phases. The Cuxhaven soil parameters for UBCSAND were adopted, with an assumed 85% relative density for the

$N1_{60}[-]$	$m_e[-]$	$n_e[-]$	$n_p[-]$	$K^e_G[-]$	$K^e_B[-]$
25.0	0.5	0.5	0.95	1432	854
$K^p_G[-]$	$\phi_{pt}[^\circ]$	$\phi_f[^\circ]$	$c[kPa]$	$Pa[kPa]$	$\sigma_t[kPa]$
820	32.6	37.9	0	100	0
$hfac_1[-]$	$hfac_2[-]$	$hfac_3[-]$	$hfac_4[-]$	$hfac_5[-]$	$hfac_6[-]$
0.65	0.85	1.0	0.6	1.0	0.95

Table 6.8: UBCSAND model parameters for Cuxhaven Sand

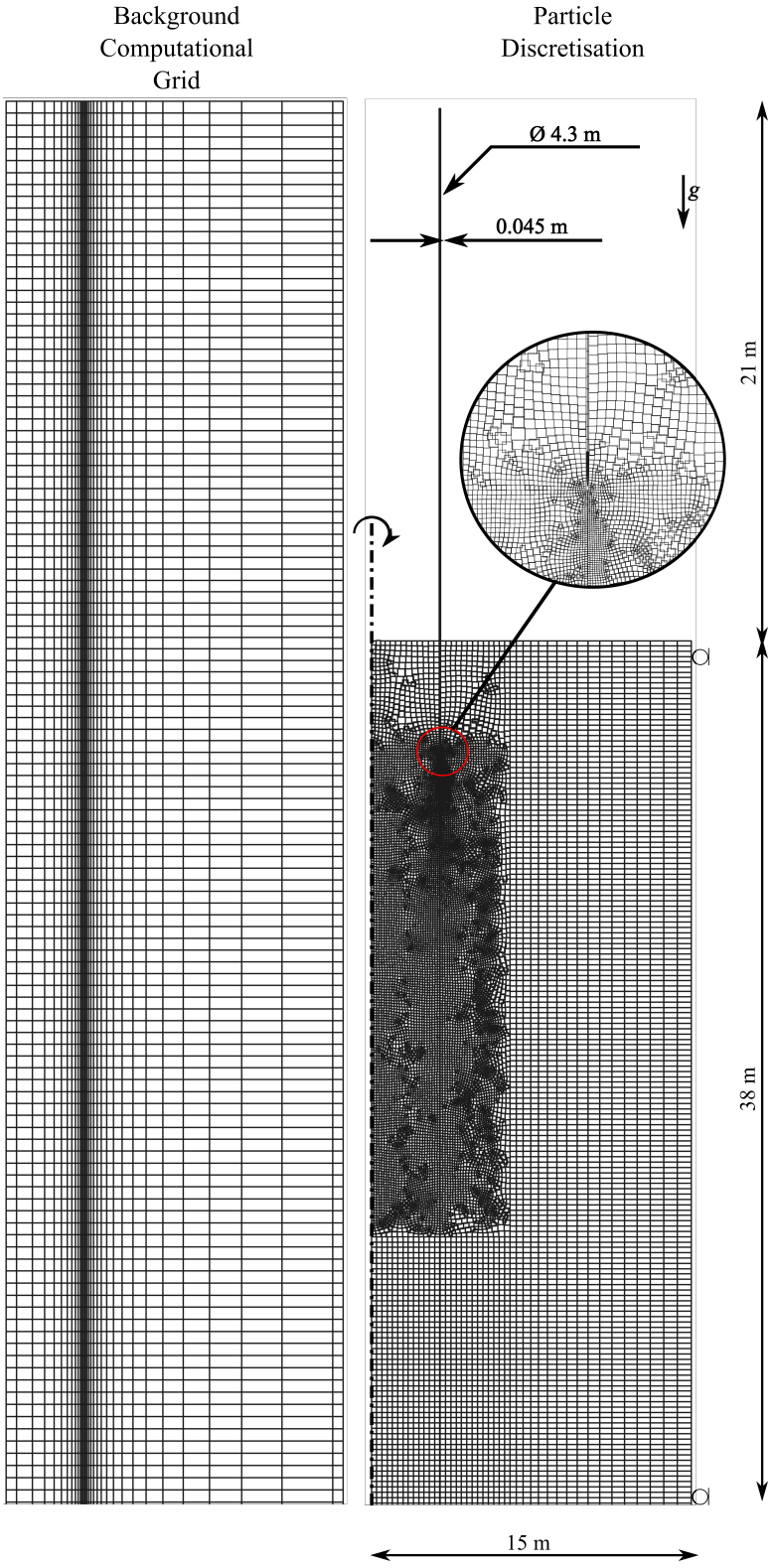

Figure 6.15: Background computational grid discretisation (Left), and Particle discretisation of pile and soil (Right)

model. The model parameters are tabulated in Table 6.8.

Discussion of vertical pile penetration results

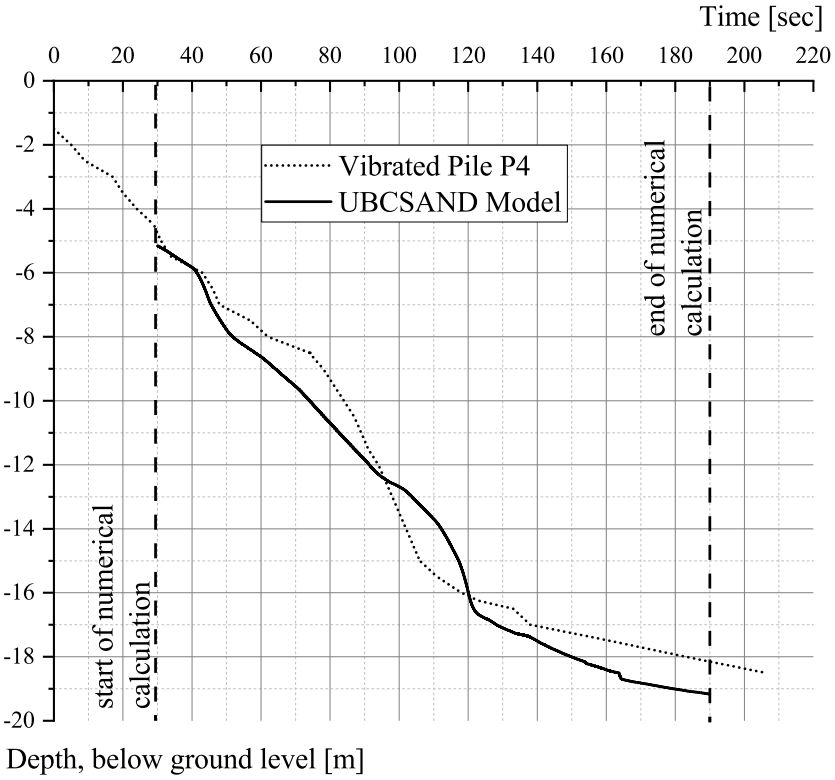

Figure 6.16: Vertical penetration of pile - Experimental vs. Numerical model

Figure 6.16 shows the results of the pile penetration simulation. During the first 10 seconds of simulation, the pile initially penetrates more slowly than observed during the experiment. This disparity in results is to be expected, given that the pile was embed 5 metres deep which causes the stress state beneath the pile's foot and around the pile's jacket to vary from the field data. Additionally, the assumption is made that the soil continuum is homogeneous, which will also affect the prediction. Figure 6.13 demonstrates that a 1 m thick clay layer begins at a depth of approximately 4 m. While the rate of pile installation between 4 and 5 m increases, a similar behaviour cannot be observed from the numerical calculation, as the non-homogeneity and altered stress state around the pile jacket from the surface to 5 m depth have been disregarded.

As previously stated, the frequency varies continuously as the simulation continues. During vibratory installation, the soil surrounding the pile's jacket is affected in numerous ways. The soil in the vicinity of the pile is partially loosened as a result of the pile's vibrations. This theory is supported by the research presented in reference [172]. This loosening of the soil facilitates the pile's penetration through the soil. According to

references [54, 146], the penetration rate increases as the frequency of the vibrator rises. When the pile is vibrated at lower frequencies, a high stress concentration is observed under the pile's toe, which is not observed at higher frequencies. This increased stress concentration provides increased resistance to the installation of piles. In the research of reference [91], a comparable change in installation rate was observed. It is more difficult to observe a comparable increase or decrease in penetration rate as frequency increases or decreases, respectively, which is attributed to the frequency fluctuating continuously throughout the installation. Throughout their simulations, both references [54, 91] assume a constant frequency, varying it as part of a parameter study. It should also be noted that as the input vibration frequency increases, the dynamic forces also update themselves.

As the simulation progresses, the installation rate closely resembles field data. According to the data, the frequency is relatively stable between 80 and 160 seconds. In addition, between 8 and 15 m in depth, which corresponds to 60 to 110 seconds, the average cone resistance of the soil is approximately 30 MPa. In this area, a constant installation rate is expected. According to the results of the numerical model, the installation rate should be roughly constant between 8 and 13 metres. As the simulation approaches a depth of 13 metres, the installation frequency reaches its maximum value of 43.7 Hz.

The dynamic force increases at an increasing rate as the installation frequency increases. From the numerical structure of the constitutive model, it can be inferred that as the mean effective stress increases in the continuum, the elastic constants also increase. Owing to the increased transfer of dynamic load from the pile to the soil particles, there is an increase in the mean effective stress. An increase in elastic stiffness is anticipated to slow the rate of pile installation, which is observed between 90 and 110 seconds when the frequency increases and between 110 and 120 seconds when the frequency decreases. After this point, the resistance on the pile's shaft begins to play a greater role in dictating the installation rate.

The numerical model overestimates the ultimate installation depth by 1 m. This overestimation can be explained by the following factors: i) a 5 m prior embedment, which was required for the numerical stability of the calculation, permitted the alteration of the stress state around the pile jacket only at the end of the simulation; ii) a homogeneous layer was assumed for the model, which is not representative of reality. Overall, a good fit is obtained between the field data and the numerical model. Importantly, the tool has demonstrated its reliability in simulating the entire pile installation process and can be used to make *Class-A* predictions of the pile installation rate, thus achieving one of the research project's original objectives.

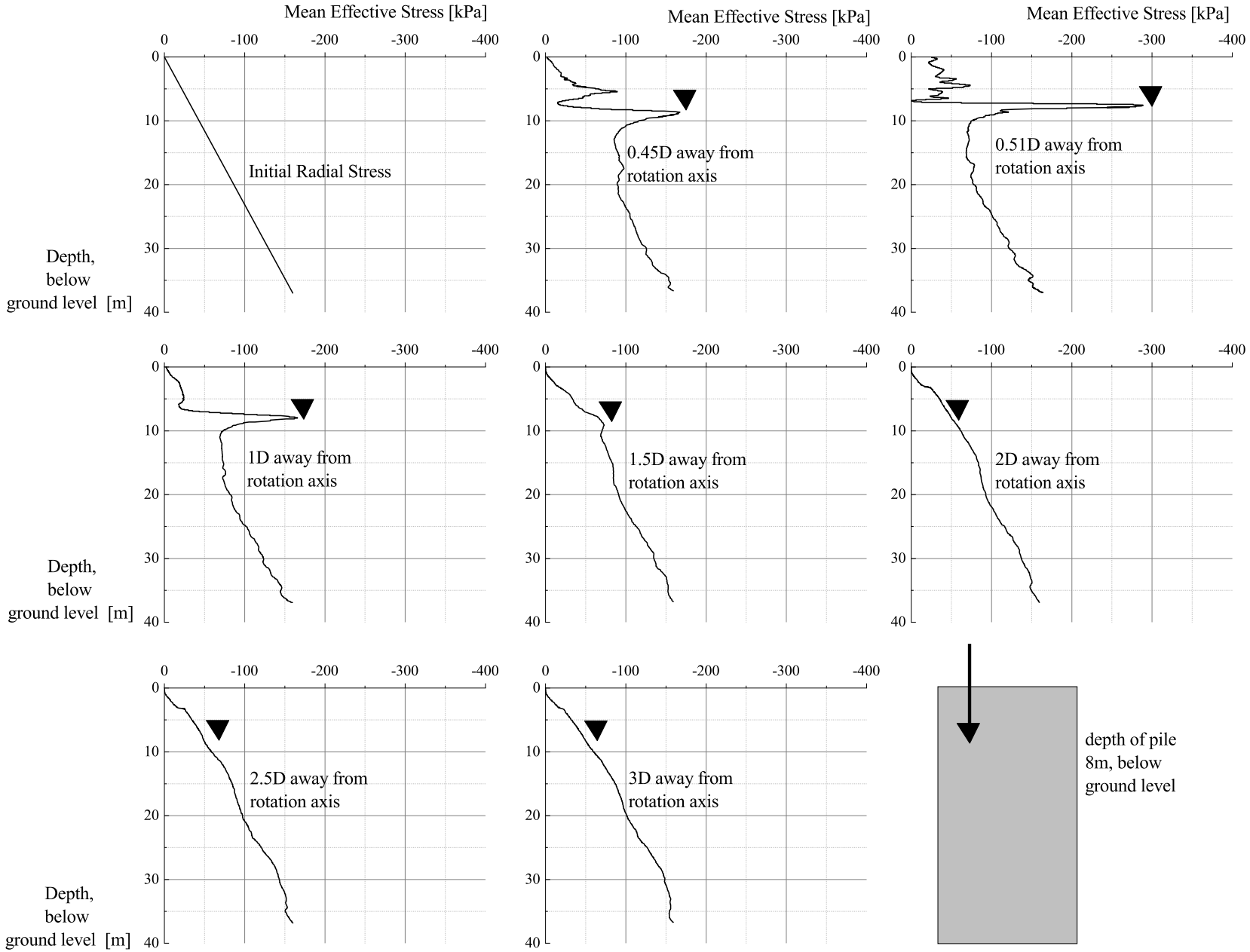

Figure 6.17: Effective Radial Stresses for vibrated pile at a depth of 8m at varying distances from rotation axis

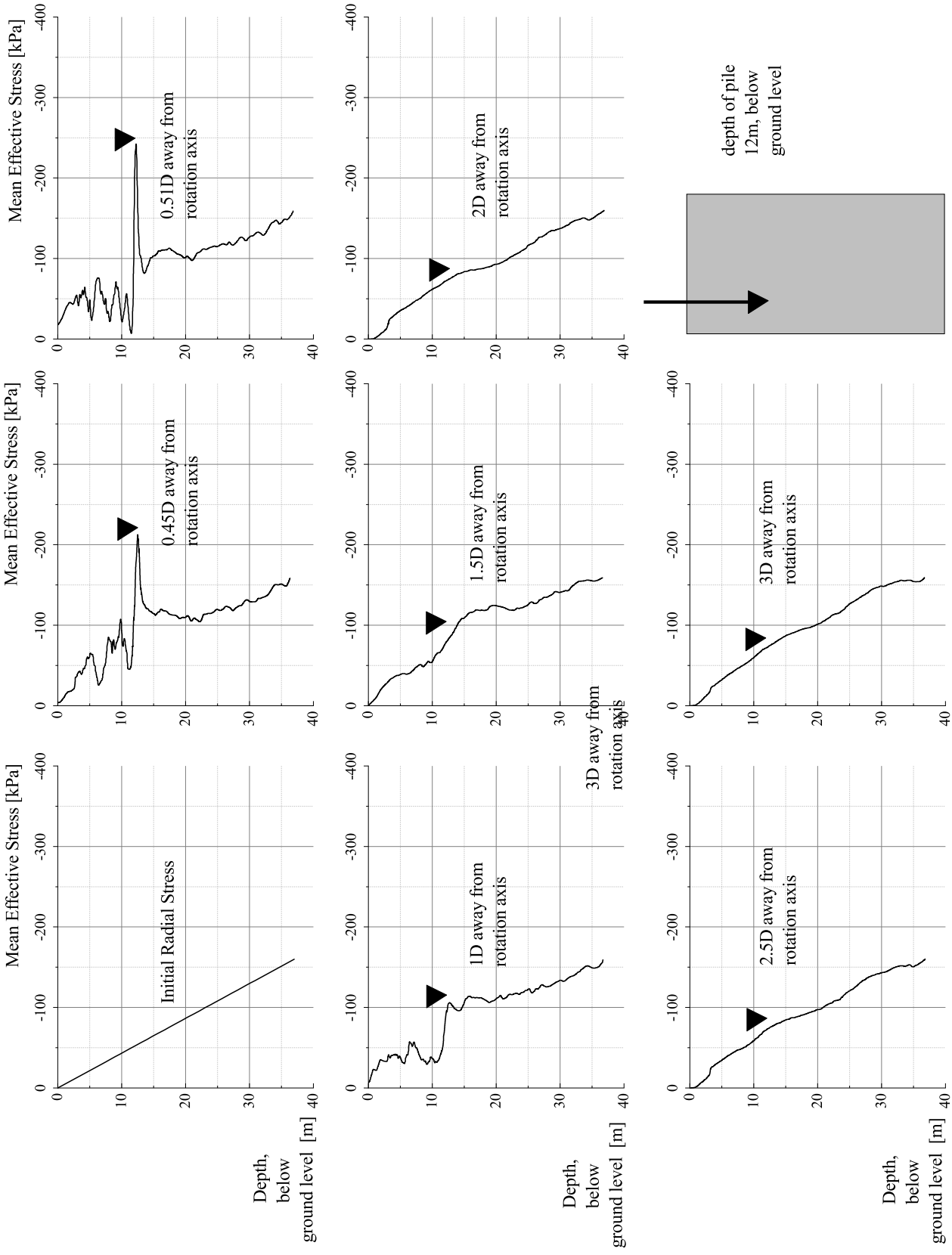

Figure 6.18: Effective Radial Stresses for vibrated pile at a depth of 12m at varying distances from rotation axis

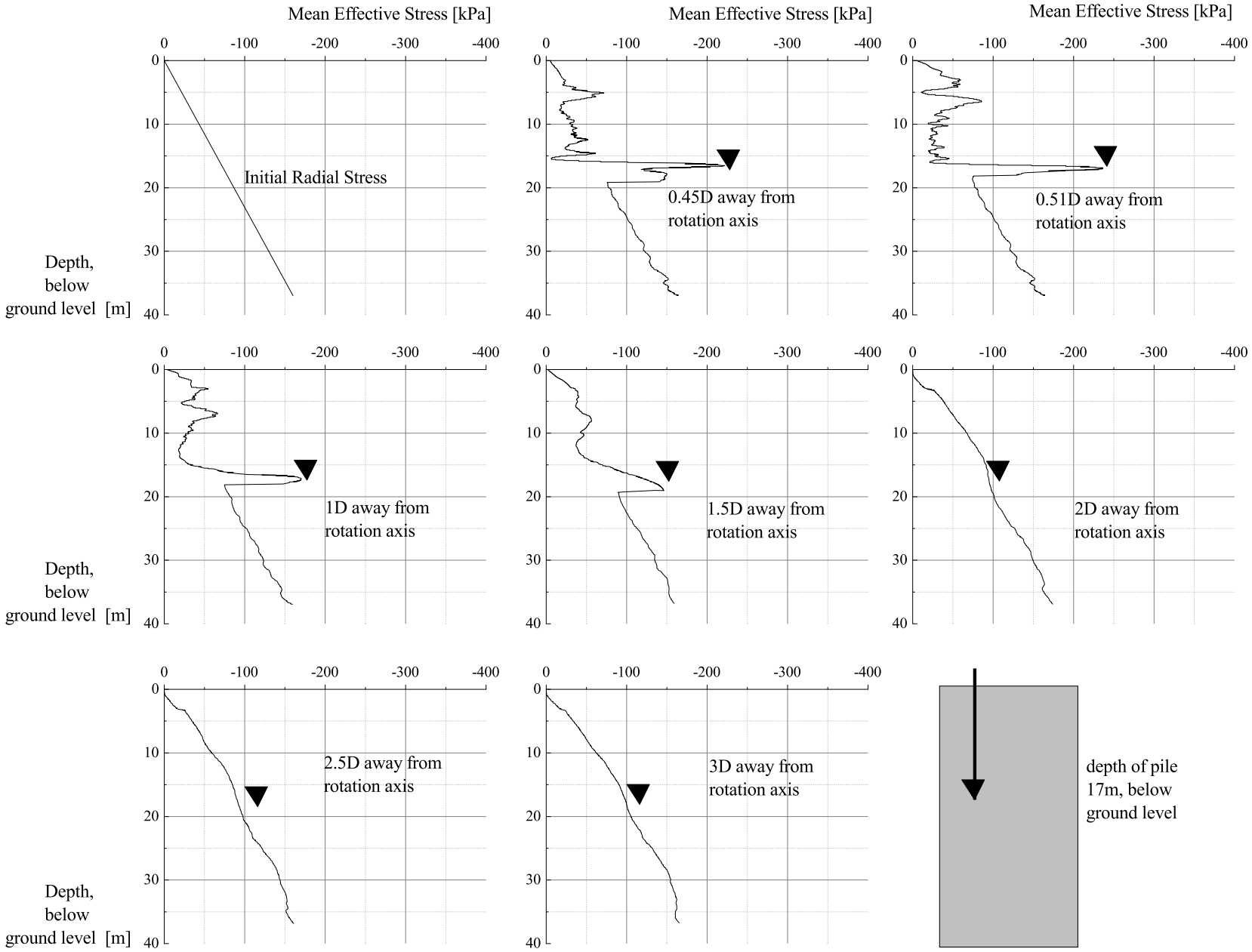

Figure 6.19: Effective Radial Stresses for vibrated pile at a depth of 17m at varying distances from rotation axis

Comments on the effective radial stress

In the context of a field study, stress analysis is not straightforward. This study is made more complicated by the multitude of sensors required to precisely measure the stress change. In their work with pile installation, White and Bolton [216] identified three 'zones' of behaviour in the vicinity of the pile: i) very near, ii) near, and iii) far field. The work also references an interface zone. This zone is immediately adjacent to the pile and extends horizontally for 2 to 3 mm. Identifying this region's numerical behaviour accurately would necessitate an extremely fine mesh, which would impose a significant computational burden. Owing to the small size of this area, no reliable Particle Image Velocimetry analysis was possible. Experiments were conducted on jacked piles, but efforts have been made to determine if such zoning is discernible in vibrated piles.

Figures 6.17, 6.18 and 6.19 depict the effective radial stress for the vibrated pile at different depths. All calculations indicate that there is a region of significant radial stress increase beneath the pile tip. Additionally, stresses within the pile are calculated and plotted. In their simulation of a jacked pile, reference [92] found a stress increase of up to 4.5 times the pile's geostatic value. A similar increase in radial stress was reported in reference [218]. At a depth of 8 metres below the surface, a similar increase in stress is observed in the case of vibratory piles, even though the installation method is arguably distinct. This depth corresponds to approximately fifty seconds of pile installation, or twenty seconds after simulation initiation. Outside the jacket of the pile (*0.51D*), a stress increase of approximately eight times the initial value is calculated. This is roughly consistent with what was observed for model monopiles in the preceding section, in which an increase in stress up to seven times the initial value was calculated. This difference is due to factors intrinsic to the soil and extrinsic to varying dynamic loads. Phuong et al. [179] examined the effect of initial sand density on radial stresses during installation for simulations of pile installation using the Material Point Method (MPM). According to the report, the effective radial stresses under the pile tip in the case of looser sand were 1.5 times lower than in its denser configuration. The observed outcomes of this study are consistent with the reported findings.

Ko et al. [115] analysed the plugging effects in open-ended steel pipe pile in FE analyses. A zone of increased radial stress was observed for small diameter piles, whereas plugging effects, or a zone of massively increased radial stress regime, was not observed for larger diameter piles ($\geq$2 m). Due to the large diameter of the pile utilised in this study, it is reasonable to conclude that plugging would not develop in this simulation and that a zone of massively increased radial stress can be ruled out. Consistent with this conclusion, a zone of increased effective radial stresses, similar to the one observed outside the pile, is calculated within the pile as well. This observation is also consistent with experimental and field data from other researchers [22, 114, 174].

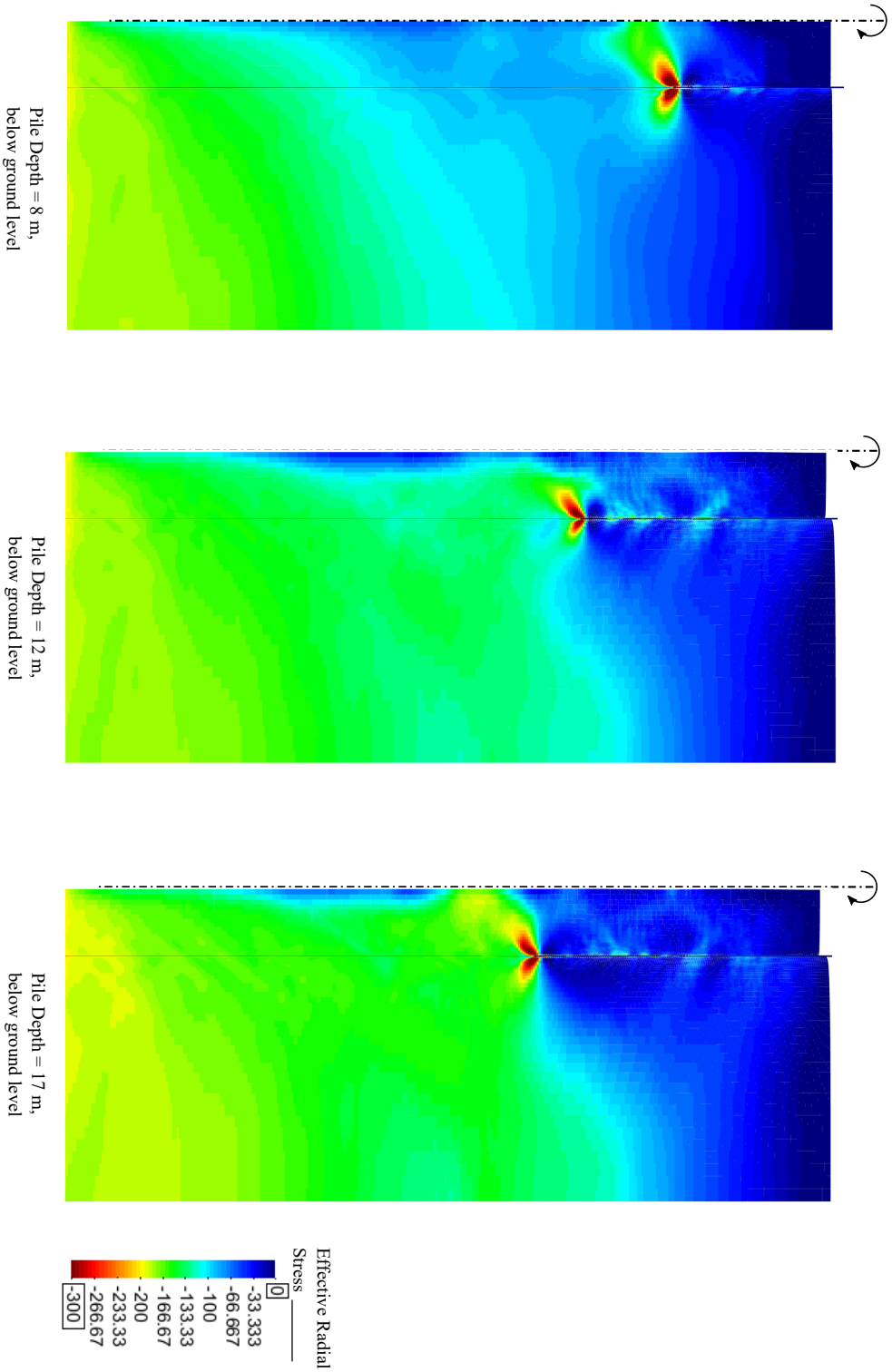

Figure 6.20: Countours of Effective Radial Stress of soil around Pile P4, at depths 8 m(left), 12 m (middle), and 17 m (right) from surface

The effective radial stresses are slightly lower than those observed outside the pile, which is due to the use of an axially-symmetric boundary condition. Figure 6.20 depicts the contour plot of the effective radial stress at a depth of 8, 12 and 17 metres from surface. The region of elevated stresses, both external and internal to the pile, is evident in the figure. Underneath the tip of the pile, both within and outside the monopile, there is a zone of increased radial stresses, which is observed as the simulation progresses (see Figures 6.18,6.19). This indicates that the soil beneath the pile hardens during the installation process, which is consistent with the findings of Ko et al. [115], in which the zone of elevated stresses extended well below the pile's tip.

Figures 6.18 and 6.19, which depict the radial stresses at depths of 12 and 17 m, respectively, demonstrate a similar pattern of behaviour. At each of the three snapshots, it was observed that the effect of pile installation on stress elevation decreases as the plane of measurement moves further from the axis of symmetry, from the *1D* distance from the rotation axis to the *3D* far field plane. In their work with numerically modelling pile installation in saturated sand using MPM, Phuong [180] reached similar conclusions regarding the effective radial stresses in the far-field region compared to the region close to the pile jacket.

In each of the three snapshots, the region adjacent to the pile shaft (*0.51D*) displays modified effective stresses. This is to be expected because the vibration of the pile primarily excites the soil near the pile. The conclusion that can be drawn is that the effective stresses are less than their initial value. References [8, 164] draw similar conclusions by observing the results of field tests using measurements of the earth pressure acting near the pile's shaft after installation. Since the effective stresses never disappear entirely, it can be concluded that there is no total liquefaction of the soil near the pile's jacket. According to Seed and Idriss [192], the absence of complete liquefaction is entirely plausible, given the 85 percent relative density of soil, whose susceptibility to complete liquefaction, is diminished.

In conclusion, the results of an examination of the effective stresses would be useful when more granular data on the state change of soil are required. Having obtained a reasonable pile installation prediction over time, it is reasonable to assume that the radial stresses, which play a significant role in the lateral behaviour of the monopile [52], are also reasonable and reflect reality.

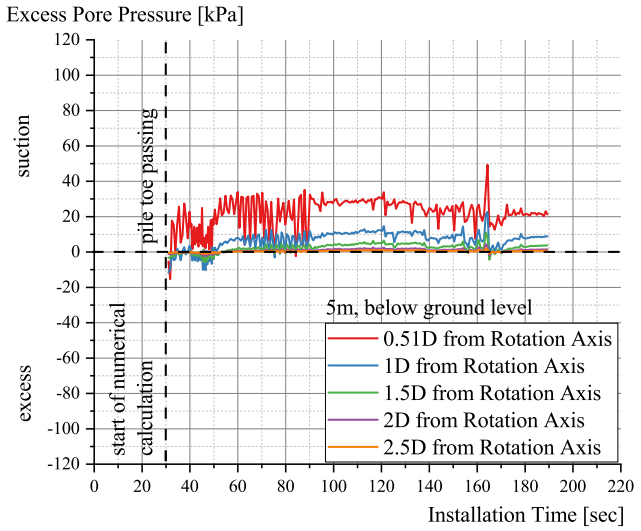

(a) Excess Pore Pressure calculated 5m below ground level

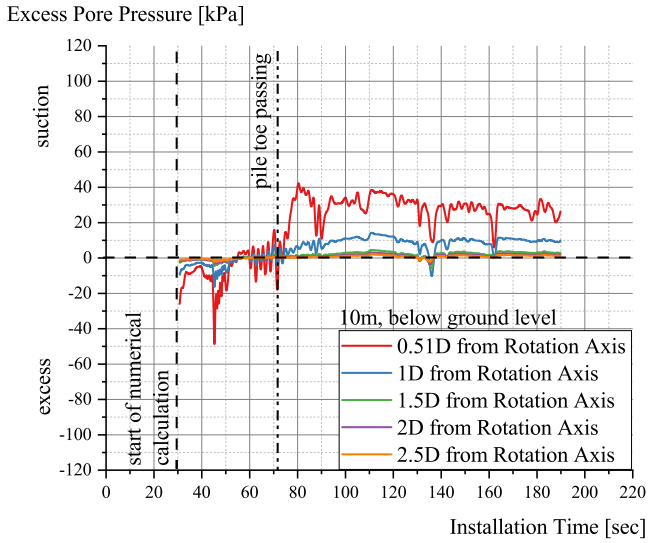

(b) Excess Pore Pressure calculated 10m below ground level

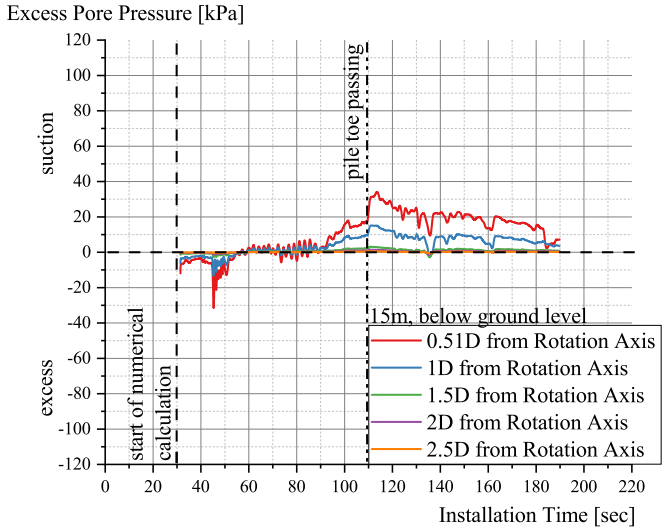

(c) Excess Pore Pressure calculated 15m below ground level

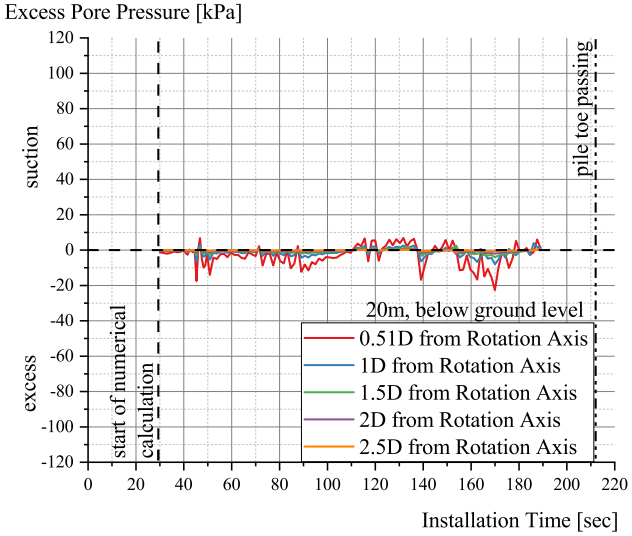

(d) Excess Pore Pressure calculated 20m below ground level

Figure 6.21: Calculated Excess Pore Pressures varying distances from rotation axis

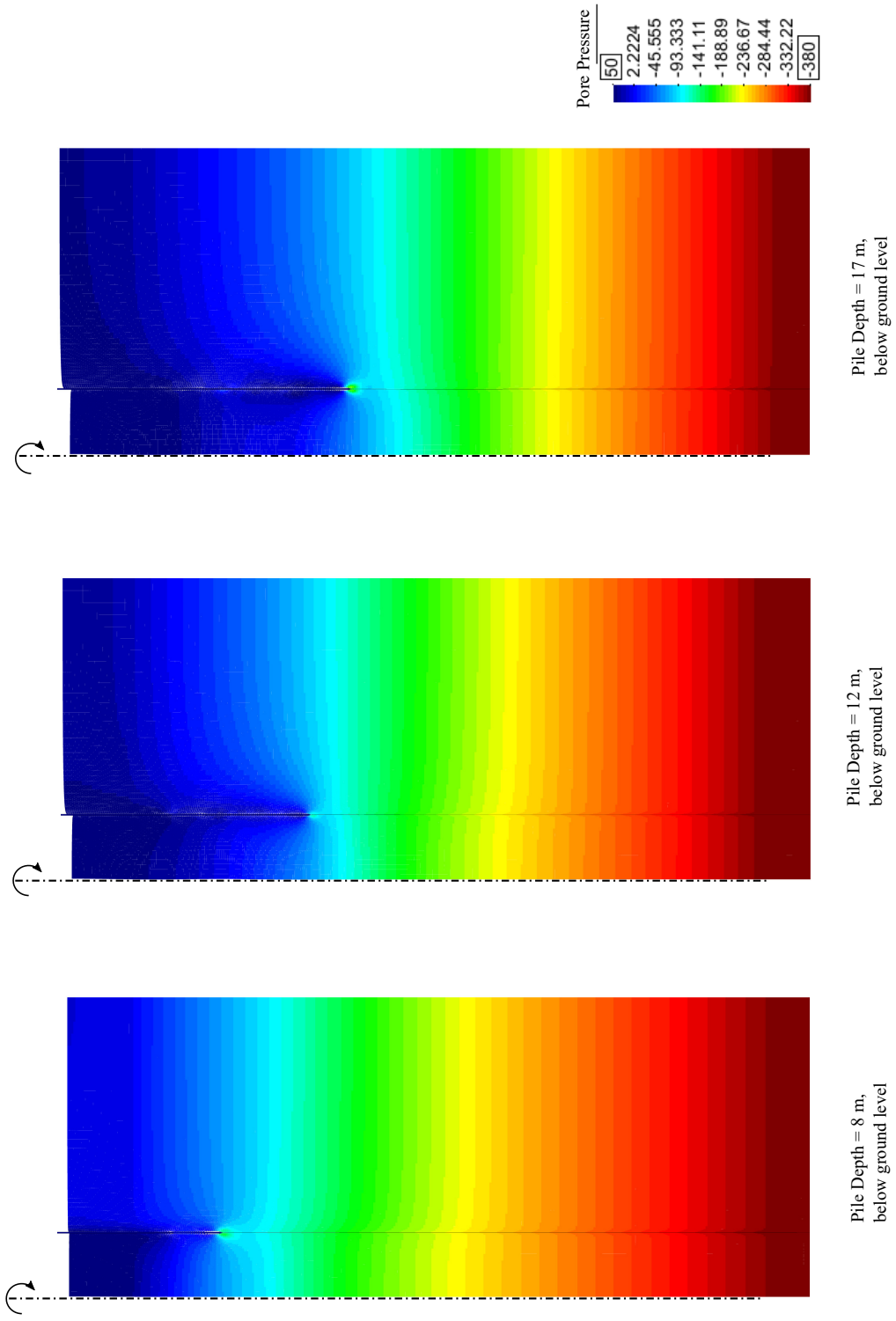

Figure 6.22: Countours of Pore Pressures of soil around Pile P4, at depths 8 m(left), 12 m (middle), and 17 m (right) from surface

Comments on the excess pore pressures

Figure 6.21 plots the pore pressure is plotted at different locations; i.e., at depths of 5, 10, 15, and 20 m, and at distances of *0.51D*, *1D*, *1.5D*, *2D*, and *2.5D* from the rotation axis. The pore pressures are compared to installation time. The pore pressures tend to be proportional to the vertical distance between the pile toe and the control point in all four figures. As the pile approaches the control point, the excess negative pore pressure rises. As the pile toe approaches the control point, the excess pore pressure flips to a positive value. Positive pore pressure corresponds to the suction zone, while negative pressure corresponds to the excess zone. As the pile toe passes the control point, the maximum value of pore pressure was measured. After that, the excess pore pressures exhibited a slow tendency to approach their geostatic value. As the horizontal distance between the pile and the control point increases, the pore pressures also tend to exhibit a lower peak value. As the horizontal distance between the control point and the pile shaft increases, it can be inferred that the accelerations in the porous soil continuum diminish, resulting in a reduced excess pore pressure response. Chai et al. [46] also reported a similar decrease in excess pore pressure as the measurement point is moved farther from the shaft. As the pile approaches the control points, the acceleration of the soil imparted by the vibrating pile is inferred to increase. As the pile passes the control point, the sole source of soil excitation is the pile shaft, resulting in a decrease in dynamic acceleration and, consequently, a reduced pore pressure response. Snapshots of the pore pressures at pile depths 8, 12 and 17 metres from the surface are shown in Figure 6.22. A localised zone of excess pore pressures below the foot of the pile, as reported by reference [172] is observed in this simulation as well.

The rise and fall in pore pressure over time must be thoroughly analysed. Reference [41] was the pioneer in correlating the change in excess pore pressures with the distance between the CPT cone and the pressure sensor. While the cone was still some distance from the sensor, an increase in negative pore pressure was observed. On the contrary, as the cone approached the sensor, a positive pore pressure reading was recorded. Positive pore pressures were attributed to a zone of compression beneath the cone, while negative pore pressures were attributed to soil dilation caused by shearing. This dilation increases the void volume, reducing the pore pressures and increasing the effective stresses; it is more pronounced in dense sands [154]. As the pile advances past the control point, the reversal of pore pressure is explicable based on the findings of reference [31]. In their research, Bonita [31] vibrated the CPT cone and measured the tip's excess pore pressure. A positive pore pressure value was always measured. Since the control point was so close to the cone structure, it could be argued that a similar analogy can be drawn in the present work as well.

Remarks on soil movement around pile

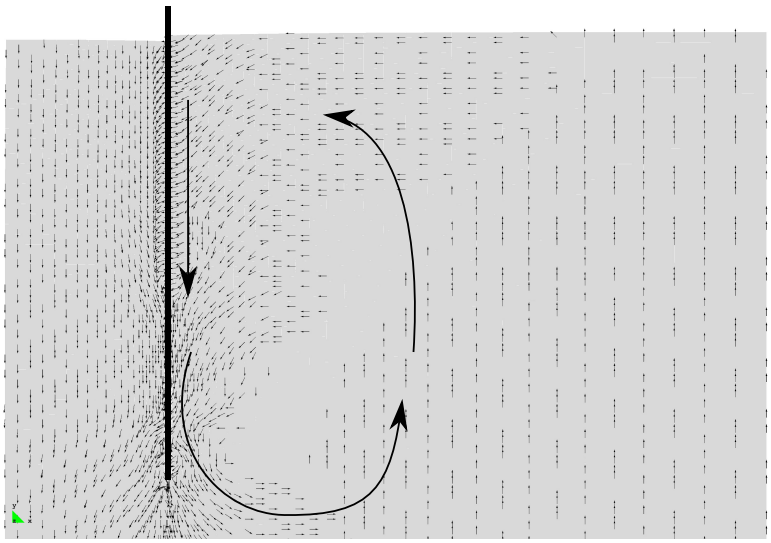

Figure 6.23: Movement of soil continuum around pile at a depth of 8 m from surface

Osinov et al. [172] examines the development of the displacement field in the area of the pile foot. In the study, a liquefaction zone was determined to exist close to the cylinder-shaped solid pile, beginning with a uniform stress state. An accumulation of residual displacement in the form of soil rotation has been observed by a numerical investigation. In the zone where excess pore pressure was detected, rotation of the soil was computed. Reference [9] also reports a similar soil rotation regime during modelling of pile hammering. Both sources were concerned with miniature pile models. In this work, however, when the monopile with a large diameter is vibrated into the saturated soil, a comparable soil rotation regime is seen. The centre of rotation is roughly in the region where excess pore pressures were recorded (See Figure 6.21), as reported in reference [172]. The CPDI model is thus capable of capturing the granular motions of the soil continuum as a result of higher pore pressures.

Concluding remarks

In conclusion, the back-analysis of the *VibroPile* project has achieved its intended purpose, namely the elimination of uncertainties associated with vibratory pile installation. Having simulated the vibratory pile installation with available field data, we may not only use the CPDI+UBCSAND numerical package developed for predicting the pile installation behaviour in advance, but also use it to gain insight into the change of soil state as the pile installation progresses. The soil's final state parameters - stresses, pore

pressure, and strain - can be transmitted to a commercial finite element software to provide the initial state for calculating the lateral pile behaviour of the installed monopile. When waves impact a pile foundation, they impart a cyclic load, which makes lateral behaviour important. The results of the simulation can also be used to make observations regarding the usability of the system. To properly validate the model, the next step would be to apply the numerical package to a *Class-A* pile installation prediction.

6.4 Application of CPDI for Class-A offshore monopile vibratory installation prediction

After validating the CPDI+UBCSAND package for the back-analyses of model- and real-scale pile installations, a *Class-A* (pre-event) prediction of the pile installation depth was performed. To the best of our knowledge, this is possibly the first time such a project has been undertaken, in which the installation forecast of a monopile being vibrated into the seabed is performed prior to the event. Prior to installation, Zaaijer [224] modelled the dynamic lateral behaviour of offshore foundations and compared the results to experimental data. In order to predict the lateral behaviour of offshore monopiles, reference [39] developed the so-called *PISA* design model, which was the result of a major European industry-academic collaboration. The project's focus was on large diameter rigid piles with low length-to-diameter (L/D) ratios that were embedded in clay. In this study, an initiative was undertaken to predict the installation behaviour of monopile installation using vibratory methods prior to offshore installation in order to provide an estimate of the time required to install the monopile. Thereafter, the results of the *Class-A* predictions are compared to field data to determine whether the developed tool is indeed reliable for use in simulations of offshore pile installation.

The forecast model for pile installation was created as part of the research project known as 'VISSKA', which is the German acronym for 'Messung Modellierung und Bewertung der alternativen Gründungsmethode **V**ibrattionsrammung in Bezug auf **I**nstallation, **S**challemissionen und Auswirkungen auf **S**chweinswale im Offshore-Windpark "**KA**S-KASI II" - "**VISSKA**"'. It can be translated into english as "Measurement, modelling and assessment of vibratory pile driving in relation to installation, noise emissions and effects on harbour porpoises at the KASKASI II offshore wind farm". The objective of the research project is to investigate the viability of vibratory pile installation for monopiles at the KASKASI II offshore wind park. Additionally, the project seeks to investigate the impact of noise emissions during installation on the behaviour of North Sea-dwelling porpoises. The German Ministry of Economic Affairs and Energy provided the research project, which is being conducted by project partners from both industry and academia. In the past, individual blows from a hydraulic hammer were used to pound offshore wind turbine foundations into the seafloor. The foundations will be driven by vertical vibrations, according to the plan. It is anticipated that this

will be the first commercial offshore windpark to use the improved vibratory installation for installing all of the wind turbine foundations into the seabed. The wind farm, with an installed capacity of 342 megawatts, is expected to generate enough renewable energy to power nearly 400,000 homes.

Model and boundary conditions

For the numerical model, an axially symmetric boundary condition and the penalty contact algorithm, together with the two-phase CPDI formulation and the UBCSAND model were considered, all of which had been utilised successfully in simulations described thus far. The UBCSAND model, which was previously employed for both model and actual scale tests of pile installation that yielded acceptable results for back-calculation or *Class-C* analysis of the experiments, is employed once again, but this time for Class A predictions. *Class-A* predictions are especially difficult because the available data to build the model are scant, if adequate. To develop a model that can simulate the dynamic process with reasonable accuracy and complete the task in a reasonable amount of time, reasonable assumptions must be made. In order to achieve this, the following assumptions are made about the model:

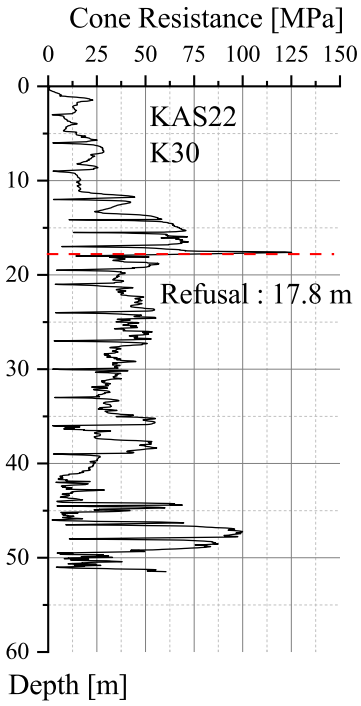

Figure 6.24: Measured CPT data at planned location of Pile K30

1. It is assumed that the soil is completely saturated.

2. It is assumed that the soil is homogenous and isotropic. The behaviour of the soil is smeared across the entire continuum to generate a single parameter set for the numerical simulation.

3. It is assumed that the pile has a constant cross section.

Given that the location of foundation installation is offshore, the assumption that the soil is fully saturated (S_r = 1) is not only reasonable, but also considered obvious. The second premise, that the soil has been homogenised, is grounded more in computational and practical reality. The only available data that sheds light on the variability of the soil is the cone resistance value from the CPT test. Within the perimeter of the site of interest, it is well known that CPT data exhibit spatial variability [30, 125, 171, 215]. The location of the CPT test conducted for the project is a few metres away from the location where the pile foundation was to be installed. Given this, it would be impractical to calibrate multiple sets of parameters for the soil model, given that the parameter set may not accurately represent the field condition. In this regard, the decision to assume a homogeneous soil continuum for the current study is entirely justified. It was assumed that the relative density, I_d of the soil was 100 percent. As depicted in Figure 6.24, this was determined by analysing CPT data from a site close to the planned location of Pile K30. The analysis and subsequent homogenisation of the CPT data is presented in Appendix E.

Lastly, it is assumed that the pile has a constant cross-section. This decision is based more on the practical realities of the CPDI code, and in part, convenience. The original geometry of the pile consists of 20 cans stacked on top of one another. The wall thickness and pile diameter of each of these cans varies. The cans, when stacked, reach a height of 59.62 metres, with each can ranging in length from 0.24 metres to 3.93 metres and wall thickness from 0.05 metres to 0.328 metres. While 0.328 m represents the pile flange section, which is an exceptional component of the monopile, the wall thickness typically ranges from 0.05 m to 0.085 m. For there to be a significant difference in the results, the current number of particles per cell, approximately nine, must change. Consequently, the background computational mesh must be significantly refined, resulting

Parameter	Value
Frequency of Vibrator	20 Hz
Static moment of the vibrator	1,920 kgm
Total mass, with mounting elements	435 ton
Static load	4,266 kN
Dynamic load	30,319 kN

Table 6.9: Vibrator parameters from VISSKA project

Parameter	Value
Outer diameter	6.0 m
Wall thickness	70 mm
Total mass of pile	646.6 ton
Total length	59.62 m
Embedded length	27.7 m

Table 6.10: Pile parameters from VISSKA project for Pile K30

in a reduction in the calculation's incremental time step. Experience with the code suggests that such an exponential increase in the complexity of mesh preprocessing is not justified by the marginal improvement anticipated from the computation. Table 6.9 tabulates the parameters of the Cape Holland Triple CV-640 VLT-U used in the installation of monopiles are tabulated. Table 6.10 illustrates the homogenised pile dimensions for pile K30 used in this study.

The Cuxhaven soil parameter are tabulated in Table 6.11. The soil characteristics and geological history of Cuxhaven are assumed to be comparable to those of the planned offshore windpark site. In addition, an abundance of high-quality laboratory data were available for the model, as were parameters for the hypoplastic soil model, which could be used to compare the results with those of the UBCSAND model. In references [73, 74], the differences between the hypoplastic soil model and the UBCSAND model within the context of the two-phase code were already investigated for Berlin Sand.

The axially-symmetric continuum depicted in Figure 6.25, which consists of the soil and pile continuum, was discretised with approximately 27,000 particles and 13,000 interface elements, which simulated pile-soil contact. The background computational grid consisted of a tartan grid, with the smallest rectangular grid measuring 0.1 m by 0.01 m. This background grid density was deemed adequate to provide a reasonably accurate solution that could converge well without imposing an excessive computational burden. Utilising a regular meshing scheme, more particles were packed in the vicinity of the pile's jacket. The pile was embedded five metres into the ground prior to start of simulations. Due to the fact that the amount of pile penetration due to gravity cannot be accurately estimated in advance, this initial depth was chosen in part to improve

$N1_{60}[-]$	$m_e[-]$	$n_e[-]$	$n_p[-]$	$K_G^e[-]$	$K_B^e[-]$
42.6	0.5	0.5	0.95	1432	854
$K_G^p[-]$	$\phi_{pt}[^\circ]$	$\phi_f[^\circ]$	$c[kPa]$	$Pa[kPa]$	$\sigma_t[kPa]$
820	32.6	37.9	0	100	0
$hfac_1[-]$	$hfac_2[-]$	$hfac_3[-]$	$hfac_4[-]$	$hfac_5[-]$	$hfac_6[-]$
0.65	0.85	1.0	0.6	1.0	0.95

Table 6.11: UBCSAND model parameters for Cuxhaven Sand, I_d = 100%

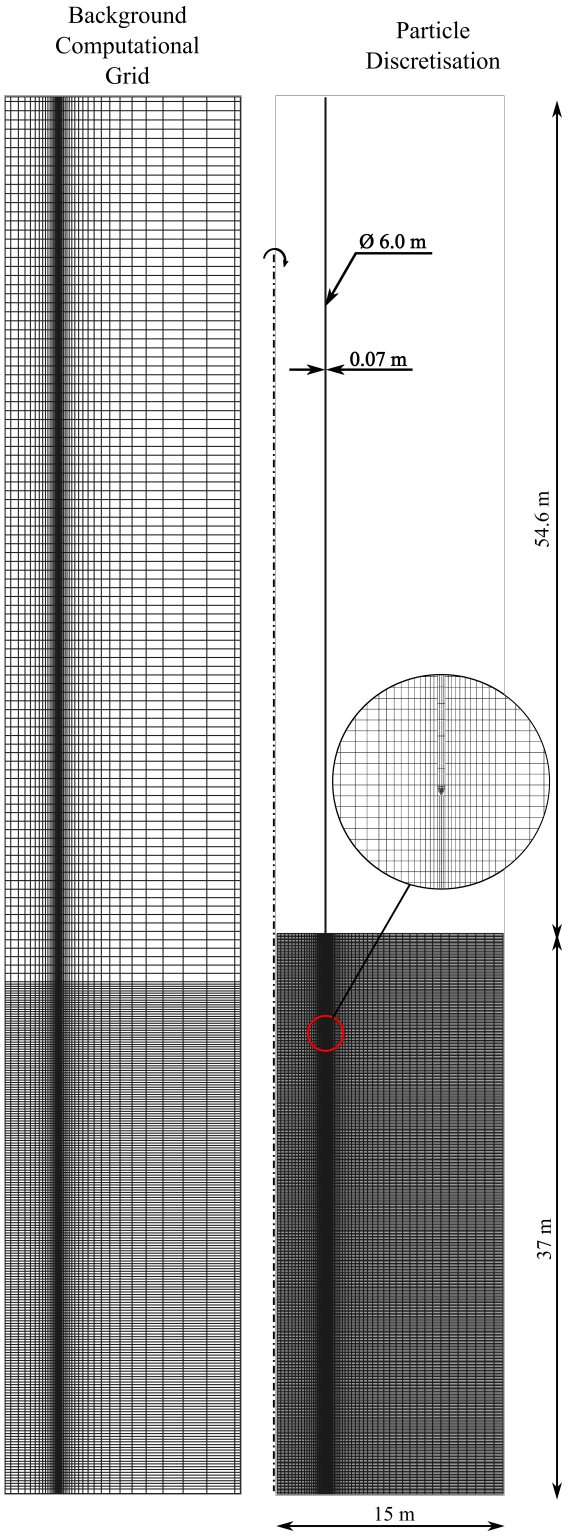

Figure 6.25: Background computational grid discretisation (Left), and Particle discretisation of pile and soil (Right)

the numerical stability of the model. Adopting a continuously-updated dynamic time marching scheme, the time step was modified every 1,000 iterations based on the continuously evolving stiffness. Two percent particle-in-cell damping was applied to both the solid and liquid phases. The simulation continued until the final embedment depth was approximately attained.

Analysis of vertical pile penetration results

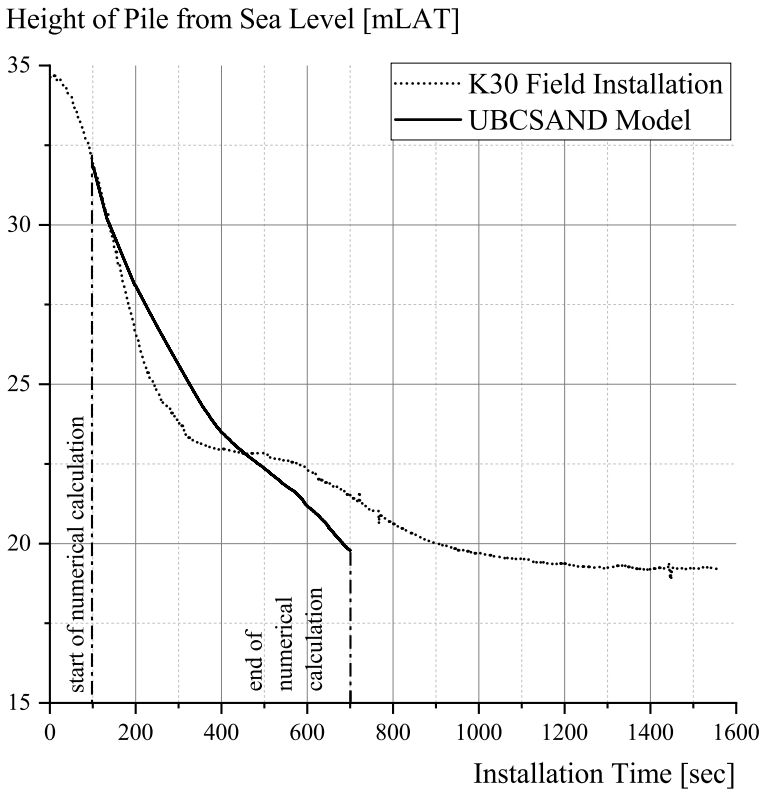

Figure 6.26: Vertical penetration of the pile - Numerical vs. Measured at field

Figure 6.26 illustrates the results of the pile penetration, including both experimentally measured data and numerical results. In comparison to the experimental results, we can observe a reasonably good penetration behaviour from the results. Despite assuming a highly homogenised and idealised model setup, there is a reasonable correlation between the field and the calculated numerical data. This indicates that the CPDI+UBCSAND tool performed well when applied to the numerical forecast of pile installation. Two triumphs of the capability of the numerical tool can be highlighted here: i) a reasonable match with the field data, in which the numerical model reaches the embedment depth reached by the offshore vibration installation, and ii) the achievement of a stable solution simulating the vibratory process of an offshore monopile. This work is, to the best of our knowledge, the first to simulate pile vibration in large time

Parameter	Value
Location	K30
Easting [m]	419219
Northing [m]	6038386
Water depth LAT [m] - GEOENG 2012	22.66
Water depth LAT [m] - LAT (FUGRO 2015)	22.57
Water depth LAT [m] used in Design	22.57

Table 6.12: Measure depth of the water at location of Pile K30

scales (greater than 10 minutes) within the framework of two-phase CPDI. While the results are encouraging, a more in-depth analysis is required.

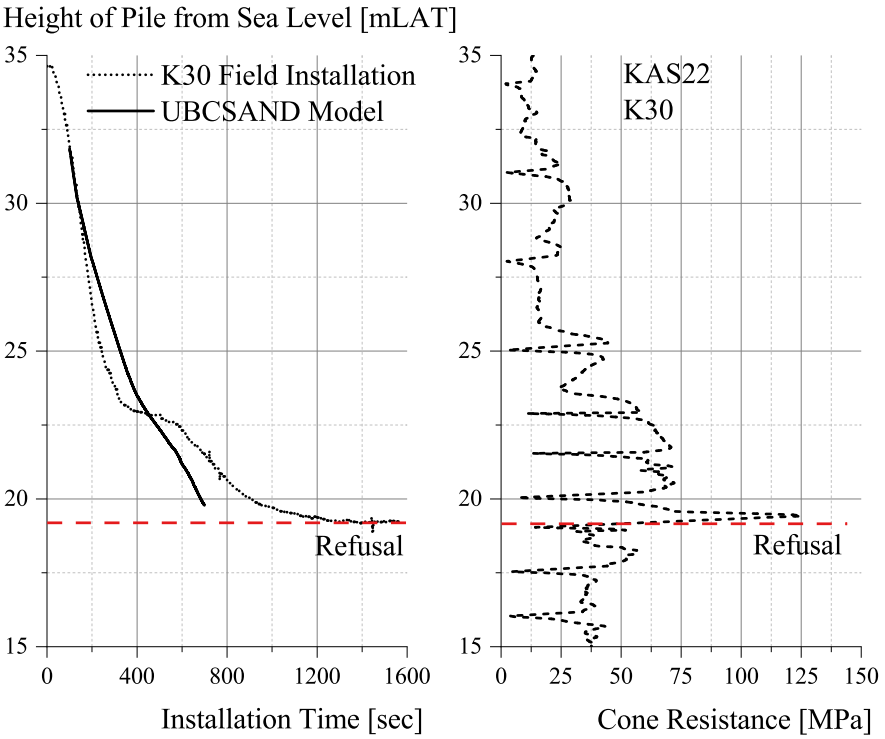

Figure 6.27: Installation compared against the CPT data measured from Sea Level for Pile K30

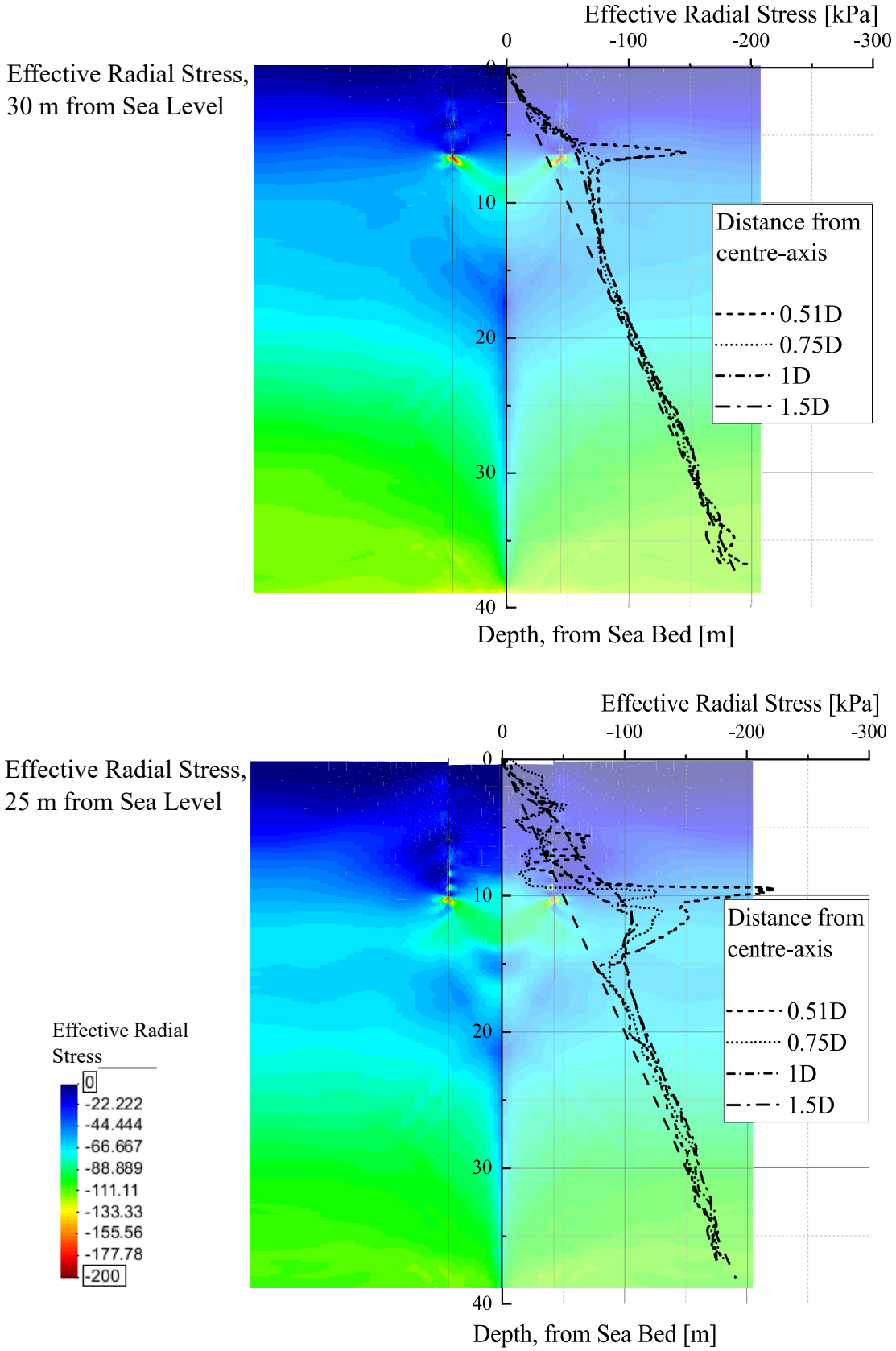

Figure 6.28: Effective stress of soil, 30 m (top) and 25 m (bottom) below Sea level

The Table 6.12 shows the depth of the seabed from the surface of the water. The pile height at which the vibration process began was recorded as 34.816 metres, which would imply a self-weight penetration of 2.234 metres. The numerical model assumed a 5 m self-penetrating depth. This decision, however, was deliberate and not the result of calculations. This decision was also dictated by numerical considerations. During the first 50 seconds of simulation, the installation rates derived from field data and numerical simulation are comparable and very close. In comparison to field data, the results of the numerical simulation indicate a stiffer response beyond the 150-second installation time. Figure 6.27 corroborates the results from CPT data for the location, which explains the softer response from the field data. In the numerical model, it is assumed that the relative density is homogeneous and constant. In the field, between depths of 30 m and 25 m below sea level, a zone of decreased cone resistance is measured, indicating a zone of decreased relative density when compared to the assumption of a density of 100 percent. This assumption of a region of greater relative density would explain why the numerical simulation result was stiffer than the field measurement.

Over a depth of 25 metres below sea level, the cone resistance tends to increase. This trend is maintained until a depth of 15 metres below sea level. This layer of denser soil explains why the rate of pile installation has decreased. Again, the homogenisation soil continuum assumed by the numerical model cannot accommodate this localised zone of extremely dense soil. At a depth of 15 metres, the cone resistance increases further, resulting in a further decrease in pile installation rate. At this point, the more rigid numerical model intersects and surpasses the field data. However, the pile in the field encounters a local zone of highly compacted soil. The pile vibrates with minimal horizontal movement for approximately one hundred seconds. In contrast, the numerical model begins to exhibit a decreased installation rate. This decrease in the numerical model can be explained by the increased friction acting on the pile shaft as it approaches greater depths, as well as the increased stress-dependent stiffness developed by the UBCSAND model. Both the numerical model and the vibrating pile in the field demonstrate a slower installation overall. In comparison to the field data, the numerical model begins to exhibit a softer behaviour beyond 15 metres depth. The vibration continues in the field to a depth of 17 metres below sea level, after which refusal was reported. The depth at which refusal is encountered correlates well with the CPT test results in which 125 MPa of cone resistance is encountered. After approximately 10 minutes of calculation time, the simulation was terminated at this point.

Figure 6.28 depicts the effective stress values at two distinct pile heights, approximately 30 m and 25 m from Sea Level. As observed in a previous simulation of *VibroPile* and as expected, the effective stress is greatest around the pile's jacket. As the control plane is moved away from the pile, the effective stress value recovers to its geostatic value. The results of this contour are consistent with expectations. In addition, the stress state around the pile can be retrieved and sent to a different commercial software that can replicate long-term lateral or axial cycle tests. Due to its two-dimensional implementation, the CPDI code employed in this work cannot simulate lateral behaviour accurately

at this time.

Following refusal, the vibrator tooling was swapped for the impact hammer tooling. This transition took about two to three hours. Later, the piles were hammered to their final embedment depths. Overall, the results of the numerical simulation indicate a very close correlation with the experimental findings. Notably, the simulations performed here are *Class-A* predictions, taking the dynamic effects of the process into account.

Remarks on pile acceleration

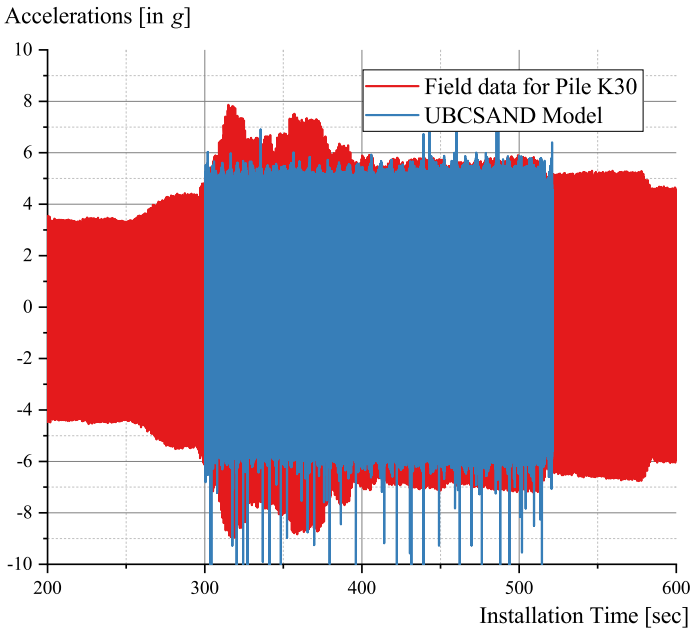

Figure 6.29: Accelerations measured 13 m below pile head

Figure 6.29 was subsequently used to compare the accelerations measured 13 m below the pile head with field data. In this comparison, accelerations from the first 200 seconds of the simulation were disregarded; the numerical simulation was started ater 100 seconds of field installation. The rationale for this decision is that the pile was embedded 5 m while the measured penetration due to gravity was only 2.2 m. Given this assumption, it is reasonable to conclude that the region of soil surrounding the pile would have a different (i.e., undisturbed) stress state than that observed in the field. After beginning the evaluation of accelerations 300 seconds after installation, the stress around the jacket of the pile could be considered comparable, or the soil around the jacket of the pile for the numerical model is at the very least disturbed. Comparing the results of calculated and measured field data reveals that the peak accelerations of the models are quite comparable. The numerical model also captures quite accurately a greater downward acceleration (represented by negative values) than an upward acceleration (shown here by positive values). Labenski [122] describes the variation in

recorded acceleration measured on the pile when vibrated in different soil densities. In light of this, it is reasonable to conclude that the accelerations recorded from the field are not regular, whereas the accelerations calculated from the pile, despite falling within the range of the measured accelerations, are quite regular. Overall, a good correlation is observed between the numerical calculation and the field data.

Concluding remarks

The developed CPDI+UBCSAND numerical package has demonstrated its ability to perform *Class-A* offshore monopile installation prediction. Given the recent push for renewable energy, wind power provides a cleaner and greener alternative to other forms of renewable energy, with the only limitation being the installation space required for monopile foundations. Installation of offshore monopiles using vibratory installation methods has been fraught with uncertainty. By providing a prediction of the installation's behaviour during the design phase, this research aimed to alleviate certain concerns. Ideally, the next step would be to incorporate this tool during the project's design and conception phases. This numerical package would provide designers with the data necessary to optimise their designs and, ultimately, the installation procedure.

6.5 Summary

The two-phase CPDI code presented in Chapter 4 and the UBCSAND model described in Chapter 5 are utilised in this chapter to simulate pile vibration in saturated sand. In addition, simulations of impact hammering on model piles were conducted. In both simulations, a strong correlation was obtained with experimental data. Simulated was also a full-scale monopile from the *VibroPile* project. In this instance, the entire installation procedure was successfully simulated, and a good correlation was seen between the experimental and numerical calculations.

A *Class-A* simulation of monopile installation was also shown. Overall, a fair prediction was made. In addition to simulating the installation rate quite accurately, the algorithm was able to replicate extremely dynamic vibratory pile vibration for over 10 minutes. According to the author's knowledge, this monograph is the first to provide *Class-A* prediction of offshore pile installation simulation. In the current modelling, it is assumed that the soil is a homogeneous continuum. While this simplification allowed for good results to be obtained in a fair amount of time, the next step would be to construct numerous layers of soil to simulate the actual ground situation.

Chapter 7

Conclusions and Recommendations

7.1 General conclusions

The work presented here was the result of research and development efforts aimed at creating a numerical tool to simulate large deformation problems. The first objective was to quantify the dynamic large deformation behaviour of sandy soils, the undrained behaviour of sandy soils, and the effect of the dynamic behaviour on the soils' strength. Due to the complexity involved in convergent to a stable solution at each time step, capturing massive deformations within the framework of finite element has always been a difficult endeavour. The robustness of the solution, and hence its dependability, depends on the precision with which the solution converges to a stable value at the conclusion of each time step. The second objective was to ensure that the soil's porous media behaviour is adequately reflected. To accurately depict the actual state of the soil as it is dynamically aroused, the method employed should ideally be hydrodynamically fully-coupled. The third objective was to establish a sophisticated constitutive equation that not only adequately models the soil and captures its response to dynamic stresses, but does so with a minimal processing overhead. All of these efforts lead to the creation of the UBCSAND+CPDI code that was utilised in this study.

A further objective was to establish a dependable calculation tool with the capability of capturing the large deformations of the model while also taking into account the fully saturated nature of the soil and accurately capturing the physics of the soil as a result of the dynamic excitations in the soil. This effort resulted in the development of a tool that provides a numerical package that is that is capable of capturing the large deformations that occurs in saturated porous media while also providing the capacity to capture the inherent physics of the fluidisation of soil. The two-phase CPDI code that was developed and used in this work has, through the validation cases shown in this study, not only was able to provide reasonable results for the back-calculation of experiments and field tests, but was also applied to *Class-A* prediction of the pile installation forecast with good accuracy. This study was carried out to determine whether or not the two-phase CPDI code that was developed and used in this work could successfully capture the soil-structure interaction of axially-symmetric two-phase systems.

Convected Particle Domain Interpolation method

The second chapter of the thesis (Chapter 2) was dedicated for a literature study on the current state of the art in terms of numerical approaches, with a particular focus on massive deformation. The Convected Particle Domain Interpolation (CPDI) Method, which is an advanced version of the Material Point Method, was chosen for the use in this study as a result of the literature review. This is despite the fact that there is a plethora of numerical methods that can be used. According to the findings of the literature review, the CPDI approach was found to demonstrate superior consistency and accuracy in comparison to the traditional MPM formulation. Because the CPDI code was used as the foundation for the numerical modelling, not only was a solid and well-developed foundation guaranteed for the subsequent simulation of the soil, but also of the structures that interact with the soil. This was accomplished by adopting the CPDI code as the base for the numerical modelling.

Chapter 3 provided the numerical makeup of the CPDI code. While in the material point method (MPM), the continuum is represented by material points, wherein the continuum paramters like stress, strain and other state variables get stored, in the case of CPDI, the material points are extended to domains. The incremental solution for the momentum equation is solved on the background computational grid. The numerical make-up for a two-dimensional element formulation, which consists of four-noded regular rectangular elements was provided in the work. It's extension to the CPDI formulation was also presented. The CPDI formulation's extension to the axially-symmetric framework, after the work of Hamad [82] was presented in this work. Through the use of Method of Manufactured solution (MMS), single element tests as well as through large continuum examples, the CPDI code was validated. Through this validation, it was ascertained that the not only is the implementation of the CPDI code proper, but also that for cases where the single-phase continuum structure will interact with the soil, the results that are expected from such interactions were reliable.

The formulation of the penalty contact algorithm, following the implementation of Hamad [82] was provided. To refine the contact between two continuums in CPDI, the predicted contact surface was further discretised with linear one-dimensional elements. On the basis of these elements, continuum contact could be evaluated. The contact algorithm implemented in CPDI was compared to the findings of the commercial finite element programme ABAQUS™.

The code was then compared to the granular collapse benchmark test. The objective of this study is to compare the final run-off calculated by the numerical model to the experimental results. In addition to handling massive deformations and capturing the intricate movement of the soil column as it collapses, the CPDI code was also able to estimate the final run-off distance with fair accuracy. Here, the knowledge-gap of the many modelling parameters of the CPDI technique was filled, specifically the influence of number of particles per computing grid, the effect of various smoothening

algorithms, and the effect of local damping on the final results. The results of this investigation were helpful in determining the values of these parameters for later, more complicated calculations. The dependence of the final result on the constitutive law was also investigated. At various time intervals, the run-off distance from the numerical simulation was compared to the experiment, and it was demonstrated that the findings obtained using the CPDI code are remarkably comparable to those from the experiment.

The extension of the single-phase CPDI algorithm to model pore fluid was presented in Chapter 4. The governing equations, as well as the extension of Kelvin-Voigt elements for saturated media, were derived by reference [107]. This formulation enabled simulation of the behaviour of saturated materials. The solid and pore fluid dynamic equilibrium was computed at the background computational grid, while the mass balance of the components and constitutive laws for both the soil and fluid are developed at the material point level. The implementation of the two-phase CPDI code was evaluated using the well-known one-dimensional consolidation problem after Terzaghi [204], with excellent convergence between the analytical solution and the two-phase CPDI code's output.

Constitutive law : UBCSAND

Chapter 5 described the numerical structure of the UBCSAND constitutive model, an elasto-plastic model capable of simulating the liquefaction of non-cohesive soils. Within the framework of a two-phase CPDI, the implemented constitutive law was programmed according to the FISH code presented in reference [159]. The implementation of the model was validated using a straightforward single element test. The test results suggested that the applied UBCSAND model was able to capture the complete liquefaction of the loose sand sample. The model was then implemented inside the framework of the two-phase CPDI, and the implementation was evaluated using the classic shake table test as a benchmark. This was done to validate the model's implementation under dynamic loading within the CPDI code. The results of the shake table test demonstrated that the UBCSAND model in conjunction with the two-phase CPDI code accurately predicted the liquefaction of the sample. The experiment-observed top-down liquefaction was likewise computed in the computational model. A parameter test was conducted to determine the influence of boundary conditions and hydraulic conductivity on the final results.

Numerical simulation of monopile installation

The purpose of this Chapter 6 was to determine if the numerical package developed here was capable of predicting the offshore monopile installation rate. After experi-

mental examination of vibratory [186] and impact installation of model monopiles [9], a back-analysis utilising the developed numerical package was conducted. As the pile vibrates or was hammered into the soil, it was essential to capture the stress state change caused by pile-soil interactions, which governs the installation rate and the development of excess pore pressures (or suction). The numerical results from the CPDI code were compared to the experimental values, and a satisfactory match was found for both the vibrated and hammered monopiles. The generation of excess pore pressure was comparable to the measured values. As the pile is being installed, the numerical code was able to record both the excess and suction zones of pore pressure that form in the soil continuum. Through the study of effective radial stresses, the installation process's effects on the soil was also determined. In the case of vibrated piles, the zone of influence extended to *1.5D*, after which the effect of pile installation on the change of soil stress state began to diminish. However, the zone of influence for the hammered pile extended beyond *1.5D*, up to *2D*, after which it began to diminish.

To investigate the viability of using the numerical package to large diameter offshore monopiles, a back-analysis of a vibrated pile performed as part of the *VibroPile* project was performed. In order to recreate the field test as accurately as feasible, the varying installation frequency was also incorporated into the input. Pile P4, one of the three vibrated monopiles, was selected for comparison with the simulation. The simulation was performed for approximately 200 seconds. When the pile depth results were compared to the field data, a very good match was found. The calculation evaluated the impact of the installation process on radial stresses of the soil. As observed in the case of the model pile, the zone where radial stresses changes may be calculated extended to *1.5D*. This knowledge can be useful to designers, who can consider this information during the planning phases of monopile foundation projects requiring the installation of many monopiles. Also analysed were the excess pore pressures observed at certain control locations. Given the difficulties of installing and monitoring these sensors, measuring such granular data from the field was a difficult undertaking. Having previously confirmed the results for the model monopile, the results from the *VibroPile* model can be deemed reliable because the same numerical approach and constitutive law were applied. Similarly, a suction zone was computed as the pile toe passes the control point, which was preceded by an excess pore pressure zone when the pile was sufficiently distant from the control point. As the monopile near this control point, the pressures reversed. It is also noted that the influence of installation on the excess pore pressure declined increasingly with distance from the measurement point. Beyond *1.5D*, there were no discernible excess pore pressures. The results of this simulation concluded the initial objective of the study, which was to comprehend the dynamic behaviour of the pile during installation. Not only do the findings of this simulation replicated the observed field behaviour pretty well, but also included granular soil state information that would otherwise be not accessible.

***Class-A* forecast of monopile installation**

The penultimate research objective of this dissertation was to model a *Class-A* offshore monopile vibratory installation and compare it to field data, which was made available after the simulation had been completed. Having assessed the soil state parameters in earlier studies, this study focussed primarily on the prediction of pile depth. When compared to field data, a fair prediction of the pile installation rate was produced. In addition, the measured accelerations for the pile were compared to the calculated numerical results, which revealed a fair forecast. Despite the fact that the current numerical model reduced the problem to two dimensions and disregarded any anisotropy or variations in the seabed soil profile, assuming a homogenous model, the vibration behaviour of piles was accurately predicted.

7.2 Future developments

When it comes to simulating reality, there is always room for improvement, even though progress was made in simulating large deformation of saturated soil, and capturing the dynamics that occurs in the soil due to loading conditions. In the application of the CPDI numerical code for pile installation, the homogeneity of the soil continuum was one of the most important assumptions. This, however, is not the case in the real world, as soil is an inherently heterogeneous material, with density and composition varying with depth. When pile installation behaviour is addressed, the presence of such interstitial layers is expected to have an effect. A multi-layered continuum simulation that is not restricted to the use of a single constitutive law will be the logical next step in the research. This will allow for a more accurate reflection of reality. In this regard, the CPT data, which are currently evaluated, homogenised, and fed into the code as a single input parameter, must be included as part of the soil characteristics input to the CPDI model. This would necessitate incorporating soil calibration procedures into the CPDI code.

Despite the fact that the CPDI code was capable of simulating the dynamics of both soils and structures, the time required for such calculations was quite extensive. The simulation performed as part of the VISSKA project, as detailed in Chapter 6, required an average of 60 minutes per second of numerical simulation. This resulted in a computation time of approximately 25 days, despite the code's OpenMP implementation. Future versions of the code must incorporate the MPI (message passing interface) standard in order to increase the computational efficiency of such models. This would enable the use of high-performance computers whose access is currently available but for which code is incompatible with their architecture.

Coupling of the CPDI code and a CFD solver to investigate the pressure wave propa-

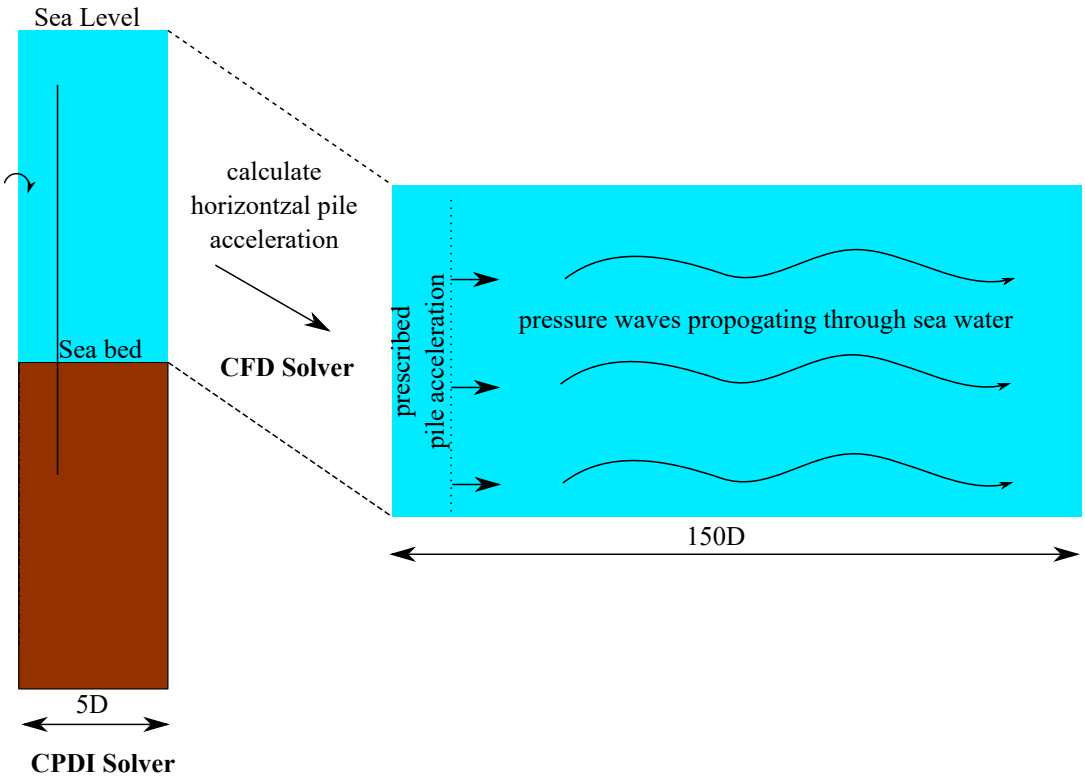

Figure 7.1: Concept of a coupling between the CPDI code and CFD solved

gation through the sea water during pile installation is another area where substantial contributions can be made. A CPDI model's computation time is proportional to the number of particles packed into the mesh. The conventional installation of piles generates high underwater sound waves, which is detrimental to aquatic life. To predict these waves prior to installation would necessitate simulating massive boundaries, which is not feasible in CPDI due to high computational time. As conceptualised in Figure 7.1, this can be mitigated by coupling the CPDI code with a CFD solver. This would aid in simulating the behaviour of the soil continuum during the installation process and monitoring the propagation of the induced pressure waves.

Bibliography

[1] Achmus, M., Schmoor, K. A., Herwig, V., and Matlock, B. (2020). Lateral bearing behaviour of vibro-and impact-driven large-diameter piles in dense sand. *Geotechnik*, 43(3):147–159.

[2] Alavi, A. H. and Gandomi, A. H. (2012). Energy-based numerical models for assessment of soil liquefaction. *Geoscience Frontiers*, 3(4):541–555.

[3] Andersen, S. (2009). *Material-point analysis of large-strain problems: modelling of landslides*. PhD thesis, Aalborg Universitet, Department of Civil Engineering.

[4] Andersen, S. and Andersen, L. (2010). Modelling of landslides with the Material-Point Method. *Computational Geosciences*, 14(1):137–147.

[5] Andrus, R. D. and Stokoe II, K. H. (2000). Liquefaction resistance of soils from shear-wave velocity. *Journal of geotechnical and geoenvironmental engineering*, 126(11):1015–1025.

[6] Aubram, D. (2014). *An arbitrary Lagrangian-Eulerian method for penetration into sand at finite deformation*. PhD thesis, Technische Universität Berlin, Fakultät VI - Planen Bauen Umwelt.

[7] Aubram, D., Rackwitz, F., and Savidis, S. A. (2017). Contribution to the non-lagrangian formulation of geotechnical and geomechanical processes. In *Holistic Simulation of Geotechnical Installation Processes*, pages 53–100. Springer.

[8] Axelsson, G. (2000). *Long-term set-up of driven piles in sand*. PhD thesis, Royal Institute of Technology, Stockholm, Department of Civil and Environmental Engineering.

[9] Bakroon, M. (2020). *Employment of a Multi-Material ALE approach using nonlinear soil models to simulate large deformation geotechnical problems*. PhD thesis, Technische Universität Berlin, Fakultät VI - Planen Bauen Umwelt.

[10] Balmforth, N. J. and Kerswell, R. R. (2005). Granular collapse in two dimensions. *Journal of Fluid Mechanics*, 538:399–428.

[11] Bandara, S. S. (2013). *Material point method to simulate large deformation problems in fluid-saturated granular medium*. PhD thesis, University of Cambridge Cambridge.

[12] Bardenhagen, S. G. and Kober, E. M. (2004). The generalized interpolation material point method. *Computer Modeling in Engineering and Sciences*, 5(6):477–496.

[13] Bathe, K.-J., Ramm, E., and Wilson, E. L. (1975). Finite element formulations for large deformation dynamic analysis. *International journal for numerical methods in engineering*, 9(2):353–386.

[14] Beaty, M. and Byrne, P. M. (1998). An effective stress model for pedicting liquefaction behaviour of sand. In *Geotechnical Earthquake Engineering and Soil Dynamics III*, pages 766–777. ASCE.

[15] Beaty, M. H. and Byrne, P. M. (2011). *UBCSAND constitutive model version 904aR*.

[16] Belkhatir, M., Arab, A., Della, N., and Schanz, T. (2014). Laboratory study on the hydraulic conductivity and pore pressure of sand-silt mixtures. *Marine Georesources & Geotechnology*, 32(2):106–122.

[17] Belytschko, T. and Hsieh, B. (1973). Non-linear transient finite element analysis with convected co-ordinates. *International Journal for Numerical Methods in Engineering*, 7(3):255–271.

[18] Belytschko, T. and Kennedy, J. M. (1978). Computer models for subassembly simulation. *Nuclear Engineering and Design*, 49(1-2):17–38.

[19] Belytschko, T., Krongauz, Y., Organ, D., Fleming, M., and Krysl, P. (1996). Meshless methods: an overview and recent developments. *Computer methods in applied mechanics and engineering*, 139(1):3–47.

[20] Belytschko, T., Liu, W. K., Moran, B., and Elkhodary, K. (2013). *Nonlinear finite elements for continua and structures*. John Wiley & Sons.

[21] Belytschko, T., Lu, Y. Y., and Gu, L. (1994). Element-free Galerkin methods. *International journal for numerical methods in engineering*, 37(2):229–256.

[22] Beringen, F., Windle, D., and Van Hooydonk, W. (1980). Results of loading tests on driven piles in sand. In *Recent developments in the design and construction of piles*, pages 213–225. Thomas Telford Publishing.

[23] Berrill, J. and Davis, R. (1985). Energy dissipation and seismic liquefaction of sands: revised model. *Soils and Foundations*, 25(2):106–118.

[24] Beuth, L. (2012). *Formulation and application of a quasi-static material point method*. PhD thesis, University of Stuttgart, Institute for Geotechnical Engineering.

[25] Bhattacharya, S., Hyodo, M., Goda, K., Tazoh, T., and Taylor, C. (2011). Liquefaction of soil in the tokyo bay area from the 2011 tohoku (japan) earthquake. *Soil Dynamics and Earthquake Engineering*, 31(11):1618–1628.

[26] Biezeno, C. B. and Grammel, R. (1939). *Technische Dynamik*. Springer-Verlag Berlin Heidelberg GmbH.

[27] Biot, M. A. (1941). General theory of three-dimensional consolidation. *Journal of applied physics*, 12(2):155–164.

[28] Bojanowski, C. (2014). Numerical modeling of large deformations in soil structure interaction problems using FE, EFG, SPH, and MM-ALE formulations. *Archive of Applied Mechanics*, 84(5):743–755.

[29] Bolton Seed, H., Tokimatsu, K., Harder, L., and Chung, R. M. (1985). Influence of SPT procedures in soil liquefaction resistance evaluations. *Journal of Geotechnical Engineering*, 111(12):1425–1445.

[30] Bong, T. and Stuedlein, A. W. (2017). Spatial variability of CPT parameters and silty fines in liquefiable beach sands. *Journal of Geotechnical and Geoenvironmental Engineering*, 143(12):04017093.

[31] Bonita, J. A. (2000). *The effects of vibration on the penetration resistance and pore water pressure in sands*. PhD thesis, Virginia Polytechnic Institute and State University.

[32] Bórawski, P., Wyszomierski, R., Bełdycka-Bórawska, A., Mickiewicz, B., Kalinowska, B., Dunn, J. W., and Rokicki, T. (2022). Development of Renewable Energy Sources in the European Union in the Context of Sustainable Development Policy. *Energies*, 15(4):1545.

[33] Borel, S., Bustamante, M., and Gianeselli, L. (2002). Two comparative field studies of the bearing capacity of vibratory and impact driven sheet piles. In *Vibratory Pile driving and deep soil compaction. Proc. intern. symp., Louvain-la-neuve, 9–10 September 2002*.

[34] Brackbill, J. U. and Ruppel, H. M. (1986). FLIP: A method for adaptively zoned, particle-in-cell calculations of fluid flows in two dimensions. *Journal of Computational Physics*, 65(2):314–343.

[35] Briaud, J.-L., Coyle, H. M., and Tucker, L. M. (1990). Axial response of three vibratory-and three impact-driven H piles in sand. *Transportation Research Record*, (1277).

[36] Bui, H. and Khoa, H. (2011). Bearing capacity of shallow foundation by smoothed

particle hydrodynamics (SPH) analysis. In *Proc., Computational Geomechanics, COMGEO II-Proceedings of the 2nd International Symposium on Computational Geomechanics*, pages 457–468.

[37] Bui, H. H., Sako, K., and Fukagawa, R. (2007). Numerical simulation of soil–water interaction using smoothed particle hydrodynamics (SPH) method. *Journal of Terramechanics*, 44(5):339–346.

[38] Burgess, D., Sulsky, D., and Brackbill, J. (1992). Mass matrix formulation of the FLIP particle-in-cell method. *Journal of Computational Physics*, 103(1):1–15.

[39] Byrne, B. W., Burd, H. J., Zdravkovic, L., Abadie, C. N., Houlsby, G. T., Jardine, R. J., Martin, C. M., McAdam, R. A., Andrade, M. P., Pedro, A. M., et al. (2019). PISA design methods for offshore wind turbine monopiles.

[40] Byrne, P. M., Park, S.-S., Beaty, M., Sharp, M., Gonzales, L., and Abdoun, T. (2004). Numerical modeling of dynamic centrifuge tests. In *13th world conference in Earthquake Engineering*.

[41] Caillemer, B. M. (1975). *An experimental study in the UF static cone test calibration chamber: Part 1, Density distribution of pluvially placed sand. Part 2, Pore pressure distribution around Fugro tip*. PhD thesis, University of Florida.

[42] Calvello, M., Cuomo, S., and Ghasemi, P. (2017). The role of observations in the inverse analysis of landslide propagation. *Computers and Geotechnics*, 92:11–21.

[43] Cameron, D. G., Saadi, R., and Hughes, D. W. (2018). Developments for the Gwynty-Môr Offshore Wind Farm at Mostyn. In *Coasts, Marine Structures and Breakwaters 2017: Realising the Potential*, pages 141–151. ICE Publishing.

[44] Castro, G. and Poulos, S. J. (1977). Factors affecting liquefaction and cyclic mobility. *Journal of the Geotechnical Engineering Division*, 103(6):501–516.

[45] Ceccato, F. (2015). *Study of large deformation geomechanical problems with the Material Point Method*. PhD thesis, University of Padova.

[46] Chai, J.-c., Hossain, M. J., Yuan, D.-J., Shen, S.-l., and Carter, J. P. (2016). Pore pressures induced by piezocone penetration. *Canadian Geotechnical Journal*, 53(3):540–550.

[47] Chen, X., Zhang, L., Chen, L., Li, X., and Liu, D. (2019). Slope stability analysis based on the Coupled Eulerian–Lagrangian finite element method. *Bulletin of Engineering Geology and the Environment*, 78(6):4451–4463.

[48] Chen, Z., Qiu, X., Zhang, X., and Lian, Y. (2015). Improved coupling of finite element method with material point method based on a particle-to-surface contact algorithm. *Computer Methods in Applied Mechanics and Engineering*, 293:1–19.

[49] Clough, R. W. (1960). The finite element method in plane stress analysis. In *Proceedings of 2nd ASCE Conference on Electronic Computation, Pittsburgh PA., Sept. 8 and 9, 1960*.

[50] Costantino, C. J. (1967). Finite element approach to stress wave problems. *Journal of the Engineering Mechanics Division*, 93(2):153–176.

[51] Courant, R. et al. (1943). *Variational methods for the solution of problems of equilibrium and vibrations*. CRC Press.

[52] Cui, L. and Bhattacharya, S. (2016). Soil–monopile interactions for offshore wind turbines. volume 169, pages 171–182. Thomas Telford Ltd.

[53] Dafalias, Y. F. and Manzari, M. T. (2004). Simple plasticity sand model accounting for fabric change effects. *Journal of Engineering mechanics*, 130(6):622–634.

[54] Daryaei, R., Bakroon, M., Aubram, D., and Rackwitz, F. (2018). Numerical investigation of the frequency influence on soil characteristics during vibratory driving of tubular piles. In *International Congress and Exhibition "Sustainable Civil Infrastructures: Innovative Infrastructure Geotechnology"*, pages 48–61. Springer.

[55] Daryaei, R., Bakroon, M., Aubram, D., and Rackwitz, F. (2020). Numerical evaluation of the soil behavior during pipe-pile installation using impact and vibratory driving in sand. *Soil Dynamics and Earthquake Engineering*, 134:106177.

[56] Davis, R. and Berrill, J. (1996). Liquefaction susceptibility based on dissipated energy: A consistent design methodology. *Bulletin of the New Zealand National Society for Earthquake Engineering*, 29(2):83–91.

[57] De Boer, R. (1992). Development of porous media theories - A brief historical review. *Transport in porous media*, 9(1):155–164.

[58] De Boer, R. (1996). Highlights in the historical development of the porous media theory: Toward a consistent macroscopic theory. *Applied Mechanics Reviews*, 49(4):201–262.

[59] De Boer, R. and Ehlers, W. (1988). A historical review of the formulation of porous media theories. *Acta Mechanica*, 74(1):1–8.

[60] De Groot, M., Bolton, M., Foray, P., Meijers, P., Palmer, A., Sandven, R., Sawicki,

A., and Teh, T. (2006). Physics of liquefaction phenomena around marine structures. *Journal of waterway, port, coastal, and ocean engineering*, 132(4):227–243.

[61] Doyle, E. E., Huppert, H. E., Lube, G., Mader, H. M., and Sparks, R. S. J. (2007). Static and flowing regions in granular collapses down channels: Insights from a sedimenting shallow water model. *Physics of Fluids*, 19(10):106601.

[62] Duncan, J. M. and Chang, C.-Y. (1970). Nonlinear analysis of stress and strain in soils. *Journal of the soil mechanics and foundations division*, 96(5):1629–1653.

[63] Elgamal, A., Yang, Z., Parra, E., and Ragheb, A. (2003). Modeling of cyclic mobility in saturated cohesionless soils. *International Journal of Plasticity*, 19(6):883–905.

[64] Estorff, O. v., Heitmann, K., Lippert, S., Lippert, T., Reimann, K., Ruhnau, M., and Schwarz, M. (2013). Unterwasser-Rammschall: eine herausforderung bei der errichtung von Offshore-Windparks und für die numerische Simulation [Underwater noise due to pile driving: a challenge both for the installation of offshore wind energy farms and for numerical simulation]. *Lärmbekämpfung*, 8(2):61–71.

[65] Fern, E. J. and Soga, K. (2016). The role of constitutive models in MPM simulations of granular column collapses. *Acta Geotechnica*, 11(3):659–678.

[66] Fern, J., Rohe, A., Soga, K., and Alonso, E., editors (2019). *The material point method for geotechnical engineering: a practical guide*. CRC Press.

[67] Finn, W. L., Lee, K. W., and Martin, G. R. (1977). An Effective Stress Model for Liquefaction. *Journal of the Geotechnical Engineering Division*, 103(6):517–533.

[68] Frazer, R. A., Jones, W. N. P., and Skan, S. W. (1937). *Approximations to functions and to the solutions of differential equations*. HSMO.

[69] Frewer, M. (2009). More clarity on the concept of material frame-indifference in classical continuum mechanics. *Acta Mechanica*, 202(1-4):213.

[70] Galavi, V., Martinelli, M., Elkadi, A., Ghasemi, P., and Thijssen, R. (2019). Numerical simulation of impact driven offshore monopiles using the material point method. In *Proceedings of the XVII ECSMGE-2019*.

[71] Galerkin, B. G. (1915). Series solution of some problems of elastic equilibrium of rods and plates. *Vestnik inzhenerov i tekhnikov*, 19(7):897–908.

[72] Gaume, J., van Herwijnen, A., Gast, T., Teran, J., and Jiang, C. (2019). Investigating the release and flow of snow avalanches at the slope-scale using a unified model based on the material point method. *Cold Regions Science and Technology*, 168:102847.

[73] Giridharan, S., Gowda, S., Stolle, D. F., and Moormann, C. (2020). Comparison of ubcsand and hypoplastic soil model predictions using the Material Point Method. *Soils and Foundations*, 60(4):989–1000.

[74] Giridharan, S., Stolle, D., and Moormann, C. (2019). Modelling liquefaction using the material point method–an evaluation using two constitutive models. *Cambridge, UK*.

[75] Girolami, L., Wachs, A., and Vinay, G. (2013). Unchannelized dam-break flows: Effects of the lateral spreading on the flow dynamics. *Physics of Fluids*, 25(4):043306.

[76] Givoli, D. and Cohen, D. (1995). Nonreflecting boundary conditions based on Kirchhoff-type formulae. *Journal of Computational Physics*, 117(1):102–113.

[77] Gonzalez, L., Abdoun, T., and Sharp, M. K. (2002). Modelling of seismically induced liquefaction under high confining stress. *International Journal of Physical Modelling in Geotechnics*, 2(3):01–15.

[78] Gowda, S., Hamad, F., Moormann, C., and Stolle, D. (2016). Simulation of Water-Structure Interaction using CPDI. In *19th International Conference on Soil Mechanics and Geotechnical Engineering, Seoul*.

[79] Gowda, S. and Moormann, C. (2019). Parameter study for the effective pile installation in saturated sand using Material Point Method (MPM). In *Proceedings of the XVII ECSMGE-2019, Reykjavik, Geotechnical Engineering Foundation of the Future*.

[80] Green, R. A. and Mitchell, J. K. (2004). Energy-based evaluation and remediation of liquefiable soils. In *Geotechnical engineering for transportation projects*, pages 1961–1970.

[81] Guilkey, J. E., Bardenhagen, S., Roessig, K., Brackbill, J., Witzel, W., and Foster, J. (2001). Improved contact algorithm for the material point method and application to stress propagation in granular material.

[82] Hamad, F. (2014). *Formulation of a dynamic material point method and applications to soil-water-geotextile systems*. PhD thesis, Universität Stuttgart, Institute for Geotechnical Engineering.

[83] Hamad, F. (2016). Formulation of the axisymmetric CPDI with application to pile driving in sand. *Computers and Geotechnics*, 74:141–150.

[84] Hamad, F., Giridharan, S., and Moormann, C. (2017). A penalty function method for modelling frictional contact in MPM. In *Proceedings of the 1st International Conference on the Material Point Method (MPM 2017)*, volume 175, pages 116–123. Elsevier.

[85] Hamann, T., Qiu, G., and Grabe, J. (2015). Application of a coupled eEulerian–Lagrangian approach on pile installation problems under partially drained conditions. *Computers and Geotechnics*, 63:279–290.

[86] Harlow, F. H. (1964). The particle-in-cell computing method for fluid dynamics. *Methods Computational Physics*, 3:319–343.

[87] Hartung, M. (1994). *Einflüsse der Herstellung auf die Pfahltragfähigkeit in Sand*. Schmidt.

[88] Hashiguchi, K. (1977). Elastoplastic constitutive laws of granular materials. *Constitutive Equations of Soils (Proc. 9th ICFSME, Spec. Session 9)*, pages 73–82.

[89] Hazen, A. (1919). Hydraulic-fill dams. *Transactions of the American Society of Civil Engineers*, 83(1):1713–1745.

[90] Heider, Y. (2012). *Saturated porous media dynamics with application to earthquake engineering*. PhD thesis, University of Stuttgart.

[91] Heins, E., Hamann, T., Grabe, J., and Hannot, S. (2016). Numerical investigation of the influence of the driving frequency during pile installation of tubular piles. *Geotechnik*, 39(2):98–109.

[92] Henke, S. and Grabe, J. (2006). Simulation of pile driving by 3-dimensional finite-element analysis. In *Proceedings of 17th European Young Geotechnical Engineers' Conference*, pages 215–233. Zagreb, Crotia. Croatian Geotechnical Society.

[93] Hill, R. (1959). Some basic principles in the mechanics of solids without a natural time. *Journal of the Mechanics and Physics of Solids*, 7(3):209–225.

[94] Hirt, C. W., Amsden, A. A., and Cook, J. (1974). An arbitrary Lagrangian-Eulerian computing method for all flow speeds. *Journal of computational physics*, 14(3):227–253.

[95] Huang, P., Zhang, X., Ma, S., and Huang, X. (2011). Contact algorithms for the material point method in impact and penetration simulation. *International journal for numerical methods in engineering*, 85(4):498–517.

[96] Hughes, T. J. (2012). *The finite element method: linear static and dynamic finite element analysis*. Courier Corporation.

[97] Hughes, T. J. and Winget, J. (1980). Finite rotation effects in numerical integration of rate constitutive equations arising in large-deformation analysis. *International journal for numerical methods in engineering*, 15(12):1862–1867.

[98] Idelsohn, S. R., Oñate, E., and Pin, F. D. (2004). The particle finite element method: a powerful tool to solve incompressible flows with free-surfaces and breaking waves. *International journal for numerical methods in engineering*, 61(7):964–989.

[99] Ishac, M. F. and Heidebrecht, A. C. (1982). Energy dissipation and seismic liquefaction in sands. *Earthquake Engineering & Structural Dynamics*, 10(1):59–68.

[100] Islam, M. R., Rahman, M., Hayano, K., et al. (2020). Application of smoothed particle hydrodynamics (SPH) for simulating various geotechnical problems. *SN Applied Sciences*, 2(4):1–14.

[101] Itasca, C. (1997). *FLAC3D User's Manual*.

[102] Jamiolkowski, M., Lo Presti, D., and Manassero, M. (2003). Evaluation of relative density and shear strength of sands from CPT and DMT. In *Soil behavior and soft ground construction*, pages 201–238.

[103] Jefferies, M. and Been, K. (2015). *Soil liquefaction: a critical state approach*. CRC press.

[104] Juang, C., Chen, C., Tang, W., and Rosowsky, D. (2000). CPT-based liquefaction analysis, part 1: Determination of limit state function. *Geotechnique*, 50(5):583–592.

[105] Juang, C. H. and Jiang, T. (2000). Assessing probabilistic methods for liquefaction potential evaluation. In *Soil Dynamics and Liquefaction*, pages 148–162.

[106] Juang, C. H., Jiang, T., and Andrus, R. D. (2002). Assessing probability-based methods for liquefaction potential evaluation. *Journal of Geotechnical and Geoenvironmental Engineering*, 128(7):580–589.

[107] Kafaji, I. (2013). *Formulation of a dynamic material point method (MPM) for Geomechanical Problems*. PhD thesis, Institute for Geotechnical Engineering, University of Stuttgart.

[108] Kamojjala, K. and Brannon, R. M. (2011). Verification of frame indifference for complicated numerical constitutive models. In *ASME early career technical conference*.

[109] Kanagalingam, T. (2006). Liquefaction assessment by energy approach. Technical report, University of Buffalo, State University of New York.

[110] Kayen, R., Moss, R., Thompson, E., Seed, R., Cetin, K., Kiureghian, A. D., Tanaka, Y., and Tokimatsu, K. (2013). Shear-wave velocity–based probabilistic and deterministic assessment of seismic soil liquefaction potential. *Journal of Geotechnical and Geoenvironmental Engineering*, 139(3):407–419.

[111] Kermani, E., Li, T., and Qiu, T. (2014). Discrete element method simulation of granular column collapse. In *Advances in Transportation Geotechnics and Materials for Sustainable Infrastructure*, pages 1–8.

[112] Kim, N.-H. (2014). *Introduction to nonlinear finite element analysis*. Springer Science & Business Media.

[113] Kim, N. H., Park, Y. H., and Choi, K. K. (2001). Optimization of a hyper-elastic structure with multibody contact using continuum-based shape design sensitivity analysis. *Structural and multidisciplinary optimization*, 21(3):196–208.

[114] Klos, J. and Tejchman, A. (1981). Bearing capacity calculation for pipe piles. In *Proceedings of the 10th International Conference on Soil Mechanics and Foundation Engineering, Stockholm, Sweden*, volume 2, pages 751–754.

[115] Ko, J., Jeong, S., and Lee, J. K. (2016). Large deformation FE analysis of driven steel pipe piles with soil plugging. *Computers and Geotechnics*, 71:82–97.

[116] Kokusho, T. (2013). Liquefaction potential evaluations: energy-based method versus stress–based method. *Canadian Geotechnical Journal*, 50(10):1088–1099.

[117] Kondner, R. L. (1963). Hyperbolic stress–strain formulation for sands. In *Proceedings of the Second Pan-American Conference on Soil Mechanics and Foundation Engineering, Brazil*.

[118] Kularathna, S. (2018). *Splitting solution scheme for material point method*. PhD thesis, University of Cambridge, Department of Engineering.

[119] Kumar, K., Delenne, J.-Y., and Soga, K. (2017). Mechanics of granular column collapse in fluid at varying slope angles. *Journal of Hydrodynamics*, 29(4):529–541.

[120] Kumar, K., Soga, K., and Delenne, J.-Y. (2013). Multi-scale modelling of granular avalanches. In *AIP Conference Proceedings*, volume 1542, pages 1250–1253. American Institute of Physics.

[121] Kunar, R. and Rodriguez-Ovejero, L. (1980). A model with non-reflecting boundaries for use in explicit soil–structure interaction analyses. *Earthquake Engineering & Structural Dynamics*, 8(4):361–374.

[122] Labenski, J. (2020). *Untersuchungen zum Einbringverhalten und dem lateralen Tragverhalten unter monotoner Einwirkung von in nichtbindigen Böden vibrierend installierten Monopiles*. PhD thesis, Institut für Geotechnik, Universität Stuttgart.

[123] Lajeunesse, E., Mangeney-Castelnau, A., and Vilotte, J. (2004). Spreading of a granular mass on a horizontal plane. *Physics of fluids*, 16(7):2371–2381.

[124] Le, V. H. (2015). *Zum verhalten von sand unter zyklischer beanspruchung mit polarisationswechsel im einfachscherversuch*. PhD thesis, Technical University Berlin.

[125] Lenz, J. A. and Baise, L. G. (2007). Spatial variability of liquefaction potential in regional mapping using CPT and SPT data. *Soil Dynamics and Earthquake Engineering*, 27(7):690–702.

[126] Lewis, M. J. (2016). Early windmill. *History of Technology Volume 15*, page 141.

[127] Li, X. (2002). A sand model with state-dependent dilatancy. *Géotechnique*, 52(3):173–186.

[128] Liang, L., Figueroa, J. L., and Saada, A. S. (1995). Liquefaction under random loading: unit energy approach. *Journal of Geotechnical Engineering*, 121(11):776–781.

[129] Liao, S. S., Veneziano, D., and Whitman, R. V. (1988). Regression models for evaluating liquefaction probability. *Journal of Geotechnical Engineering*, 114(4):389–411.

[130] Liu, G. R. and Jerry, S. Q. (2003). A non-reflecting boundary for analyzing wave propagation using the finite element method. *Finite elements in analysis and design*, 39(5-6):403–417.

[131] Liu, G.-R. and Liu, M. B. (2003). *Smoothed particle hydrodynamics: a meshfree particle method*. World scientific.

[132] Llano-Serna, M. A., Farias, M. M., and Pedroso, D. M. (2016). An assessment of the material point method for modelling large scale run-out processes in landslides. *Landslides*, 13(5):1057–1066.

[133] Lube, G., Huppert, H. E., Sparks, R. S. J., and Freundt, A. (2005). Collapses of two-dimensional granular columns. *Physical Review E*, 72(4):041301.

[134] Lube, G., Huppert, H. E., Sparks, R. S. J., and Freundt, A. (2007). Static and flowing regions in granular collapses down channels. *Physics of Fluids*, 19(4):043301.

[135] Lube, G., Huppert, H. E., Sparks, R. S. J., and Hallworth, M. A. (2004). Axisymmetric collapses of granular columns. *Journal of Fluid Mechanics*, 508:175.

[136] Lucy, L. B. (1977). A numerical approach to the testing of the fission hypothesis. *The astronomical journal*, 82:1013–1024.

[137] Luttwak, G. and Rabie, R. (1985). Multimaterial arbitrary lagrangian eulerian code MMALE and its application to some problems of penetration and impact. Technical report, Los Alamos National Lab.(LANL), Los Alamos, NM (United States).

[138] Lysmer, J. and Kuhlemeyer, R. L. (1969). Finite dynamic model for infinite media. *Journal of the engineering mechanics division*, 95(4):859–877.

[139] Mabsout, M. E., Reese, L. C., and Tassoulas, J. L. (1995). Study of pile driving by finite-element method. *Journal of Geotechnical Engineering*, 121(7):535–543.

[140] Madsen, S., Andersen, L. V., and Ibsen, L. B. (2012). Instability during installation of foundations for offshore structures. In *NGM 2012 Proceedings: Proceedings of the 16th Nordic Geotechnical Meeting*, pages 499–505. Dansk Geoteknisk Forening.

[141] Mahutka, K., König, F., and Grabe, J. (2006). Numerical modelling of pile jacking, driving and vibratory driving. In *Proceedings of International Conference on Numerical Simulation of Construction Processes in Geotechnical Engineering for Urban Environment (NSC06), Bochum, ed. T. Triantafyllidis, Balkema, Rotterdam*, pages 235–246.

[142] Makra, A. (2013). Evaluation of the UBC3D-PLM constitutive model for prediction of earthquake induced liquefaction on embankment dams. Master's thesis, TU Delft, Faculty of Civil Engineering and Geosciences.

[143] Malvern, L. E. (1969). *Introduction to the Mechanics of a Continuous Medium*. Number Monograph. Englewood Cliffs, NJ : Prentice-Hall.

[144] Mangeney, A., Staron, L., Volfson, D., and Tsimring, L. (2007). Comparison between discrete and continuum modeling of granular spreading. *WSEAS Transactions on Mathematics*, 6(2):373.

[145] Manzari, M. T. and Dafalias, Y. F. (1997). A critical state two-surface plasticity model for sands. *Geotechnique*, 47(2):255–272.

[146] Massarsch, K. R., Fellenius, B. H., and Bodare, A. (2017). Fundamentals of the vibratory driving of piles and sheet piles. *Geotechnik*, 40(2):126–141.

[147] Mast, C. M. (2013). *Modeling landslide-induced flow interactions with structures using the Material Point Method*. PhD thesis, University of Washington, Department of Civil Engineering.

[148] Mast, C. M., Arduino, P., Mackenzie-Helnwein, P., and Miller, G. R. (2015). Simulating granular column collapse using the material point method. *Acta Geotechnica*, 10(1):101–116.

[149] Mast, C. M., Arduino, P., Miller, G. R., and Mackenzie-Helnwein, P. (2014). Avalanche and landslide simulation using the material point method: flow dynamics and force interaction with structures. *Computational Geosciences*, 18(5):817–830.

[150] Matsuoka, H. (1977). Stress-strain relationship of soil based on the SMP. In *Proceedings of 9th ICSMFE, Specialty Session 9*.

[151] Mieremet, M., Stolle, D., Ceccato, F., and Vuik, C. (2016). Numerical stability for modelling of dynamic two-phase interaction. *International Journal for Numerical and Analytical Methods in Geomechanics*, 40(9):1284–1294.

[152] Minatti, L. and Paris, E. (2015). A SPH model for the simulation of free surface granular flows in a dense regime. *Applied Mathematical Modelling*, 39(1):363–382.

[153] Molenkamp, F. (1986). Limits to the Jaumann stress rate. *International Journal for Numerical and Analytical methods in Geomechanics*, 10(2):151–176.

[154] Moller, B. and Bergdahl, U. (1981). Dynamic pore pressure during pile driving in fine sand. In *Proceedings of the 10th International Conference on Soil Mechanics And Foundation Engineering, AA Balkema, Rotterdam, The Netherlands*, volume 2, pages 791–794.

[155] Monaghan, J. J. (1988). An introduction to SPH. *Computer Physics Communications*, 48(1):89–96.

[156] Moormann, C., Gowda, S., and Giridharan, S. (2018). Numerical simulation of pile installation in saturated soil using CPDI. In *Proceedings of the 9th European Conference on Numerical Methods in Geotechnical Engineering*, pages 665–672.

[157] Moormann, C., Kirsch, F., and Herwig, V. (2016). Vergleich des axialen und lateralen Tragverhaltens von vibrierten und gerammten Stahlrohrpfählen. *Proceedings of the 34. Baugrundtagung*, 15(17.09):2016.

[158] Moss, R., Seed, R. B., Kayen, R. E., Stewart, J. P., Der Kiureghian, A., and Cetin, K. O. (2006). CPT-based probabilistic and deterministic assessment of in situ seismic soil liquefaction potential. *Journal of Geotechnical and Geoenvironmental Engineering*, 132(8):1032–1051.

[159] Naesgaard, E. (2011). *A hybrid effective stress–total stress procedure for analyzing soil embankments subjected to potential liquefaction and flow*. PhD thesis, University of British Columbia.

[160] Nairn, J. A. (2015). Numerical simulation of orthogonal cutting using the material point method. *Engineering Fracture Mechanics*, 149:262–275.

[161] Nairn, J. A. and Guilkey, J. E. (2015). Axisymmetric form of the generalized interpolation material point method. *International journal for numerical methods in engineering*, 101(2):127–147.

[162] Nazem, M., Carter, J. P., and Airey, D. W. (2009). Arbitrary lagrangian–eulerian method for dynamic analysis of geotechnical problems. *Computers and Geotechnics*, 36(4):549–557.

[163] Nemat-Nasser, S. and Shokooh, A. (1979). A unified approach to densification and liquefaction of cohesionless sand in cyclic shearing. *Canadian Geotechnical Journal*, 16(4):659–678.

[164] Ng, E. (1988). Pile foundation : The behaviour of single pile in cohesionless soils. Technical Report FHWA-RD-88-081, Federal Highway Administration Report.

[165] Niemunis, A. and Herle, I. (1997). Hypoplastic model for cohesionless soils with elastic strain range. *Mechanics of Cohesive-frictional Materials: An International Journal on Experiments, Modelling and Computation of Materials and Structures*, 2(4):279–299.

[166] Nishi, K. and Kanatani, M. (1990). Constitutive relations for sand under cyclic loading based on elasto-plasticity theory. *Soils and Foundations*, 30(2):43–59.

[167] Noh, W. F. (1963). CEL: A time-dependent, two-space-dimensional, coupled Eulerian-Lagrange code. Technical report, Lawrence Radiation Lab., Univ. of California, Livermore.

[168] Nøst, H. A. (2019). *Iteratively coupled implicit dynamic MPM-FVM*. PhD thesis, Norwegian University of Science and Technology, Institutt for bygg- og miljøteknikk.

[169] Oka, F., Yashima, A., Tateishi, A., Taguchi, Y., and Yamashita, A. (1999). A cyclic elasto-plastic constitutive model for sand considering a plastic-strain dependence of the shear modulus. *Geotechnique*, 49(5):661–680.

[170] Oñate, E., Idelsohn, S. R., Del Pin, F., and Aubry, R. (2004). The particle finite element method – An overview. *International Journal of Computational Methods*, 1(02):267–307.

[171] O'Neill, M. W. and Yoon, G. L. (2003). Spatial variability of CPT parameters at university of houston NGES. *Probabilistic site characterization at the national geotechnical experimentation sites*, pages 1–12.

[172] Osinov, V., Chrisopoulos, S., and Triantafyllidis, T. (2013). Numerical study of the deformation of saturated soil in the vicinity of a vibrating pile. *Acta Geotechnica*, 8(4):439–446.

[173] O'Sullivan, C. (2011). *Particulate discrete element modelling: a geomechanics perspective*. CRC Press.

[174] Paikowsky, S. G. (1989). *A static evaluation of soil plug behavior with application to the pile plugging problem*. PhD thesis, Massachusetts Institute of Technology.

[175] Pastor, M. and Zienkiewicz, O. (1986). A generalized plasticity, hierarchical model for sand under monotonic and cyclic loading. In *International symposium on numerical models in Geomechanics*, pages 131–150.

[176] Pestana, J. M., Hunt, C. E., and Bray, J. D. (2002). Soil deformation and excess pore pressure field around a closed-ended pile. *Journal of geotechnical and geoenvironmental engineering*, 128(1):1–12.

[177] Petalas, A. and Galavi, V. (2013). Plaxis liquefaction model UBC3DPLM. Technical report, PLAXIS bv, The Netherlands.

[178] Pfister, J. and Eberhard, P. (2002). Frictional contact of flexible and rigid bodies. *Granular Matter*, 4(1):25–36.

[179] Phuong, N., van Tol, A., Elkadi, A., and Rohe, A. (2014). Modelling of pile installation using the material point method (MPM). *Numerical methods in Geotechnical engineering*, 271:276.

[180] Phuong, N. T. V. (2019). *Numerical Modelling of Pile Installation Using Material Point Method*. PhD thesis, Delft University of Technology.

[181] Potts, D. M., Zdravković, L., Addenbrooke, T. I., Higgins, K. G., and Kovačević, N. (2001). *Finite element analysis in geotechnical engineering: application*, volume 2. Thomas Telford London.

[182] Prevost, J. H. and Keane, C. M. (1990). Multimechanism elasto-plastic model for soils. *Journal of engineering mechanics*, 116(9):1924–1944.

[183] Puebla, H., Byrne, P. M., and Phillips, R. (1997). Analysis of CANLEX liquefaction embankments: prototype and centrifuge models. *Canadian Geotechnical Journal*, 34(5):641–657.

[184] Qiu, G., Henke, S., and Grabe, J. (2011). Application of a Coupled Eulerian–Lagrangian approach on geomechanical problems involving large deformations. *Computers and Geotechnics*, 38(1):30–39.

[185] Rayleigh, J. W. S. B. (1896). *The Theory of Sound*, volume 2. Macmillan.

[186] Remspecher, F., Le, V. H., Rackwitz, F., Herwig, V., and Matlock, B. (2018). Vibratory driven installation of monopiles–an experimental investigation of the soil-pile interaction. In *Vietnam Symposium on Advances in Offshore Engineering*, pages 171–176. Springer.

[187] Roache, P. J. (2002). Code verification by the method of manufactured solutions. *Journal of Fluids Engineering*, 124(1):4–10.

[188] Sadeghirad, A., Brannon, R., and Guilkey, J. (2013). Second-order convected particle domain interpolation (CPDI2) with enrichment for weak discontinuities at material interfaces. *International Journal for numerical methods in Engineering*, 95(11):928–952.

[189] Sadeghirad, A., Brannon, R. M., and Burghardt, J. (2011). A convected particle domain interpolation technique to extend applicability of the material point method for problems involving massive deformations. *International Journal for numerical methods in Engineering*, 86(12):1435–1456.

[190] Schmertmann, J. (1976). An updated correlation between relative density DR and fugro-type electric cone bearing, qc. Technical report, Contract report DACW.

[191] Schümann, B. and Grabe, J. (2011). FE-based modelling of pile driving in saturated soils. In *Proceedings of the 8th international conference on structural dynamics, EURODYN*, pages 894–900.

[192] Seed, H. B. and Idriss, I. M. (1971). Simplified procedure for evaluating soil liquefaction potential. *Journal of Soil Mechanics & Foundations Division*.

[193] Seed, H. B. and Lee, K. L. (1966). Liquefaction of saturated sands during cyclic loading. *Journal of the Soil Mechanics and Foundations Division*, 92(6):105–134.

[194] Shriro, M. and Bray, J. D. (2013). Calibration of numerical model for liquefaction-induced effects on levees and embankments. In *Seventh International conference on case histories inn Geotechnical Engineering*.

[195] Soga, K., Alonso, E., Yerro, A., Kumar, K., and Bandara, S. (2016). Trends in large-deformation analysis of landslide mass movements with particular emphasis on the material point method. *Géotechnique*, 66(3):248–273.

[196] Sołowski, W. and Sloan, S. (2013). Modelling of sand column collapse with material point method. In *Proceedings of the 3rd international symposium on computational geomechanics (ComGeo III)*, pages 698–705.

[197] Sołowski, W. and Sloan, S. (2015). Evaluation of material point method for use in

geotechnics. *International Journal for Numerical and Analytical Methods in Geomechanics*, 39(7):685–701.

[198] Speziale, C. G. (1998). A review of material frame-indifference in mechanics. *Applied Mechanics Reviews*.

[199] Staron, L. and Hinch, E. (2005). Study of the collapse of granular columns using DEM numerical simulation. *Journal of Fluid Mechanics*, 545:1–27.

[200] Stein, L. R., Gentry, R. A., and Hirt, C. W. (1977). Computational simulation of transient blast loading on three-dimensional structures. *Computer Methods in Applied Mechanics and Engineering*, 11(1):57–74.

[201] Sulsky, D., Chen, Z., and Schreyer, H. L. (1994). A particle method for history-dependent materials. *Computer methods in applied mechanics and engineering*, 118(1-2):179–196.

[202] Sulsky, D. and Schreyer, H. L. (1996). Axisymmetric form of the material point method with applications to upsetting and Taylor impact problems. *Computer Methods in Applied Mechanics and Engineering*, 139(1-4):409–429.

[203] Sulsky, D., Zhou, S.-J., and Schreyer, H. L. (1995). Application of a particle-in-cell method to solid mechanics. *Computer physics communications*, 87(1-2):236–252.

[204] Terzaghi, K. (1925). Erdbaumechanik. *Franz Deuticke, Vienna*, 1.

[205] Terzaghi, K., Peck, R. B., and Mesri, G. (1996). *Soil mechanics in engineering practice*. John Wiley & Sons.

[206] Tran, Q., Wobbes, E., Sołowski, W. T., Möller, M., and Vuik, C. (2019a). Moving least squares reconstruction for B-spline material point method. In *International Conference on the Material Point Method for Modelling Soil-Water-Structure Interaction*.

[207] Tran, Q.-A. et al. (2019b). *Material Point Method: algorithm development and application to landslide modelling*. PhD thesis, Aalto University.

[208] Turner, M., Dill, E., Martin, H., and Melosh, R. (1960). Large deflections of structures subjected to heating and external loads. *Journal of the Aerospace Sciences*, 27(2):97–106.

[209] Utili, S., Zhao, T., and Houlsby, G. (2015). 3D DEM investigation of granular column collapse: evaluation of debris motion and its destructive power. *Engineering Geology*, 186:3–16.

[210] Vaid, Y., Fisher, J., Kuerbis, R., and Negussey, D. (1990). Particle gradation and liquefaction. *Journal of Geotechnical Engineering*, 116(4):698–703.

[211] Verruijt, A. (2009). *An introduction to soil dynamics*, volume 24. Springer Science & Business Media.

[212] von Terzaghi, K. (1923). Die berechnung der durchassigkeitsziffer des tones aus dem verlauf der hydrodynamischen spannungs. erscheinungen. *Sitzungsber. Akad. Wiss. Math. Naturwiss. Kl. Abt. 2A*, 132:105–124.

[213] Von Wolffersdorff, P.-A. (1996). A hypoplastic relation for granular materials with a predefined limit state surface. *Mechanics of Cohesive-frictional Materials: An International Journal on Experiments, Modelling and Computation of Materials and Structures*, 1(3):251–271.

[214] Wallstedt, P. C. and Guilkey, J. (2008). An evaluation of explicit time integration schemes for use with the generalized interpolation material point method. *Journal of Computational Physics*, 227(22):9628–9642.

[215] Wang, C., Chen, Q., Shen, M., and Juang, C. H. (2017). On the spatial variability of CPT-based geotechnical parameters for regional liquefaction evaluation. *Soil Dynamics and Earthquake Engineering*, 95:153–166.

[216] White, D. and Bolton, M. (2004). Displacement and strain paths during plane-strain model pile installation in sand. *Géotechnique*, 54(6):375–397.

[217] Więckowski, Z. (2004). The material point method in large strain engineering problems. *Computer methods in applied mechanics and engineering*, 193(39-41):4417–4438.

[218] Yang, Z. X., Jardine, R., Zhu, B., and Rimoy, S. (2014). Stresses developed around displacement piles penetration in sand. *Journal of Geotechnical and Geoenvironmental Engineering*, 140(3):04013027.

[219] Yegian, M. K. and Whitman, R. V. (1978). Risk analysis for ground failure by liquefaction. *Journal of Geotechnical and Geoenvironmental Engineering*, 104(ASCE 13900 Proceeding).

[220] Yerro Colom, A. (2015). *MPM modelling of landslides in brittle and unsaturated soils*. PhD thesis, Departament d'Enginyeria Civil i Ambiental.

[221] Youd, T. and Idriss, I. (1997). NCEER workshop on evaluation of liquefaction resistance of soils. *National Center for Earthquake Engineering Research Technical Report NCEER-97-0022*, page 276.

[222] Youd, T. L. and Idriss, I. M. (2001). Liquefaction resistance of soils: summary report from the 1996 NCEER and 1998 NCEER/NSF workshops on evaluation of liquefaction resistance of soils. *Journal of geotechnical and geoenvironmental engineering*, 127(4):297–313.

[223] Youd, T. L. and Noble, S. K. (1997). Liquefaction criteria based on statistical and probabilistic analyses. In *Proceedings of NCEER Workshop on Evaluation of Liquefaction Resistance of Soils*, number NCEER-97.

[224] Zaaijer, M. (2006). Foundation modelling to assess dynamic behaviour of offshore wind turbines. *Applied Ocean Research*, 28(1):45–57.

[225] Zenit, R. (2005). Computer simulations of the collapse of a granular column. *Physics of Fluids*, 17(3):031703.

[226] Zhang, D. Z., Ma, X., and Giguere, P. T. (2011). Material point method enhanced by modified gradient of shape function. *Journal of Computational Physics*, 230(16):6379–6398.

[227] Zhao, T. (2017). *Coupled DEM–CFD analyses of landslide-induced debris flows*. Springer.

[228] Zhu, H., Zhou, Z., Yang, R., and Yu, A. (2007). Discrete particle simulation of particulate systems: theoretical developments. *Chemical Engineering Science*, 62(13):3378–3396.

[229] Zienkiewicz, O. and Shiomi, T. (1984). Dynamic behaviour of saturated porous media; the generalized biot formulation and its numerical solution. *International journal for numerical and analytical methods in geomechanics*, 8(1):71–96.

[230] Zienkiewicz, O., Watson, M., and King, I. (1968). A numerical method of visco-elastic stress analysis. *International Journal of Mechanical Sciences*, 10(10):807–827.

[231] Zienkiewicz, O. C., Chan, A., Pastor, M., Schrefler, B., and Shiomi, T. (1999). *Computational Geomechanics*, volume 613. Citeseer.

[232] Zienkiewicz, O. C. and Cheung, Y. (1970). The finite element method in structural and continuum mechanics.

[233] Ziotopoulou, A. K. (2014). *A sand plasticity model for earthquake engineering applications*. PhD thesis, University of California, Davis.

Appendix A

Appendix to Chapter 3.4 : Performance of the single phase CPDI model

After implementing the CPDI numerical code, its performance is evaluated to ensure that it behaves as expected and that the error is within the expected range. This study compares all of the available MPM iterations, including the classical formulation, Generalised Interpolation Material Point (GIMP), and the CPDI. The results of this study are also used to justify the increased computational overhead caused by the CPDI implementation and to quantify the difference between formulations numerically. The purpose of this Appendix's study is to ensure that the code performs as expected during unit tests and simple tests. The continuum tests conducted in Chapter 3 are described.

A.1 Frame-indifference of CPDI

The principle of material frame indifference is an essential component of the numerical modelling of large deformations. This necessitates that the spatial stresses rotate with the material while the reference stresses remain unaffected by rotation. According to the principle of material frame indifference, if a deformed material is rotated, the spatial traction and stresses must also rotate. However, the reference stresses must be rotationally insensitive. In their work, Speziale [198] provided a critical analysis of the concepts of material frame-indifference. However, the concept of basis indifference is distinct from that of frame indifference. The work of Frewer [69] provides a comprehensive description of the terminology and formulations used to explain the concept of material frame-indifference.

As an object undergoes deformation, the spatial tractions and stresses must rotate according to the principle of material frame-indifference. While the rotation of spatial tractions is simple and can be implemented by calculating updated normals, the same cannot be said for stresses. The *material objectivity* or *material frame indifference* principle stipulates that the material response must be independent of the observer [143]. Constitutive laws should therefore be written with an objective reference frame in mind. A difference between the reference and deformed configurations of a deforming body may develop over time. This is typically disregarded for problems with small deformations, but cannot be assumed for problems with finite deformations. Over small incremental deformations, it is possible to linearize the nonlinear finite deformation problem. For an elastic constitutive equation, the objective stress rate tensor $\mathring{\sigma}$ is given

by the form:

$$\mathring{\sigma} = f\left(\dot{\varepsilon}\right) , \tag{A.1}$$

where, $\dot{\varepsilon}$ represents the strain rate and f represents the constitutive equation. The Cauchy stress tensor, σ is symmetric and objective. Materially, it is a time derivative, but it can be demonstrated that it is not objective. In the context of continuum mechanics, references such as [20, 143] provide a comprehensive list of the various objective stress rates. The relation between the *Jaumann co-rotational stress rate* and the Cauchy stress rate is given by:

$$\mathring{\sigma}_{ij} = \dot{\sigma}_{ij} - \omega_{ik}\,\sigma_{kj} + \sigma_{ik}\,\omega_{kj} , \tag{A.2}$$

where, ω, the spin tensor is given by the relation:

$$\omega_{ij} = \frac{1}{2}\left(\frac{\partial v_i}{\partial x_j} - \frac{\partial v_j}{\partial x_i}\right) . \tag{A.3}$$

Here, v represents the velocities of the continuum. Hill [93] advanced Equation A.2 by introducing volume change effects. The so-called *Hill rate* or more commonly referred to as the *co-rotational rate of Kirchoff* stress tensor $\overset{\triangledown}{\sigma}$ is given by:

$$\overset{\triangledown}{\sigma}_{ij} = \dot{\sigma}_{ij} - \omega_{ik}\,\sigma_{kj} + \sigma_{ik}\,\omega_{kj} + \dot{\varepsilon_{kk}}\,\sigma_{ij} , \tag{A.4}$$

where, $\dot{\varepsilon_{kk}}$ is the spherical part of the strain rate tensor. The objective stress rate definition, from Equations A.2 and A.4 can be summarised for the constitutive equation as:

$$\overset{\triangledown}{\sigma}_{ij} = D_{ijkl}\,\dot{\varepsilon}_{kl} , \tag{A.5}$$

where, D_{ijkl} is the constitutive tensor.

The reference [153] demonstrates that the accuracy of the Jaumann stress rate has certain limitations. It has been shown that the Jaumann stress rate is inaccurate for moderate to large deformations with deviatoric strains exceeding 10 percent. This error is caused by the assumption that the spin tensor ω is the rotation rate tensor. This assumption is accurate for rigid body rotations and plausible for small strains and large material rotations. As shown in reference [153], a significant difference between fabric rotation rate and spin tensor may occur in the case of large deformations and large material rotations [97]. However in case of large deformations and large material rotations, a significant difference between rotation rate of fabric and spin tensor may occur, as was shown in reference [153]. For numerical calculations of material rotations, it is suggested that an approach outlined in the work [153] based on polar decomposition be utilised.

Kamojjala and Brannon [108] provide an efficient algorithm for taking into account the principle of material frame indifference via polar decompositions. The presented algo-

rithm has been incorporated into the CPDI code. The rationale behind the algorithm was to emphasise that the common approaches used by finite element codes to satisfy frame difference, namely working in an approximate un-rotated frame for which rotation during the increment is implicitly neglected by using only a single orthogonal tensor for all un-rotation operations during the step, are insufficient and require the use of different polar rotations if the material undergoes rotation. The fundamental algorithm to account for frame-indifference is as follows:

Stress update algorithm

- Initialise stresses σ_n, and symmetric part of velocity gradient, D_n, where n is the time step.
- The stress and the symmetric part of velocity gradient are un-rotated using the relations:

$$\bar{\sigma}_n = R_n^T \cdot \sigma_n \cdot R_n,$$
$$\bar{D}_n = R_n^T \cdot D_n \cdot R_n,$$

  where, R_n is the rotation matrix at time step, n.
- The updated stresses $\bar{\sigma}_{n+1}$ are computed using the un-rotated stress and strain measures by means of an appropriate constitutive law.
- The updated un-rotated stresses and the strain measures are re-rotated using the relation:

$$\sigma_{n+1} = R_{n+1}^T \cdot \bar{\sigma}_{n+1} \cdot R_{n+1},$$
$$D_{n+1} = R_{n+1}^T \cdot \bar{D}_{n+1} \cdot R_{n+1}$$

In order to test the stress update algorithm, a classical single-element test is performed in CPDI. The test problem consists of two phases,

- The element is subjected to uniaxial deformation. During the initialisation phase, zero-stresses are assigned to the element. In one second, the acceleration due to gravity, g, increases linearly from 0 to its maximum value.
- The deformed configuration is permitted to undergo a 90-degree superimposed rotation. This is accomplished by changing the direction of g from vertical to horizontal over the course of one second, while maintaining the block's position.

For simulation, a linear elastic constitutive law is selected. 500 kPa is assigned to the Young's Modulus, E, and 0.30 is assigned to the Poisson's ratio, μ. One background computational grid containing a single particle is selected. The solution procedure makes use of an explicit time stepping algorithm. It can be inferred from Figure A.1 that during the first phase of the calculation, the vertical and horizontal stresses increase

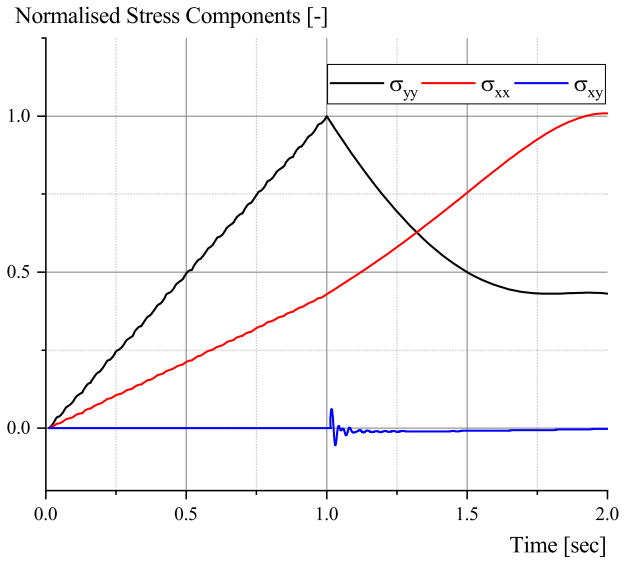

Figure A.1: Normalised stress components vs. time

linearly until they reach their maximum value. As anticipated, no shear stresses are developed. The out-of-plane stress, σ_{zz}, is not displayed because rotation has no effect on it. As expected, when the gravity vector is rotated by 90 degrees in the second phase, the vertical and horizontal stresses trade places. As the simulation continues, a slight accumulation of shear stresses dissipates. The test results indicate that the numerical code satisfies the objectivity criterion regardless of large rotations. Reference [108] contains information regarding the comparison of objectivity corrections algorithms and the outcomes of a Method of Manufactured Solutions test.

A.2 Comparison of MPM and CPDI : Cantilever beam problem

Compared to traditional MPM, the CPDI method's ability to handle large deformations is evaluated. In this numerical example, the extension instability, a common shortcoming of particle-based methods, is examined. Simulation of the deformation of a vertical bar of unit length (1 m by 1 m) due to its own weight. On the top portion of the continuum, roller boundary conditions are imposed; all other boundaries are assumed to be free. E = 1000 kPa, ν = 0.3 and ρ_0 = 1.05 g/cm^3 are set as the modulus of Young, Poisson's ratio, and density, respectively. The acceleration due to gravity (g) is equal to 1000 m/s^2 (g = 1000 m/s2). To obtain very large deformations, a high, unrealistic value for g is assumed. The continuum is meshed with 100 grids of dimension 0.1 by 0.1 m and populated with 9 particles per grid, totaling 900 particles for the problem. A total of 300 computational grids are selected for the simulation's background. The simulation is performed for a total of 0.24 seconds using standard MPM and the CPDI

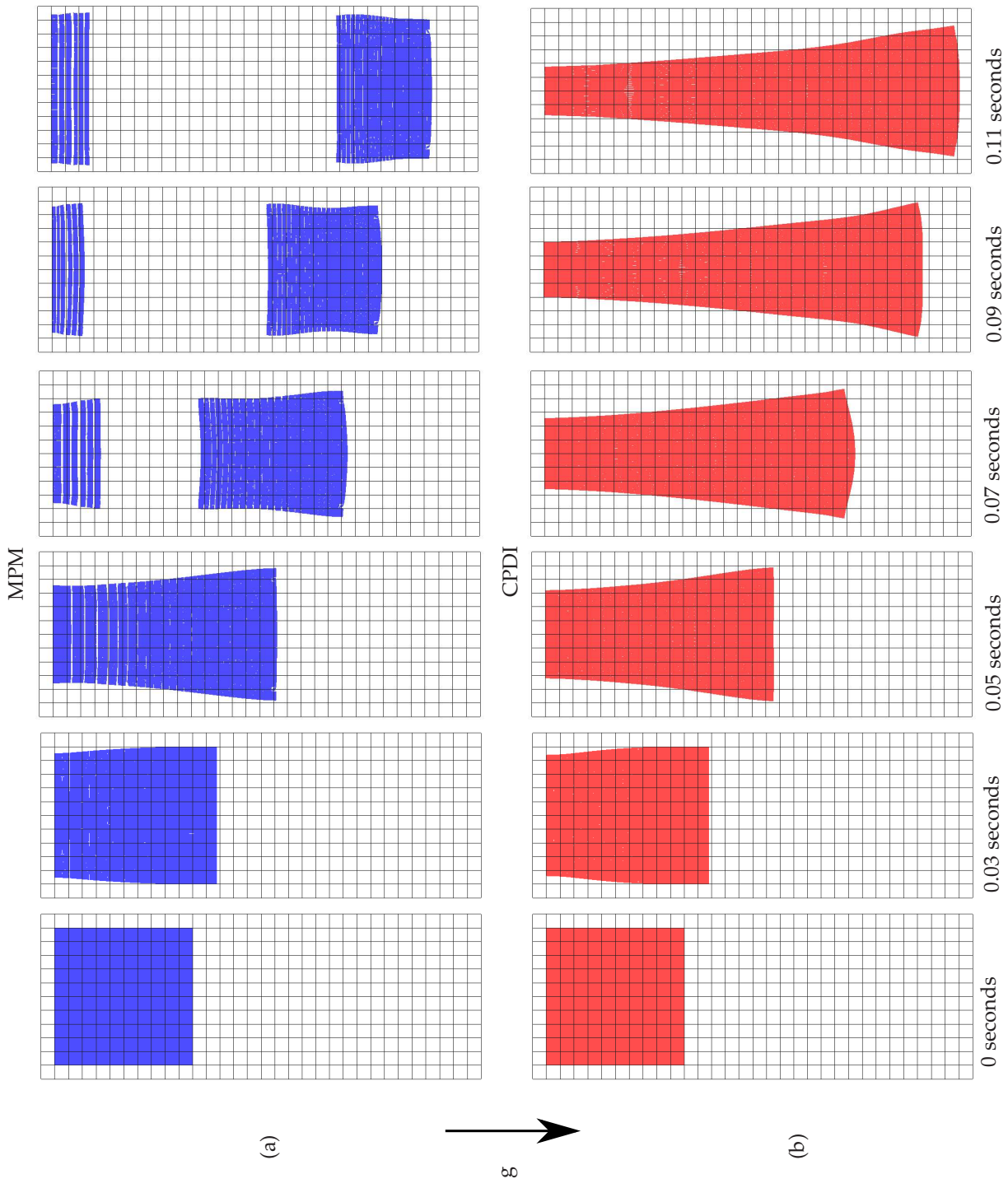

Figure A.2: Six snapshots of the vertical bar simulation using: (a) MPM and (b) CPDI method

formulation, with a time step increment of Δt = 0.00006 seconds. The simulation begins with an instantaneous application of full gravity, which is maintained until the conclusion.

Figure A.2 depicts a comparative examination of the simulation. Using the CPDI discretisation, the simulation does not exhibit extension instabilities. The classical material point method, on the other hand, fails to capture the substantial deformation that results from an increase in bar load. MPM fails to account for the shear portion of the deformation and predicts gaps in the domains that are unrealistic. The inaccuracy of the solution is exacerbated by jumps in the particle's internal energy as it crosses grid boundaries. In contrast, the CPDI method maintains contact throughout the computation. Alternative nodal basis functions have been incorporated into the CPDI algorithm to aid in maintaining particle contact even during extreme deformation. Six snapshots presented in Figure A.2 demonstrate that particles remain in contact for 0.03 seconds in both MPM and CPDI simulations. Between 0.03-0.05 seconds, the MPM particles begin to lose contact. notably in the region where the body undergoes the most extreme tensile deformation. Between 0.05 and 0.07 seconds in MPM, the particles completely lose contact and begin to behave as two separate bodies. Comparing this result to that of CPDI, the particles remain in constant contact.

Large deformations of the continuum are examined, and large particle rotations are anticipated. The CPDI method, which employs parallelograms for its domains, takes into account large rotation, whereas the MPM and uGIMP methods do not. This numerical

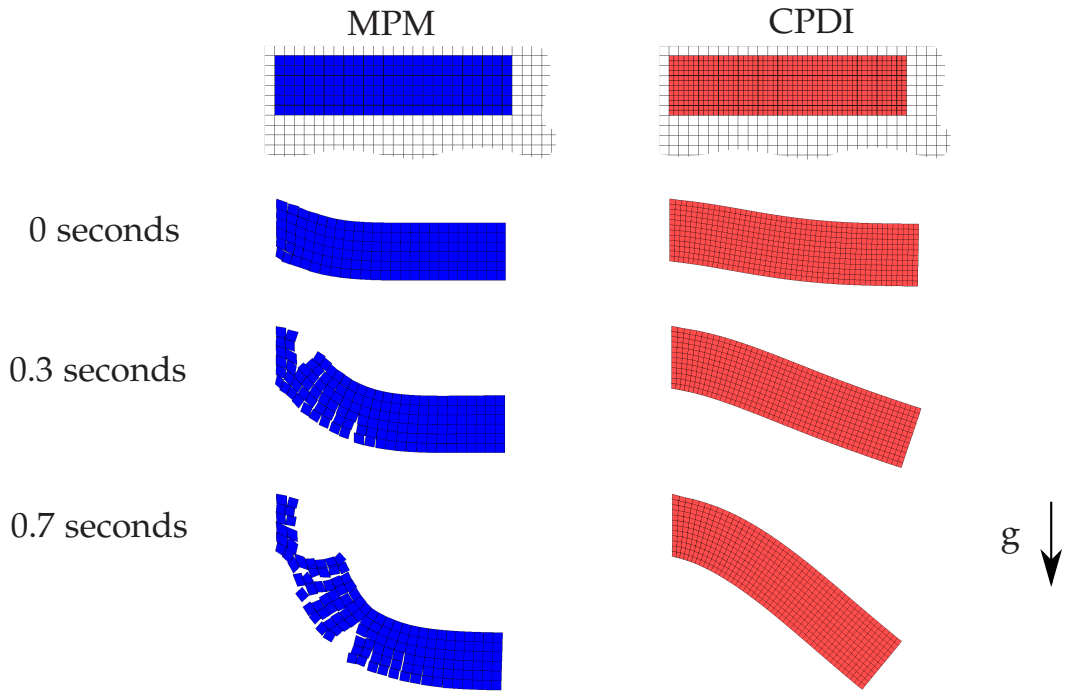

Figure A.3: Displacement of cantilever bar: MPM vs. CPDI

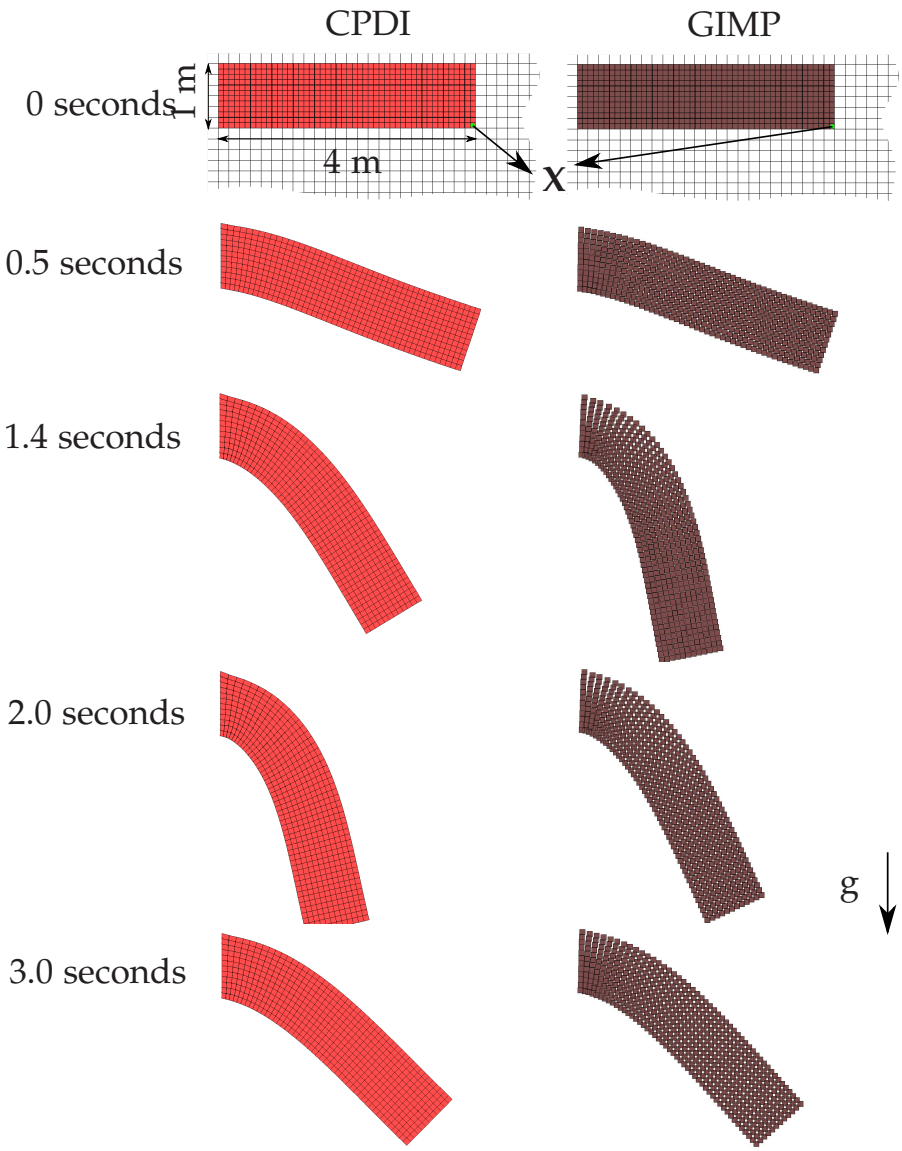

Figure A.4: Deformation of cantilever bar: CPDI vs. GIMP

example verifies the performance of all three methods. This test assumes a cantilever beam of length 4 m and thickness 1 m. By abruptly applying gravity at the start of the simulation, large deformation vibrations of the beam under its own weight are produced. One end of the cantilever beam is encastered. The modulus of Young, Poisson's ratio, and initial beam density are E = 1000 kPa, ν = 0.3, and ρ_0 = 1.05 g/cm^3, respec-

tively. Gravitational acceleration is set to be 10 m/s^2. The calculation is performed for a total of 3 seconds, with an increment of 0.001 seconds assigned to each time step. The beam is discretised using 64 elements, with each element having a dimension of 0.25 by 0.25 m. Each element is comprised of nine particles, totaling 576 for the simulation of the cantilever beam. We use a total of 900 background computational grid elements, which allows us to effectively assign 4 particles per computational grid. Calculations are performed using traditional MPM, uGIMP, and CPDI, and comparisons are made.

Figure A.3 depicts snapshots of the simulation's results, which were performed using classical MPM. Evidently, the simulation failed as a result of spurious material separation. This numerical exercise demonstrates the robustness of advanced versions of MPM versus the original formulation. Owing to the spurious oscillation of stresses in the particles, the original formulation of MPM causes the particles to lose contact with one another. The enhanced CPDI formulation can accurately track the particle's large deformation without losing contact with the particles. Repeating the simulation using GIMP and CPDI. In both instances, the simulations are stable and the calculation is carried out as intended, with no erroneous material separation.

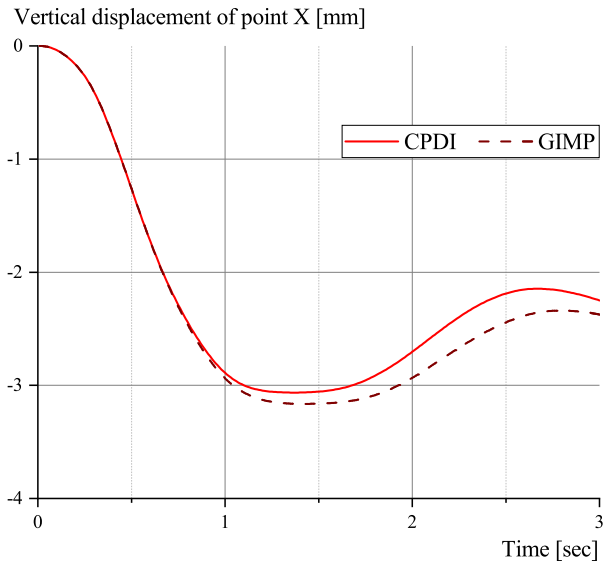

Figure A.5: Vertical diplacement of point **X** of Cantilever bar: CPDI vs. GIMP

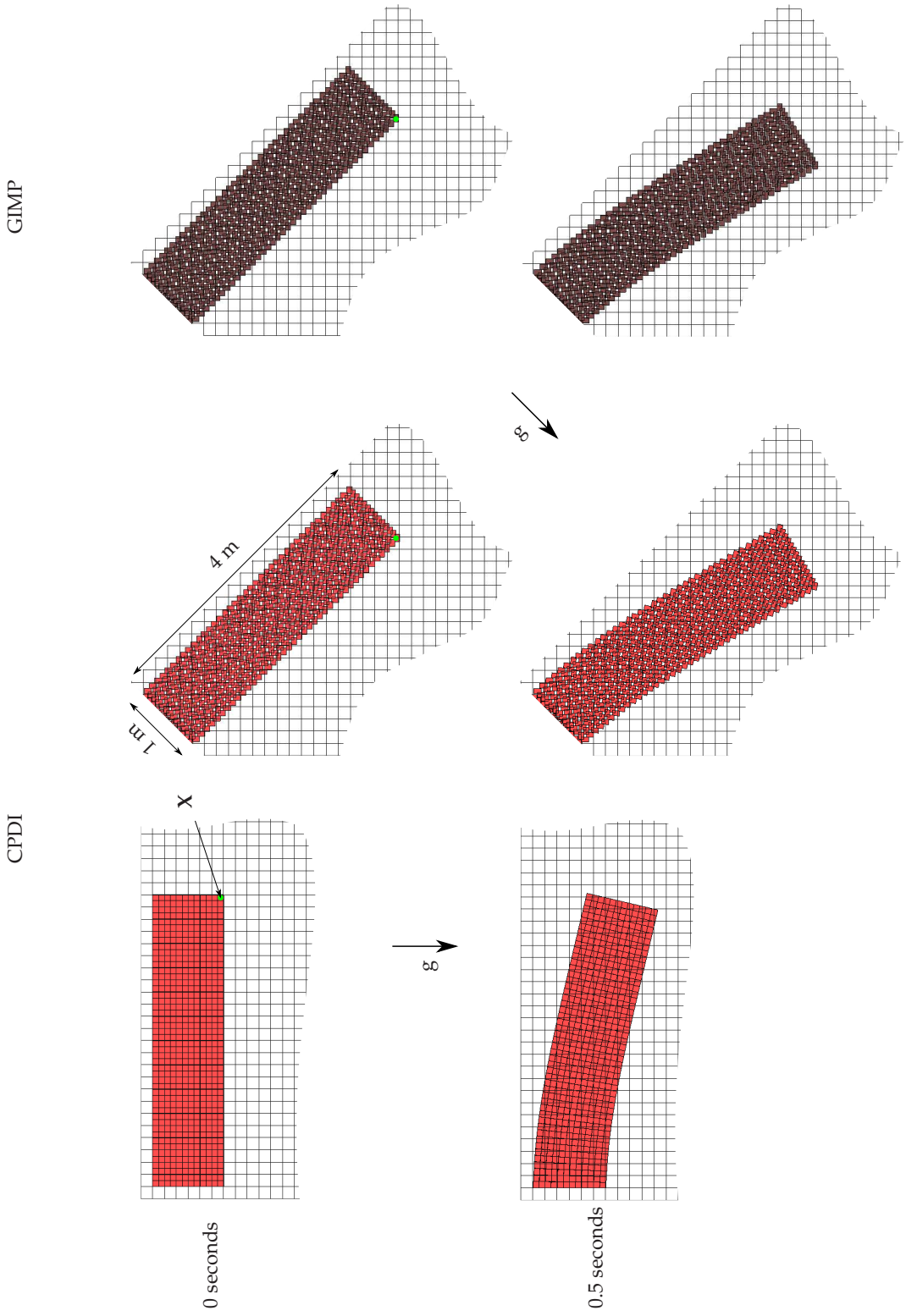

Figure A.6: Displacement of rotated cantilever bar: CPDI vs GIMP

Figure A.4 demonstrates that the deformation of CPDI and GIMP appear comparable, but the deformation of individual particles cannot be compared. The CPDI's implementation of alternative grid functions permits extension of the material point, which is not captured by the uGIMP simulation. It should be noted that if cpGIMP is implemented with extension taken into account, the results will not be comparable to those of CPDI because deformation in only one direction, either horizontal or vertical, will be considered. In contrast, the CPDI formulation permits extension, compression, and shear deformation of the particle.

Figure A.5 captures the displacement of point **X** as shown in Figure A.3. It can be seen that while the results look initially similar, they start to diverge after around 1 second of the simulation. The results are not entirely comparable. A similar study was carried out in the work of Sadeghirad et al. [189] and a conclusion drawn that results from the CPDI method are indeed more accurate.

It is investigated how particle domain shapes affect the performance of CPDI and GIMP. Due to the nature of the formulation in the MPM formulation family, the edges of the initial rectangular domains in GIMP are restricted to being parallel to the global coordinate axes. In the case of CPDI, the edges of the parallelogram are also parallel to the global coordinates. The geometry of the previously discussed cantilever beam was rotated by 45 degrees in order to examine the difference in performance under identical loading conditions in a modified configuration. In this instance, the problem cannot be discretised precisely using rectangles with parallel edges to the global coordinates. In this instance, the bar subjected to significant tensile deformation, as depicted pre-

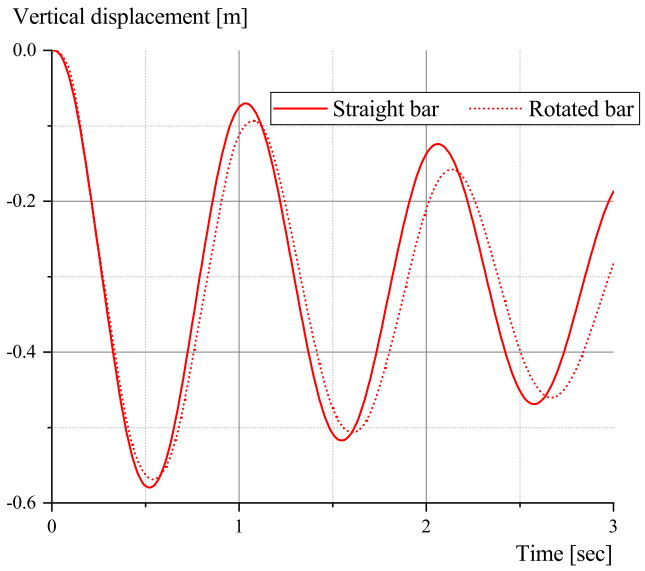

Figure A.7: Vertical displacement of point **X** of cantilever bar using CPDI discretisation: Straight vs Rotated initial configuration

viously, is modelled. For both the uGIMP and CPDI simulations, 1024 particles and 600 background grids were used to discretise the bar. The gravitational acceleration applied to the model was rotated to fit the model's configuration. Encastering one end of the rotated cantilever bar. Such a boundary condition is not typically imposed in the current implementation of the code. Typically, boundary conditions can only be assigned to the boundaries whose edges are parallel with the global coordinate system. There is no need to define any particle boundary conditions. In this case, however, the particles were assigned boundary conditions that were used as a switch to identify the computational grids in the background where these particles reside in order to apply the boundary conditions. This deviation in calculation procedure was necessitated by the cantilever beam's rotated geometry. Figure A.6 illustrates the initial configuration and deformation of a normal cantilever bar, as well as the direction of the resulting gravity vector, as well as the rotation of a cantilever bar and its corresponding gravity vector. In both instances, the direction of the background computation grid is similar and its edges are aligned with the global coordinate axes. In every instance, there was no instability and the simulation was completed as intended.

The displacements of the straight bar is compared with that of a rotated geometrical configuration. Figure A.7 provides the displacement of point **X** as introduced in Figure A.6. It can be seen that the results for a cantilever beam problem assuming CPDI for the straight and rotated bars are slightly different. The bar with a rotated configuration exhibts a softer behaviour than the straight bar. This difference in results per reference [189] can be attributed to the initial configuration of the particles, wherein the edges of particles are aligned to the global axis. Since the idea of this simulation was to perform

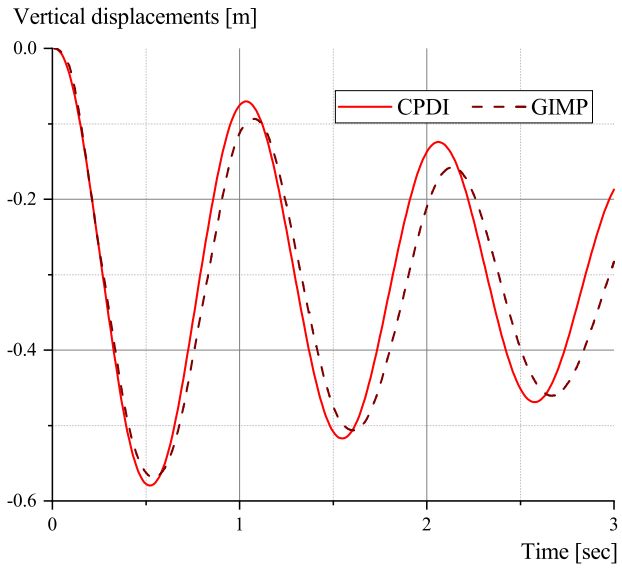

Figure A.8: Vertical displacement of point **X** of cantilever bar in rotated configuration: CPDI vs. GIMP

a parameter study to compare the results between a straight and a rotated bar, this deviation in the results was acknowleged.

Figure A.8 compares the simulation results between CPDI and GIMP. Figure A.8 demonstrates that the results from the GIMP simulation deviate slightly from the CPDI simulation, despite the fact that it has been established that the results from the CPDI discretisation for the rotated configuration differ slightly from the unrotated configuration. Comparing the performance of the rotated GIMP simulation to that of the straight CPDI configuration reveals a significant error. It should be noted that, fundamentally, the forces exerted on the straight and rotated bars should be identical. Due to the orientation of the particle boundaries in the initial configuration, there is a difference in outcomes. Due to the proposed alternative grid basis functions and its ability to capture the tensile deformation, which is otherwise neglected by the uGIMP, it can be concluded that the CPDI method provides more accurate results than the uGIMP when the geometry is rotated.

Appendix B

Appendix to Chapter 3.5 : Verification of the penalty contact algorithm

The penalty contact algorithm implemented in Chapter 3 has been applied to problems for which a closed-form solution is known. The outcomes of the CPDI code are also compared to the outcomes of the commercial finite element software, ABAQUS™. Results presented in this Appendix have been published in part in Reference [84], to which the author of this monograph contributed to the simulation using ABAQUS™ and the development of the contact formulation in CPDI.

Cylinder rolling on inclined plane

Owing to the current two-dimensional implementation, the problem of a sphere rolling on an inclined surface presented in reference [81] has been replaced by a cylinder. As an enhanced version of MPM, CPDI is utilised in this study to test the proposed and conventional contact algorithms. In this problem, a cylinder with a radius of 1.6 m rolls on a plane measuring 20 m in length and 0.8 m in thickness. In two cases, the inclination of the plane is 60° and 45°, corresponding to a surface coefficient of 0.286 and 0.495. The bottom and sides of the plane are completely fixed as boundary conditions. The first case will be referred to as *slip* and the second as *no-slip*. The Neo-Hookean hyperelastic material model is adopted for the rolling cylinder with the following mechanical properties: bulk modulus 6 MPa, shear modulus 3 MPa, and density 1 g/cm^2. The same elastic constitutive model is applied to the plane, but its properties are multiplied by a factor of ten. In all cases, a gravitational acceleration of 10 m/s^2 is considered.

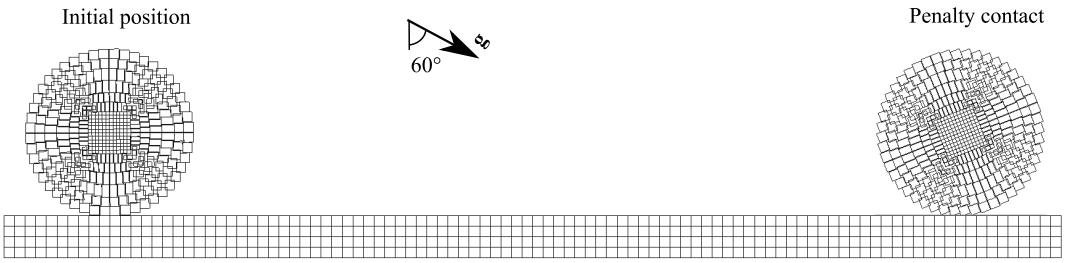

Figure B.1: Initial and finial location of the slip case of the rolling cylinder showing the gap of the MPM contact

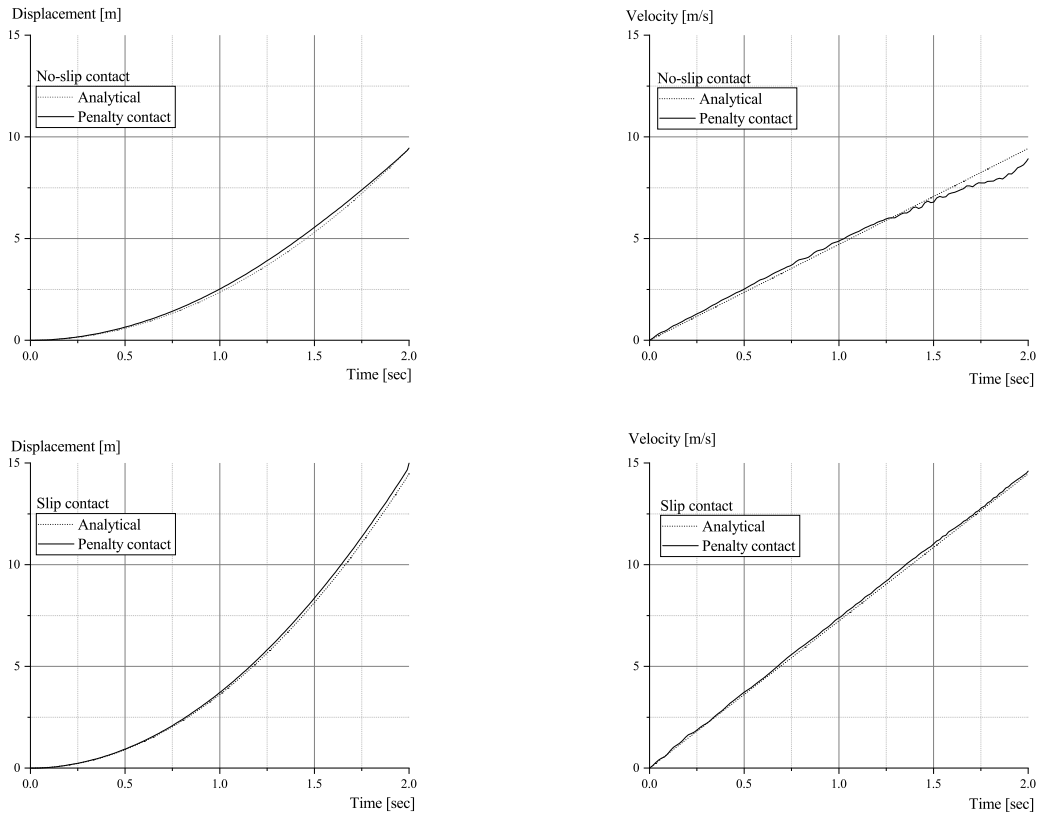

Figure B.2: Displacement and velocity of the centre point of rolling cylinder: No-slip contact (upper row), and slip contact (lower row)

A plane-strain analysis is conducted using a computational mesh consisting of four-node regular cells of size 0.4 m. See Figure B.1 for the irregular CPDI discretisation in which the maximum particle size is 0.2 m. A 0.001 m interface layer is discretized using a two-node element of 0.1 m size, yielding a total of 517 linear segments. The analytical solution for the location of the cylinder's centre when it rolls on a surface is given by:

$$d_s(\tau) = \frac{5}{2}\left(\sqrt{3} - \frac{2}{7}\right)\tau^2 \quad \text{and} \quad d_n(\tau) = \frac{5\sqrt{2}}{3}\tau^2, \tag{B.1}$$

with d_s and d_n being the position along the plane at time τ for the *slip* and *no-slip* case, respectively.

The numerical solution is obtained by calculating the initial gravity stresses at zero inclination, followed by a sudden tilt of the plane and cylinder. Figure B.2 illustrates the proposed method along with the analytical for comparison purposes. The proposed scheme based on penalty function manages to accurately predict the contact forces, compared with the analytical solutions, in both slip and non-slip situations. The approach based on the penalty function yields a straight line for the velocity variation, with the exception of the final portion of the no-slip case.

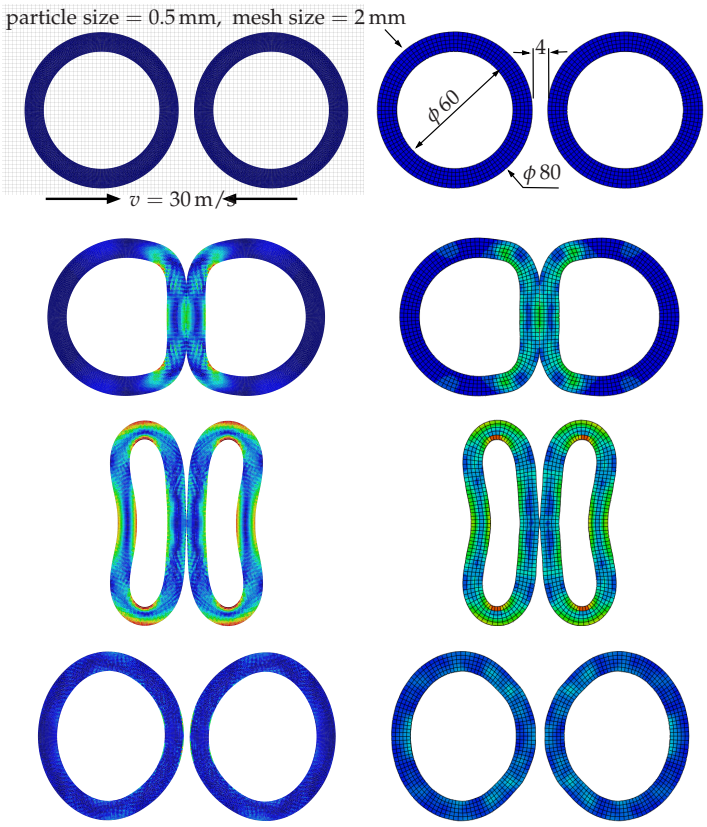

Figure B.3: Von Mises stresses $(0 - 20\,MPa)$ of the CPDI (left) and FEM (right) analyses using penalty contact algorithm at: 0, 0.4, 1.6, and 3.2 ms

Collision of two elastic rings

To demonstrate the efficacy and precision of the proposed contact algorithm, the collision of two elastic rings is reproduced. In this issue, the interface along the interaction between the deformable bodies is severely deformed. Following Huang et al. [95] and the references cited therein, the inner and outer diameters of the two rings are 60 mm and 80 mm, respectively. They are separated by 4 mm. Each ring has a 1.01 g/cm^3 density, a 121.7 MPa bulk modulus, and a 26.1 MPa shear modulus, and conforms to the Neo-Hookean model adopted earlier. Both rings are assigned an initial velocity of 30 m/s in opposite directions. The computational mesh employed has a 2 mm cell size, while the particle size of the CPDI domains is 0.5 mm. The surface is discretized with a 2 mm mesh size and an assumed friction coefficient of 0.1.

The software ABAQUS™ where the penalty algorithm is implemented in the FE framework is chosen as a reference solution. The rings in this analysis are discretized with a 2 mm mesh size. In addition, similar constitutive model routines are integrated into FEM. As illustrated in Figure B.3, the present algorithm is capable of capturing the highly dynamic collision behaviour. In addition, the suggested mapping procedure of the contact forces to the computational grid in Equation 3.58 provides a weighted average of the

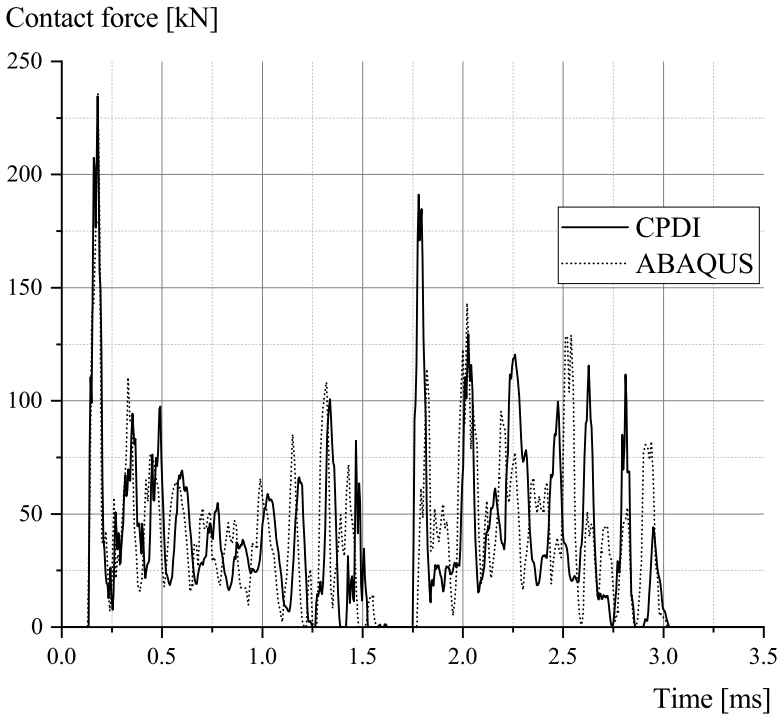

Figure B.4: Variation of the total contact forces during the collision

interface forces and subsequently generates relatively smooth contact stresses. Across the line of symmetry, symmetric deformations and stresses are observed for the same reason. As depicted in Figure B.4, the contact forces of the two analyses are monitored during the collision. Despite the fact that this application is regarded as a multi-contact problem in which the configuration of the interface changes during continuous deformation, the trend indicates that the contact forces of the two schemes are in good agreement. Figure B.4 demonstrates that, beyond 1.6 ms, the rings interact at the outer edges rather than the centre, which accounts for the small difference between FEM and the present CPDI analysis.

Appendix C

Appendix to Chapter 5 and Chapter 6: Hypoplastic Model for sand

This section presents a brief overview of the hypoplastic model for sand and its extension to small strain stiffness. The material model of sand is based on the work of Von Wolffersdorff [213] and its extension to small strain stiffness, on the work of Niemunis and Herle [165]. For the sake of completeness, the hypoplastic model implemented in the CPDI code is discussed in this section briefly. For a more detailed understanding of the model, the readers are directed towards reference [165].

Model Formulation

Hypoplasticity is an approach to non-linear constitutive modelling of geo-materials. Following from Von Wolffersdorff [213], the hypoplastic constitutive relation in the rate form is expressed as

$$\dot{\boldsymbol{\sigma}} = \boldsymbol{G}\ (\boldsymbol{\sigma}, e, \dot{\boldsymbol{\varepsilon}})\,, \tag{C.1}$$

where, $\dot{\boldsymbol{\sigma}}$ is the Zareba-Jaumann stress rate tensor, $\dot{\boldsymbol{\varepsilon}}$ is the strain rate tensor, and e is the current void ratio. The rate of void ratio is follows from

$$\dot{e} = (1+e)\ \ tr\,(\boldsymbol{\varepsilon})\,. \tag{C.2}$$

The general form of the tensorial function $\boldsymbol{G}$ is selected such that

$$\dot{\boldsymbol{\sigma}} = \boldsymbol{L}\dot{\boldsymbol{\varepsilon}} + \boldsymbol{N}\|\dot{\boldsymbol{\varepsilon}}\|, \tag{C.3}$$

where, $\boldsymbol{L}$ and $\boldsymbol{N}$ are the fourth-order linear and second-order non-linear constitutive tensors, respectively. The term $\|\dot{\boldsymbol{\varepsilon}}\|$ is the Euclidean norm of the strain rate tensor. For ease of representation, Equation C.3 is represented in index notation as

$$\dot{\sigma_{ij}} = L_{ijkl}\dot{\varepsilon_{kl}} + N_{ij}\sqrt{\dot{\varepsilon_{ij}}\dot{\varepsilon_{ij}}}, \tag{C.4}$$

with L_{ijkl} and N_{ij} being the linear and non-linear constitutive tensors, respectively. The decomposition of function $\boldsymbol{G}$ into a linear and non-linear tensors is performed to achieve the inelastic behaviour of sand without having to decompose the strain into elastic and plastic parts. Tensors L_{ijkl} and N_{ij} are functions of stress and void ratio.

They are represented as

$$L_{ijkl} = f_b\, f_e \frac{1}{\hat{\sigma}_{ij}\hat{\sigma}_{ij}} \left(f^2\, \delta_{ik}\, \delta_{jl} + a^2\, \hat{\sigma}_{ik}\, \hat{\sigma}_{jl} \right), \tag{C.5}$$

$$N_{ij} = f_d\, f_b\, f_e \frac{af}{\hat{\sigma}_{ij}\hat{\sigma}_{ij}} \left(\hat{\sigma}_{ij} + \hat{\hat{\sigma}}_{ij} \right). \tag{C.6}$$

The tensors $\hat{\sigma}_{ij}$ and $\hat{\hat{\sigma}}_{ij}$ are the normalised stress tensor and the deviatoric stress tensor, respectively. They are represented as

$$\hat{\sigma}_{ij} = \frac{\sigma_{ij}}{I_1}, \quad \text{with} \quad I_1 = \sigma_{11} + \sigma_{22} + \sigma_{33}, \tag{C.7}$$

$$\hat{\hat{\sigma}}_{ij} = \hat{\sigma}_{ij} - \frac{1}{3}\delta_{ij}. \tag{C.8}$$

From Equation C.5, the constant a is represented as

$$a = \frac{\sqrt{3}\ \left(3 - \sin\phi_c\right)}{2\ \sqrt{2}\ \sin\phi_c}, \tag{C.9}$$

where ϕ_c is the critical state friction angle, and the factor f is represented as

$$f = \sqrt{\frac{1}{8}\tan^2\psi + \frac{2 - \tan^2\psi}{2 + \sqrt{2}\ \tan\psi\ \cos 3\theta}} - \frac{1}{2\sqrt{2}}\tan\psi, \tag{C.10}$$

where, $\cos 3\theta$ is the Lode angle function and is given by

$$\cos 3\theta = -\sqrt{6}\ \frac{\mathrm{tr}(\hat{\hat{\sigma}} \cdot \hat{\hat{\sigma}} \cdot \hat{\hat{\sigma}})}{\left[\hat{\hat{\sigma}} : \hat{\hat{\sigma}}\right]^{3/2}}\ . \tag{C.11}$$

$\tan\psi$ is defined as

$$\tan\psi = \sqrt{3}\ \|\hat{\hat{\sigma}}\|\ . \tag{C.12}$$

We define three characteristic void ratios namely, critical void ratio e_c, the minimum possible void ratio e_d corrected to the corresponding density, and the maximum possible void ratio e_i corresponding to the minimum density. The variables e_{c0}, e_{d0} and e_{i0} correspond to the void ratios at vanishing pressure represented by the first stress invariant I_1. From Equation C.6, the factors f_e and f_d are represented as

$$f_e = \left(\frac{e_c}{e}\right)^{\beta}, \quad \text{and} \quad f_d = \left(\frac{e - e_d}{e_c - e_d}\right)^{\alpha} \tag{C.13}$$

with β and α being the input indices. From Equation C.5, the pressure dependency of

the soil stiffness, represented by the factor f_b is defined as

$$f_b = \frac{h_s}{n}\left(\frac{1+e_i}{e_i}\right)\left(\frac{e_{i0}}{e_{c0}}\right)^{\beta}\left(\frac{-I_1}{h_s}\right)^{1-n}\left[3+a^2-\sqrt{3}\,a\left(\frac{e_{i0}-e_{d0}}{e_{c0}-e_{d0}}\right)^{\alpha}\right]^{-1}, \tag{C.14}$$

where, h_s is the pressure independent granular stiffness and n is an input index. The characteristic void ratios are updated according to the relation

$$\frac{e_i}{e_{i0}} = \frac{e_c}{e_{c0}} = \frac{e_d}{e_{d0}} = \exp\left[-\left(\frac{-I_1}{h_s}\right)^{n}\right]. \tag{C.15}$$

Finally, substituting Equations C.5 and C.6 into Equation C.4, the final constitutive equation is expressed as

$$\mathring{\sigma}_{ij} = f_b f_e \frac{1}{\hat{\sigma}_{ij}\hat{\sigma}_{ij}}\left[f^2\dot{\varepsilon}_{ij} + a^2\left(\hat{\sigma}_{ik}\hat{\sigma}_{jl}\right)\dot{\varepsilon}_{kl} + a f f_d\left(\hat{\sigma}_{ij}+\hat{\hat{\sigma}}_{ij}\right)\sqrt{\dot{\varepsilon}_{ij}\dot{\varepsilon}_{ij}}\right] \tag{C.16}$$

Extension to small strain stiffness

To predict the very small strain stiffness and recent stress history effects, the model is combined with the intergranular strain concept [165]. The formulation is extended to account for small strain stiffness, by introducing a new state variable called the intergranular strain δ denoted by

$$\delta = \int \dot{\delta} dt\ , \tag{C.17}$$

where,

$$\dot{\delta} = \begin{cases} (\boldsymbol{I} - \hat{\delta}\otimes\hat{\delta}\rho^{\beta_r}) : \dot{\varepsilon}, & \text{for } \hat{\delta} : \dot{\varepsilon} > 0 \\ \dot{\varepsilon}, & \text{for } \hat{\delta} : \dot{\varepsilon} \leq 0\ , \end{cases} \tag{C.18}$$

with, $\hat{\delta}$ being the direction tensor for the intergranular strain. It is defined as

$$\hat{\delta} = \begin{cases} \delta/\|\delta\|, & \text{for } \delta \neq \mathbf{0} \\ \mathbf{0}, & \text{for } \delta = \mathbf{0}\ . \end{cases} \tag{C.19}$$

ρ is defined as the normalised intergranular strain magnitude defined as

$$\rho = \frac{\|\delta\|}{R}\ . \tag{C.20}$$

β_r and R are intergranular strain concept parameters. The constitutive relation of the extended hypoplastic model is written as

$$\mathring{\sigma} = \boldsymbol{M} : \dot{\varepsilon}\ . \tag{C.21}$$

The stiffness tensor of the intergranular strain concept formulation $\boldsymbol{M}$ is constructed from tensors $\boldsymbol{L}$ and $\boldsymbol{N}$ and is modified by two scalars m_T and m_R. The tensor is represented as

$$\begin{aligned}\boldsymbol{M} &= \left[\rho^{\chi} m_T + \left(1-\rho^{\chi}\right) m_R\right] \boldsymbol{L} \\ &+ \begin{cases} \rho^{\chi}\left(1-m_T\right) \boldsymbol{L} : \hat{\boldsymbol{\delta}} \otimes \hat{\boldsymbol{\delta}} + \rho^{\chi} \boldsymbol{N} \hat{\boldsymbol{\delta}}, & \text{for } \hat{\boldsymbol{\delta}} : \dot{\boldsymbol{\varepsilon}} > 0\,, \\ \rho^{\chi}\left(m_R - m_T\right) \boldsymbol{L} : \hat{\boldsymbol{\delta}} \otimes \hat{\boldsymbol{\delta}}, & \text{for } \hat{\boldsymbol{\delta}} : \dot{\boldsymbol{\varepsilon}} \leq 0\,. \end{cases}\end{aligned} \tag{C.22}$$

In index notation, Equation C.22 is written as

$$\begin{aligned}M_{ijkl} &= \left[\rho^{\chi} m_T + \left(1-\rho^{\chi}\right) m_R\right] L_{ijkl} \\ &+ \begin{cases} \rho^{\chi}\left(1-m_T\right) L_{ijmn}\left(\hat{\delta}_{mk}\hat{\delta}_{nl}\right) + \rho^{\chi} N_{ik}\hat{\delta}_{jl}, & \text{for } \hat{\delta}_{ij}\dot{\varepsilon}_{ij} > 0\,, \\ \rho^{\chi}\left(m_R - m_T\right) L_{ijmn}\hat{\delta}_{mk}\hat{\delta}_{nl}, & \text{for } \hat{\delta}_{ij}\dot{\varepsilon}_{ij} \leq 0\,, \end{cases}\end{aligned} \tag{C.23}$$

with, variables m_R and m_T defined as

$$m_R = p_r A_g \left(\frac{p}{p_r}\right)^{n_g} \frac{4 A_m \alpha_G}{2 p \alpha_E} \left(\frac{\lambda^* \kappa^*}{\lambda^* + \kappa^*}\right) \frac{1}{\left(1 - \nu_{pp} - 2\frac{\alpha_E}{\alpha_\nu^2}\nu_{pp}^2\right)}\,, \tag{C.24}$$

$$m_T = m_{rat}\, m_R. \tag{C.25}$$

Variables χ and m_{rat} are the intergranular strain concept parameters. A_g and n_g are parameters quantifying the dependency of shear modulus at very small strain on mean effective stress parameter.

Constrained Modulus Calculation

For the MPM formulation, time integration of momentum equation is restricted by the CFL (Courant, Friedrichs and Lewy) condition where the critical time step is bound by the characteristic length of the element and the wave speed of the material. This condition requires the constrained modulus E^c to calculate the wave speed and ultimately, the size of critical time step. We consider the case of one-dimensional straining similar to that of oedometer test. We take all the components in the strain rate tensor equal to zero except $\dot{\varepsilon}_{22}$. For the sake of simplicity, the stresses are assumed to be isotropic and are given by

$$\hat{\sigma}_{ij} = \frac{1}{3}\delta_{ij}, \quad \text{and} \quad \hat{\bar{\sigma}}_{ij} = 0. \tag{C.26}$$

The above values are obtained given that $\hat{\sigma}_{ij}\hat{\sigma}_{ij} = \frac{1}{3}$. Given these conditions, and with $\psi = 0$ and $f = 1$, it is shown that

$$L = f_b\, f_e \left(3 + \frac{a^2}{3}\right), \text{and} \tag{C.27}$$

$$N = a\ f_b\ f_d\ f_e \tag{C.28}$$

With L and N being the components of the tensor L_{ijkl} and N_{ij}, respectively. This corresponds to $\dot{\varepsilon}_{22} \neq 0$. The constrained modulus thus becomes

$$E^c = L \mp N, \tag{C.29}$$

with the minus and plus sign indicating the loading and unloading conditions, respectively. This yields the constrained modulus

$$\begin{aligned} E^c = & \left[\rho^\chi m_T + \left(1-\rho^\chi\right) m_R\right] L \\ & + \begin{cases} \rho^\chi \left(1-m_T\right) L + \rho^\chi N, & \text{for } \hat{\delta}_{ij}\dot{\varepsilon}_{ij} > 0\ , \\ \rho^\chi \left(m_R - m_T\right) L, & \text{for } \hat{\delta}_{ij}\dot{\varepsilon}_{ij} \leq 0\ . \end{cases} \end{aligned} \tag{C.30}$$

Appendix D

Appendix to Chapter 3.6 and 5.3 : Comparison of performance of Constitutive laws

This Appendix covers the impacts of constitutive law, along with equivalent simulation parameters. In this Appendix, two constitutive laws are discussed: the hypoplastic sand model [213] and the UBCSAND model, which was implemented in-house for the CPDI code.

D.1 Granular Column Collapse

The influence of constitutive laws on final outcomes is not a novel research topic. Reference [147] compared the results of the collapse of a granular column for various failure laws. The Mohr-Coulomb failure criterion was compared to the more complex NorSand soil model in Reference [65].

To examine the potential impact of constitutive laws on the final result, a comparison is made between the simple Mohr-Coulomb model and the much more complex UBCSAND model. In Chapter 5, the formulation of the UBCSAND model will be described in detail. In order to compare simulations, it is necessary to ensure that the input parameters used to describe the soil are comparable. In order to accomplish this, the parameters of the UBCSAND will be calibrated. While the results of the column collapse experiments were taken from references [133, 134], there was no data regarding the description of the Quartz sand mixture in the form of Oedometer or Triaxial tests.

The UBCSAND parameters were fitted as closely as possible to the limited data available from the Mohr-Coulomb model's results. Figure D.1 depicts the final results of the

$N1_{60}[-]$	$m_e[-]$	$n_e[-]$	$n_p[-]$	$K^e_G[-]$	$K^e_B[-]$
10.7	0.7	0.7	0.4	100	125
$K^p_G[-]$	$\phi_{pt}[^\circ]$	$\phi_f[^\circ]$	c $[kPa]$	Pa $[kPa]$	$\sigma_t[kPa]$
5	31	31.1	0	100	0
$hfac_1$ [-]	$hfac_2$ [-]	$hfac_3$ [-]	$hfac_4$ [-]	$hfac_5$ [-]	$hfac_6$ [-]
0.65	0.85	1.0	0.6	1.0	0.95

Table D.1: Calibrated UBCSAND model parameters for Quartz Sand

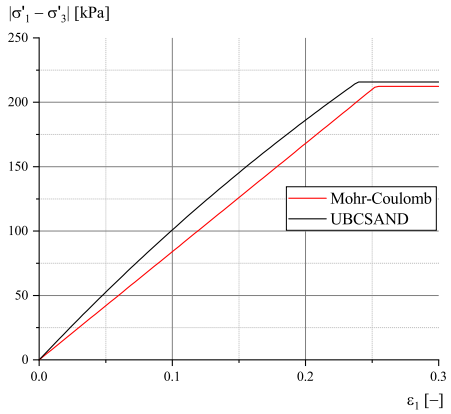

(a) Deviatoric stress ($|\sigma_1' - \sigma_3'|$) vs. Axial strain (ε_1)

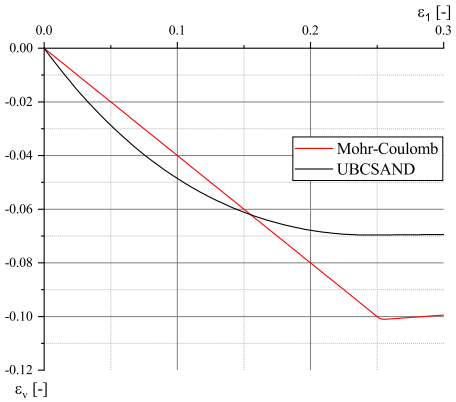

(b) Volumetric strain (ε_v) vs. Axial strain (ε_1)

Figure D.1: Calibration of UBCSAND on drained triaxial compression test at p_0' = 100 kPa

calibration exercise, in which the final strengths were matched as closely as possible for this study. Note that the UBCSAND is primarily used for modelling granular saturated sands susceptible to liquefaction under dynamic loading. In order to numerically represent the soil with some precision, UBCSAND's parameter calibration must be exhaustive. In this case, the lack of high-quality data presents a challenge. Observing the behaviour of this simulation using a complex constitutive law is still of interest. The calibrated parameters of the UBCSAND model are listed in Table D.1.

The simulation is conducted assuming that there are 9 particles per grid. The simulation from the UBCSAND model is compared to the simulation experiment and results presented in the preceding section. The simulation performed with the UBCSAND model is subjected to deviatoric strain smoothening. In this instance, numerical damping was reduced to 2%, a value considered low enough to contribute to the numerical stability

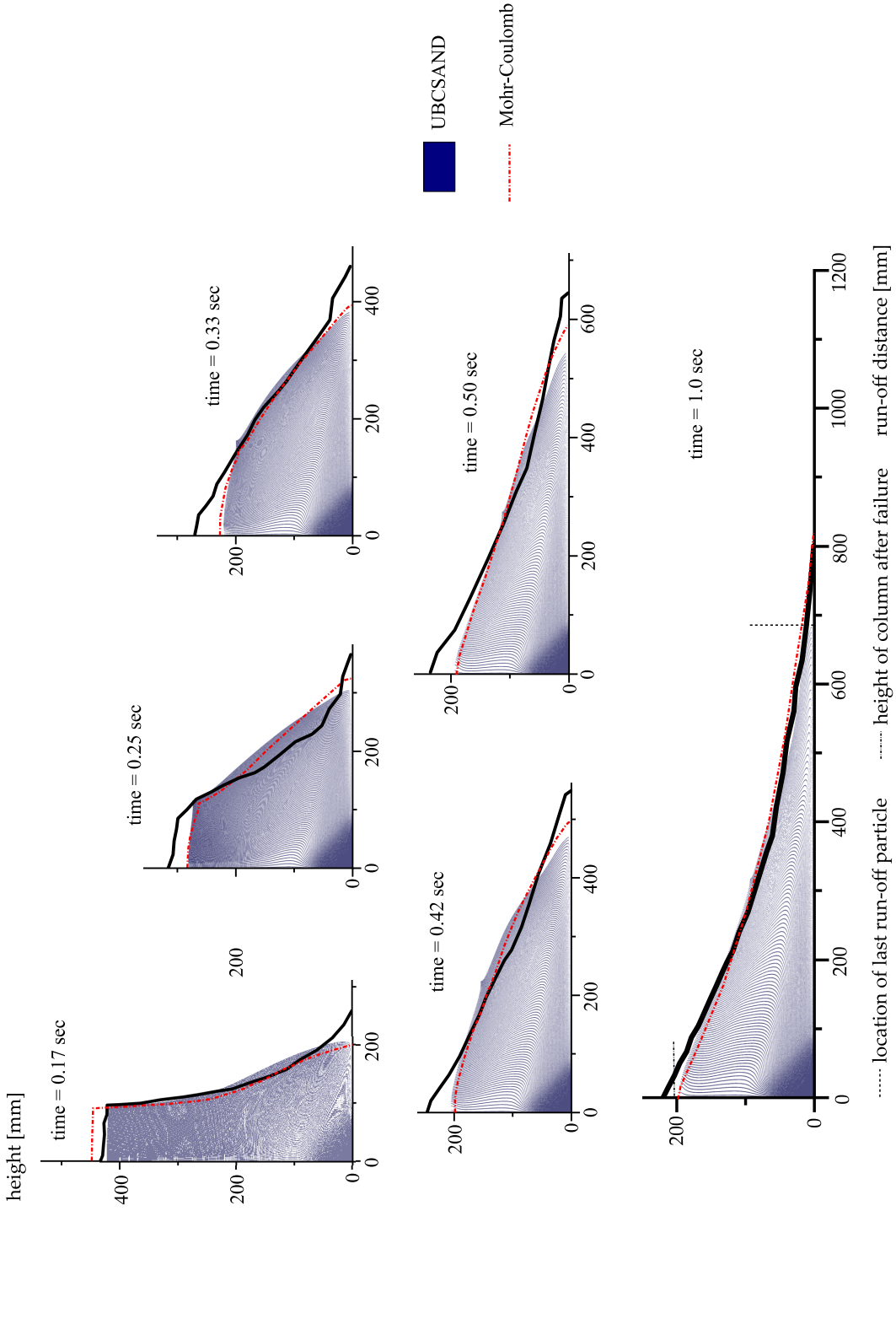

Figure D.2: UBCSAND model results compared with Mohr-Coulomb

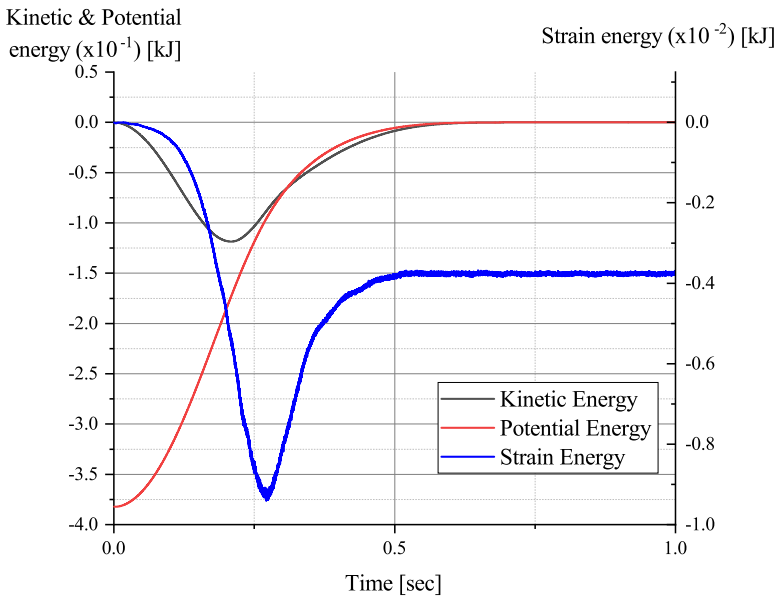

Figure D.3: Kinetic, Potential and Strain energies of the system run using UBCSAND model

of the solution. In contrast to the Mohr-Coulomb model, the UBCSAND model allows for softening/hardening behaviour. In order to account for this change, the damping is decreased. The Mohr-Coulomb simulation assumed a 7.5% local damping coefficient.

Figure D.2 depicts the simulation results and the effects of constitutive law on runoff, while Figure D.3 displays the corresponding energies. The surface of the Mohr-Coulomb simulation result is compared to the UBCSAND simulation result and the experiment results. During the initial milliseconds of the simulation, the Mohr-Coulomb and UBC-SAND simulations produce comparable results. The shapes of the soil column during deformation for the Mohr-Coulomb and UBCSAND models are examined.

Already, it is obvious that the softening or hardening behaviour of the constitutive law must be considered when attempting to back-calculate experimental results, such as in this study. In order to accurately replicate the non-linear behaviour of sand, it is also essential that the soil parameters be calibrated prior to simulation. Due to a lack of high-quality data, only a cursory parameter identification was performed in this simulation. It is hypothesised that with improved calibration, the need for artificial numerical tricks to fit the numerical simulation to experiment can be reduced and the constitutive law can handle it on its own.

D.2 Shake Table Test : Performance comparison of the UBCSAND and hypoplastic models

$N1_{60}[-]$	$m_e[-]$	$n_e[-]$	$n_p[-]$	$K_G^e[-]$	$K_B^e[-]$
11.5	0.5	0.5	0.4	1224	1120
$K_G^p[-]$	$\phi_{pt}[^\circ]$	$\phi_f[^\circ]$	$c[kPa]$	$Pa[kPa]$	$\sigma_t[kPa]$
423	31.5	37.5	0	100	0
$hfac_1[-]$	$hfac_2[-]$	$hfac_3[-]$	$hfac_4[-]$	$hfac_5[-]$	$hfac_6[-]$
0.65	0.85	1.0	0.6	1.0	0.95

Table D.2: UBCSAND model parameters for Berlin Sand

$\phi_c[^\circ]$	$p_t[-]$	$h_s[MPa]$	$n[-]$	$e_{d0}[-]$
31.5	-	$230e6$	0.3	0.391
$e_{c0}[-]$	$e_{i0}[-]$	$\alpha[-]$	$\beta[-]$	$m_R[-]$
0.688	0.791	0.13	1	4.4
$m_T[-]$	$R[-]$	$\beta_r[-]$	$\chi[-]$	$e_0[-]$
2.2	$1e-4$	0.2	6	-

Table D.3: Hypoplastic model parameters for Berlin Sand

Using the properties of Berlin sand, simulations for the shake-table test were then conducted in order to compare the predictions of the UBCSAND and HPS soil models for a boundary-valued problem with well-defined boundary and loading conditions. The boundary and loading conditions remained unchanged, as did the number of particles and the background grid. In this instance, the particle-in-cell damping was increased from 1 percent to 2 percent. This increase in damping value was strictly required to maintain numerical stability. Given that Berlin sand parameters existed for the hypoplastic sand model and high-quality experimental data were available for calibrating

Parameter	**Nevada Sand**	**Berlin Sand**
$G_s[-]$	2.67	2.61
$e_0[-]$	0.68	0.465
$e_{min}[-]$	0.511	0.391
$e_{max}[-]$	0.877	0.688
$D_{10}[mm]$	0.11	0.20
$D_{50}[mm]$	0.17	0.55
$C_u[-]$	1.75	3.25
$C_c[-]$	0.88	0.60

Table D.4: Physical properties of Nevada and Berlin Sand

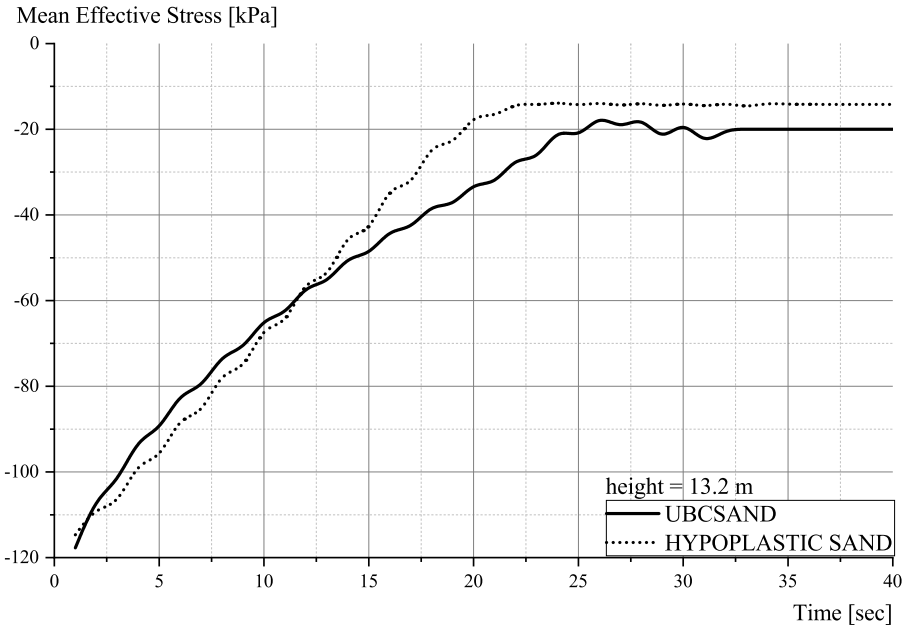

(a) Mean Effective Stress at height 13.2 m

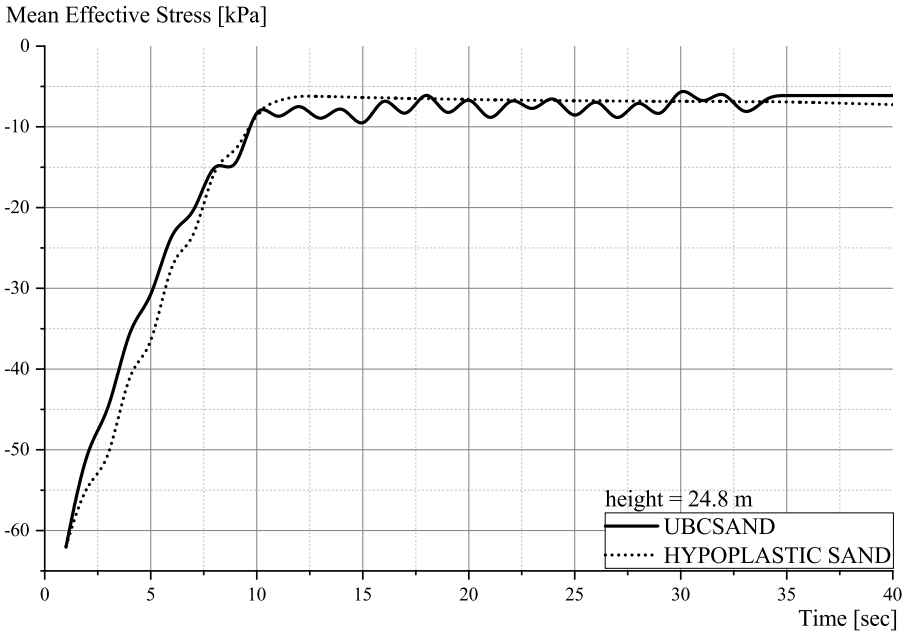

(b) Mean Effective Stress at height 24.8 m

Figure D.4: CPDI simulation of shake table test : Comparison of the mean effective stress for both models at heights 13.2 m and 24.8 m

the UBCSAND sand model, the properties of Berlin sand were adopted. In addition, Berlin sand was utilised in the experimental study described in the following Chapters (Chapter 6). The numerical makeup of the hypoplastic model is described in Appendix C.

The monotonic and cyclic test data from reference [124], which corresponded to a relative density Dr = 75%, were utilised to calibrate the constitutive models. The procedure described in [194] was used to estimate the reference values for the stiffness parameters and stress exponents during the calibration of the UBCSAND model. Later, these values were refined through an iterative process to better match the published results. Tables D.2 and D.3 describe the properties of Berlin sand. Table D.4 outlines the physical properties of both types of sand. It should be noted that the Berlin sand is coarser than the Nevada Sand.

Figure D.4 compares the cyclically induced evolution of mean effective stress at heights of 13.2 m (Figure D.4a) and 24.8 m (Figure D.4b). Clearly, top-down liquefaction developed as the mean effective stress approached zero and plateaued near the column's top before plateauing below 13.2 m is observed. This behaviour is consistent with the experimentally observed results depicted in Figure D.5 during the test with Nevada sand. It is evident that the predicted rates of strength loss along the upper portion of the column (24.8 m) for both constitutive models are nearly identical. The average rate of liquefaction associated with the hypoplastic sand model is greater than that of the UBCSAND model; i.e., the effective stress plateaus sooner. Each model predicts a slightly different final strength of the soil following liquefaction, with the hypoplastic sand model predicting a lower strength than the UBCSAND model. We observe incomplete liquefaction in both cases. The outcomes are comparable to those predicted by the UBCSAND model when the Nevada sand soil parameters are utilised.

The Figure D.5 depicts the evolution of excess pore pressure. As observed in Figure D.5b, the rate of evolution of excess pore pressure is comparable in the top portion of the column (24.8 m), although the average rate of evolution of excess pore pressure in the case of the HPS model is slightly higher than that of the UBCSAND model. Figure D.5a depicts that the behaviour of the bottom portion of the section is comparable to what can be discerned by examining the evolution of mean effective stresses. The comparison of predictions is generally satisfactory.

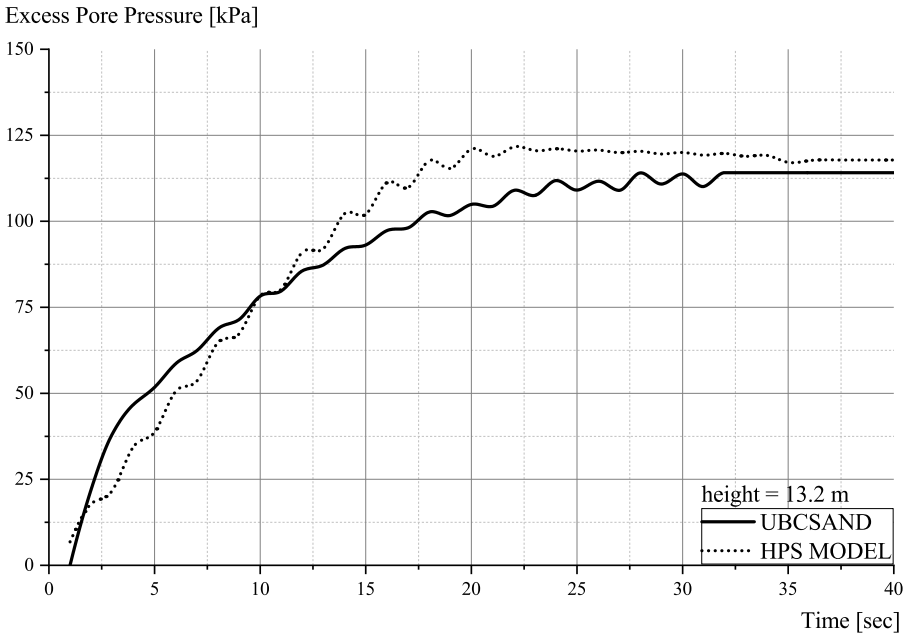

(a) Excess Pore Pressure at height 13.2 m

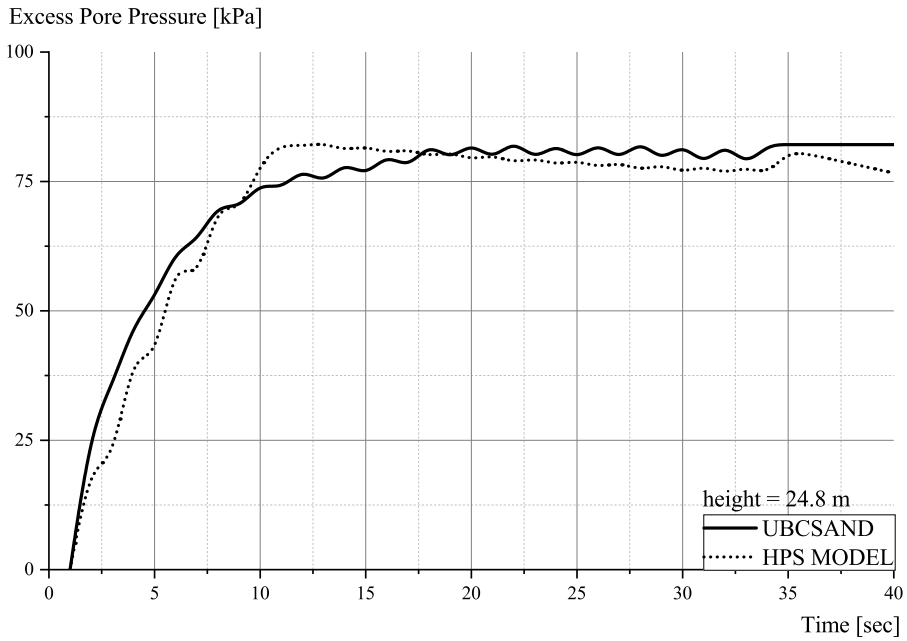

(b) Excess Pore Pressure at height 24.8 m

Figure D.5: CPDI simulation of shake table test : Comparison of the mean effective stress for both models at heights 13.2m and 24.8m

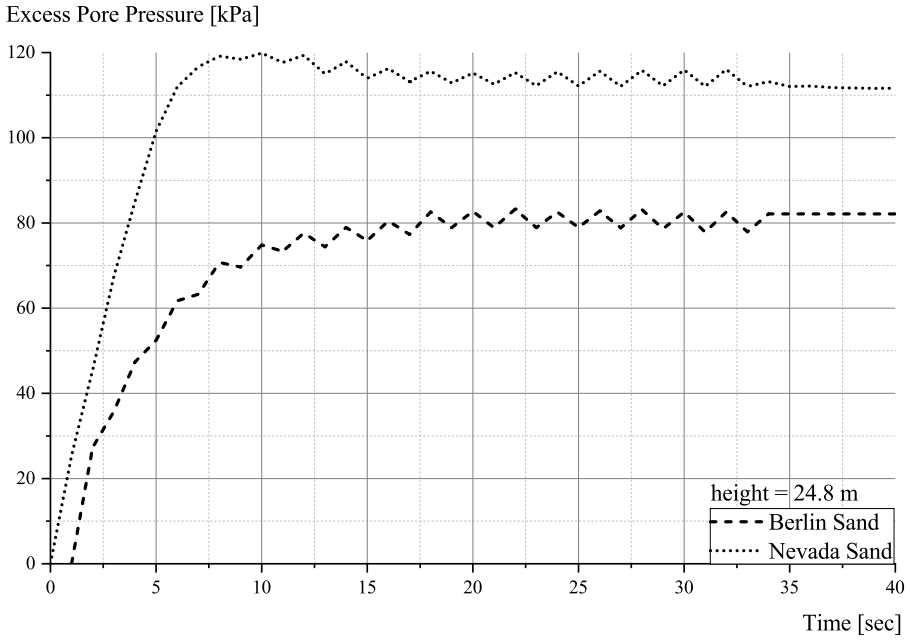

Figure D.6: Evolution of Excess Pore Pressure at height 24.8m from UBCSAND Model - Nevada vs. Berlin Sand

Comparing the excess pore pressures of Nevada and Berlin sand in Figure D.6 reveals that the rates of pressure increase captured numerically given the same permeability are initially roughly equivalent for both sands. The times at which the values plateau are also roughly the same, whereas the peak values attained by the models are vastly different. Both models exhibit incomplete liquefaction, consistent with what was previously explained. The parameters selected for Berlin sand correspond to a denser soil than those selected for Nevada sand, with initial void ratios of 0.68 and 0.4655 for Nevada and Berlin sands, respectively. According to [210], poorly graded soils ($C_u < 6$) and soils with lower relative densities (in this case, Nevada sand) have a lower cyclic strength. At higher relative densities, the reverse trend was observed (in this case Berlin sand).

Appendix E

Appendix to Chapter 6.4 : Summary of data from field test

Determination of relative density

The relative density (I_D) of the soil is determined based on the cone resistance by two methods. The simplest method is based on DIN 4020:2010-12, given by the relation:

$$I_D = -0.33 + 0.75\, log(q_c)\,, \tag{E.1}$$

where, q_c is the cone resistance in MN, with no correlation to depth. Alternatively, the method proposed by Schmertmann [190] can be used, and is given by the relation:

$$q_c = C_0\, p_a \left(\frac{\sigma'}{p_a}\right)^{C_1} exp(C_2\, I_D)\,, \tag{E.2}$$

where, q_c is the measured cone resistance, σ' is the inital effective vertical geostatic stress component, and p_a is the atmospheric pressure. Rearranging Equation E.2, it is possible to obtain the relative density as:

$$I_D = \frac{1}{C_2}\, ln\left[\frac{q_c/p_a}{C_0\left(\sigma'/p_a\right)^{C_1}}\right]\,, \tag{E.3}$$

where, C_0, C_1, C_2 are non dimensional empirical correlation factors, investigated in the work of Jamiolkowski et al. [102]. The correlations are tabulated in Table E.1.

$\sigma' = \sigma'_{v0}$	TS	TS+TOS+HS
C_0	17.74	17.68
C_1	0.55	0.50
C_2	2.90	3.10
R	0.90	0.89
$\overline{\sigma}$	0.12	0.10
N	305	180

Table E.1: Coefficients for Equation E.3, after Jamiolkowski et al. [102]

Layer	Depth [m]		Average Cone Penetration Resistance [MPa]	Average Unit Weight [kN/m³]	Vertical Stress at Mid-Point [kPa]	DIN Method [%]	DIN Method Average[%]	Relative Density [%]	Average Relative Density [%]	Homogenised Relative Density [%]
	From	To		(submerged)						
1	0.00	1.00	25	8.5	4.25	71.85	71.85	136.70	111.71	
	1.00	2.00	25	8.5	8.50	71.85		125.52		
	2.00	3.00	25	8.5	12.75	71.85		118.98		
	3.00	4.00	25	8.5	17.00	71.85		114.34		
	4.00	5.00	25	9.5	21.75	71.85		110.37		
	5.00	6.00	25	10	26.75	71.85		107.03		
	6.00	7.00	25	10	31.75	71.85		104.27		
	7.00	8.00	25	10	36.75	71.85		101.91		
	8.00	9.00	25	10	41.75	71.85		99.85		
	9.00	10.00	25	9.5	46.50	71.85		98.11		
2	10.00	11.00	70	9.5	51.25	105.38	105.38	129.76	125.06	
	11.00	12.00	70	10.5	56.50	105.38		128.18		
	12.00	13.00	70	10.5	61.75	105.38		126.75		
	13.00	14.00	70	10.5	67.00	105.38		125.43		
	14.00	15.00	70	10.5	72.25	105.38		124.22		
	15.00	16.00	70	10.5	77.50	105.38		123.09		
	16.00	17.00	70	10.5	82.75	105.38		122.03		
	17.00	18.00	70	10.5	88.00	105.38		121.04		
3	18.00	19.00	38	10.5	93.25	85.48	85.48	100.40	93.33	109.46
	19.00	20.00	38	10.5	98.50	85.48		99.51		
	20.00	21.00	38	10.5	103.75	85.48		98.67		
	21.00	22.00	38	10.5	109.00	85.48		97.88		
	22.00	23.00	38	10.5	114.25	85.48		97.12		
	23.00	24.00	38	10.5	119.50	85.48		96.40		
	24.00	25.00	38	10.5	124.75	85.48		95.70		
	25.00	26.00	38	10.5	130.00	85.48		95.04		
	26.00	27.00	38	10.5	135.25	85.48		94.40		
	27.00	28.00	38	9	139.75	85.48		93.87		
	28.00	29.00	38	9	144.25	85.48		93.36		
	29.00	30.00	38	9	148.75	85.48		92.86		
	30.00	31.00	38	9	153.25	85.48		92.38		
	31.00	32.00	38	9	157.75	85.48		91.92		
	32.00	33.00	38	9	162.25	85.48		91.46		
	33.00	34.00	38	9	166.75	85.48		91.02		
	34.00	35.00	38	9	171.25	85.48		90.59		
	35.00	36.00	38	10	176.25	85.48		90.13		
	36.00	37.00	38	10	181.25	85.48		89.68		
	37.00	38.00	38	10	186.25	85.48		89.24		
	38.00	39.00	38	10.5	191.50	85.48		88.79		
	39.00	40.00	38	10.5	196.75	85.48		88.35		
	40.00	41.00	38	10.5	202.00	85.48		87.93		
4	41.00	42.00	75	10	207.00	107.63	107.63	109.47	107.74	
	42.00	43.00	75	10	212.00	107.63		109.08		
	43.00	44.00	75	10	217.00	107.63		108.71		
	44.00	45.00	75	10	222.00	107.63		108.34		
	45.00	46.00	75	10	227.00	107.63		107.98		
	46.00	47.00	75	12	233.00	107.63		107.56		
	47.00	48.00	75	12	239.00	107.63		107.15		
	48.00	49.00	75	12	245.00	107.63		106.75		
	49.00	50.00	75	12	251.00	107.63		106.36		
	50.00	51.00	75	11	256.50	107.63		106.01		

Table E.2: CPT Evaluation for Pile K30

In Table E.1, TS, TOS and HS refer to Ticino, Toyoura and Hokksund sands, respectively. Assuming the parameters for TS+TOS+HS, the relative density for Pile K30, simulated in Chapter 6 is evaluated in Table E.2.

E.1 CPT Data at other locations

While all the piles are planned to be vibrated under the framework of the project VISSKA, one of the five piles at different locations is planned to be the locations which will be calculated numerically prior to installation. Pile K30 is chosen, in part due to it being installed one among the first. The CPT data for the rest of the locations K05, K11, K14 and K26 are provided in Figures E.1, E.2, E.3 and E.4, respectively. A procedure similar to one explained in the previous section can be used to evaluate the relative density.

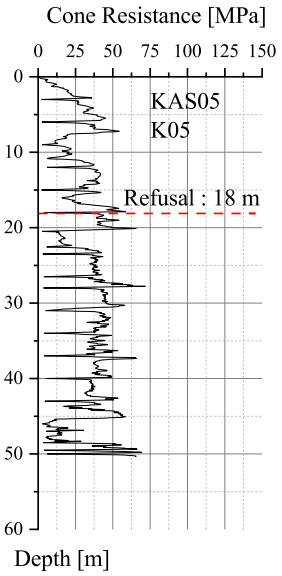

Figure E.1: CPT data at location for pile K05

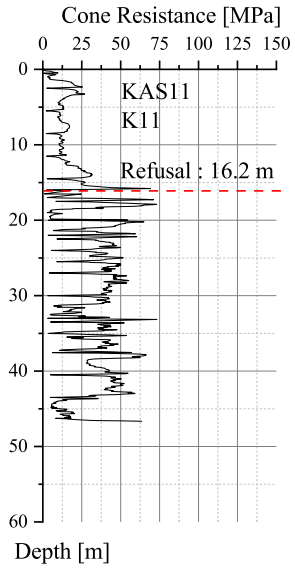

Figure E.2: CPT data at location for pile K11

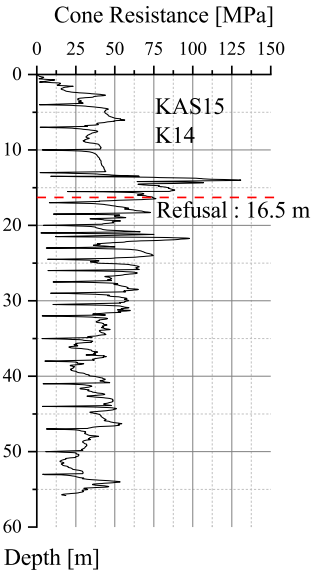

Figure E.3: CPT data at location for pile K14

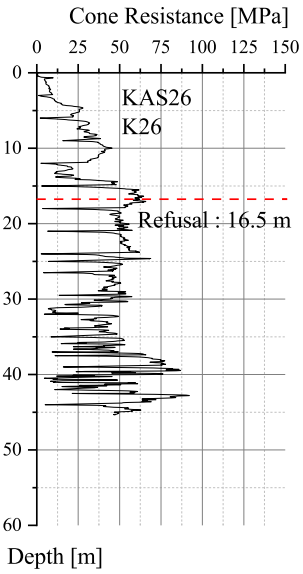

Figure E.4: CPT data at location for pile K26

E.2 Installation data for other measured piles

While providing the installation forecast for all the vibrated piles was beyond the scope of this work, it's vertical penetration is nevertheless provided in Figures E.5, E.6, E.7 and E.8. This data may be used to calibrate the numerical model in the future by means of running *Class-C* simulations.

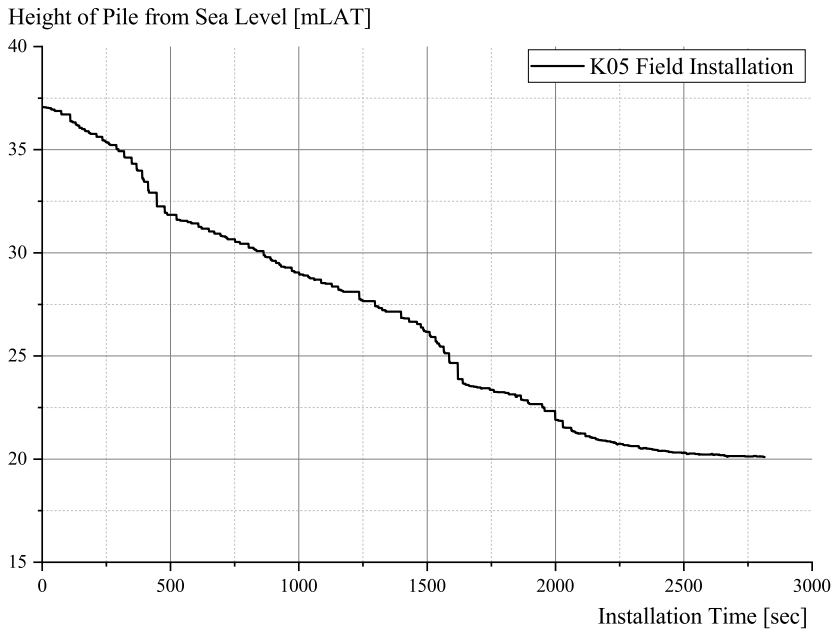

Figure E.5: Measured vertical penetration of the Pile K05

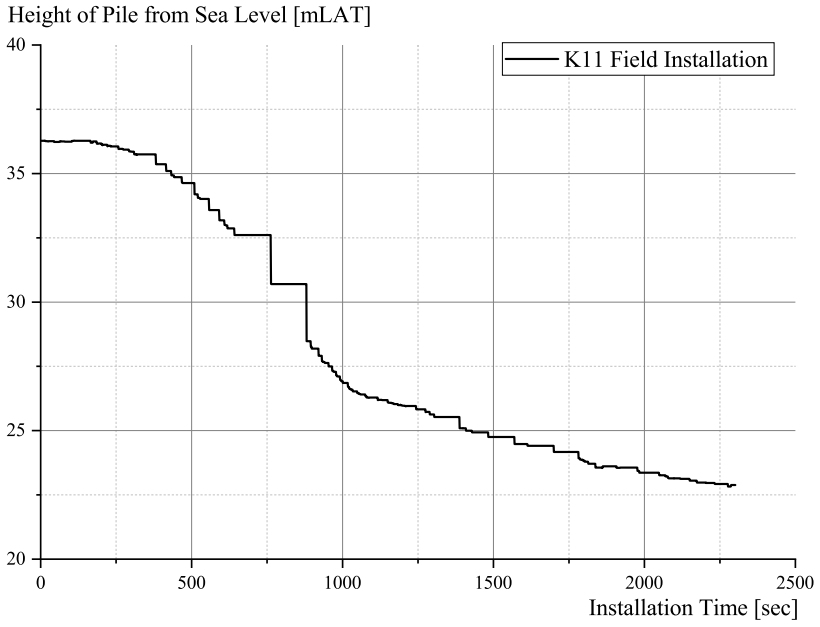

Figure E.6: Measured vertical penetration of the Pile K11

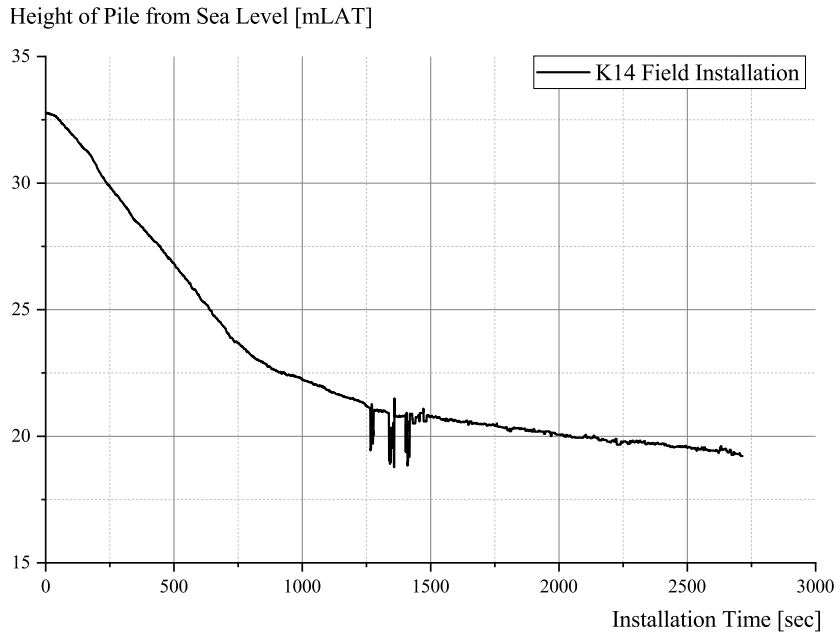

Figure E.7: Measured vertical penetration of the Pile K14

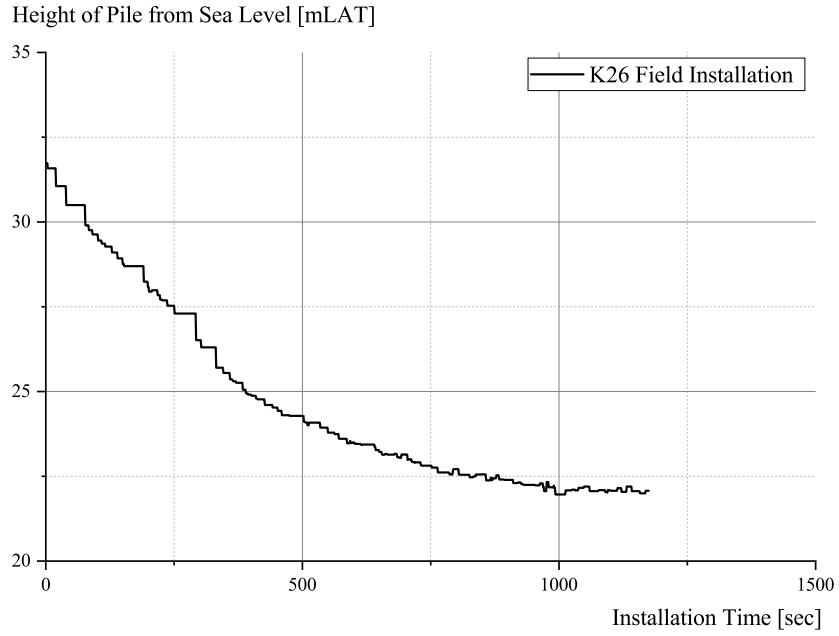

Figure E.8: Measured vertical penetration of the Pile K26

(this page intentionally left blank)

Curriculum Vitæ

20 March 1991	Born in Chennai, India
Aug 2006 - May 2008	Senior School Certificate Examination, Kendriya Vidyalaya, C.L.R.I, Chennai
Aug 2008 - May 2012	Bachelor of Technology in Mechanical Engineering, S.R.M. University, Chennai
Sep 2012 - Aug 2014	Assistant Manager, Sundram Fasteners Limited, Chennai
Oct 2014 - Nov 2016	Masters of Science, Computational Mechanics of Materials and Structures, University of Stuttgart
Feb 2017 - Jan 2023	Research and Teaching Associate, Institute of Geotechnical Engineering, University of Stuttgart
Since Feb 2023	Postdoctoral Research and Teaching Associate, Institute of Geotechnical Engineering, University of Stuttgart

Mitteilungen des Instituts für Geotechnik der Universität Stuttgart

Mitteilungen des Baugrundinstitutes Stuttgart (Institut für Grundbau und Bodenmechanik) der Universität Stuttgart Hrsg.: Prof. Dr.-Ing. Dr. h.c. U. Smoltczyk

Nr. 01	Thamm, B. R.	(1974)	Anfangssetzungen und Anfangsporenwasserüberdrücke eines normalverdichteten wassergesättigten Tones
Nr. 02	Gußmann, P.	(1975)	Einheitliche Berechnung von Grundbruch und Böschungsbruch
Nr. 03	Feeser, V.	(1975)	Die Bedeutung des Kalziumkarbonats für die bodenphysikalischen Eigenschaften vom Löß
Nr. 04	Du Thin, K.	(1976)	Standsicherheit von Böschungen: Programm-Dokumentation
Nr. 05	Smoltczyk, U. / Pertschi, O. / Hilmer, K.	(1976)	Messungen an Schleusen in der UDSSR. Schleusennorm der UDSSR (SN 30365)
Nr. 06	Hilmer, K.	(1976)	Erddruck auf Schleusenkammerwände
Nr. 07	Laumans, Q.	(1977)	Verhalten einer ebenen, in Sand eingespannten Wand bei nicht-linearen Stoffeigenschaften des Bodens
Nr. 08	Lächler, W.	(1977)	Beitrag zum Problem der Teilflächenpressung bei Beton am Beispiel der Pfahlkopfanschlüsse

Nr. 09	Spotka, H.	(1977)	Einfluß der Bodenverdichtung mittels Oberflächenrüttelgeräten auf den Erddruck einer Stützwand bei Sand
Nr. 10	Schad, H.	(1979)	Nichtlineare Stoffgleichungen für Böden und ihre Verwendung bei der numerischen Analyse von Grundbauaufgaben
Nr. 11	Ulrich, G.,	(1980)	Verschiebungs- und kraftgesteuerte Plattendruckversuche auf konsolidierenden Böden
	Gußmann, P.		Zum Modellgesetz der Konsolidation
Nr. 12	Salden, D.	(1980)	Der Einfluß der Sohlenform auf die Traglast von Fundamenten
Nr. 13	Seeger, H.	(1980)	Beitrag zur Ermittlung des horizontalen Bettungsmoduls von Böden durch Seitendruckversuche im Bohrloch
Nr. 14	Schmidt, H. H.	(1981)	Beitrag zur Ermittlung des Erddrucks auf Stützwände bei nachgiebigem Baugrund
Nr. 15	Smoltczyk, U. / Schweikert, O.	(1981)	Vorstudie über bauliche Alternativen für Durchgangsstraßen in Siedlungen
Nr. 16	Malcharek, K. / Smoltczyk, U.	(1981)	Vergleich nationaler Richtlinien für die Berechnung von Fundamenten
Nr. 17	Gruhle, H. D.	(1981)	Das Verhalten des Baugrundes unter Einwirkung vertikal gezogener Ankerplatten als räumliches Problem des Erdwiderstandes
Nr. 18	Kobler, W.	(1982)	Untersuchungen über Böschungs- und Grundbruch bei begrenzten Lastflächen
Nr. 19	Lutz, W.	(1983)	Tragfähigkeit des geschlitzten Baugrunds neben Linienlasten
Nr. 20	Smoltczyk, U.	(1983)	Studienunterlagen “Bodenmechanik und Grundbau”: überarbeitete Ausgabe 1993

Nr. 21	Schweikert, O.	(1984)	Der Einfluß des Böschungswinkels auf die Berechnung des aktiven Erddrucks
Nr. 22	Vogt, N.	(1984)	Erdwiderstandsermittlung bei monotonen und wiederholten Wandbewegungen in Sand
Nr. 23	Buchmaier, R.	(1985)	Zur Berechnung von Konsolidationsproblemen bei nichtlinearem Stoffverhalten
Nr. 24	Schad, H.	(1985)	Möglichkeiten der Böschungssicherung bei kleinen Baugruben
	Smoltczyk, U. / Schad, H. / Zoller, P.		Sonderkonstruktionen der Böschungssicherung
Nr. 25	Gußmann, P.	(1986)	Die Methode der Kinematischen Elemente
Nr. 26	Steinmann, B.	(1985)	Zum Verhalten bindiger Böden bei monotoner einaxialer Beanspruchung
Nr. 27	Lee, S. D.	(1987)	Untersuchungen zur Standsicherheit von Schlitzen im Sand neben Einzelfundamenten

Mitteilungen des Instituts für Geotechnik der Universität Stuttgart
Hrsg.: Prof. Dr.-Ing. Dr. h.c. U. Smoltczyk

Nr. 28	Kolb, H.	(1988)	Ermittlung der Sohlreibung von Gründungskörpern unter horizontalem kinematischen Zwang
Nr. 29	Ochmann, H.	(1988)	Ebene Grenzzustände von Erdböschungen im stochastischen Sicherheitskonzept
Nr. 30	Breinlinger, F.	(1989)	Bodenmechanische Stoffgleichungen bei großen Deformationen sowie Be- und Entlastungsvorgängen

Nr. 31	Smoltczyk, U. / Breilinger, F. / Schad, H. / Wittlinger, M.	(1989)	Beitrag zur Bemessung von Tunneln in offener Bauweise
Nr. 32	Gußmann, P. / Schanz, T. / Smoltczyk, U. / Willand, E.	(1990)	Beiträge zur Anwendung der KEM (Erddruck, Grundbuch, Standsicherheit von Böschungen)
Nr. 33	Gruhle, H. D.	(1990)	Der räumliche Erdwiderstand vor überwiegend horizontal belasteten Ankerplatten
Nr. 34	Henne, J.	(1995)	Zur Bewehrung von verformten Bodenschichten durch Einsatz zugfester Geokunststoffe
Nr. 35	Wittlinger, M.	(1994)	Ebene Verformungsuntersuchungen zur Weckung des Erdwiderstandes bindiger Böden
Nr. 36	Schad, H.	(1992)	Zeit- und geschwindigkeitsabhängiges Materialverhalten in der Geotechnik – Experimentelle Erfassung und numerische Analyse
Nr. 37	Belz, I.	(1992)	Zur Ermittlung dynamischer Bodenkennwerte in situ aus der Systemantwort des Erregers
Nr. 38	Ma, J.	(1994)	Untersuchungen zur Standsicherheit der durch Stützscheiben stabilisierten Böschungen
Nr. 39	Smoltczyk, U.	(1994)	Sonderheft: 25 Jahre Lehre und Forschung in der Geotechnik
Nr. 40	Rilling, B.	(1994)	Untersuchungen zur Grenztragfähigkeit bindiger Schüttstoffe am Beispiel von Lößlehm

Mitteilungen des Instituts für Geotechnik der Universität Stuttgart

Hrsg.: Prof. Dr.-Ing. P.A. Vermeer

Nr. 41	Vermeer, P. A.	(1996)	Deponiebau und Geotechnik
Nr. 42	Vermeer, P. A.	(1997)	Baugruben in Locker- und Festgestein
Nr. 43	Brinkmann, C.	(1998)	Untersuchungen zum Verhalten von Dichtungsübergängen im Staudammbau
Nr. 44	Fiechter-Scharr, I.	(1998)	Beeinflussung von Erdbaustoffen durch Beimischen eines organophilen Bentonits
Nr. 45	Schanz, T.	(1998)	Zur Modellierung des mechanischen Verhaltens von Reibungsmaterialien
Nr. 46	Akinrogunde, A. E.	(1999)	Propagation of Cement Grout in Rock Discontinuities Under Injection Conditions
Nr. 47	Vogt-Breyer, C.	(1999)	Experimentelle und numerische Untersuchungen zum Tragverhalten und zur Bemessung horizontaler Schraubanker
Nr. 48	Vermeer, P. A.	(1999)	Neue Entwicklungen in der Geotechnik
Nr. 49	Marcher, T.	(2002)	Resultate eines Versuchsprogramms an Beaucaire Mergel
Nr. 50	Marcher, T.	(2003)	Nichtlokale Modellierung der Entfestigung dichter Sande und steifer Tone
Nr. 51	Ruse, N. M.	(2004)	Räumliche Betrachtung der Standsicherheit der Ortsbrust beim Tunnelvortrieb
Nr. 52	Beutinger, P. H.	(2005)	Ein geotechnischer Beitrag zur Standsicherheit mobiler Baumaschinen
Nr. 53	Wehnert, M.	(2006)	Ein Beitrag zur drainierten und undrainierten Analyse in der Geotechnik
Nr. 54	Möller, S. C.	(2006)	Tunnel induced settlements and forces in linings
Nr. 55	Benz, T.	(2007)	Small-Strain Stiffness of Soils and its Numerical Consequences

Nr. 56	Abed, A.	(2008)	Numerical Modelling of Expansive Soil Behaviour
Nr. 57	Hintner, J.	(2008)	Analyse der Fundamentverschiebungen infolge vertikaler und geneigter Belastung
Nr. 58	Russelli, C.	(2008)	Probabilistic Methods applied to the Bearing Capacity Problem
Nr. 59	Peña Olarte, A. A.	(2008)	Influence of Particle Shape on the Global Mechanical Response of Granular Packings: Micromechanical Investigation of the Critical State in Soil Mechanics
Nr. 60	Neher, H. P.	(2008)	Zeitabhängiges Materialverhalten und Anisotropie von weichen Böden – Theorie und Anwendung
Nr. 61	Vermeer, P. A.	(2008)	Von der Forschung zur Praxis: Symposium zum 80. Geburtstag von Prof. U. Smoltczyk
Nr. 62	Satibi, S.	(2009)	Numerical Analysis and Design Criteria of Embankments on Floating Piles
Nr. 63	Lächler, A.	(2009)	Bedeutung herstellungsbedingter Einflüsse auf das Trag- und Verformungsverhalten von Schlitzwänden
Nr. 64	Möllmann, A.	(2009)	Probabilistische Untersuchung von Hochwasserschutzdeichen mit analytischen Verfahren und der Finite-Elemente-Methode

Mitteilungen des Instituts für Geotechnik der Universität Stuttgart Hrsg.: Prof. Dr.-Ing. habil. Ch. Moormann

Nr. 65	Moormann, Ch.	(2011)	7. Stuttgarter Geotechnik-Symposium
Nr. 66	Beuth, L.	(2012)	Formulation an Application of a Quasi-Static Material Point Method

Nr. 67	Moormann, Ch. / Huber, M. / Proske, D.	(2012)	Proceedings of the 10th International Probabilistic Workshop
Nr. 68	Schneider, M.	(2013)	Zur energetischen Nutzung von Tunnelbauwerken - Messungen und numerische Berechnungen am Beispiel Fasanenhoftunnel
Nr. 69	Huber, M.	(2013)	Soil variability and its consequences in geotechnical engineering
Nr. 70	Hamad, F. M.	(2014)	Formulation of a Dynamic Material Point Method and Applications to Soil–Water–Geotextile Systems
Nr. 71	Klein, L.	(2019)	Untersuchungen zum räumlichen aktiven Erddruck bei Baugruben mit rechteckigem Grundriss
Nr. 72	Aschrafi, J.	(2019)	Beitrag zur Seitendruckbeanspruchung von Pfählen in bindigen Böden
Nr. 73	Buhmann, P.	(2019)	Energetisches Potential geschlossener Tunnelgeothermiesysteme
Nr. 74	Labenski, J.	(2020)	Untersuchungen zum Einbringverhalten und dem lateralen Tragverhalten unter monotoner Einwirkung von in nichtbindigen Böden vibrierend installierten Monopiles
Nr. 75	Knopp, J.	(2020)	Verwitterungsabhängige Entfestigungsvorgänge von veränderlich festen Ton- und Tonschluffsteinen am Beispiel von Keupergesteinen
Nr. 76	Salimi, A.	(2021)	Investigation and Evaluation of Rock Mass Characteristics for Development of New TBM Performance Prediction Model in Hard Rock Conditions

Nr. 77	Giridharan, S.	(2022)	Convected Particle Domain Interpolation Method for Large Deformation Geotechnical Problems